SEISMICITY AND TOMOGRAPHIC IMAGING OF THE YELLOWSTONE CRUSTAL MAGMATIC-TECTONIC SYSTEM

by

Jamie Mark Farrell

A dissertation submitted to the faculty of
The University of Utah
in partial fulfillment of the requirements for the degree of

Doctor of Philosophy

in

Geophysics

Department of Geology and Geophysics

The University of Utah

December 2013

The University of Utah Graduate School

STATEMENT OF DISSERTATION APPROVAL

The dissertation of **Jamie Mark Farrell**

has been approved by the following supervisory committee members:

Robert B. Smith	, Chair	**7/1/2013** Date Approved
Ronald L. Bruhn	, Member	**7/1/2013** Date Approved
Barbara Nash	, Member	**7/1/2013** Date Approved
Michael S. Thorne	, Member	**7/1/2013** Date Approved
Stephan Husen	, Member	**7/1/2013** Date Approved

and by **John M. Bartley** , Chair/Dean of

the Department/College/School of **Geology and Geophysics**

and by David B. Kieda, Dean of The Graduate School.

ABSTRACT

Here I evaluate the relationship between the seismicity in the Yellowstone region, in particular the properties of the dominant earthquake swarms, and the three-dimensional Vp seismic velocity structure employing local earthquake tomography. The Yellowstone region averages ~1,500-2,000 earthquakes per year and ~40% occur in swarms. Two of the largest Yellowstone swarms have provided an important opportunity to better understand how and why swarms occur in Yellowstone and how they may be related to active volcanic and tectonic processes. The 2008-2009 Yellowstone Lake swarm consisted of ~800 events with magnitudes ranging from $-0.5 \leq M_C \leq 4.1$ and was modeled by a migration at up to 1 km per day as an upper-crustal dike-intrusion of magma or magmatically-derived aqueous fluids. The 2010 Madison Plateau swarm exhibited over 2,200 earthquakes with magnitudes ranging from $-0.6 \leq M_C \leq 3.9$ and may have occurred on structures at depth related to the nearby Hebgen Lake fault or may have been facilitated by the movement of hydrothermal fluids away from the Yellowstone caldera. Both swarms occurred during a period of caldera deformation reversal from uplift to subsidence and may be indicative of processes involving pressurized fluids escaping the caldera into the surrounding region, allowing the caldera to enter into a time of subsidence. These fluids are derived from the Yellowstone magma reservoir, a large body of crystallizing rhyolite magma that underlies most of the Yellowstone caldera.

To better understand the extent and composition of the Yellowstone magmatic system, we have used data from the Yellowstone Seismic Network from 1984-2011 to image the P-wave velocity structure of the Yellowstone crust using local earthquake tomography using the 83-station Yellowstone seismic network. P-wave tomographic images revealed a large, low P-wave anomaly with values up to -7% change from a background normal crustal velocity structure, underlying most of the Yellowstone caldera at depths of 5-16 km, notably ~50% larger than imaged in earlier studies. The low P-wave velocity body extends ~20 km beyond the caldera to the NE at depths of less than 5 km and has aerial dimension of 30 km wide and 90 km long.

TABLE OF CONTENTS

LIST OF FIGURES

LIST OF TABLES

ACKNOWLEDGEMENTS

I appreciate the support that I've had in conducting research on the Yellowstone volcanic system during my time as a graduate student at the University of Utah. I have been fortunate to have two important projects (including my M.S. thesis work) that have provided me with new data on Yellowstone seismicity as well as challenges and opportunities that have made me think and learn and become a better researcher. There are many individuals and organizations that have assisted me throughout my time here at the University of Utah.

First and foremost I would like to thank Robert B. Smith for being a great advisor during my time as a graduate student at the University of Utah. I have learned a great deal about how to approach and solve scientific problems. Most importantly, Dr. Smith has been a great example to me on how to be continuously curious about how things in the earth work and how we can use geophysical tools to gain knowledge about these processes. We both share a great appreciation for the Yellowstone area. In addition, Dr. Smith has tirelessly strived to upgrade the Yellowstone seismic network to be one of the best volcano monitoring networks in the U.S., providing me with critical data to get the results I present here.

I am greatly indebted to my wife, Nicole, for being extremely patient with me as I have pursued my goal of obtaining my Ph.D. I would like to thank her for all of her

sacrifices that she has made on my behalf. This wouldn't have been possible without you.

Stephan Husen has been a great teacher to me and has materially contributed to my growth as a seismologist and graciously hosted me for two weeks at ETH Zurich. He was always available to answer any questions that I may have had and this project would not have come to fruition without his help.

I would also like to thank my other advisory committee members, Ron Bruhn, Michael Thorne, and Barbara Nash for always being available to answer my questions.

Many other individuals at the University of Utah have also helped me along my graduate path, including my fellow graduate students and office mates and those at the University of Utah Seismograph Stations. These include Greg Waite, Fred Massin, Christine Puskas, Wu-Lung Chang, Michael Jordan, Taka-aki Taira, Bonnie Pickering-White, Katrina and Aaron DeNosaquo, Paul Gettings, Jim Pechmann, Kris Pankow, Relu Burlacu, Keith Koper, Paul Roberson, Mark Hale, Katherine Whidden, Bill Blycker, Martha Knowlten, and Sheryl Peterson.

I would especially like to thank Dave Drobeck for all his hard work in maintaining and upgrading the Yellowstone Seismic Network from which my data was derived and for sharing many trips together in Yellowstone including getting chased by an angry cow elk while trying to fix a broken seismograph station.

The staff of the Yellowstone Center for Resources has been instrumental in allowing us to work in Yellowstone and collect the data that we need to do these kinds of studies. In particular, I would like to thank Hank Heasler for many conversations about Yellowstone and for aiding in multiple field seasons.

Tobias Diehl was instrumental in helping me with the tomographic inversion project and has provided me with many of his codes and has helped me understand them. Ludger Küperkoch and Sebastian Wehling-Benatelli were instrumental in helping me to use the picking program, PILOT and spent many hours working on the code on my behalf to get it to work with my data.

The staff of the University of Utah Department of Geology and Geophysics have helped me in administrative tasks and travel including Chris Carver, Thea Hatfield, Judy Martinez, Anita Austin Tromp, and Kim Atwater. Computer support at the University of Utah was provided by Dan Trentman, Erwin McPherson, and Mickey Begent.

Funding for my research has come from multiple sources including The Brinson Foundation, the U.S. Geological Survey Volcano Hazards Program grant 01HQAG0008 Operation and Development of an Earthquake Information System at Yellowstone: The Yellowstone Seismic and GPS Network as well as grants from the Carrico Foundation. Additional funding was provided by the National Science Foundation Continental Dynamics Program grants EAR 9725431, 0314298, and 9316289 and the NSF GEOsciences Network (GEON) project, EAR-072426. Funding support also came from teaching assistantships through the Department of Geology and Geophysics at the University of Utah.

I made extensive use of Lawrence Livermore National Laboratory's Seismic Analysis Code, SAC2000 for data processing. Most of the figures were generated with GMT [*Wessel and Smith*, 1998].

CHAPTER 1

INTRODUCTION

The Yellowstone volcanic system (Figure 1.1) is of key interest because it is an active continental hotspot that is readily accessible for geophysical research. Because of this, there is a long history of geophysical monitoring in the Yellowstone region. The initial seismic network was installed in 1972 and geodetic monitoring began when the road system was established in the park in 1923. Today, a modern, digital seismic and GPS network provides high quality data that is necessary for such in depth, integrative geophysical studies.

This study uses the seismic and geodetic data that has been collected from 1984 – 2011 in Yellowstone to investigate the relationship between Yellowstone seismicity and the active crustal magma system. The Yellowstone magma reservoir provides the energy for the world famous hydrothermal system found in Yellowstone as well as the ground deformation and intense seismicity. Understanding how these things are related and how the magma reservoir influences the seismicity and deformation patterns is an important topic. A better understanding of these processes will help us to better estimate the seismic hazards as well as enable us to better respond to events, such as large earthquakes or earthquake swarms. In addition, it will provide us critical information on assessing volcanism, magma transport, heat flow, earthquakes, and tectonic-volcano interactions in

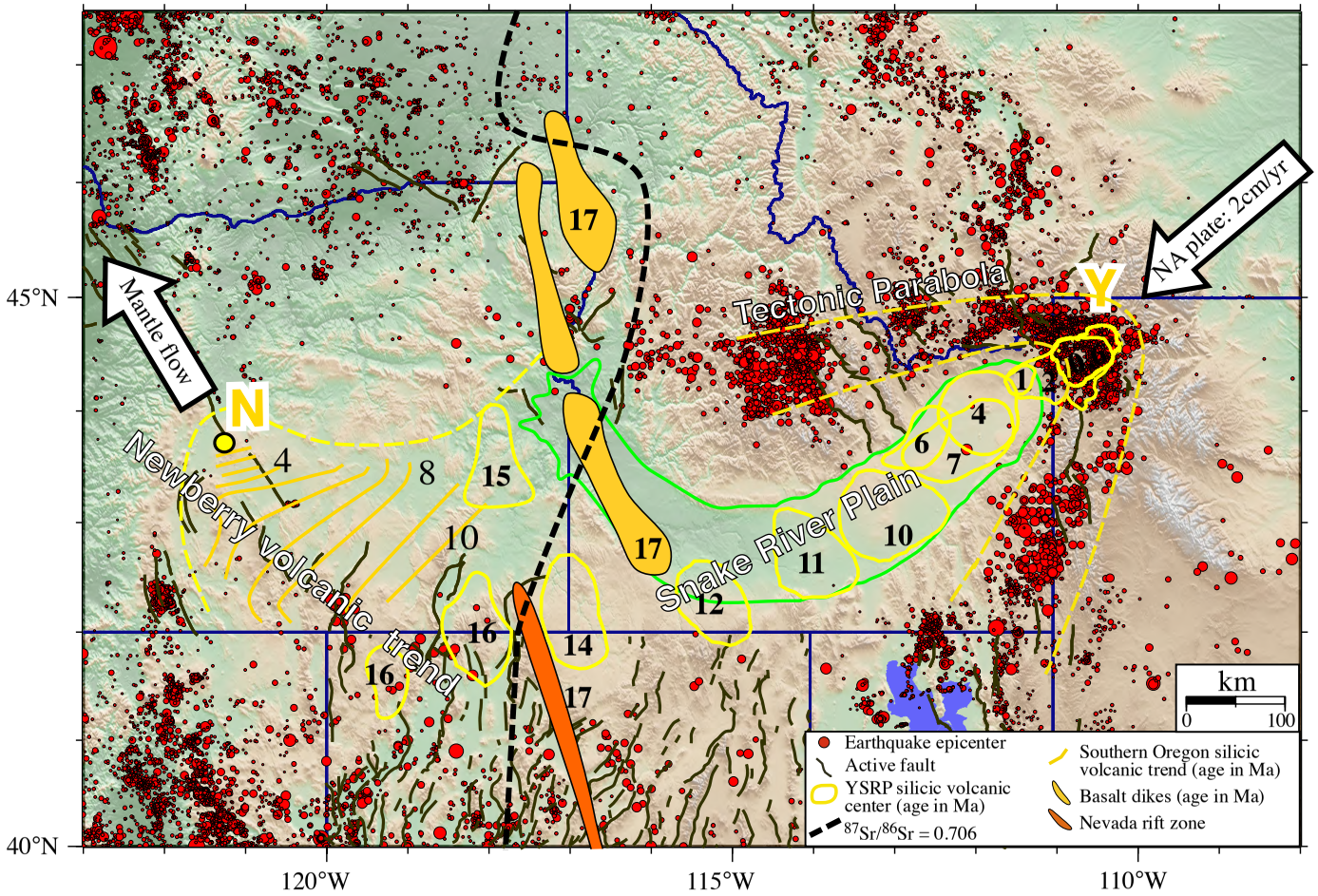

Figure 1.1. The Yellowstone-Snake River Plain silicic volcanic system showing the track of theYellowstone hotspot (Y) and its ~17My progression as the North American Plate moved across the Yellowstone mantle plume. After *Smith and Siegel* [2000]. This map shows the relative motion of age-transgressive SRP silicic volcanic centers [*Armstrong et al.*, 1975; *Smith and Braile*, 1984; *Pierce and Morgan*, 1990, 1992; *Kuntz et al.*, 1992; *Smith and Braile*, 1994; *Perkins and Nas*h, 2002] opposite to the direction of North America plate motion (large arrow) [*Smith and Sbar*, 1974].

the region. Moreover, the influence of the Yellowstone volcanic system extends well beyond the border of the National Park, extending to other large tectonic systems such as the Hebgen Lake and Teton faults. Understanding how the Yellowstone volcanic system can influence the broader region has implications on our understanding of the seismic and volcanic hazards of the Intermountain west.

We utilize the seismic and GPS data to investigate two large earthquake swarms that occurred in Yellowstone in 2008 and 2010. Results show that these swarms may be indicative of fluid movement in the shallow crust related to the Yellowstone magma reservoir. We also analyzed the 2010 Gros Ventre earthquake sequence that occurred in 2010 around 70 km south of the Yellowstone caldera. In addition, we investigate the P-wave velocity structure of the crust using local earthquake tomography. Results show a large, low P-wave velocity anomaly that underlies much of the Yellowstone caldera, extending ~20 km NE of the caldera boundary.

Yellowstone Hotspot

The Yellowstone National Park, WY, region has experienced three giant silicic caldera-forming eruptions in the past 2 million years, as well as numerous smaller eruptions (primarily rhyolite flows) in between and post-super eruptions. The last three major eruptions occurred 2.05 million years, 1.2 million years, and 0.64 million years ago with an estimated total eruption of ~6,500 km^3 of material in the past 2 million years [*Christiansen*, 2001]. The Yellowstone hotspot track can be traced 800 km along the eastern Snake River Plain, which contains a line of progressively older eruptive silicic volcanic centers extending from Yellowstone National Park, SW to the 16 Ma McDermitt

volcanic field on the Oregon-Nevada border [*Christiansen and Yeats*, 1992] (Figure 1.1). Approximately 142 ash-fall eruptions have been identified along the track of the Yellowstone hotspot, each of which may represent a single explosive caldera-forming eruption [*Perkins and Nash,* 2002].

Recent seismic tomography of the Yellowstone hotspot shows that it is associated with an upper mantle plume [*Smith et al., 2009*; *Waite et al.*, 2006] that dips to the northwest down into the transition zone. The surprising discovery of the dipping plume is a result of tilt due to mantle flow [*Smith et al.*, 2009]. More recently, using data from the EarthScope Transportable Array as well as regional networks, *Obrebski et al.* [2010] show the plume extending beyond the transition zone into the lower mantle at ~900 km. However, the plume reverses and dips back to the SE beyond the transition zone. The plume provides the heat source for the bimodal basaltic-rhyolitic volcanism found throughout the Yellowstone-Snake River Plain (YSRP), the notable 600-km wide topographic swell that is 300 m high and coincident with a geoid anomaly 12 m above background levels [*Smith and Braille*, 1994], and frequent earthquakes [*Massin et al.*, 2013; *Farrell et al.,* 2009; *Smith and Sbar*, 1974]. It also provides that heat and energy source needed to produce the shallow, crustal magma reservoir that underlies the current hotspot location beneath Yellowstone National Park. High heat flow of up to 2000 mW/m^2, which is about 30 times the continental average, is indicative of crystallization and cooling of 0.1 km^3 of rhyolitic magma from 900º to 500ºC per year [*Fournier*, 1989]. Moreover, a -60 mGal gravity anomaly roughly within the youngest 0.64 Ma caldera with the strongest gravity low located NE of the caldera (Figure 1.2) is evidence for a large, shallow low-density body.

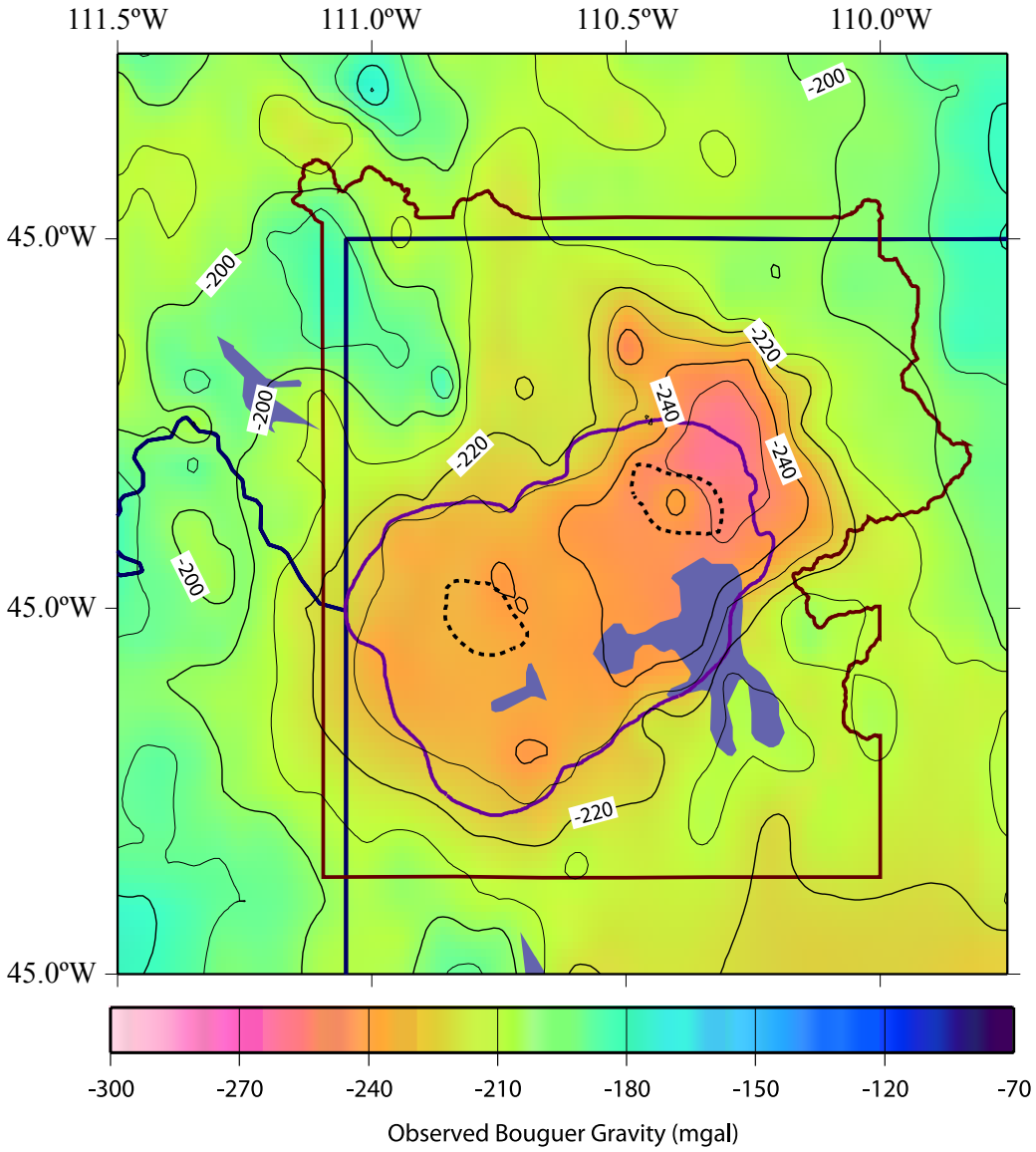

Figure 1.2. Bouguer gravity anomaly of the Yellowstone region showing the -60 mGal gravity low associated with the Yellowstone caldera (purple line). The largest low gravity anomaly is located in the NE caldera region and extends ~20 km to the NE of the mapped caldera boundary.

Yellowstone Seismicity

Yellowstone is well known as one of the most seismically active areas in the United States and is part of the Intermountain Seismic Belt (ISB) (Figure 1.3), an area of persistent seismicity that marks the eastern edge of the Basin and Range province with the Colorado Plateau/Rocky Mountains that extends from northern Arizona through the Wasatch Front, eastern Idaho, western Wyoming, Yellowstone, and western Montana [*Smith and Arabasz*, 1991]. Over 34,000 earthquakes ($-1.0 < M_C < 6.1$) have been located in the Yellowstone region with an annual rate of 1,500 – 2,000 earthquakes per year from 1973 to 2013 [*Farrell et al.,* 2009] (Figure 1.4). Furthermore, the Yellowstone area has experienced the largest historic earthquake in the ISB, the deadly August, M_W7.3 1959 Hebgen Lake, Montana, earthquake located ~25 km northwest of the Yellowstone caldera that claimed 28 lives [*Doser*, 1985]. It is generally taken as the maximum credible earthquake for earthquake hazard studies in extensional tectonic regimes. The 1959 Hebgen Lake earthquake occurred on the two south dipping fault planes of the Hebgen Lake and Red Canyon faults, which are Basin and Range style faults about 20 km northwest of the Yellowstone caldera. The caldera has also experienced a M_L6.1 earthquake in 1975 southeast of Norris Junction [*Pitt et al*., 1979; *Smith and Arabasz*, 1991].

Prior to the arrival of the Yellowstone hotspot, the region was influenced by the Sevier and Laramide orogenies, which were dominated by east-west compression expressed by low angle reverse (thrust) faults. The thin-skinned thrusting of the Sevier Orogeny resulted in thicker sediments in the fold and thrust belt. The thick-skinned thrusting of the Laramide Orogeny is responsible for the numerous basement uplifts

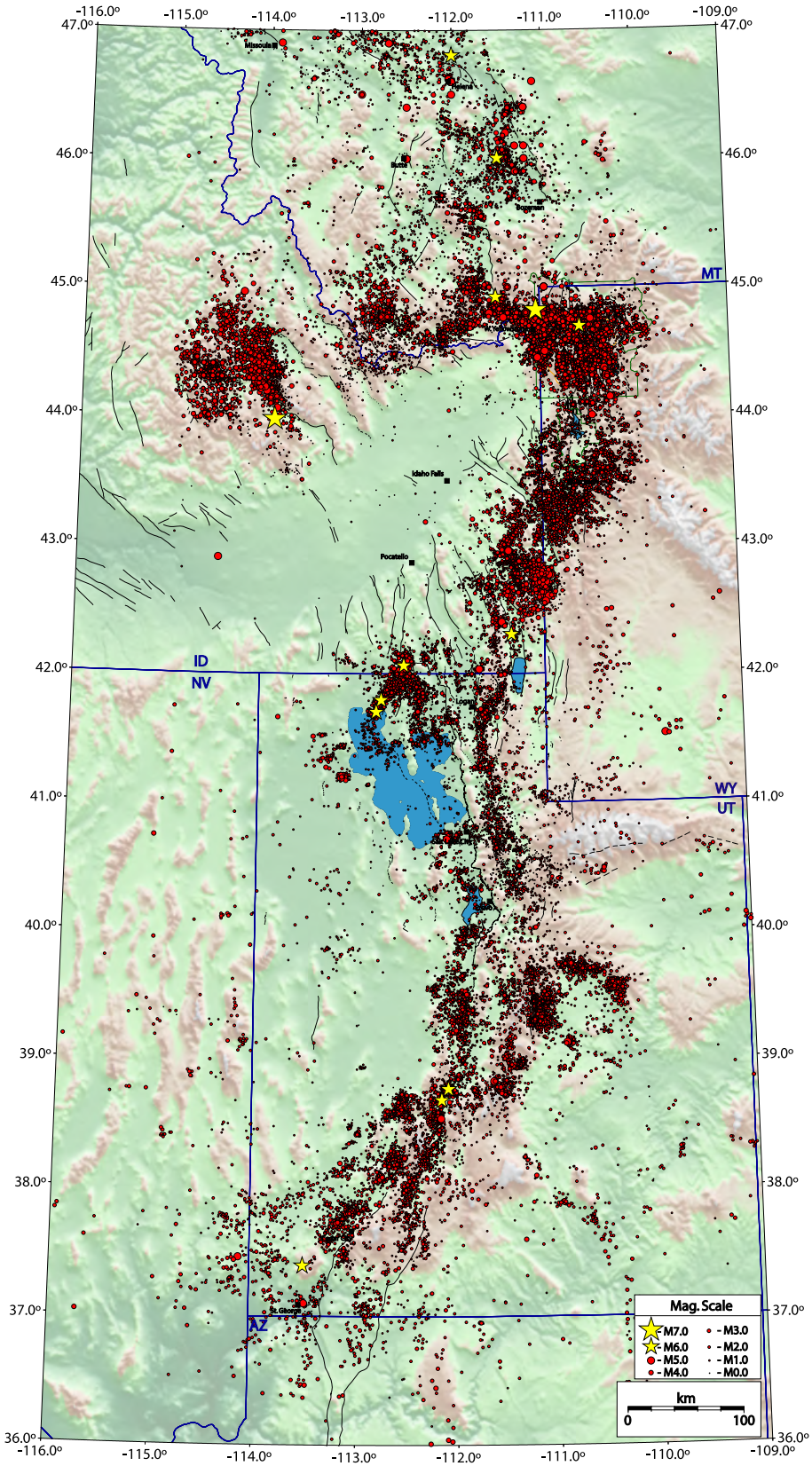

Figure 1.3. Earthquakes of the Intermountain Seismic Belt (ISB). Yellow stars are earthquakes with magnitudes greater than 6.

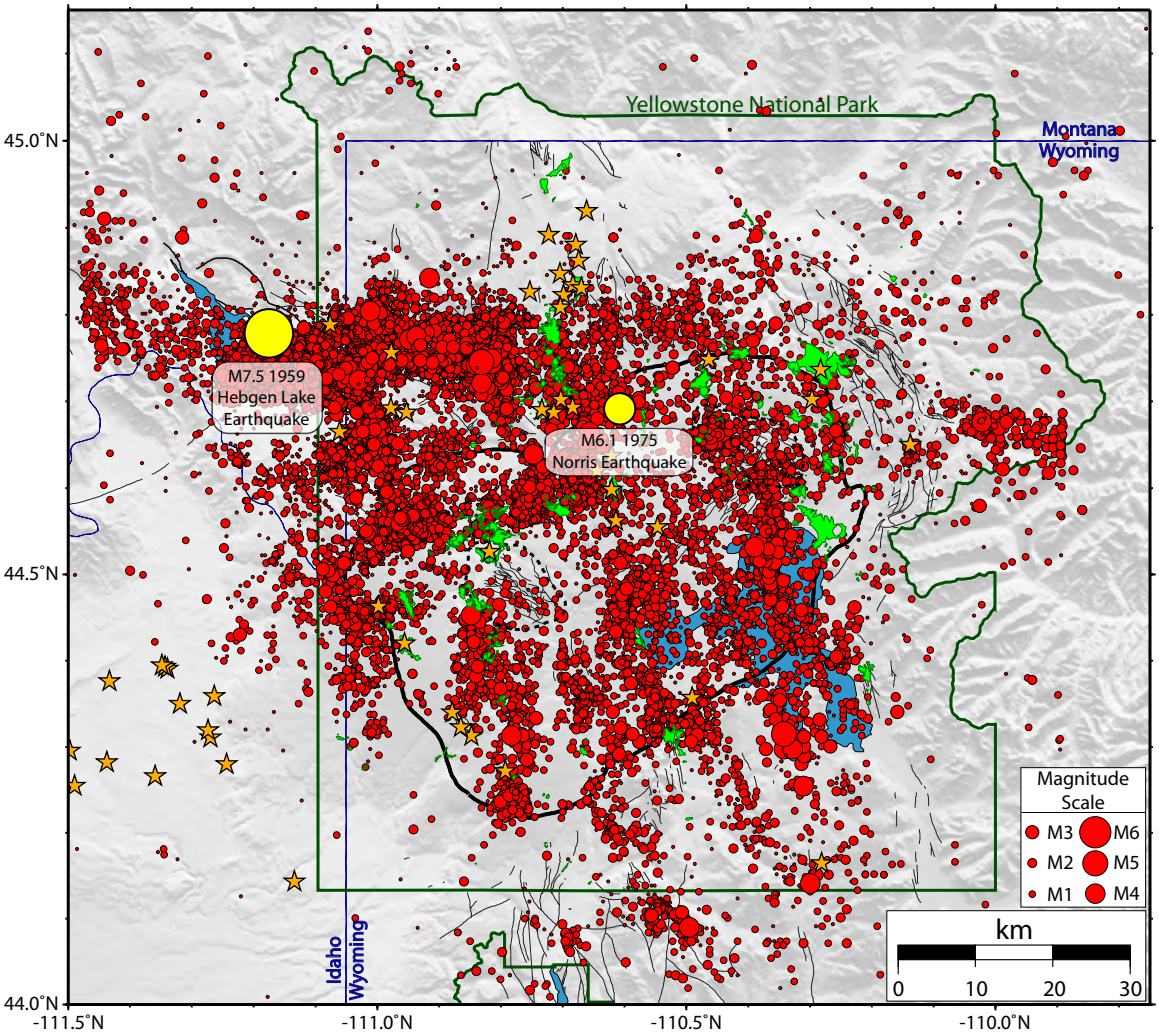

Figure 1.4. Yellowstone earthquakes from 1973 to 2013. Epicenters are shown as red dots, postcaldera, 0.64 My, volcanic vents are shown as orange stars, and Quaternary faults are shown as black lines. The outline of the 0.64 Ma Yellowstone caldera from the last major Yellowstone eruption is shown in black. The two volcanic resurgent domes are outlined as black dotted lines. Hydrothermal areas are shown in green.

observed in Wyoming and Montana [*Settles*, 2007].

Following this period of compression, the interior west of the U.S. moved into an episode of extension giving rise to the Basin and Range Province that is still today actively stretching the crust by as much as 100-300% [*Proffett*, 1977], with the majority of the extension occurring before 10 Ma [*Zoback et al.*, 1981]. Coincidentally, the initiation of the Yellowstone hotspot 16 Mya occurred at the same time as the initiation of Basin and Range extension leading some to believe that the thinning of the crust by Basin and Range extension was necessary to allow the Yellowstone plume to penetrate to the surface [*Rogers et al.*, 1990]. For the last 16 million years the North American plate has been moving southwest over the hotspot toward its present location beneath Yellowstone National Park (Figure 1.1).

Because of the complex tectonic history of the region, the young Yellowstone volcanic system has overprinted its signature over those that preceded it. There are large Basin and Range normal faults in and around Yellowstone that have moderate to high Quaternary slip rates such as the Hebgen Lake, Teton, Gallatin, and Mt. Sheridan faults (Figure 1.5). However, these large normal faults are truncated at the caldera boundary (Figure 1.5). It is believed that these faults were once continuous features across the region and were destroyed/buried in the cataclysmic caldera forming eruptions over the last 2 million years [*Smith and Seigel*, 2000].

Overall, seismic activity in Yellowstone is characterized by episodic occurrences of small, generally shallow, earthquake swarms [discussed here in Chapter 2; *Farrell et al.*, 2009]. The most intense area of seismicity extends from the Hebgen Lake area east to the northern caldera boundary near Norris Junction (Figure 1.4). Although this area

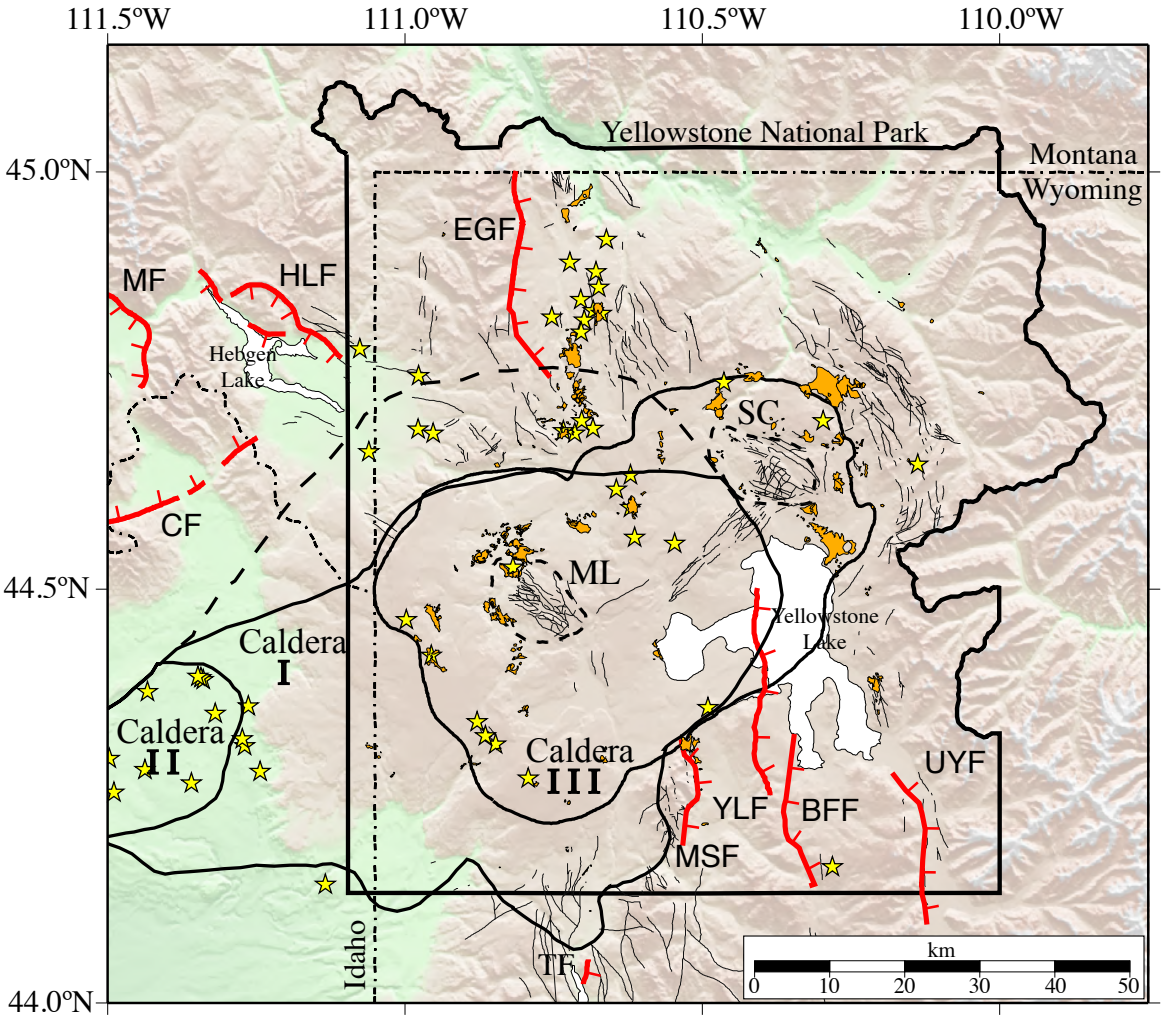

Figure 1.5. A topographic map of the Yellowstone volcanic field showing the three calderas and Cenozoic faults as mapped by *Christiansen* [2001]. Major faults are shown in red. MF = Madison fault, HLF = Hebgen Lake fault, CF = Centennial fault, EGF = East Gallatin fault, TF = Teton fault, MSF = East Mt. Sheridan fault, YLF = Yellowstone Lake fault, BFF = Buffalo Fork fault, and UYF = Upper Yellowstone Valley fault. The calderas are shown by age: I-2.0 Ma, II-1.2 Ma, and III-0.64 Ma. The youngest caldera is commonly called the Yellowstone caldera. The dashed line outlines a region of highly fractured crust and high seismicity that may mark the extent of caldera I. The northern boundary of that region is highlighted by a topographic contrast that may have resulted from the 2.1 Ma catastrophic eruption. ML and SC represent the Mallard Lake and Sour Creek resurgent domes, which are outlined with a dashed line (modified from *Waite* [1999]).

only constitutes 16% of the area, it contains 75% of the epicenters. Linear bands of epicenters occur within and adjacent to the caldera and are aligned generally north-northwest parallel to alignments of postcaldera volcanic vents and the surrounding large regional faults. These normal faults are cut by the 0.64 Ma caldera and are believed to have once been continuous Basin-Range faults [*Smith and Seigel*, 2000] (Figure 1.5).

A Deforming Yellowstone Caldera System

Geodetic measurements (GPS and spirit leveling) in Yellowstone began when the road system was established in 1923 with leveling surveys. After resurveying the extensive network of leveling benchmarks for the vertical component of deformation, to first order, first class precision in 1975, 1976 and 1977, *Pelton and Smith* [1982] discovered that there was an extraordinary signal of caldera deformation of ~740 mm of caldera uplift in ~50 year time period, averaging ~15 mm/yr (Figure 1.6). Subsequent leveling found different rates of uplift in the northeast and southwest caldera continuing through 1984 [*Dzurisin et al*., 1990]. An unexpected episode of caldera subsidence at 10 ± 20 mm/yr that began in 1984-1985 was first measured by the first GPS campaigns, giving an estimate of both vertical and horizontal deformation rates [*Meertens and Smith*, 1991]. More recent interferometric Synthetic Aperture Radar (InSAR) measurements between 1992 and 2003 revealed changing centers of subsidence and uplift in the northeast caldera boundary region [*Wicks et al.*, 1998, 2006]. In 2004, the Yellowstone caldera entered a period of accelerated uplift with rates as high as 7 cm/yr [*Chang et al.*, 2007, 2010]. Modeling of this uplift period, using both GPS and InSAR data, revealed the source as an inflating sill near the top of the tomographically imaged magma reservoir

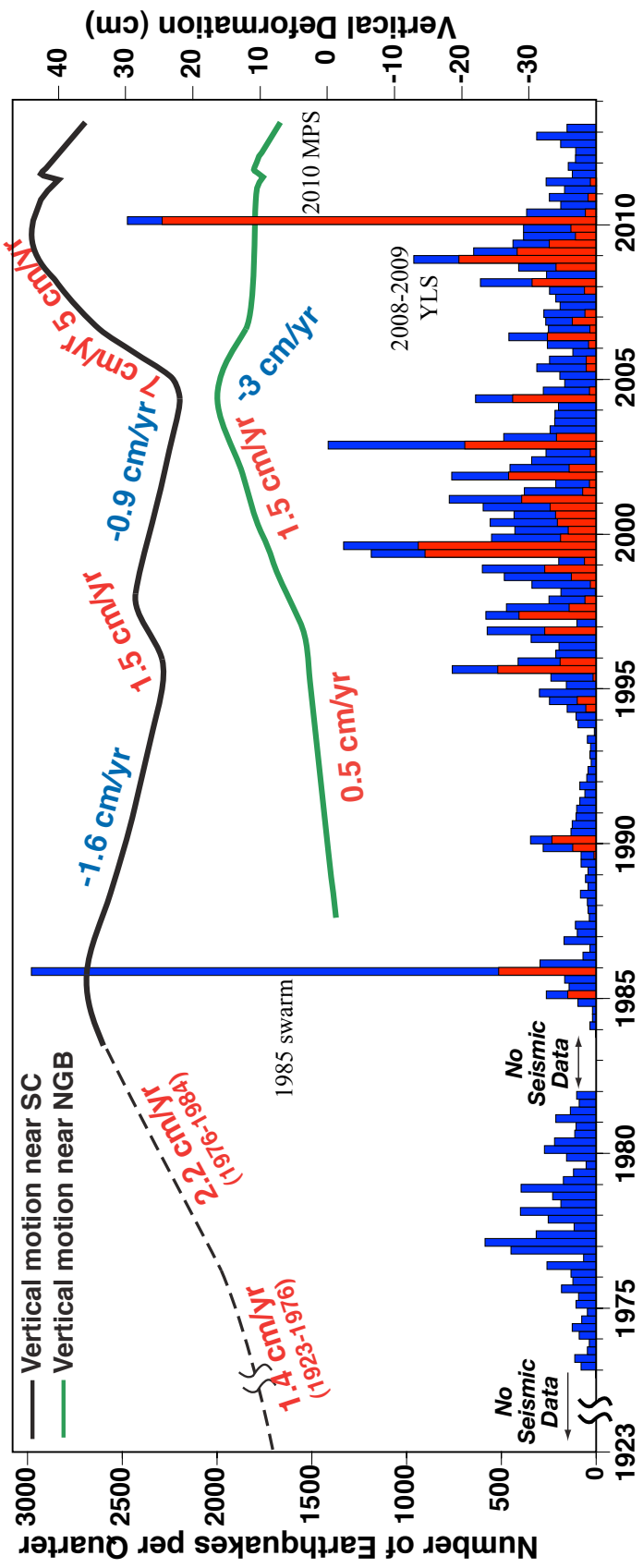

Figure 1.6. Time history of Yellowstone seismicity and deformation, 1923-2013. Quarterly earthquakes counts in the Yellowstone region are shown as blue bars. Red bars indicate seismicity associated with earthquake swarms. The black line represents the deformation of areas within the caldera and the green line represents deformation of the Norris Geyser Basin area outside the caldera.

at about 8-10 km depth [*Chang et al.*, 2007, 2010].

Overall, Yellowstone experiences decadal periods of uplift and subsidence that are believed to be due to vertical and lateral migration during recharge of the crustal magma reservoir (Figure 1.6). Notably, large earthquake swarms in Yellowstone appear to be correlated with the onset of periods of deformation reversal from uplift to subsidence (Figure 1.6) suggesting that these swarms are an indication of fluid movement in the shallow crust escaping the caldera into the surrounding region. The three largest modern Yellowstone swarms all coincided with one of these deformation reversals.

The 1985 swarm, the largest swarm recorded in Yellowstone, occurred near the northwest boundary of the 0.64 Ma Yellowstone caldera and was modeled as a migrating swarm front moving ~150 m/day to the NW and outward from the caldera [*Waite and Smith*, 2002]. The 2008-2009 Yellowstone Lake swarm occurred beneath northern Yellowstone Lake and experienced an unusually high migration rate of ~1 km/day with shallowing focal depths from 10 to 2 km through time [*Farrell et al.*, 2010; *Massin et al.*, 2013; this study]. The accelerated uplift rate decreased from ~3.5 cm/yr to ~1.7 cm/yr prior and after this swarm.

The 2010 Madison Plateau swarm on the western caldera boundary occurred about 10 km to the south of the 1985 swarm and showed similar focal mechanisms and source geometries [*Massin et al.*, 2013; *Shelly et al.*, 2013; this study]. Following the 2010 swarm, caldera deformation reversed from uplift at a rate of ~1.7 cm/yr prior to the swarm to ~2.6 cm/yr of subsidence following the swarm. It is hypothesized that the movement of magmatic or magmatically derived fluids triggers these swarms as they move away from the caldera [*Massin et al.*, 2013; *Shelly et al.*, 2013]. The escaping

fluids in turn cause a pressure decrease that allows the caldera to move into a phase of subsidence.

Yellowstone Crustal Structure

Several studies have progressively imaged the Yellowstone crustal structure using controlled source [*Schilly et al.*, 1982; *Smith et al.*, 1982; *Lehman et al.*, 1982] and local earthquake tomographic (LET) techniques [*Benz and Smith*, 1984; *Miller and Smith*, 1999; *Husen et al.*, 2004].

The first studies to find evidence of a low P-wave body beneath the Yellowstone caldera used controlled source data from eleven in-line refraction profiles, recorded with a 150-station array during the 1978 Yellowstone-Snake River Plain seismic experiment [*Schilly et al.*, 1982; *Smith et al.*, 1982; *Lehman et al.*, 1982]. *Schilly et al.* [1982] found evidence for a major low-velocity body with a decrease in velocity of at least 10%, coincident with a -30-mgal gravity low in the northeast part of the Yellowstone Plateau, with a maximum depth to the top of the body of 3 km and a minimum depth of 9 km to the bottom. Importantly, using a fan profile of stations and a source shot in the northeast corner of Yellowstone, *Schilly et al*. [1982] observed large first arrival delays (up to 1.5 s) for stations that were recording raypaths that passed through the NE caldera region (Figure 1.7).

A study by *Lehman et al.* [1982], using 173 raypaths, also found low P-wave velocities beneath the caldera with modeled Vp as low as 4.0 km/s beneath the NE caldera region that is interpreted to represent a zone of high temperature associated with a partial melt and/or large steam-water volumes near the Hot Spring Basin (Figure 1.8).

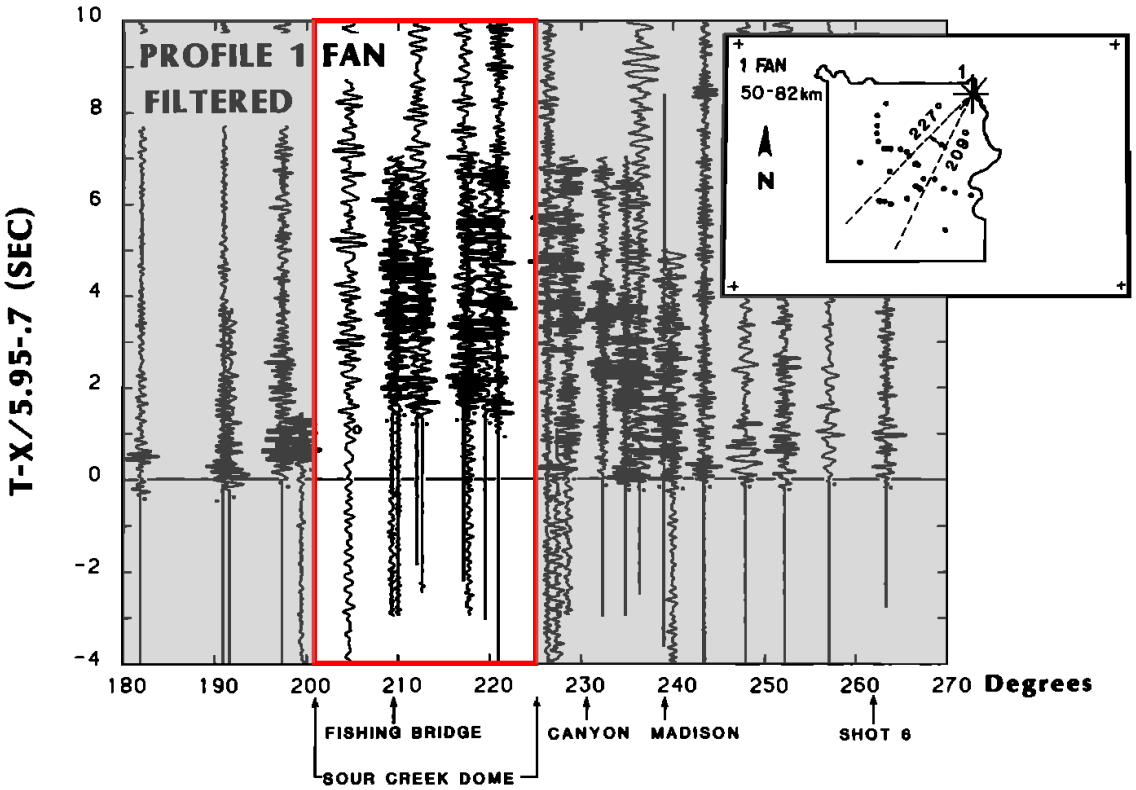

Figure 1.7. Seismic record section plotted in an azimuthal fan. The seismograms are plotted in reduced travel-time vs. azimuth from 180º to 264º recorded from shot point 1. Data correspond to distance range of 50-82 km, and all are interpreted to lie along the P2 (Pg) branch. Seismograms have been band-pass-filtered with a 3.1-Hz to a 10.9-Hz pass band. Seismograms outlined by the red box indicate those that show large delay times of up to 1.5s. Modified from *Schilly et al.* [1982].

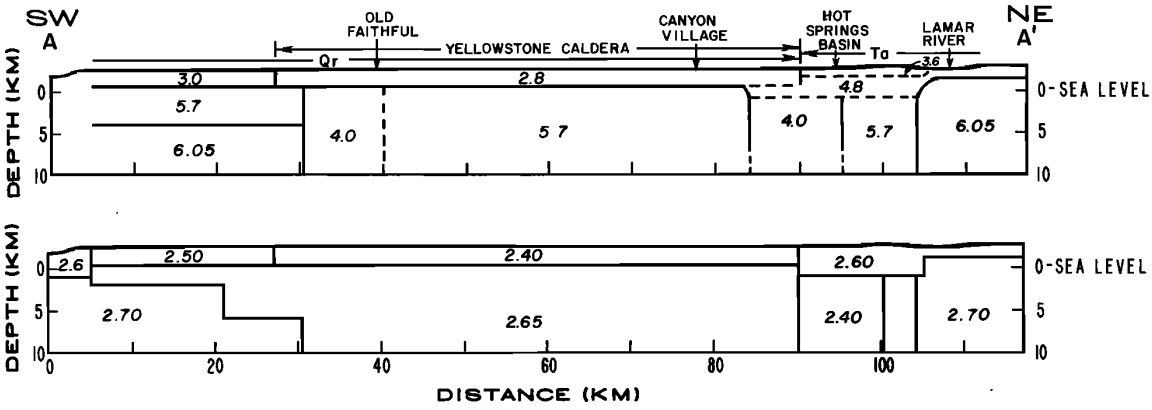

Figure 1.8. Northeast-southwest cross sections through three-dimensional seismic P-wave velocity model (top) and corresponding density model (lower) of *Lehman et al.* [1982].

These early controlled source experiments and the first evidence of a body of low P-wave velocities beneath the caldera paved the way for later LET studies that were able to image an extended body of low P-wave velocity of around -5% to -10% Vp at depths of 6-16 km, which is interpreted to be crystallizing magma beneath the Yellowstone caldera. *Benz and Smith* [1984], using 422 raypaths, showed two zones of unusually low velocities (Figure 1.9). In the northeast, velocities are as low as 4.9 km/s and are interpreted as evidence for a possible vapor-dominated body or shallow melt. In the southwest caldera, *Benz and Smith* [1984] find velocities as low as 5.2 km/s and interpreted them as a thermally influenced fracture system.

A later LET study of the Yellowstone volcanic system by *Miller and Smith* [1999] used a combination of 7,942 local earthquakes and 16 controlled-source explosions and found a caldera-wide 15% decrease from regional P-velocities at depths of 6 to 12 km that is coincident with a -60 mGal gravity anomaly. In addition, they found a smaller but more pronounced low velocity zone underlies the northeast caldera rim from depths less than 2 km to greater than 4 km. P-velocities in this zone are as low as 3.4 km/s at 4 km depth, a 37% reduction from the starting P-velocity of 5.4 km/s and are explained by the presence of a fractured fluid (gas or gas/liquid) saturated, and possibly hydrothermally altered volume of rock [*Miller and Smith*, 1999].

The most recent LET study, prior to this study, of the Yellowstone volcanic system used 3,374 earthquakes, including 34,538 P-arrival times and 5,875 S-P arrival times. Results confirmed the existence of a low Vp-body beneath the Yellowstone caldera at depths greater than 8 km, possibly representing hot, crystallizing magma [*Husen et al.*, 2004]. In addition, they found a volume of anomalously low Vp and Vp/Vs in the

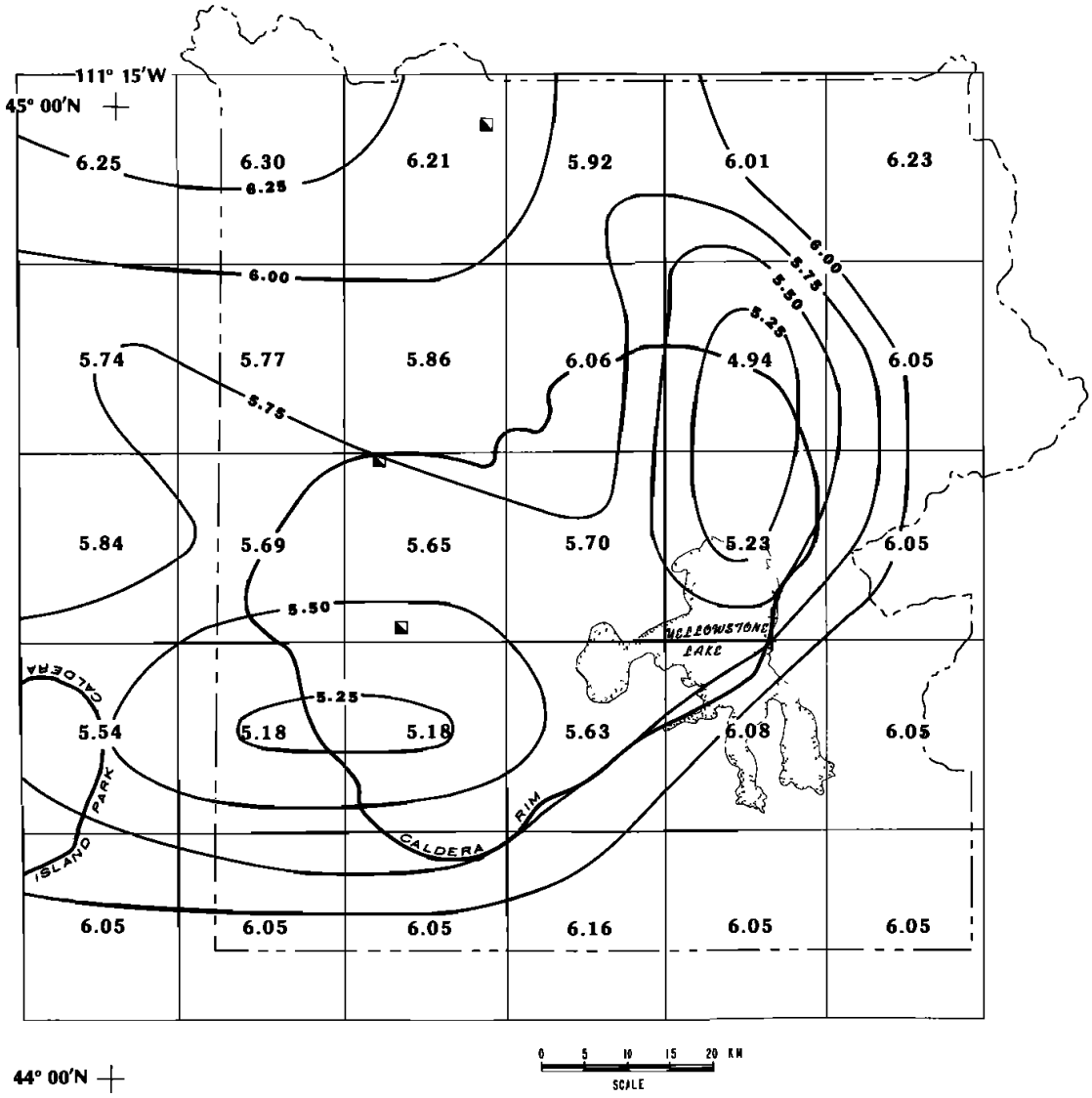

Figure 1.9. Contoured P-wave velocity model of *Benz and Smith* [1984] showing the reduced P-wave velocity in the northeast caldera region.

northwestern part of the Yellowstone volcanic field at shallow depths < 2.0 km. Theoretical calculations of changes in P- to S-wave velocity ratios indicate that this anomaly can be interpreted as porous, gas-filled rock [*Husen et al.*, 2004].

These studies use limited data from the University of Utah Seismograph Stations (UUSS) due to limited time periods or limited station coverage. Using the entire database of Yellowstone earthquakes (1984-2011) would provide better coverage due to more earthquakes and also due to the ability to use newer stations that have been installed in the NE caldera region. Using the entire dataset, from 1984 – 2011, as well as using newer stations, allows us to get better ray coverage increasing our resolution and expanding the area in which we are able to resolve crustal structures.

DeNosaquo et al. [2009], using gravity taken at over 30,000 stations in the Yellowstone-Snake River Plain and surrounding region, modeled the density structure of the crust. The Yellowstone Plateau volcanic field density model reveals low-density partial melt 10 km beneath the caldera that shallows under the northeastern caldera and continues laterally 20 km north of the caldera boundary and notably increases the previously estimated size of the magma reservoir by ~20%. The caldera melt body has a density of 2,520 kg/m_3 and a significantly lower value of 2,470 kg/m_3 for the northeastern caldera melt body [*DeNosaquo et al.,* 2009].

Krukoski [2002] evaluated the density field of Yellowstone by inverting the complete Bouguer gravity data to model the three-dimensional density structure. A three-dimensional "focusing" inversion technique was employed to construct the density model. The Yellowstone complete Bouguer gravity inversion produced a model that contained a large negative density anomaly, from the 2.7 gm/cm^3 background density,

beneath the northeast corner of the Yellowstone caldera. The density contrast ranged from $-0.4 < \Delta\rho < -0.1$ gm/cm^3 with an error of +/-0.1 gm/cm^3. The density anomaly ranges in depth from 6-16 km and shows the largest density contrast at 10 km depth. The density anomaly spatially coincides with the Hot Springs Basin hydrothermal system as well as the Mirror Plateau rim-boundary fault zone similar to the past tomography results described above.

Objectives

The objectives of my research are to evaluate the Yellowstone crustal magmatic system by mapping the three-dimensional distribution of seismic velocities to determine the source, composition, and geometry of the Yellowstone crustal magma reservoir. In addition, I analyze large earthquake swarms and seismic sequences in the area to evaluate the relationship between the Yellowstone volcanic system and the accompanying seismicity both locally and regionally.

I used data from the evolving University of Utah Seismograph Stations (UUSS) database of earthquake hypocenters and waveforms to examine some of the large earthquake sequences that have occurred in and around the Yellowstone-Teton region. In addition to collecting more data with time, the Yellowstone seismic network continues to expand by both adding additional stations, and upgrading single-component short-period seismometers to 3-component broadband and accelerometer stations (Figure 1.10).

In addition, I use the entire waveform database including 1,159,724 event based waveforms as well as the accompanying phase data for 45,643 earthquakes, from 1984-2011 and an automatic picking algorithm to create a consistent set of earthquake P-wave

Figure 1.10. Time history plot of the Yellowstone Seismic Network showing the build out and steady improvement in both number of stations and an increased amount of digital, 3-component, broadband and accelerometer stations.

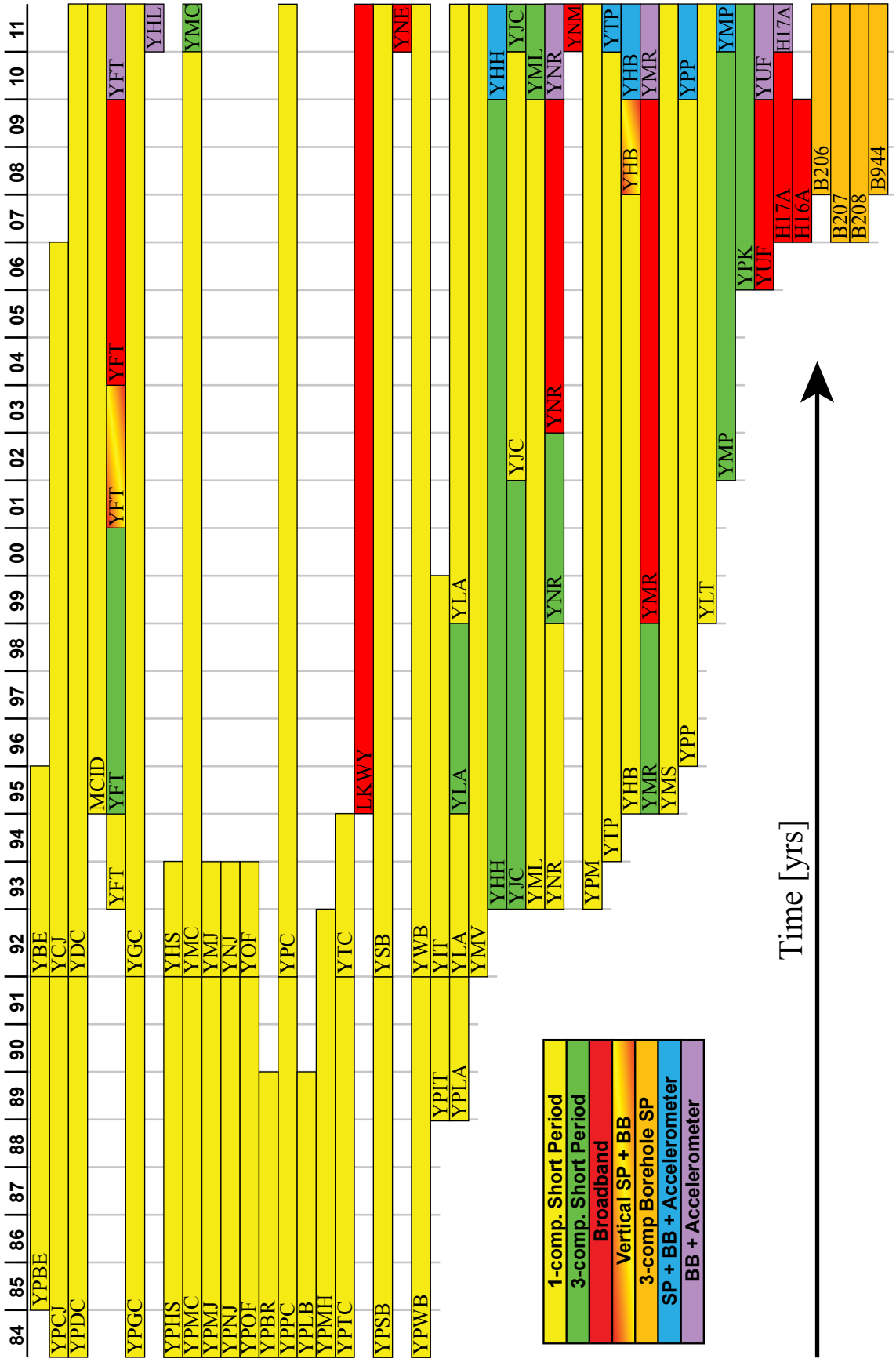
84
85
86
87
88
89
90
91
92
93
94
95
96
97
98
99
00
01
02
03
04
05
06
07
08
09
10
11
YPBE
YBE
YPCJ
YCJ
YPDC
YDC
MCID
YFT
YFT
YFT
YFT
YPGC
YGC
YHL
YPHS
YHS
YMC
YPMC
YMC
YPMJ
YMJ
YPNJ
YNJ
YPOF
YOF
YPBR
YPPC
YPC
YPLB
YPMH
YTC
YPTC
LKWY
YPSB
YSB
YNE
YPWB
YWB
YPIT
YIT
YLA
YPLA
YLA
YLA
YMV
YHH
YHH
YJC
YJC
YJC
YML
YML
YNR
YNR
YNR
YNR
YNM
YPM
YTP
YTP
YHB
YHB
YHB
YMR
YMR
YMR
YMS
YPP
YPP
YLT
YMP
YMP
YPK
YUF
YUF
H17A
H17A
H16A
B206
B207
B208
B944
1-comp. Short Period
3-comp. Short Period
Broadband
Vertical SP + BB
3-comp Borehole SP
SP + BB + Accelerometer
BB + Accelerometer
Time [yrs]

first arrival picks with consistent uncertainty estimates. This dataset will be used to perform a three-dimensional inversion to invert for the velocity structure.

Moreover, I studied the occurrence of an important earthquake sequence in 2010 70 km south of Yellowstone in the Gros Ventre Range, a part of the transition between the deforming Basin-Range south of the caldera and the stable N. American continent that occurred during the time of my dissertation work. This sequence was examined in the framework of how seismicity in the surrounding area of the Yellowstone hotspot is effected by large scale uplift and subsidence of the general hotspot structure and how uplift of Yellowstone could trigger surrounding earthquakes.

My dissertation is organized in chapters following the logical sequence of the research that I have performed. This includes the introduction and basic geologic framework of the Yellowstone volcanic and tectonic system, the general properties of seismicity, crustal structure and kinematics of ground deformation from geodetic methods. These lead into detailed studies of Yellowstone earthquake swarms, emphasizing new computer codes required for analyses of the data. I evaluate the two most recent swarms. I then evaluate the Gros Ventre earthquake swarm and some observations of precise gravity changes across the caldera, which compliments the GPS studies, in order to evaluate the complimentary change in height and elevation that theoretically separate out the free-air gravity signal from that of mass, in our case, magma migration. I then conclude with the major part of my dissertation research, an entirely new analysis of the three-dimensional P-wave velocity structure of the Yellowstone caldera, updated from much earlier 2004 studies, incorporating automatic picking of the entire Yellowstone digital seismic dataset using data from 1984-2011. These chapters are

described in detail below.

Chapter 2 describes the quantitative discrimination procedures used to identify and characterize Yellowstone earthquake swarms from the background seismicity. These data and discrimination algorithms were employed for data processing in the subsequent chapters to analyze some of the larger swarms and earthquake sequences that have been recorded. Chapter 3 presents the analyses of two of the largest earthquake swarms that have been recorded in Yellowstone: the 2008-2009 Yellowstone Lake earthquake swarm and the 2010 Madison Plateau swarm. Both of these swarms contained numerous M3+ earthquakes that were widely felt throughout Yellowstone and the surrounding region. My modeling of the time sequence of the 2008-2009 Yellowstone Lake swarm suggests it was most likely caused by the movement of magmatic material (magma at depth and hydrothermal fluids at shallower depths) as the swarm of earthquakes propagated along a dike in the shallow crust. The 2010 Madison Plateau swarm occurred near the western caldera boundary and may have been caused by the movement of hydrothermal fluids as they escaped from the caldera into the surrounding region along pre-existing fractures that may be related to the southeast extension of the Hebgen Lake fault. These large swarms may be indicative of a very important process in which magmatic or magmatially derived fluids migrate out of the caldera, thereby facilitating the reversal of caldera uplift to subsidence.

Chapter 4 reports on the fortuitous occurrence and study of the 2010 Gros-Ventre earthquake sequence that occurred in August of 2010 70 km south of the Yellowstone caldera in an area east of the Teton normal fault and in an area of Laramide thrusts. We evaluated this sequence because it may have been triggered by stresses associated with

the overall Yellowstone hotspot uplift or subsidence. This sequence began with a mainshock of magnitude 5 followed by more than 150 aftershocks. Analysis shows that the earthquake sequence most likely nucleated on reactivated buried Laramide-aged thrust faults or anticline structures. We also look at the possibility of seismically induced landslide hazards in the region.

Chapter 5 describes annual precision gravity surveys that have been done in Yellowstone since 2007 in response to the period of accelerated caldera uplift that began in 2004. This study was done to compliment the GPS studies of Yellowstone to assess if the gravity change field mimics or correlates with the temporal variation of ground deformation measured by GPS. To date, the measured gravity changes show little direct correlation between caldera uplift and changes in the gravity field.

Chapter 6 is the major portion of my Ph.D. research that focuses on a detailed study of the P-wave seismic velocity structure of the Yellowstone volcanic system using local earthquake tomography. Waveform data from the entire Yellowstone digital dataset from 1984-2011 was compiled, quantitatively edited and used, in conjunction with an automatic picking algorithm to produce a high quality, consistent dataset of P-wave traveltimes for the Yellowstone volcanic system. These data, that consisted of 48,622 waveforms from 4,520 hypocenters selected to provide geographic coverage of the Yellowstone caldera, were then input into a full tomographic inversion scheme to invert for the P-wave velocity structure. Results revealed a large, low P-wave velocity body below the Yellowstone caldera at depths of 5-16 km, 30 km wide, and 90 km long. This body extends ~20 km NE of the caldera at depths less than 5 km corresponding to the largest negative gravity anomaly in Yellowstone. The results and error analyses are

discussed in Chapter 7.

References

Benz, H. M., and R. B. Smith (1984), Simultaneous inversion for lateral velocity variations and hypocenters in the Yellowstone region using earthquake and refraction data, *J. Geophys. Res.*, *89*, 1208-1220.

Chang, W. -L, R. B. Smith, C. Wicks, C. M. Puskas, and J. Farrell (2007), Accelerated uplift and source models of the Yellowstone caldera, 2004-2006, from GPS and InSAR observations, *Science, 318*(5852): 952-956, doi:10.1126/science.1146842.

Chang, W. -L., R. B. Smith, J. Farrell, and C. M. Puskas (2010), An extraordinary episode of Yellowstone caldera uplift, 2004-2010, from GPS and InSAR observations, *Geophys. Res. Lett.*, *37*, L23302, doi:10.1029/2010GL045451.

Christiansen, R. L. (2001), The Quaternary and Pliocene Yellowstone plateau volcanic field of Wyoming, Idaho, and Montana, *U.S. Geol. Surv. Profess. Pap. 729-G*, 145.

Christiansen, R. L., and R. S. Yeats (1992), Post-Laramide geology of the U.S. Cordilleran region, in *The Cordilleran Orogen: Conterminus U.S.,* edited by B. C. Burchfiel, P. W. Lipman, and M. L. Zoback, pp. 261-406, Geological Society of America, Boulder, Colorado.

DeNosaquo, K., R. B. Smith, and A. R. Lowry (2009), Density and lithospheric strength models of the Yellowstone-Snake River Plain volcanic system from gravity and heat flow data, *J. Volcanol. Geotherm. Res*., *188*, 108-127.

Doser, D. I. (1985), Source parameters and faulting processes of the 1959 Hebgen Lake, Montana, earthquake sequence, *J. Geophys. Res.*, *90*, 4537-4555.

Dzurisin, D., J.C. Savage, R.O. Fournier (1990), Recent crustal subsidence at Yellowstone caldera, Wyoming, *Bull. Volcanol.*, *52*, 247-270.

Farrell, J., S. Husen, and R.B. Smith (2009), Earthquake swarm and *b*-value characterization of the Yellowstone volcano-tectonic system. *J. Volcanol. Geotherm. Res.*, *188*, 260-276.

Farrell, J., R. B. Smith, T. Taira, W. L. Chang, and C. M. Puskas (2010), Dynamics and rapid migration of the energetic 2008-2009 Yellowstone Lake earthquake swarm, *Geophys. Res. Lett.*, *37*, L19305, doi:10.1029/2010GL044605.

Fournier, R. O. (1989), Geochemistry and dynamics of the Yellowstone National Park hydro-thermal system, *Ann. Rev. Earth Planet. Sci.*, *17*, 13-53.

Husen, S., R. B. Smith, and G. P. Waite (2004), Evidence for gas and magmatic sources beneath the Yellowstone volcanic field from seismic tomographic imaging, *J. Volcanol. Geotherm. Res.*, *131*, 397-410.

Krukoski, J. C. (2002), A geologic database (GEOGIS) and three-dimensional inversion for the density structure of the Yellowstone volcanic system, M. S. thesis, University of Utah, Salt Lake City.

Lehman, J. A., R. B. Smith, and M. M. Schilly (1982), Upper crustal structure of the Yellowstone caldera from seismic delay time analyses and gravity correlations, *J. Geophys. Res.*, *87*(B4), 2713-2730.

Massin, F., J. Farrell, and R. B. Smith (2013), Repeating earthquakes in the Yellowstone volcanic field: Implications for rupture dynamics, ground deformation, and migration in earthquake swarms, *J. Volcanol. Geotherm. Res.*, *257*, 159-173, doi: 10.1016/j.jvolgeores.2013.03.022.

Meertens, C. M., and R. B. Smith (1991), Crustal deformation of the Yellowstone caldera from first GPS measurements: 1987-1989, *Geophys. Res. Lett.*, *18*(9), 1763-1766.

Miller, D. S., and R. B. Smith (1999), *P* and *S* velocity structure of the Yellowstone volcanic field from local earthquake and controlled source tomography, *J. Geophys. Res.*, *104*, 15105-15121.

Obrebski, M., R. M. Allen, M. Xue, and S-H. Hung (2010), Slab-plume interaction beneath the Pacific Northwest, *Geophys. Res. Lett., 37*, L14305, doi:10.1029/2010GL043489.

Pelton, J.R., R. B. Smith (1982), Contemporary vertical surface displacements in Yellowstone National Park, *J. Geophys. Res.*, *87*, 2745-2761.

Perkins, M. E., and B. P. Nash (2002), Explosive silicic volcanism of the Yellowstone hotspot: the ash fall tuff record, *Geol. Soc. Am. Bull., 114* (3), 367–381.

Pitt, A. M., C. S. Weaver, and W. Spence (1979), The Yellowstone Park earthquake of June 30, 1975, *Bull. Seismol. Soc. Am.*, *69*, 187-205.

Proffett, J. M. (1977), Cenozoic geology of the Yerington district, Nevada and implications for the nature and origin of Basin and Range faulting, *Geol. Soc. Am. Bull.*, *88*, 247-266.

Rogers, D. W., W. R. Hackett, and H. T. Ore (1990), Extension of the Yellowstone plateau, eastern Snake River Plain, and Owyhee plateau, *Geology*, *18*, 1138-1141.

Schilly, M. M., R. B. Smith, L. W. Braile, and J. Ansorge (1982), The 1978 Yellowstone-Eastern Snake River Plain seismic profiling experiment: Data and upper crustal structure of the Yellowstone region, *J. Geophys. Res.*, *87*(B4), 2692-2704.

Settles, K. R. (2007), Crustal structure and tectono-magmatic processes of the Yellowstone-Snake River Plain volcanic system from gravity-density and lithospheric strength modeling with seismic and heat flow constraints, M. S. thesis, University of Utah, Salt Lake City.

Shelly, D. R., D. P. Hill, F. Massin, J. Farrell, and R. B. Smith (2013), A fluid-driven earthquake swarm on the margin of the Yellowstone caldera, *in preparation*.

Smith, R. B. and M. Sbar (1974), Contemporary tectonics and seismicity of the Western United States with emphasis on the Intermountain Seismic Belt, *Bull. Geol. Soc. Am.*, *85*, 1205-1218.

Smith, R. B., and W. J. Arabasz (1991), Seismicity of the Intermountain Seismic Belt, in *Neo-tectonics of North America*, edited by D. B. Slemmons, E. R. Engdahl, M. D. Zoback, and D. D. Blackwell, Geological Society of America, Boulder, Colorado., Pg. 185-228.

Smith, R. B., and L. W. Braile (1994), The Yellowstone Hotspot, *J. Volcanol. Geotherm. Res.*, *61,* 121-187.

Smith, R. B., and L. Siegel (2000), *Windows into the Earth: The Geology of Yellowstone and Grand Teton Parks*, Oxford University Press, London, 247.

Smith, R. B., M. M. Schilly, L. W. Braile, J. Ansorge, J. L. Lehman, M. R. Baker, C. Prodehl, J. H. Healy, S. Mueller, and R. W. Greensfelder (1982), The 1978 Yellowstone-Eastern Snake River Plain seismic profiling experiment: Crustal structure of the Yellowstone region and experiment design, *J. Geophys. Res*., *87*(B4), 2583-2596.

Smith, R.B., M. Jordan, B. Steinberger, C.M. Puskas, J. Farrell, G.P. Waite, S. Husen, W.L. Chang, and R. O'Connell (2009), Geodynamics of the Yellowstone hotspot and mantle plume: Seismic and GPS imaging, kinematics, and mantle flow, *J. Volcanol. Geotherm. Res.*, *188*, 26-56.

Waite, G. P., and R. B. Smith (2002), Seismic evidence for fluid migration accompanying subsidence of the Yellowstone caldera, *J. Geophys. Res.*, *107*(B9), 2177, doi:10.1029/2001JB000586.

Waite, G. P., R. B. Smith, and R. M. Allen (2006), Vp and Vs structure of the Yellowstone hot spot: evidence for an upper mantle plume, *J. Geophys. Res., 111*(B4), B04303, doi:10.1029/2005JB003867.

Wicks, C., W. Thatcher, and D. Dzurisin (1998), Migration of fluids beneath Yellowstone caldera inferred from satellite radar interferometry, *Science*, *282*, 458-462.

Wicks, C., W. Thatcher, D. Dzurisin, and J. Svarc (2006), Uplift, thermal unrest and magma intrusion at Yellowstone caldera, *Nature*, *440*, 72-75.

Zoback, M. L., R. E. Anderson, and G. A. Thompson (1981), Cenozoic evolution of the state of stress and style of tectonism of the Basin and Range province of the western United States, in Vine, F. J., and A. G. Smith, eds., Extensional tectonics associated with convergent plate boundaries, *Royal Soc. London*, 189-216.

CHAPTER 2

EARTHQUAKE SWARM AND *b*-VALUE CHARACTERIZATION OF THE YELLOWSTONE VOLCANO-TECTONIC SYSTEM

This chapter is published in the Journal of Volcanology and Geophysical Research:

Farrell, J., S. Husen, and R. B. Smith (2009), Earthquake swarm and *b*-value characterization of the Yellowstone volcano-tectonic system, *J. Volcanol. Geotherm. Res.*, *188*, 260-276, doi: 10.1016/j.jvolgeores.2009.08.008

Abstract

The Yellowstone volcanic field, Yellowstone National Park, is one of the most seismically active areas of the western U.S., experiencing the deadly 1959 M7.5 Hebgen Lake, Montana, earthquake adjacent to the 0.64-Ma caldera, as well as more than 30,000 earthquakes from 1973 to 2007. This well-recorded seismic activity offers the opportunity to study the temporal and spatial occurrence of earthquakes and extensive earthquake swarms and how they relate to active volcanic and tectonic processes. We characterize the distribution of earthquakes by analyzing the rate of occurrence characterized by the *b*-value. To accurately determine *b*-values, the earthquake catalog was filtered to identify statistically time- and spatially-dependent related events, defined as swarms, from independent single main and aftershocks. An algorithm was employed that identified 69 swarms for 1984-2006 based on interevent times and spatial clustering.

The swarms varied in duration from 1 to 46 days with the number of events varying from 30 to 722 with magnitudes of -1.2 to 4.8. All of the swarm events as well as the 597 events triggered by the 2002 Denali fault, Alaska, earthquake were removed from the catalog for analysis. The catalog data were then filtered for a magnitude of completeness (M_{COMP}) of 1.5 and the *b*-value distribution for the Yellowstone region was determined with the deswarmed data. *b*-values ranged from 0.6 ± 0.1 to 1.5 ± 0.05 with the highest values associated with the youthful 150,000-year old Mallard Lake resurgent dome. These variations are interpreted to be related to variations in stresses accompanying the migration of magmatic and hydrothermal fluids. An area of high *b*-values (up to 1.3 ± 0.1) associated with the Hebgen Lake fault zone west of the Yellowstone caldera could be related to the transport of magmatic fluids out of the Yellowstone volcanic system or could be indicative of a relative low stress regime resulting from the stress release by the Hebgen Lake earthquake. An area of low *b*-values (0.6 ± 0.1) south of the Yellowstone caldera is interpreted as evidence of a relatively higher stress regime associated with an area of dominantly extensional stress. This seismicity was associated with a nearly 90° change in the principal stress axes direction to NE-SW, compared to EW within the Yellowstone caldera, and may be influenced by buoyancy loading by the Yellowstone hotspot.

Introduction

The Yellowstone Plateau, centered on Yellowstone National Park, Wyoming, Idaho, and Montana, reflects an area of widespread hydrothermal features and Quaternary silicic volcanism characterized by three giant caldera-forming eruptions [*Christiansen*,

1984, 2001], extensive postcaldera rhyolitic eruptions as young as 70,000 years ago [*Christiansen*, 1984, 2001], in addition extraordinarily high heat flow (>2,000 mWm^2) [*Morgan et al.,* 1977; *DeNosaquo et al.,* 2009], unprecedented high rates of modern crustal deformation, and a well seismically defined crustal magma chamber and extensive seismicity [*Smith et al.,* 2009] characterize the system. Thirty-three years of seismic recording by the Yellowstone seismic network has allowed the assessment of the frequency of earthquake occurrence, characterized by *b*-values, that were then correlated with active volcanic and tectonic features.

The *b*-value is a measure of the relative number of small to large earthquakes that occur in a given area in a given time period. In particular, the *b*-value is the slope of the frequency-magnitude distribution [*Ishimoto and Iida*, 1939; *Gutenberg and Richter*, 1944] for a given population of earthquakes. Studies have shown that the *b*-value changes with material heterogeneity [*Mogi*, 1962], thermal gradient [*Warren and Latham*, 1970] and applied stress [*Scholz*, 1968; Wyss, 1973; *Urbancic et al.,* 1992; *Schorlemmer and Wiemer,* 2004; *Schorlemmer et al*., 2005]. In tectonic areas, the *b*-value is generally around 1.0 [*Frolich and Davis*, 1993]. In contrast, volcanic areas are characterized by *b*-values greater or less than 1.0 with values as high as 3.0 [*McNutt*, 2005].

Over 30,000 earthquakes, $-0.5<M_C<6$, have been recorded in the Yellowstone area since 1973 (Figure 1.4). This earthquake dataset offers the opportunity to study the temporal and spatial occurrence of earthquakes, parameterized by the *b*-value, which is the slope of the earthquake recurrence curve. The Gutenberg-Richter relationship is the commonly assumed frequency of occurrence distribution that assumes a Poisson

(random) distribution of earthquake magnitudes assuming that all dependent (nonrandom) events must first be removed from the catalog. Dependent events include foreshocks, aftershocks, earthquake swarms, and triggered events. It has been suggested that earthquake swarms occur because of stress perturbations associated with the migration of magmatic or hydrothermal fluids through new or previously formed crustal inhomogeneities including crustal fractures [*Hill*, 1977; *Toda et al.*, 2002; *Waite and Smith*, 2002] or because of aseismic slip and fluid pressure variations [*Vidale et al.*, 2006].

Seismicity in Yellowstone is dominated by earthquake swarms, generally defined as the spatial and temporal clustering of earthquakes without an outstanding event of magnitude greater than one unit from the swarm average. Thus it is imperative to accurately identify earthquake swarms before calculating *b*-values. The combination of the high seismicity and distinct swarm activity, the complex volcanic and tectonic setting, and dynamic nature of the Yellowstone system suggest that spatial as well as temporal changes in the *b*-value may be an important characteristic of the volcano-tectonic system. This analysis, however, requires accurate hypocenter locations.

The data used here are a subset of the high-precision data developed by *Husen and Smith* [2004] of relocated hypocenters determined using tomographically determined three-dimensional P-wave velocity models for seismicity from 1973 – 2002. Hypocenters for the later period, 2003-2006, were relocated using the velocity model for the time period 1995-2002 of *Husen and Smith* [2004] and added to the catalog providing a total of 29,336 earthquakes.

The events were then classified into four quality classes: A, B, C, and D based on

the Root Mean Square (RMS), the difference (in km) between the expected (the linearized location) and the maximum likelihood hypocenter location, and the average location error as approximated by the 68% confidence ellipsoid [*Husen and Smith*, 2004]. Standardized magnitudes were recalculated by the coda lengths, defined as the Coda magnitudes (M_C) using available instrument calibrations and an improved magnitude equation from *Pechmann et al.* [2001].

$$M_C = -2.60 + 2.44 \log \tau + 0.0040\Delta \quad (2.1)$$

where τ is signal duration in seconds measured on a short-period vertical component seismogram, and Δ is epicentral distance in kilometers.

Because of the elimination of previous systematic time-dependent magnitude shifts, the recomputed M_C values are considered more consistent and reliable than previous M_C estimations. Essentially all the earthquakes in the catalog have magnitudes less than or equal to M_c= 4.0; 99.1% have $M_c \leq$ 3.0; 91.2% have $M_c \leq$ 2.0; and 53.6% have $M_c \leq$ 1.0. Because of the importance of high quality locations and well-constrained magnitudes in calculating *b*-values, only A, B, or C quality events were used because they have RMS values less than 0.5 seconds. A total of 123 quality D events were rejected from the analysis ranging in magnitude from less than 0 to 3.5. Also, only earthquakes from 1984 to 2006 were used in this study because of the more consistent and reliable nature of the magnitudes due to improved digital monitoring and geographic network coverage with more instruments. This left 23,054 events in the dataset, hereafter referred to as the catalog of earthquakes. The average M_C for the time period of 1984 to 2006 is 1.0, and only 10% of the earthquakes have $M_C > 2.0$.

Earthquake swarms were then identified and were removed from the dataset using the algorithm from *Waite* [1999] in which swarms are identified based on an interevent time and a distance between two related events. Earthquakes triggered by the M7.9 2002 Denali fault earthquake [*Husen et al.,* 2004b; *Husen et al.*, 2004c] were also identified and removed from the data. The magnitude of completeness was then calculated for different spatial and temporal subsets and the catalog was cut at the highest magnitude of completeness value. The remaining events were used to calculate the *b*-value distribution for the Yellowstone volcanic-tectonic system.

A total of 69 distinct earthquake swarms were identified comprising 8,924 earthquakes, or 39% of the total number of earthquakes from 1984-2006. These events were also removed from the catalog which was limited to the threshold of completeness of M_C=1.5. The remaining 2,747 earthquakes were used to calculate *b*-values. Results show that the *b*-value varies laterally in Yellowstone from 1.5 ± 0.05 near the Mallard Lake resurgent dome to 0.6 ± 0.1 south of the Yellowstone caldera near the Mt. Sheridan fault and the northern segment of the Teton fault

Geological Setting and Seismicity in Yellowstone

The Yellowstone volcanic system is one of the largest active silicic volcanic systems in the world [*Christiansen*, 2001]. It forms a topographically high plateau of ~500 m excess elevation relative to the Basin-Range/Rocky Mountains as the result of mantle hotspot bouyancy [see summary by *Smith et al*., 2009]. The youthful volcanic history of Yellowstone is dominated by three cataclysmic caldera-forming eruptions in the past 2 million years at 2.05, 1.3 and 0.64 Ma [*Christiansen*, 2001]. The latest

eruption (0.64 Ma) created what is subsequently referred to as the Yellowstone caldera, which extends 40 x 60 km (Figure 2.1). Two structural resurgent domes formed after the caldera eruptions: the Mallard Lake resurgent dome in the southwestern portion of the Yellowstone caldera and the Sour Creek resurgent dome in the northeast part of the Yellowstone caldera (Figure 2.1). In the last 640,000 years, at least 30 much smaller rhyolitic and basaltic flows as young as 70,000 years old have covered much of the Yellowstone Plateau.

With over 10,000 geysers, hot springs, and fumaroles, Yellowstone has the world's highest concentration of hydrothermal features reflecting its extraordinarily high convective ground water circulation [*Fournier*, 1989]. The large hydrothermal systems are considered to be the result of hot water circulating along fractures in the crust heated by crystallizing magma [*Fournier*, 1989].

Four local earthquake tomography studies of Yellowstone [*Benz and Smith*, 1984; *Lynch*, 1999; *Miller and Smith*, 1999; *Husen et al.*, 2004a] have imaged at various resolutions, with progressions in data access and expansion of the seismic network, a well defined low (-6%) *Vp* body in the upper crust beneath the Yellowstone caldera has been interpreted as a body of 8-15% partial melt [*Miller and Smith*, 1999; *Husen et al*., 2004a]. By the addition of several three-component seismographs in the Yellowstone region, *Husen et al*. [2004a] was able to extend the earlier work by selecting 3,374 local earthquakes between 1995 and 2001 and using 34,538 P-wave arrival times and 5,875 S-P times to image the three-dimensional V_P and V_P/V_S structure of the upper crust beneath Yellowstone. *Husen et al.* [2004a] imaged a low (-10%) *Vp* body at ~2 km depth on the northwest boundary of the Yellowstone caldera as well as a low (-5%) *Vp*/*Vs* body in the

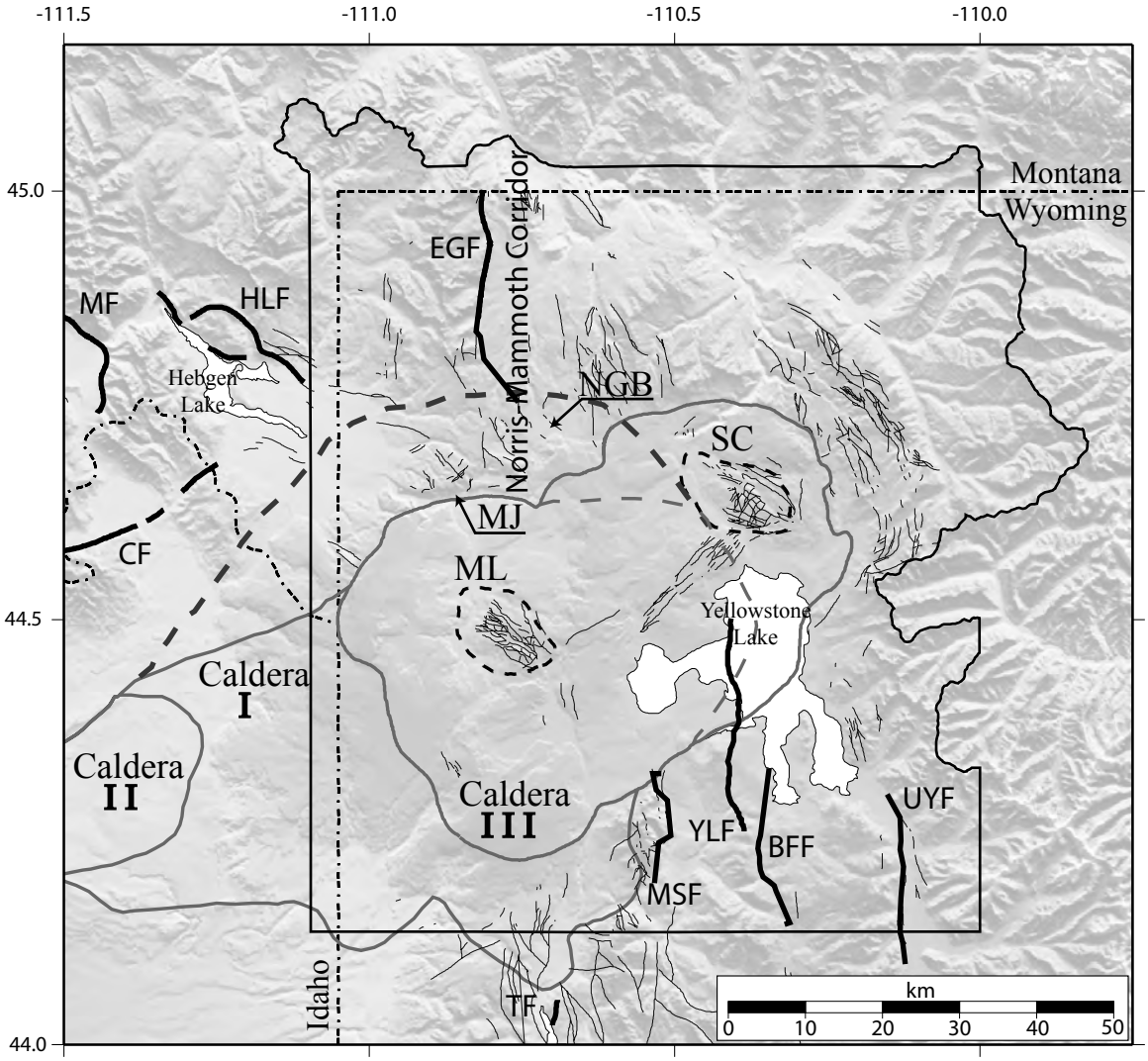

Figure 2.1. Gray-shaded topographic relief map of the Yellowstone volcanic field showing calderas and Cenozoic faults after *Christiansen* [2001]. Major faults are shown as thick black lines. The abbreviations refer to the faults and resugent domes in the Figure caption of Figure 1.4.

same area. This low *Vp* and *Vp*/*Vs* body has been interpreted as a CO_2 gas-filled body [*Husen et al.*, 2004a].

Crustal deformation monitoring of Yellowstone by precise spirit leveling and more recent Global Positioning System (GPS) and Interferometric Synthetic Aperture Radar (InSAR) measurements have shown unprecedented caldera uplift and subsidence during the last 80 years. This caldera-wide deformation includes uplift of up to 1 m from 1923 to 1984 as measured by leveling [*Pelton and Smith*, 1982; *Dzurisin et al.*, 1990]. Beginning in 1987 the University of Utah began campaign GPS studies in the Yellowstone region and in 1996 data from continuous GPS stations were used to measure ground deformation. From 1987 to the present, ground deformation was measured from campaign and continuous GPS measurements. The results show that from 1987-1995 the Yellowstone caldera subsided at a maximum rate of -14 ± 3 mm/yr centered near the Sour Creek dome for a total of 112 mm. From 1995-2000 the Yellowstone caldera returned to uplift with a maximum rate of 15 ± 4 mm/yr for a total of 75 mm [*Puskas et al.*, 2007]. However, the center of uplift during this time period was centered northwest of the Yellowstone caldera in the Norris-Mammoth corridor (Figure 2.1). From 2000-2003 the uplift continued northwest of the Yellowstone caldera at a maximum rate of 12 ± 4 mm/yr for an additional 36 mm of displacement but the central caldera axis returned to subsidence at a maximum rate of -9 ± 6 mm/yr for an additional 27 mm subsidence [*Puskas et al.*, 2007].

Remarkably, since late 2004, Yellowstone has been experiencing accelerated uplift of the 0.64-Ma caldera with rates up to 70 mm/yr, three times greater than previously observed deformation episodes [*Chang et al.*, 2007]. Source modeling of the

deformation suggests a near-horizontal expanding magma body over an area 40 x 60 km^2, at 9 km beneath the Yellowstone caldera, notably located near the top of the seismically imaged crustal magma chamber. In addition, tens to hundreds of small earthquakes (M < 3) occurred during the deformation period and were concentrated within the modeled dilatation zone while the rest of the Yellowstone caldera experienced low seismicity [*Chang et al.*, 2007].

Perhaps one of the most striking features of the Yellowstone Plateau is its extraordinarily high heatflow. The presence of crystallizing magma at shallow depths (~8 km) fuels the regional heat flow at Yellowstone by combined conduction and convection, estimated at more than 2,000 mW/m^2 [*Blackwell*, 1969; *Fournier*, 1989; *DeNosaquo et al.*, 2009], this is more than 30 times the continental average [*Fournier*, 1989]. Given a conductive heat flow of ~200 mW/m^2, the Nusselt number (which is the ratio of convective heat flow and conductive heat flow) for the Yellowstone caldera is ~10. This compares to values of ~6 to 8 for the Long Valley caldera in eastern California [*Hill*, 1992].

The Yellowstone Plateau is one of the most seismically active areas of the western U.S. and is part of the distinct N-S band of intraplate seismicity known as the Intermountain Seismic Belt [*Smith and Sbar*, 1974; *Smith and Arabasz*, 1991] (Figures 1.3 & 1.4). Moreover, the Yellowstone area has experienced the largest historic earthquake of the ISB: the August, M_S7.5 1959 Hebgen Lake, Montana event located ~25 km northwest of the Yellowstone caldera [Doser, 1985]. The Yellowstone caldera has also experienced a M_L6.1 earthquake in 1975 southeast of Norris Junction [*Pitt et al.*, 1979, *Smith and Arabasz*, 1991].

Overall, seismic activity in Yellowstone is characterized by swarms of small, shallow earthquakes. Focal depths within the Yellowstone caldera are limited by high temperatures to the shallow depth of the brittle-ductile transition at 4-6 km and deepen to up to 18 km in the much cooler tectonic regime in the Hebgen Lake, Montana area west of the Yellowstone caldera [*Smith et al.*, 2009]. The most intense seismicity extends from the Hebgen Lake area east to the northern Yellowstone caldera boundary near Norris Junction (Figure 1.4). Although this area only constitutes 16% of the Yellowstone area, it contains 75% of the earthquakes from 1973-2006. Linear bands of epicenters within and adjacent to the Yellowstone caldera are aligned generally north-northwest parallel to alignments of postcaldera volcanic vents and large regional faults (Figure 1.4). These normal faults are assumed to be buried at depth beneath young postcaldera rhyolite flows and are inferred to have once been continuous normal faults bounding mountain blocks of Basin-Range origin [*Christiansen*, 1984; *Smith and Braile*, 1994] (Figure 2.1).

The largest earthquake swarm recorded in Yellowstone occurred in October of 1985 and consisted of over 3,000 earthquakes ($M_C < 5$) that spanned more than 3 months [*Waite and Smith*, 2002]. The temporal pattern of epicenters in the 1985 swarm was characterized by northwest migration away from the 0.64-Ma caldera at an average rate of 150 m/d. The swarm also coincided with a pronounced change of Yellowstone caldera uplift to subsidence. *Waite and Smith* [2002] suggested that the subsidence was partially accommodated by the migration of magma-derived fluids out of the Yellowstone caldera toward the northwest. The most likely scenario explaining this process involves the rupture of a self-sealed hydrothermal layer and subsequent migration of hydrothermal fluids through a pre-existing fracture zone out of the Yellowstone caldera, causing the

earthquakes of the 1985 swarm [*Waite and Smith*, 2002].

The second largest swarm recorded in Yellowstone occurred December 27, 2008 to January 7, 2009 beneath northern Yellowstone Lake, Wyoming [*Farrell et al.*, 2010]. This sequence consisted of over 1,000 earthquakes, 21 of which had magnitudes greater than 3.0. The area of activity migrated progressively north at about ~1000 m/day. Also, earthquakes nucleated from as deep as ~10 km and shallowed significantly to 4 km at the north end of the sequence. The largest event had a magnitude of 4.0 and a moment tensor solution that revealed ~50% of the radiated energy as an explosion source with east-west expansion. We particularly note that this unusual earthquake source mechanism is strikingly similar to that of a M 3.3, November 2007, event near the southern caldera boundary that *Taira et al.* [2010] modeled as a dominantly explosive source earthquake. GPS vectors from nearby stations also suggest east-west expansion of the surface motions. Shortly after the swarm ended on January 7th, a small swarm occurred ~12 km to the north and may have been triggered by the Yellowstone Lake swarm.

Earthquakes in Yellowstone have been routinely monitored since 1973 by permanent and temporary deployments of seismic stations operated by the U.S. Geological Survey (USGS), the University of Utah Seismic Stations (UUSS), *Smith et al.* [1977], and *Doser and Smith* [1983]. This deployment has provided the complete earthquake dataset that was used for this study. The seismograph station characteristics and locations of the Yellowstone seismic network are summarized by *Husen and Smith* [2004].

Implications of *b*-value Distributions from Previous Studies

The frequency-magnitude distribution [*Ishimoto and Iida*, 1939; *Gutenberg and Richter*, 1944] derives from the power-law relationship between the frequency of occurrence and the magnitude of earthquakes:

$$\log N = a - bM, \tag{2.2}$$

where N is the cumulative number of earthquakes having magnitudes larger than M, and a and b are constants. It has been shown in laboratory studies, mines, and numerical simulations that the slope of the frequency-magnitude distribution curve, or *b*-value, depends on stress conditions.

Statistically significant variations of *b*-values have been measured in laboratory experiments, mines and various tectonic and volcanic regimes such as subducting slabs, near magma chambers, along fault zones, and in aftershock zones [see for example *Wiemer and Wyss*, 2002]. Seismologists consider that various factors influence *b*-values: 1) increased material heterogeneity, such as a large number of randomly oriented cracks may increase *b*-values [*Mogi*, 1962]; 2) spatial and temporal changes in applied shear stress [*Scholz*, 1968; *Urbancic et al.*, 1992; *Schorlemmer and Wiemer*, 2004; *Schorlemmer et al.*, 2005] or effective stress [*Wyss*, 1973] can decrease *b*-values; and 3) an increase in the thermal gradient may increase *b*-values [*Warren and Latham*, 1970].

In tectonic areas, the *b*-value averages about 1.0 [*Frolich and Davis*, 1993]. In contrast, volcanic areas are characterized by *b*-values greater or less than 1.0 with values as high as 3.0 [*McNutt*, 2005]. *Wiemer and Benoit* [1996] used a dense spatial grid to study *b*-values at subduction zones. These studies were later extended to volcanic areas.

All the aforementioned criteria that favor high *b*-values are found in volcanic areas, such as high heterogeneity due to layering of lava flows and ash, the presence of cooling cracks, dikes and sills, and high thermal gradients. Moreover, because of the dynamic nature of volcanic areas, *b*-values tend to change with changing stress conditions through both time and space.

Seismicity associated with volcanic settings have been studied using *b*-values at several volcanoes including Mt St. Helens and Mt. Spurr, Alaska [*Wiemer and McNutt*, 1997], Off-Ito volcano, Japan [*Wyss et al.*, 1997], Long Valley Caldera and Mammoth Mountain, California [*Wiemer et al.*, 1998], Soufriere Hills, Montserrat [*Power et al.*, 1998], Mt. Etna, Italy [*Murru et al.*, 1999], Katmai, Alaska [*Jolly and McNutt*, 1999], Mt. Redoubt, Alaska [*Wiemer and Wyss*, 2000], Kilauea, Hawaii [*Wyss et al.*, 2001], and Mt. Pinatubo, Philippines [*Sanchez et al.*, 2004]. These volcanoes have shown high spatial variability of *b*, with regions of normal *b* (1.0) adjacent to regions with anomalously high *b* (up to 3.0). Most studies have found that in general, *b* is high at depths of 7-10 km where the earthquakes are adjacent to inferred magma bodies. However, some studies also show significant high *b* anomalies at depths of 3-4 km. This is the approximate depth at which magma with 4 wt% gas starts to exsolve gas, and further, is near the depth at which open cracks may exist in the host rock [*McNutt*, 2005].

b-values have also been used to infer the state of stress on active faults [*Scholz*, 1968; *Wyss*, 1973; *Urbancic et al.*, 1992; *Schorlemmer and Wiemer*, 2004; *Schorlemmer et al.*, 2005]. *Schorlemmer et al.* [2005] show that there is a general inverse relationship between differential stress and the *b*-value and later conclude that the *b*-value can therefore be interpreted as a "stressmeter" in the Earth's crust. This idea is supported by

the magnitude 6.0 Parkfield, California, event in 2004, which almost exclusively ruptured areas of the San Andreas fault previously mapped as regions of low *b*-values [*Wiemer and Wyss*, 1997; *Schorlemmer and Wiemer*, 2005].

Swarm Identification

Method

There are three different types of earthquake sequences [*Mogi*, 1963]: (I) a mainshock followed by a number of aftershocks of decreasing magnitude and frequency (Figure 2.2A); (II) a slow build up of seismicity (foreshocks) leading to a type I sequence (Figure 2.2B); and (III) a gradual increase and decay of seismicity in time without a distinct mainshock (Figure 2.2C) [also see *Sykes*, 1970]. Type III sequences are also known as earthquake swarms and are common in volcanic areas or other remarkably fractured regions or areas where there is a concentrated application of stress such as from intruding magma [*Mogi*, 1963].

Earthquake sequence I typically occurs in homogeneous material with a uniform external stress. Sequence II tends to occur in material that is heterogeneous to some degree, or a moderate fracture density, with a nonuniform external stress. Sequence III, or swarms, occur in material that is extremely heterogeneous or has high fracture density with a very concentrated external stress [*Mogi*, 1963] (Figure 2.2).

Various algorithms are available to detect foreshock, mainshock, and aftershock sequences [*Reasenberg*, 1985; *Youngs et al.*, 1987], but there are few algorithms written to detect earthquake swarms [*Waite*, 1999]. In this study, *Reasenberg's* [1985] code was first used to identify swarms in the Yellowstone region. However, this approach

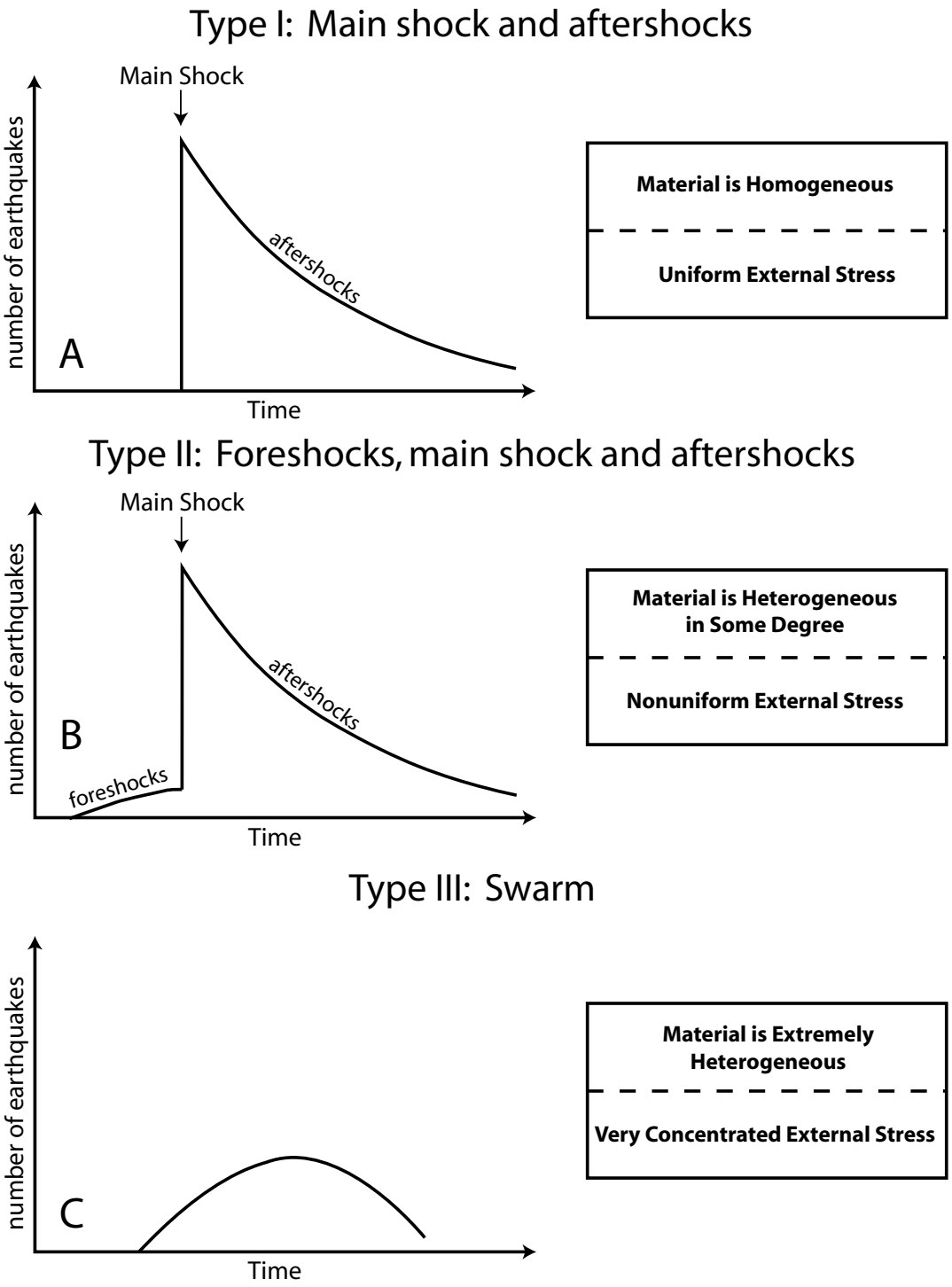

Figure 2.2. Schematic diagram of number of earthquakes vs. time for the three types of earthquake sequences including earthquake swarms, adapted from *Mogi* [1963].

identified events that were clearly not related temporally to a swarm. For example, events up to 5 years apart were classified as members of the same swarm simply because of their spatial relationship.

To identify swarms in the Yellowstone catalog, an algorithm designed by *Waite* [1999] was used. This algorithm specifies swarms based on the interevent times and distances based on the swarm definition of *Mogi* [1963]. A swarm is defined if the following criteria are met: (i) the maximum of the daily number of events in the sequence (N_d) is greater than twice the square root of the swarm duration in days (T):

$$N_d > 2\sqrt{T} \tag{2.3}$$

and (ii) the total number of earthquakes in a sequence E_T is at least 10. Swarms were identified using an E_T value of 10, 30, and 50 to see which criteria best identified both large and small swarms.

Results

Employing algorithms used to identify foreshock-mainshock-aftershock sequences [*Reasenberg*, 1985] showed that most earthquake sequences do not follow this pattern because the seismicity in Yellowstone is dominated by swarms during the time period of 1984 - 2006. Numerous combinations of interevent times (from 0.5 to 5 days) and distance values (from 2 to 15 km) were included in the swarm identification algorithm of *Waite* [1999]. In addition, various definitions of minimum number of earthquakes that constituted a swarm, from 5 to 50, were examined. The combination of an interevent time of 2 days and a distance of 5 km most reliably identified both large and

small swarms in the Yellowstone region.

Sixty-nine individual swarms were identified (Figure 2.3) using the criteria in which a swarm must have at least 30 events (30-minimum). These swarms varied in duration from 1 to 46 days, total number of events from 30 to 722, and maximum number of events per day from 9 to 295. The average number of events per swarm for all 69 swarms is 129.3. The total number of events for all 69 swarms is 8,924, which is 39.0% of the original 23,054 events. Magnitudes of swarm events range from $-1.19 \leq M_C \leq 4.82$ with 99.9% of the swarm events having magnitudes less than or equal to $M_C = 4.0$; 99.7% having $M_C \leq 3.0$; 96.2% having $M_C \leq 2.0$; and 68.0% having $M_C \leq 1.0$. Fifty-four (78.3%) of the 69 swarms are located in the region just north and northwest of the Yellowstone caldera. Fourteen (20.3%) are located within or on the boundary of the 0.64 Ma caldera. One (1.4%) is located outside the 0.64 Ma caldera to the east or south.

Waite [1999] identified 72 swarms in the Yellowstone region for the period 1973 to 1997. Although we have identified many of the same swarms in this study, comparisons cannot be made in some cases because *Waite* [1999] used the original, non-relocated, earthquake catalog to identify swarms. Here, only the quality A, B, and C earthquakes of the relocated catalog of *Husen and Smith* [2004] were used and many additional earthquakes were eliminated in the relocation process. The relocated catalog was used in this study because in order to calculate *b*-values, high quality earthquake locations are important both for identifying swarms and for accurately mapping the spatial changes of *b*-values.

Waite [1999] identified 3,156 earthquakes in the autumn 1985 swarm. However, using the relocated catalog, the swarm was found to consist of only 462 earthquakes.

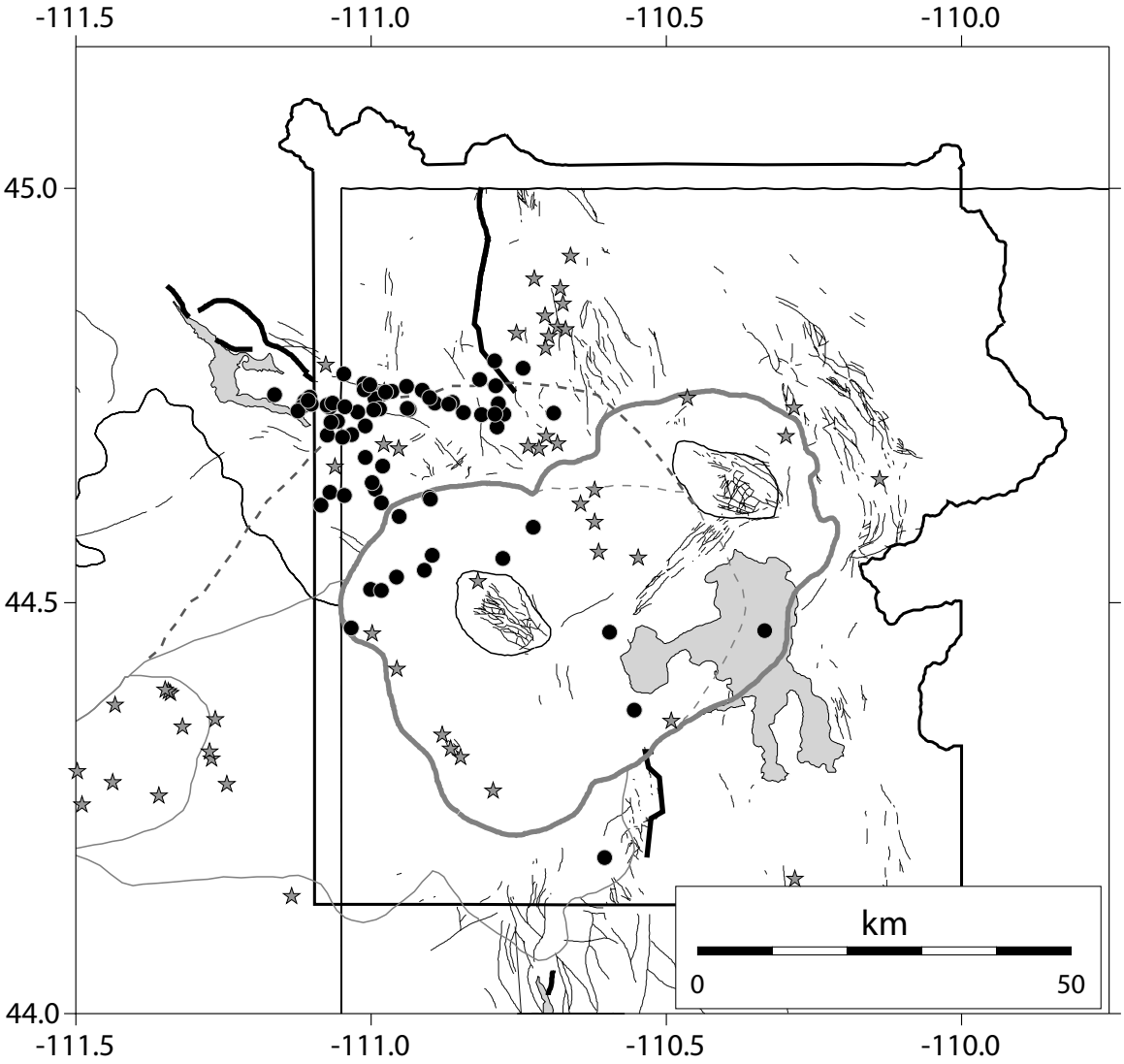

Figure 2.3. Earthquake swarm locations identified while using the 30-minimum definition of a swarm used in this study [also see *Farrell et al.*, 2009]. Average locations for the 69 swarms are shown by black dots. Postcaldera volcanic vents are shown as gray stars [*Christiansen*, 2001]. The 0.64-Ma caldera is outlined as a thick gray line and the 1.3-Ma and 2.05-Ma caldera boundaries are outlined as thin gray lines, with the possible northern extent of the 2.05-Ma caldera shown with a dashed gray line. Quaternary faults after *Christiansen* [2001] are shown as thin black lines. Major Quaternary faults are shown as thick black lines.

From 1995 to 2006 the swarms identified in this study become more similar to the swarms identified by *Waite* [1999] in both the number of swarms and the total number of earthquakes in each swarm. This is because the seismic network upgrades improved the quality of the earthquake locations so that more earthquakes made it through the relocation process.

For example, *Waite* [1999] identified a swarm on the northwest Yellowstone caldera boundary, near Madison Junction starting in June of 1995 that consists of 581 earthquakes. That same swarm calculated here was actually composed of four smaller swarms. The total number of earthquakes in these four swarms is 567. The reason that the swarm sequence was divided into four different swarms here is because a more refined search radius of 5 km was used in this study while *Waite* [1999] used a search radius of 15 km.

Although direct comparisons to results from *Waite* [1999] cannot be made with individual swarms, the patterns of swarms can be compared. The high percentage of swarms located in the area north and northwest of the Yellowstone caldera (69%, 78.3%, and 79.2 % for the 10-minimum, 30-minimum, and 50-minimum definitions, respectively) is comparable to the results of *Waite* [1999]. This suggests that the crust in that area is highly fractured and heterogeneous. The abrupt change in topography may suggest that the boundary of the 2.05-Ma caldera (caldera I) is located in this area (dashed line in Figure 2.1). Swarm epicenters in this area also tend to align in a more east-west trend, which is what would be expected from the orientation of the edge of caldera I. Another explanation for the high rate of seismicity in this region is the increased stress resulting from the 1959 M7.5 Hebgen Lake, Montana earthquake [*Chang*

and Smith, 2002).

Swarm earthquake epicenters within and adjacent to the 0.64-Ma caldera are generally aligned in a north-northwest direction. This alignment is subparallel to alignments of postcaldera volcanic vents and Quaternary faults (Figure 1.4) and implies that these events could have occurred on pre-existing zones of weakness such as buried but still active Quaternary faults [*Christiansen*, 1984].

Calculating *b*-Values

Method

Wiemer and Wyss [2000] suggest that a careful estimate of the spatial and temporal homogeneity of the magnitude of completeness (M_{COMP}) is required before deviations from a power law behavior for small magnitudes can be made. Therefore, M_{COMP}, which is the minimum magnitude in which the catalog is complete, was calculated for the Yellowstone earthquake catalog. It is well known that M_{COMP} can decrease with time in most earthquake datasets because the number of seismographs increases and the methods of analysis improve [*Wiemer and Wyss*, 2000]. M_{COMP} was calculated using the EMR method described by *Woessner and Wiemer* [2005].

The *b*-values determined in this study were calculated using the ZMAP algorithm [*Wiemer*, 2001]. Maximum-likelihood *b*-values were computed using the following equation [*Utsu*, 1965; *Aki*, 1965; *Bender*, 1983].

$$b = \frac{1}{\overline{M} - M_{\min}} \log e \,, \tag{2.4}$$

where $\overline{M}$ is the mean magnitude and $M_{\min}$ the minimum magnitude of the given sample. The sample is considered complete down to the minimum magnitude $M_{\min}$. The magnitude of completeness (M_{comp}) has to be corrected by $\Delta M/2$ to compensate the bias of rounded magnitudes to the nearest ΔM bin, thus $M_{\min} = M_{comp} - \Delta M/2$ [*Utsu*, 1965; *Guo and Ogata*, 1997]. The confidence limit of this *b*-value estimation is given by [*Shi and Bolt*, 1982]

$$\sigma(b) = 2.30b^2 \sqrt{\sum_{i=1}^{n} (M_i - \overline{M})^2 / n(n-1)} \tag{2.5}$$

where n is the total number of events of the given sample.

For volumetric sampling of earthquakes, we employed cylindrical volume centered at nodes spaced at 0.01° (latitude) x 0.01° (longitude) (~1.1km x ~0.8km) with varying radii for the cylinders. For cross-sections, sampling is done on a 0.5 km x 0.5 km grid with varying radii. For each node a minimum number of events, $N_{\min}$, with $M \geq M_{comp}$ is required in order to determine a reliable *b*-value. For samples that contain less than $N_{\min}$ events, a *b*-value is not calculated. $N_{\min}$ is set to 50 in this study because below this value the uncertainty in the *b-value* increases rapidly [*Schorlemmer and Wiemer*, 2004]. Radii were varied from 3 to 10 km and results were compared. The radius that produced robust results with the greatest spatial extent was chosen.

The *b*-value distribution for each different criterion for removing swarms and with the full catalog was mapped and compared to identify the influence of removing swarms. To compare *b*-values for different criteria for removing swarms and with the full catalog, *b*-values are spatially mapped for both types of data. If in both instances the

sample size is greater or equal to N_{min}, and thus a *b-value* can be computed, the probability P_b of the hypothesis that the *b*-values of the two catalogs are coming from the same population is computed. This probability value is derived from the Akaike Information Criterion (AIC) [*Akaike*, 1974]. Comparing the AIC_0 for both catalogs having the same *b*-value b_0 and the AIC_{12} for both catalogs having two different *b*-values b_1 and b_2 leads to the difference ΔAIC of these two AIC scores as given by *Utsu* [1992]:

$$\Delta AIC = -2(N_1 + N_2)\ln(N_1 + N_2) + 2N_1 \ln(N_1 + \frac{N_2 b_1}{b_2}) + 2N_2 \ln(\frac{N_1 b_2}{b_1} + N_2) - 2 \tag{2.6}$$

where N_1 and N_2 are the number of earthquakes in each group and b_1 and b_2 are the *b*-value of each group. The probability P_b that the *b*-values are not different is given by

$$P_b = e^{[(\frac{-\Delta AIC}{2})-2]} \tag{2.7}$$

Using the criteria from *Utsu* [1999], the difference in *b*-values is considered not significant if $\Delta AIC < 2$. If $\Delta AIC > 2$, the difference is significant. $\Delta AIC = 2$ corresponds to $P_b \approx 0.05$. The difference is considered highly significant if $\Delta AIC > 5$, with a corresponding probability of $P_b \approx 0.01$. Applying the logarithm leads to log-probabilities of $\log P_b \leq -1.3$ for significantly different *b*-values and $\log P_b \leq -1.9$ for highly significant differences in *b*-values [*Schorlemmer and Wiemer*, 2004; *Schorlemmer et al.*, 2005].

Threshhold of Magnitude Completeness

The seismicity rate for quality A, B, and C earthquakes in the Yellowstone region increased from ~200 earthquakes per year before 1995 to ~1,500 earthquakes per year after 1995 (Figure 2.4). However, this change in seismicity rate is due to upgrades and expansion of the seismic network. Beginning in 1995, 3-component short-period and broadband seismometers were added to the network. Therefore the catalog data were divided into two time periods, 1984-1994 and 1995-2006. Also, due to the higher density of both seismometers and earthquakes, events in the area that extend from Hebgen Lake east to the northern caldera boundary near Norris Junction were separated from the rest of the catalog (Figure 2.5). Figure 2.5 shows the magnitude of completeness values calculated for the various spatial and temporal areas. The highest value of M_{COMP} was selected (M_{COMP} = 1.5 based on the time period 1984-1994 for the remaining region), and the catalog was cut there and the remaining events were then used to calculate *b*-values to ensure that M_{COMP} is consistent throughout the time period of the catalog as well as throughout the entire area. Figure 2.6 shows the number of earthquakes remaining to calculate *b*-values after a) deswarming, b) removing triggered events from the 2002 M7.9 Denali fault earthquake, and c) cutting the catalog at M_{COMP} = 1.5.

b-Value Results

Epicenter locations used to calculate *b*-values for the various swarm definitions are plotted in Figure 2.6. As expected, as the minimum number of events that constitute a swarm is increased, more events are left in the catalog to calculate *b*-values. To investigate the influence of using different swarm definitions on the stability of the *b*-

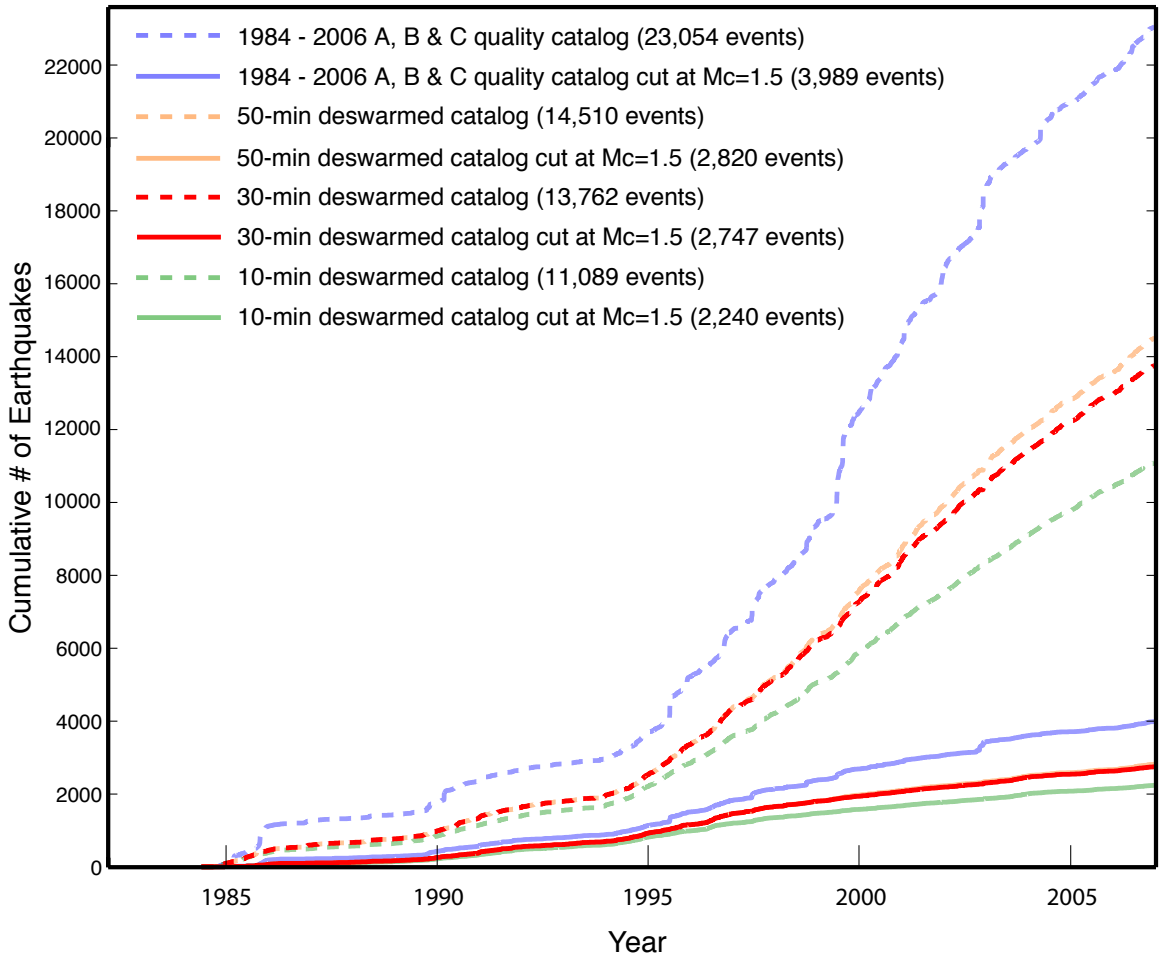

Figure 2.4. Cumulative number of earthquakes vs. time for the various Yellowstone earthquake datasets used to calculate *b*-values. Blue dashed line shows the original catalog consisting of A, B, and C quality events from 1984 to 2006. Dashed lines represent the deswarmed catalogs using the various definitions of a swarm. Solid blue line represents the quality A, B, and C events from 1984 to 2006 cut at a magnitude of completeness (*MCOMP*)=1.5. Remaining solid lines represent the deswarmed catalogs cut at *MCOMP*=1.5.

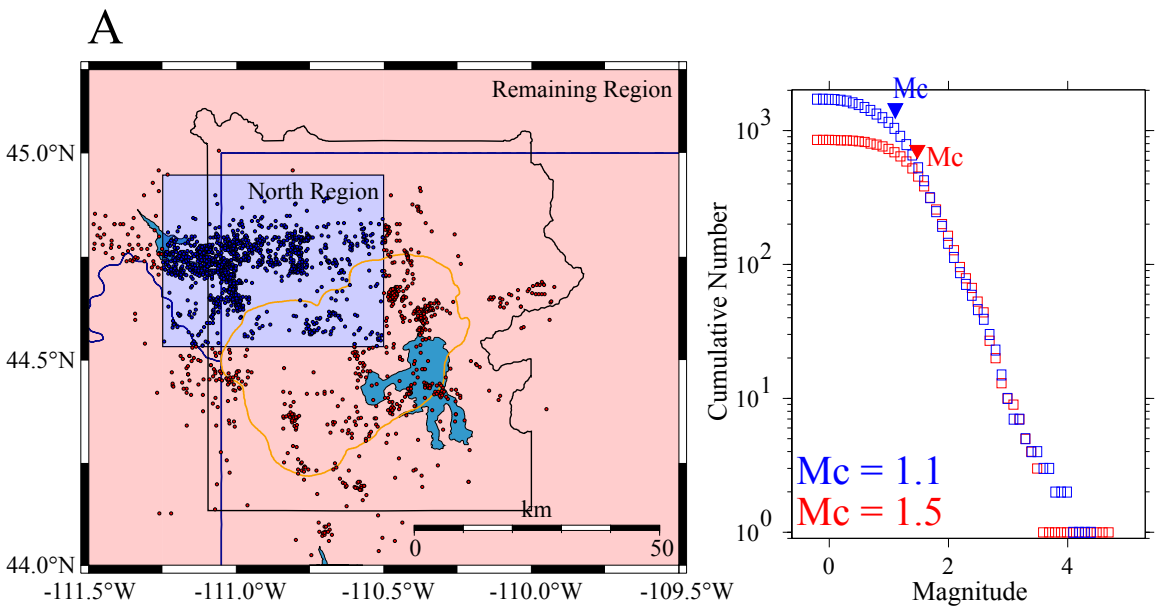

North = 1,718 events

Remaining = 824 events

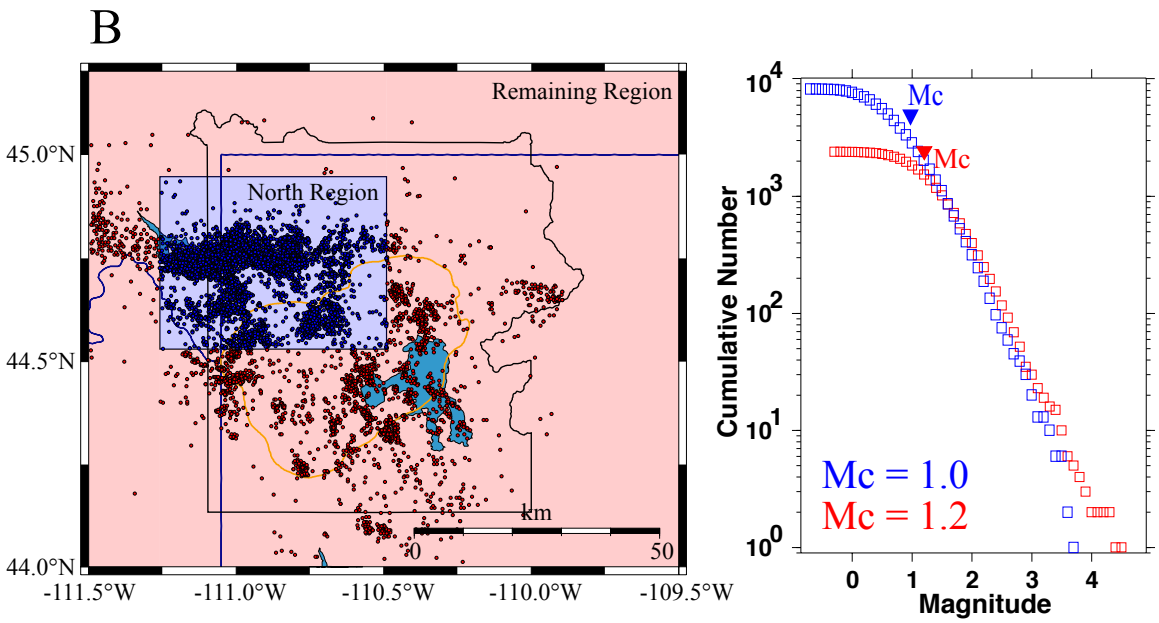

North = 8,206 events

Remaining = 3,014 events

Figure 2.5. Threshold of earthquake completeness (*MCOMP*) calculations for the 30-minimum deswarmed catalog. (A) shows *MCOMP* values for the years 1984 – 1994 and (B) shows *MCOMP* values for the years 1995 – 2006. Blue color represents the north region and red color represents the remaining region.

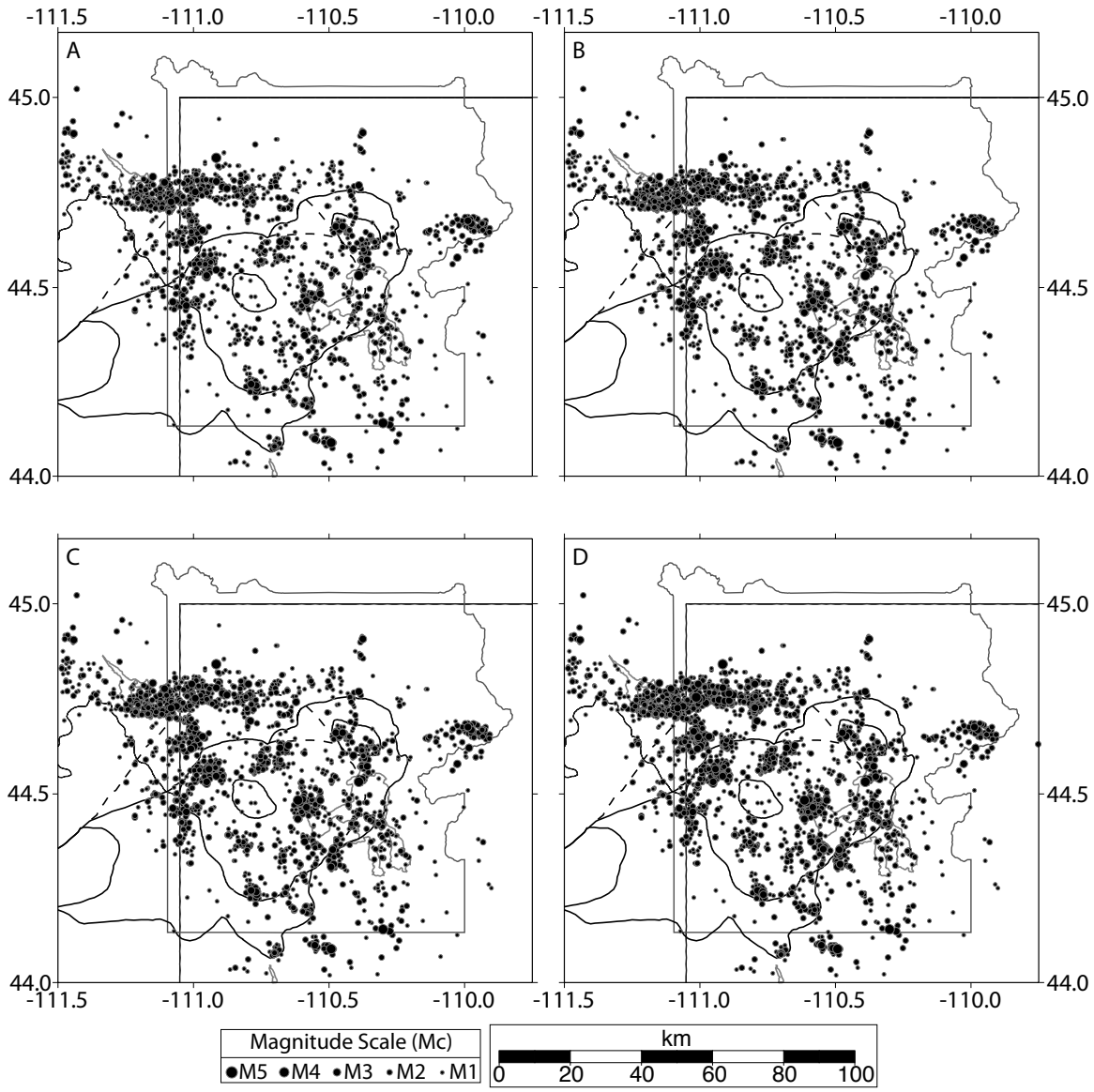

Figure 2.6. Earthquakes of the Yellowstone region used to calculate *b*-values for the various deswarmed and non-deswarmed catalogs. (A) shows the 2,240 epicenters for the 10-minimum deswarmed catalog, (B) shows the 2,747 epicenters for the 30-minimum deswarmed catalog, (C) shows the 2,820 epicenters for the 50-minimum deswarmed catalog, and (D) shows the 3,989 epicenters for the non-deswarmed catalog.

value results we computed *b*-values using the different datasets, including the complete, non-deswarmed catalog. The resulting spatial distribution of *b*-values in Yellowstone shows areas of high and low *b*-values and areas of normal crustal values ($b \approx 1.0$) (Figure 2.7). A constant 10 km radius was chosen to calculate the *b*-values because this radius allowed the maximum coverage while still showing details of the areas with both high and low *b*-values.

The probability P_b of the possibility that the *b*-values of the two catalogs are from the same population is computed in order to quantitatively identify the differences between the *b*-value maps for the three different deswarmed catalogs as well as the non deswarmed catalog (equation 2.7). In Figure 2.8, *b*-values are significantly different when $\log P_b \leq -1.3$ and the *b*-values show highly significant differences for $\log P_b \leq -1.9$ [*Schorlemmer and Wiemer*, 2004; *Schorlemmer et al.*, 2005].

Statistically, there is little difference between the *b*-values using the deswarmed catalogs from the 10-minimum events and 30-minimum events definition of a swarm (Figure 2.8A). The 30-minimum catalog is preferred over the catalog from the 10-minimum definition of a swarm due to the fact that using the catalog from the 30-minimum definition of a swarm provides greater spatial coverage for mapping *b*-values. When comparing the *b*-values from the 30-minimum dataset and the 50-minimum dataset, there are slight differences in the center of the Yellowstone caldera. Overall only 0.24% of the nodes are different between the two datasets (Figure 2.8B). The reason for the differences is a swarm that occurred in August of 1999. This swarm consisted of 35 earthquakes, so it is only identified and subsequently removed by the algorithm with the 30-minimum definition of a swarm. This swarm contained an earthquake of $M_C = 4.82$,

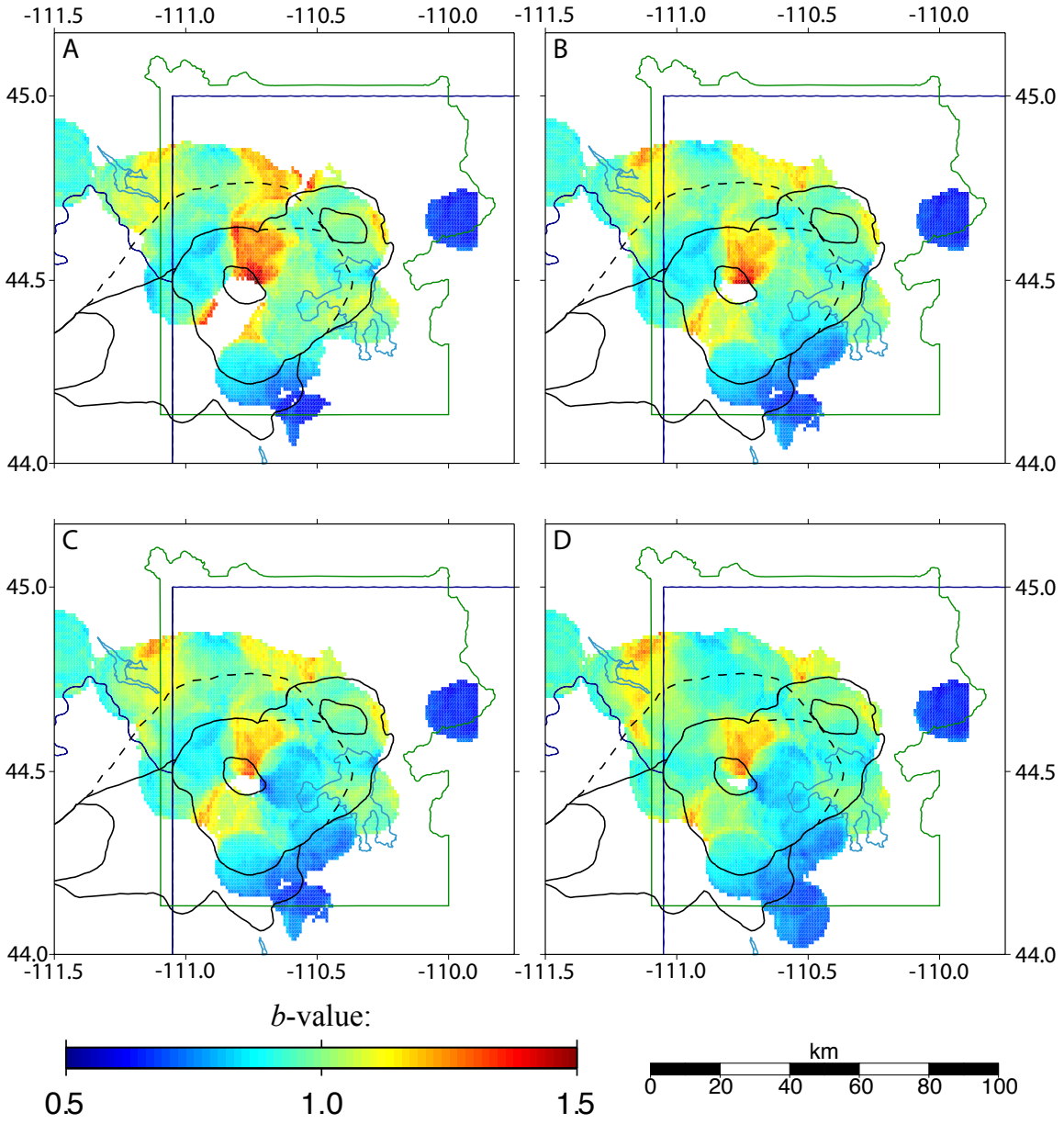

Figure 2.7. *b*-value maps for all the earthquake listings shown in Fig. 2.6. (A) *b*-values calculated for the 10-minimum deswarmed catalog, (B) *b*-values calculated for the 30-minimum deswarmed catalog, (C) *b*-values calculated for the 50-minimum deswarmed catalog, and (D) *b*-values calculated for the non-deswarmed catalog. Red-orange colors indicate high *b*-values and blue-green colors represent low *b*-values.

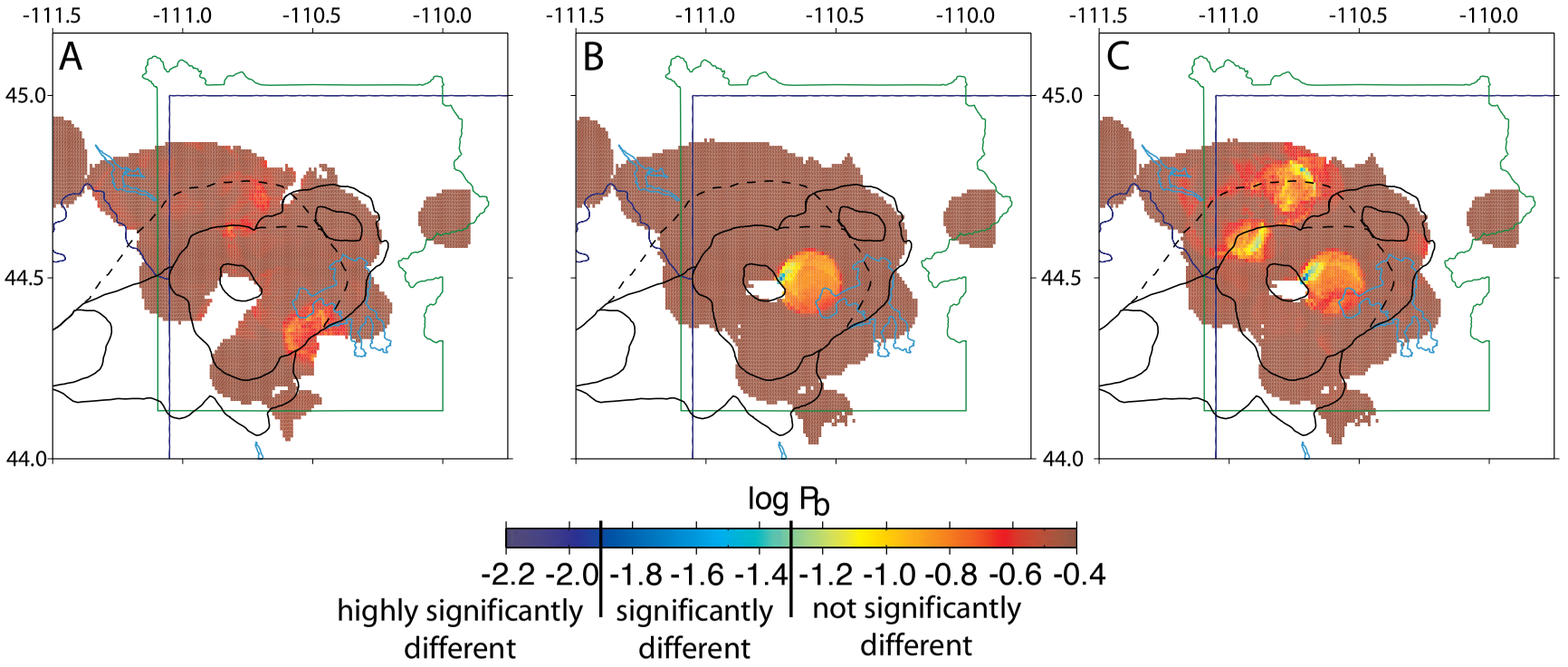

Figure 2.8. Utsu Test results [*Utsu*, 1992] comparing the various *b*-value maps. (A) Ten-minimum vs. 30-minimum, (B) 30-minimum vs. 50-minimum, and (C) 30-minimum vs. non-deswarmed. Red colors show values that are not significantly different and blue to green colors show values that are statistically different.

which introduced a significant difference between the 30-minimum and 50-minimum models by biasing the *b*-value calculations (Figure 2.9). Because this swarm could be considered an outlier, we prefer to remove it from the catalog by using the dataset from the 30-minimum swarm definition.

Only data at 0.18% of the sampling interval are significantly different (Figure 2.8C) when comparing the *b*-values from the 30-minimum dataset with the *b*-values from the original, unsorted dataset. Some of these differences are due to the same swarm event that was just discussed. Just to the north of the Yellowstone caldera another area shows significantly different *b*-values. The differences here are attributed to five events ranging from $3.0 \leq M_C \leq 3.8$. These five earthquakes were identified in two swarms and were removed in the 30-minimum dataset. Because they all occurred in the same area, they all influenced the *b*-value calculation for the original catalog. The unfiltered catalog was discarded and the 30-minimum dataset was chosen as the most stable and best catalog to use when interpreting *b*-values because the *b*-value is influenced heavily by just these five events.

There are three areas of relatively high *b*-values for the 30-minimum event catalog (Figure 2.10). The area with the highest *b*-values is associated with earthquakes of the Mallard Lake resurgent dome (MLD) where *b*-values are as high as 1.5 ± 0.05. This area of high *b*-values extends north from the MLD to Madison Junction. A secondary area with high *b*-values is located near Norris Geyser Basin (NGB) and extends north along the Norris-Mammoth Corridor and east to the northern boundary of the Yellowstone caldera. The Gallatin fault bounds this area of elevated *b*-values to the west. Here we see values of *b* up to 1.3 ± 0.05. The third area where we see elevated *b*-

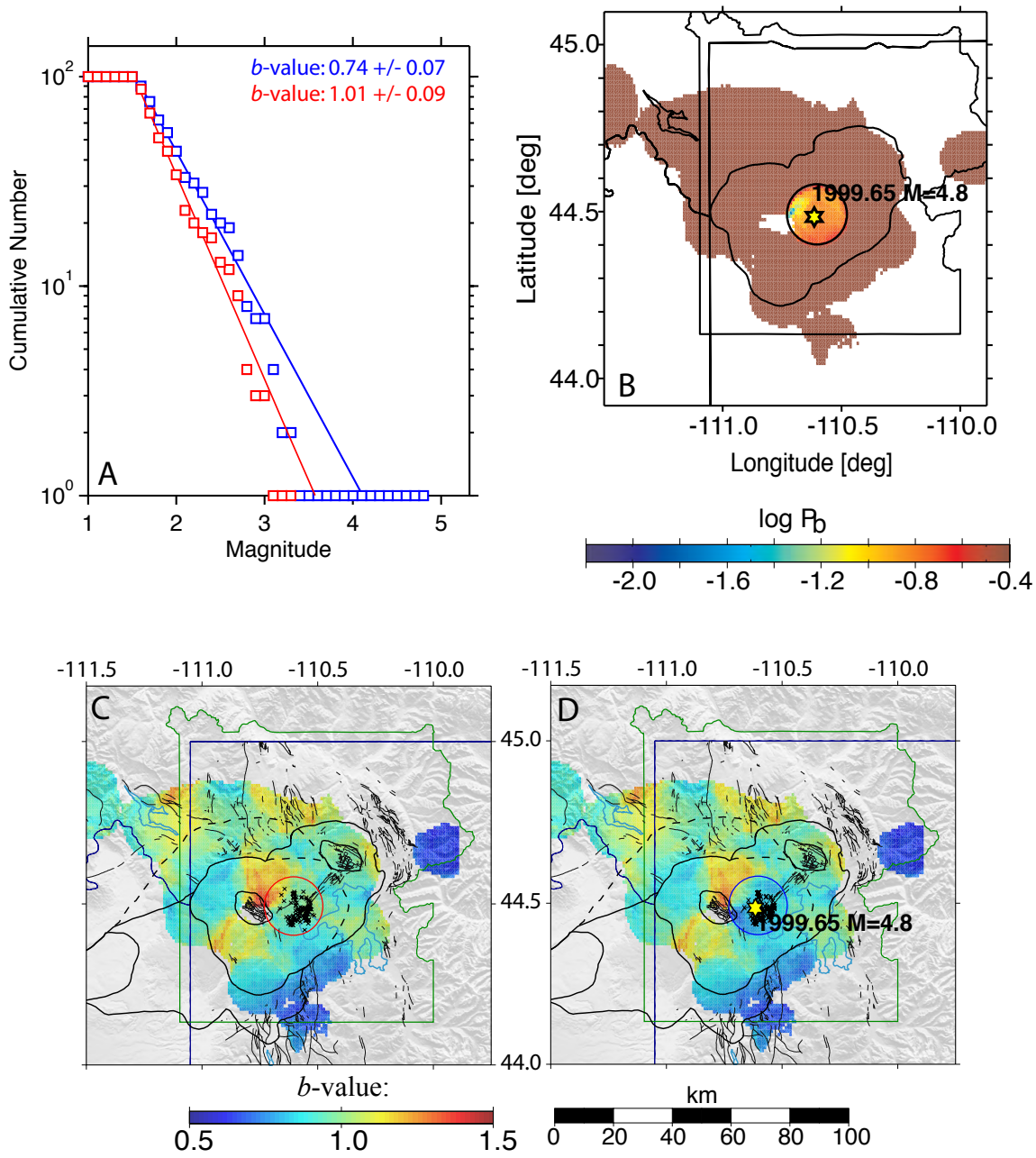

Figure 2.9. Frequency–magnitude distribution (FMD) of earthquakes comparison for the 30-minimum *b*-value map vs. the 50-minimum *b*-value map. (A) shows the FMDs for the two samples shown in C and D. Colors match the colors of the sampling radii shown in the circles in C and D. (B) shows the Utsu test results with significantly different *b*-values in the central Yellowstone caldera. (C) shows the *b*-value distribution with the sampling radius (red) for the 30-minimum de-swarmed catalog. (D) shows the *b*-value distribution with the sampling radius (blue) for the 50-minimum deswarmed catalog.

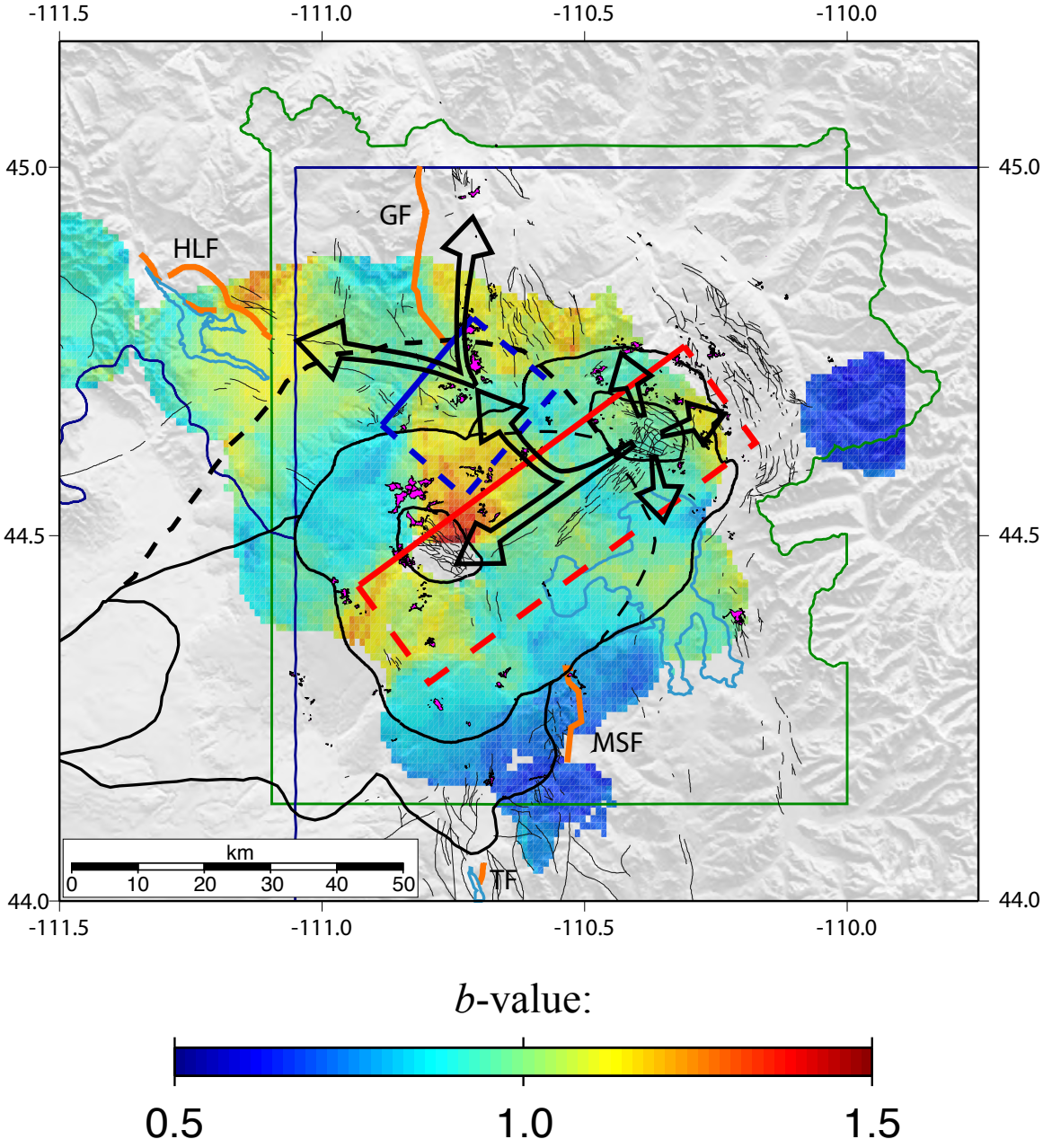

Figure 2.10. Spatial *b*-value distribution for the 30-minimum Yellowstone deswarmed catalog. Red to orange colors represent high *b*-values and cool colors represent low *b*-values. Areas of hydrothermal activity are plotted in purple. Light blue lines represent the outline of lakes. Arrows show interpreted magma migration paths from *Wicks et al.* [2006]. Red and blue polygons show the location of the expanding sill and the deflating sill, respectively, from *Chang et al.* [2007]. MSF = Mt. Sheridan fault, HLF = Hebgen Lake fault, GF = Gallatin fault, and TF = Teton fault.

values is in the Hebgen Lake area just west of the Yellowstone National Park border. This area is also the site of the M 7.5 Hebgen Lake earthquake in 1959. The highest *b*-value in the Hebgen Lake area was 1.3 ± 0.1 just to the northeast of the Red Canyon fault.

Two areas had relatively low *b*-values. The first is east of the Sour Creek Resurgent Dome (SCD) on the park border, with *b*-values as low as 0.5 ± 0.1. This is an area that has experienced persistent seismic activity throughout the entire time span of Yellowstone earthquake recording. The second area of low *b*-values is located at the southern portion of the Yellowstone caldera near the Mt. Sheridan fault (MSF) and near the northern extent of the Teton fault. In this area *b*-values are as low as 0.6 ± 0.1.

We have determined the errors in our calculations to assess the validity of our calculations (Figure 2.11). The majority of the errors in *b*-values are less than 0.1. The largest errors in *b* (~0.15) are located on the eastern side of the 0.64-Ma caldera. These larger errors are due to the inclusion of a M_C=4.8 earthquake that occurred in 1999. The difference in the frequency-magnitude distribution due to this single event can also be seen in Figure 2.9. The lowest errors (< 0.05) occur in the area north of the 0.64-Ma caldera where the highest concentration of epicenters is located.

The depth distribution and temporal changes in *b*-values was also examined, but because of our limited range in epicenter depths, our sampling radius of 5 km was too large to image differences in the *b*-value with depth. In addition, after filtering, there were too few earthquakes to adequately detect changes in *b*-values over time.

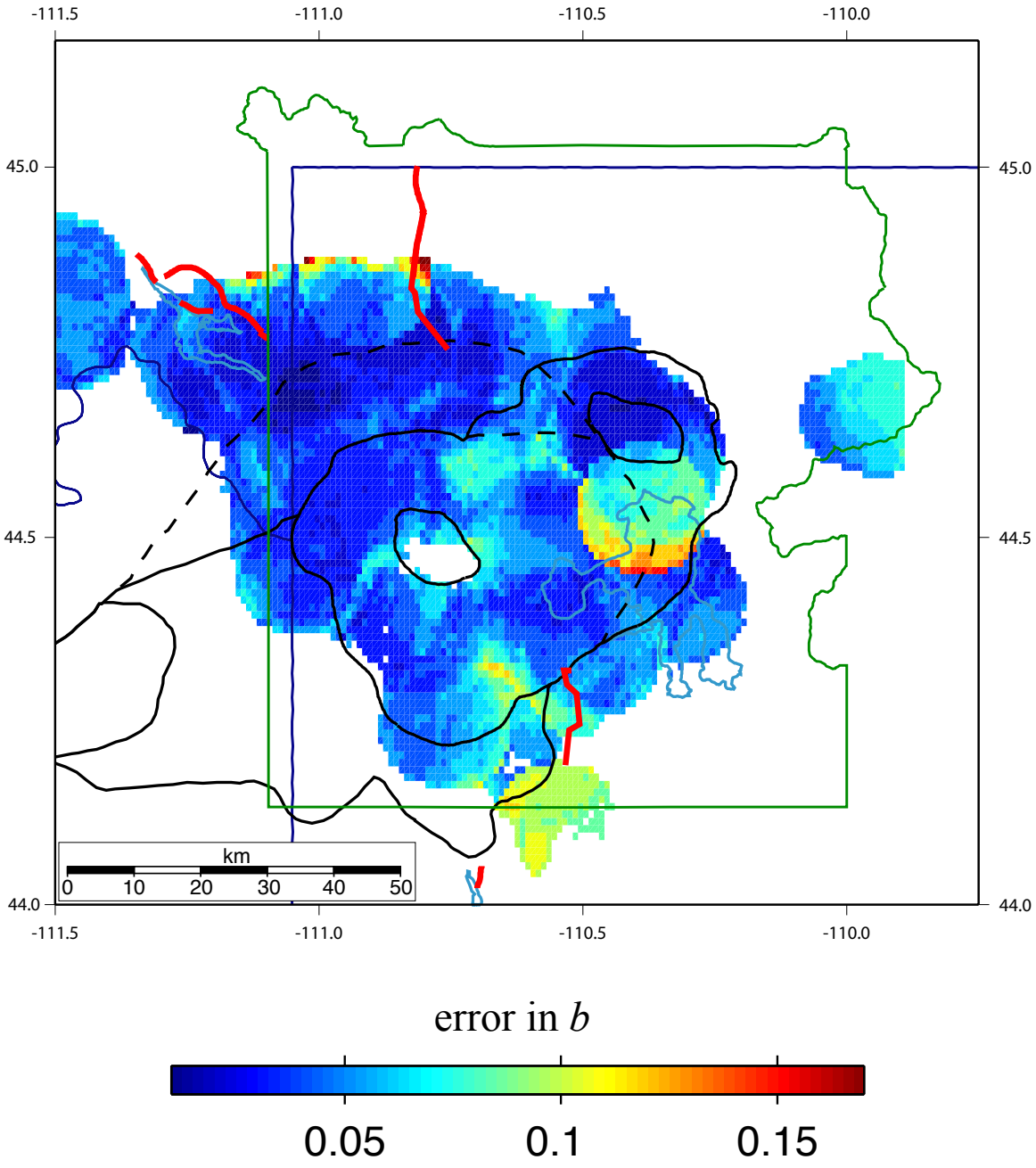

Figure 2.11. Errors in the *b*-value calculations. Calderas I, II, and III are outlined in black. Major Quaternary faults are shown as thick red lines. Symbols are as shown above.

Discussion

Swarm Identification

Using the definition that a swarm had to contain at least 30 events, ~39% of the recorded earthquakes in the Yellowstone region are associated with swarms. Of the 69 swarms identified, 54 (78.3%) are located in the region north and northwest of the Yellowstone caldera while 14 (20.3%) are located within or at the Yellowstone caldera boundary (Figure 2.3).

Because a high number of swarms were identified in the east-west band of seismicity extending from the Hebgen Lake fault to the Norris Geyser Basin, we interpret the seismogenic upper crust here to be highly fractured, with a large number of small magnitude earthquakes occurring on numerous small fractures. This interpretation is based on the concentration of earthquake swarms that are often associated with volcanic features or other fractured regions where there is a concentrated application of stress such as intruding magma [*Mogi*, 1963]. There is also an abrupt change in the topography in this region and the east-west alignment of swarm epicenters here indicates that this is the location of the northern rim of the 2.05-Ma caldera, which is about 15 km north of the mapped Yellowstone caldera rim of *Christiansen* [2001].

Moreover, it is considered that the Gallatin Range was once continuous to the south but is now covered beneath young volcanic rocks of the Yellowstone giant silicic eruptions [*Christiansen*, 2001]. During the first catastrophic eruption 2.05 million years ago, the mountain range was destroyed by the explosive caldera-forming eruption and by caldera collapse [*Smith and Siegel*, 2000]. The east-west alignment of swarm epicenters in this area is significant in that the swarms may be occurring on pre-existing zones of

weakness from the 2.05-Ma caldera eruption.

It also has been shown that Yellowstone swarms can be attributed to the migration of magmatic or hydrothermal fluids [*Waite and Smith*, 2002]. Although these swarms are much smaller in both the number of earthquakes as well as the spatial extent of earthquakes than the 1985 swarm that was examined by *Waite and Smith* [2002], it is plausible to hypothesize that the associated earthquakes are the result of a migration of fluids (magmatic and/or hydrothermal) along either pre-existing cracks or propagating dikes.

Hill [1977], for example, suggested a process to explain earthquake swarms: In a series of dikes oriented with their long dimension parallel to the regional greatest principal stress, shear failures occur along oblique fault planes connecting adjacent tips of en echelon or parallel dikes when a critical combination of fluid pressure in the dikes and the difference between σ_1 and σ_3 is reached.

Summarizing other swam studies, *Toda et al*. [2002] also suggested that the 2000 Izu Islands, Japan earthquake swarm was caused by a laterally propagating dike intrusion. *Waite and Smith* [2002] propose that the 1985 swarm in Yellowstone was due to the migration of magmatic or hydrothermal fluids. In particular they state that the most likely scenario for the swarm involves the rupture of a self-sealed hydrothermal layer and subsequent migration of hydrothermal fluid through a pre-existing fracture zone out of the Yellowstone caldera. More recently, *Vidale et al.* [2006] suggested that swarms may be due to nonmagmatic sources such as a variable component of background seismicity driven by aseismic slip and fluid pressure variations.

b-value Distribution

We interpret the area of high *b*-values (up to 1.5 ± 0.05) in the area located near the Mallard Lake resurgent dome (MLD) (Figure 2.10) to be influenced by high crustal heterogeneity of the local stress regime, a high thermal gradient and magmatic fluids. This high heterogeneity of stress causes numerous small cracks in the crust to be oriented in all directions. Under these conditions, the likelihood of large earthquakes occurring is decreased because a rupture terminates when it encounters an existing crack orientated unfavorably for failure. In such a highly fractured crust, many small ruptures would be observed but fewer larger ones, which is what is observed in the frequency-magnitude distribution [*Wiemer et al.,* 1998]. The average magnitude of events in this area is ~1.5 and corresponds to an average rupture length of about 70 m [*Wiemer and McNutt*, 1997; *Kanamori and Anderson*, 1975]. Small cracks produce only small earthquakes because of their short source length. This is comparable with results from the Long Valley Caldera in eastern California, which is a similar large silicic volcanic center where *Wiemer et al.* [1998] found high *b*-values ($b>1.5$) in the area near the resurgent dome and interpreted these to be the result of a highly fractured crust [*Hill*, 1992].

The high thermal gradient in the Yellowstone caldera is considered to be attributed to the presence of magmatic fluids below the surface [*Eaton et al.*, 1975; *Fournier*, 1989; *Husen et al.*, 2004a]. The shallowest earthquakes in the area occur beneath the MLD (Figure 1.5) where the depth of 80% of the hypocenters is ~5 km [*Smith et al.*, 2009]. This depth is interpreted as the brittle-ductile transition zone with a temperature of ~400°C [*Sibson*, 1982; *Smith and Bruhn*, 1984; *Fournier*, 1999] and gives a thermal gradient of ~80°C/km for the area beneath the Mallard Lake resurgent dome. If

the average 80th percentile depth of 8 km inside the 0.64-Ma caldera is used, an average thermal gradient of ~50°C/km is determined. *Smith and Braile* [1994] estimated an average thermal gradient for the Yellowstone region of ~45°C/km. This supports the results of *Warren and Latham* [1970], in which they show that an increase in the thermal gradient causes an increase in *b*.

The emplacement of magma and the accompanying crustal expansion as suggested by *Wicks et al.* [2006] and *Chang et al.* [2007] for the high crustal deformation rates would give rise to factors responsible for high *b*-value measurements: mainly high heterogeneity of the crust due to numerous cracks from the increased stress and a high thermal gradient, which is also supported by focal depth distribution. Given that the period of uplift and the period of high *b*-values overlap in time, these could be the underlying reasons for the high *b*-values measured in this study.

The area of high *b*-values of up to 1.3 ± 0.05 north of the Yellowstone caldera rim extending from Norris Geyser Basin may also be a result of magmatic fluids migrating from the Yellowstone caldera north into the Norris-Mammoth corridor [*Wicks et al.*, 2006] (Figure 2.10). Again, the presence of magma gives rise to the main factors causing higher *b*-values, mainly high heterogeneity, and high thermal gradient. The presence of partial melt causes higher temperatures. In turn, a zone of relatively lower stress around the area of partial melt is created because the high temperatures reduce the strength of the material which would not allow significant stress buildup. Numerous small cracks would form as the area of partial melt pushed up through the crust as well.

The area of high *b*-values located near Hebgen Lake, exhibiting values up to 1.3 ± 0.1, could also be the result of magma migrating laterally from the Yellowstone caldera

(Figure 2.10). More likely, high *b*-values in this area are a reflection of a relatively low stress regime as a result of the 1959 Hebgen Lake earthquake. *Chang and Smith* [2002] show that the 1959 M7.5 Hebgen Lake earthquake caused a decrease in the Coulomb failure stress of about 0.4 MPa (compared to a static-stress drop of 12 MPa observed for the Hebgen Lake mainshock [*Doser*, 1985] in the areas immediately north and south of the fault where we see higher *b*-values.

Another explanation for higher *b*-values within the Yellowstone caldera and in the Norris-Mammoth Corridor (Figure 2.1) could be because of the high concentration of hydrothermal features in the area. Hydrothermal waters of Yellowstone circulate through the crust in an intricate system of cracks and are heated from below by a body of crystallizing magma [*Fournier*, 1989]. The presence of extensive hydrothermal activity shows that the crust is very heterogeneous due to the numerous fractures that facilitate the flow of hydrothermal waters through the crust. There is a correlation between higher *b*-values and the location of hydrothermal features in the western half of Yellowstone (Figure 2.10). This would indicate that the high *b*-values may be due to both the highly fractured (heterogeneous) crust and the high temperatures as well as high pore pressures that allow hydrothermal fluid flow. Therefore, the high *b*-values could be an indication of the highly fractured crust that facilitates the movement of hot, hydrothermal fluids. *Wall* [2005] showed that northeast-southwest and northwest-southeast trending fractures in the 0.64-Ma Lava Creek Tuff provide major flow pathways for hydrothermal fluids at Norris Geyser Basin.

The area of low *b*-values in the southern part of the park where *b*-values are as low as 0.6 ± 0.1 (Figure 2.10) can be attributed to high stress accumulation from large

Basin-Range faults south of the Yellowstone caldera and outside the dominant influence of the magma system. Stress accumulation would take place mainly on the Mt. Sheridan fault and the Teton fault. The northern segment of the Teton fault appears to extend northward under the 70,000-yr-old Pitchstone Plateau Rhyolite, and the eastern segment of the fault merges into the remains of the ring-fracture system from the 2.05 Ma caldera in Yellowstone National Park [*Christiansen and Blank*, 1972; *Christiansen*, 2001]. North-south bands of seismicity extend from the northern extent of the Teton fault into the Yellowstone caldera (Figure 1.4) suggesting that these earthquakes occur on existing zones of weakness that may be a buried remnant of the Teton fault.

White et al. [2009] suggested that the transition from northeast-southwest extension in the northern Teton region to east-west extension in the central and southern Teton region indicates that the stress field along the northern Teton fault may be affected by the stress field of the Yellowstone volcanic system. Given the rapid change in stress orientation around the northern Teton fault segment, the fault may be locked due to westward compression, which would also be loading the fault segment at the same time [*White et al.*, 2009]. Similar results were argued by *Hampel and Hetzel* [2008] who used finite element modeling to investigate the high rates of Yellowstone caldera uplift and subsidence and its effects on the area south of the Yellowstone caldera and the Teton fault. They show that caldera uplift can induce variations of the stresses of the Teton fault including horizontal compression. *Puskas et al.* [2007] also recorded reverse motion on the Teton fault using GPS.

It is plausible that the Mt. Sheridan fault could be experiencing higher loading rates as well. The Mt. Sheridan fault is a large north-south striking normal fault

bounding the east side of Mt. Sheridan (Figure 2.1) and is about 41 km long [*Wong et al.*, 2000]. It is believed that prior to the cataclysmic caldera-forming eruptions at Yellowstone, the Mt. Sheridan fault was continuous across the Yellowstone Plateau with the faults to the north of the Yellowstone caldera [*Smith and Siegel*, 2000].

Scholz [1968], *Wyss* [1973], *Urbancic et al.* [1992], *Schorlemmer and Wiemer* [2004], and *Schorlemmer et al.* [2005] showed that an increase in applied shear stress or an increase in effective stress decreases the *b*-value. It is proposed here that the low *b*-values in the southern portion of Yellowstone National Park are due to stress buildup from the East Mt. Sheridan fault and the Teton fault [e.g., *Hampel and Hetzel*, 2008; *White et al.*, 2009]. The high stress in the area could be due to crustal deformation from the volcanic system in Yellowstone loading the faults. It is not well known how the large normal faults to the north and south interact with the Yellowstone caldera system, more specifically, whether or not the volcanic system is loading the faults or whether it is absorbing stress.

Conclusions

Significant spatial variations in the frequency-magnitude distribution are well-defined in the Yellowstone region and are related to variations in tectonic and volcanic processes. Thirty-nine percent of Yellowstone earthquakes occur in swarms. This corresponds to about 38% of the total seismic moment, which equates to an equivalent magnitude of 4.9. Sixty-nine distinct swarms (Figure 2.3) were identified during the study period, 1984-2006, comprising 8,924 earthquakes. Fifty-four of the 69 swarms occur in the east-west band of seismicity that extends from the Hebgen Lake fault to the

Norris Geyser Basin (Figure 2.3). Swarms vary in duration from 1 to 46 days and have a range of 30 to 722 total events.

The area of high *b*-values just to the north of the Mallard Lake dome, where b-values up to 1.5 ± 0.05 are present, is attributed to the presence of a high thermal gradient due to the emplacement of magmatic fluids. Using InSAR data, *Wicks et al.* [2006] interpreted this area of uplift as due to the emplacement of basaltic magma at ~15 km below the surface. Magma intrusion as well as crustal deformation are processes that would alter the frequency-magnitude distribution of earthquakes towards high *b*-values. As magmatic fluids are injected into the system, temperatures are expected to rise around the intrusion and the crust would weaken due to its inability to accumulate high amounts of stress. The high temperature, weakened crust and the expanding sill could cause the formation of numerous small fractures as magma escaped the Yellowstone caldera system. A relatively large number of smaller earthquakes are expected to accompany the formation of small fractures and would alter the frequency-magnitude distribution of earthquakes towards higher *b*-values. This supports the hypothesis that the higher *b*-values in this region are due to the presence of magmatic fluids.

Chang et al. [2007] suggest that the 2004-2006 episode of accelerated uplift of up to 7 cm/yr, occurred in response to a caldera-wide magma recharge of the Yellowstone volcanic system. The unprecedented crustal uplift as well as the increase in thermal gradient due to magma recharge would tend to alter the frequency-magnitude distribution of earthquakes towards a higher *b*-value by not allowing sufficient stress build up on the fractures.

The area of low *b*-values up to 14 km south of the 0.64-Ma caldera rim where *b*-

values are as low as 0.6 ± 0.1 is interpreted to be due to high stress in the crust from the loading of both the Mt. Sheridan fault and the Teton fault. This could also be an indication of a relatively strong crust and a thicker seismogenic layer that is resistant to fracture. It is not clear if the high stress in the crust is due to the lack of large earthquakes on the Mt. Sheridan and Teton faults in the recent past or if those faults are being loaded by the crustal deformation from the Yellowstone volcanic system.

With additional data and better broadband seismograph coverage, not only will more information be obtained for Yellowstone earthquakes, but the data will continue to be of higher quality as the network continues to be upgraded to broader frequency recording and location techniques improve. This will allow better determinations of the *b*-value distribution both laterally and with depth as well as over time. This data can be used to better understand what processes are occurring in the crust at Yellowstone and their implications for local earthquake and volcanic hazards.

Acknowledgements

We would like to thank Christine Puskas, Wu-Lung Chang, Michael Jordan, Bonnie Pickering-White, Aaron DeNosaquo, and Katrina DeNosaquo for in depth discussions. Greg Waite provided the swarm identification algorithm used in this study. We also thank Jochan Woessner and Danijel Schorlemmer for providing help with the *b*-value analysis program, ZMAP. We would also like to thank Mike Stickney and an anonymous reviewer for their comments and suggestions.

Funding for the project was provided by the National Science Foundation Continental Dynamics Program grants #EAR 9725431, 0314298, and 9316289 and the NSF

GEOsciences Network (GEON) project, EAR-0724265. Data support was partially provided by the Yellowstone Volcano Observatory. The University of Utah provided computational and technical assistance as well.

References

Akaike, H. (1974), A new look at the statistical model identification, *IEEE Trans. Automatic Control*, *19*, 716-723.

Aki, K. (1965), Maximum likelihood estimate of *b* in the formula log $N = a – bM$ and its confidence limits, *Bull. Earthquake Res. Inst. Tokyo Univ.*, *43*, 237-239.

Bender, B. (1983), Maximum likelihood estimation of *b* values for magnitude grouped data, *Bull. Seismol. Soc. Am.*, *73*, 831-851.

Benz, H. M., and R. B. Smith (1984), Simultaneous inversion for lateral velocity variations and hypocenters in the Yellowstone region using earthquake and refraction data, *J. Geophys. Res.*, *89*, 1208-1220.

Blackwell, D. D. (1969), Heat-flow determinations in the northwestern United States, *J. Geophys. Res.*, *74*, 992-1007.

Chang, W.-L., and R. B. Smith (2002), Integrated seismic-hazard analysis of the Wasatch Front, Utah, *Bull. Seismol. Soc. Am.*, *92*, 1904-1922.

Chang, W. -L, R. B. Smith, C. Wicks, C. M. Puskas, and J. Farrell (2007), Accelerated uplift and source models of the Yellowstone caldera, 2004-2006, from GPS and InSAR observations, *Science, 318*(5852): 952-956, doi:10.1126/science.1146842.

Christiansen, R. L. (1984), Yellowstone magmatic evolution: Its bearing on understanding large-volume explosive volcanism, in *Explosive Volcanism: Inception, Evolution and Hazards*, pp. 84-95, National Academy Press, Washington D.C.

Christiansen, R. L. (2001), The Quaternary and Pliocene Yellowstone plateau volcanic field of Wyoming, Idaho, and Montana, *U.S. Geol. Surv. Profess. Pap. 729-G*, 145.

Christiansen, R. L., and H. R. Blank, Jr. (1972), Volcanic stratigraphy of the Quaternary rhyolite plateau in Yellowstone National Park, *U.S. Geol. Surv. Profess. Pap. 516-E*, 6.

DeNosaquo, K., R. B. Smith, and A. R. Lowry (2009), Density and lithospheric strength models of the Yellowstone-Snake River Plain volcanic system from gravity and heat flow data, *J. Volcanol. Geotherm. Res*., *188*, 108-127.

Doser, D. I. (1985), Source parameters and faulting processes of the 1959 Hebgen Lake, Montana, earthquake sequence, *J. Geophys. Res.*, *90*, 4537-4555.

Doser, D. I., and R. B. Smith (1983), Seismicity of the Teton-Southern Yellowstone Region, Wyoming, *Bull. Seism. Soc. America*, *73*, 1369-1394.

Dzurisin, D., J.C. Savage, and R.O. Fournier (1990), Recent crustal subsidence at Yellowstone caldera, Wyoming, *Bull. Volcanol.*, *52*, 247-270.

Eaton, G. P., R. L. Christiansen, H. M. Iyer, A. D. Pitt, D. R. Mabey, H. R. Bland Jr., I. Zietz, and M. E. Gettings (1975), Magma beneath Yellowstone National Park, *Science*, *188*, 787-796.

Farrell, J., R. B. Smith, T. Taira, W.-L. Chang, and C. M. Puskas (2010), Dynamics and rapid migration of the energetic 2008-2009 Yellowstone Lake earthquake swarm, *Geophys. Res. Lett.*, *37*, L19305, doi:10.1029/2010GL044605.

Fournier, R. O. (1989), Geochemistry and dynamics of the Yellowstone National Park hydro-thermal system, *Ann. Rev. Earth Planet. Sci.*, *17*, 13-53.

Fournier, R. O. (1999), Hydrothermal processes related to movement of fluid from plastic into brittle rock in the magmatic-epithermal environment, *Economic Geology*, *94*, no. 8, 1193-1212.

Frolich, C., and S. Davis (1993), Teleseismic *b*-values: or much ado about 1.0, *J. Geophys. Res.*, *98*, 631-644.

Guo, Z., and Y. Ogata (1997), Statistical relations between the parameters of aftershocks in time, space, and magnitude, *J. Geophys. Res.*, *102*, 2857-2873.

Gutenberg, B., and C. F. Richter (1944), Frequency of earthquakes in California, *Bull. Seismol. Soc. Am.*, *34*, 185-188.

Hampel, A., and R. Hetzel (2008), Slip reversals on active normal faults related to the inflation and deflation of magma chambers: Numerical modeling with application to the Yellowstone-Teton region. *Geophys. Res. Lett.*, *35*, L07301, doi:10.1029/2008GL033226.

Hill, D. P. (1977), A model for earthquake swarms, *J. Geophys. Res.*, *82*, 1347-1352.

Hill, D. P. (1992), Temperatures at the base of the seismogenic crust beneath Long Valley Caldera, California, and the Phlegrean Fields Caldera, Italy. *in*: Gasparini, P.; Scarpa, R.; Aki, K. *ed.* Volcanic Seismology, Springer-Verlag, Berlin. Pg. 432-461.

Husen, S., and R. B. Smith (2004), Probabilistic earthquake relocation in three-dimensional velocity models for the Yellowstone National Park region, Wyoming, *Bull. Seismol. Soc. Am.*, *94*, 880-896.

Husen, S., R. B. Smith, and G. P. Waite (2004a), Evidence for gas and magmatic sources beneath the Yellowstone volcanic field from seismic tomographic imaging, *J. Volcanol. Geotherm. Res.*, *131*, 397-410.

Husen, S., S. Wiemer, and R. B. Smith (2004b), Remotely triggered seismicity in the Yellowstone National Park region by the 2002 M_w 7.9 Denali fault earthquake, Alaska, *Bull. Seismol. Soc. Am.*, *94*, no. 6B, S317-S331.

Husen, S. R. Taylor, R. B. Smith, and H. Heasler (2004c), Changes in geyser eruption behavior and remotely triggered seismicity in Yellowstone National Park produced by the 2002 M 7.9 Denali fault earthquake, Alaska, *Geology*, *32*, 537-540.

Ishimoto, M., and K. Iida (1939), Observations of earthquakes registered with the microseismograph constructed recently, *Bull. Earthquake Res. Inst. Tokyo Univ.*, *17*, 443-478.

Jolly, A. D., and S. R. McNutt (1999), Relationship between *b*-values and maximum depths of seismicity at Martin and Mageik volcanoes, Katmai National Park, Alaska; July 1995-December 1997, *J. Volcanol. Geotherm. Res.*, *93*, 173-190.

Kanamori, H., and D. L. Anderson (1975), Theoretical basis of some empirical relations in seismology, *Bull. Seism. Soc. Am.*, *65*, 1073-1095.

Lynch, D. P. (1999), Three-dimensional finite difference tomography of the Basin and Range-Colorado Plateau-Rocky Mountain transition using earthquake and controlled source data: M.S. thesis, University of Utah, Salt Lake City.

McNutt, S. R. (2005), Volcanic seismology, *Annu. Rev. Earth. Planet. Sci.*, *33*, 461-491.

Miller, D. S., and R. B. Smith (1999), *P* and *S* velocity structure of the Yellowstone volcanic field from local earthquake and controlled source tomography, *J. Geophys. Res.*, *104*, 15105-15121.

Mogi, K. (1962), Magnitude-frequency relation for elastic shocks accompanying fractures of various materials and some related problems in earthquakes, *Bull. Earthquake Res. Inst. Univ. Tokyo*, *40*, 831-853.

Mogi, K. (1963), Some discussions on aftershocks, foreshocks and earthquake swarms – The fracture of a semi-infinite body caused by an inner stress origin and its relation to the earthquake phenomena, 3, *Bull. Earthquake Res. Inst. Tokyo Univ.*, *41*, 615-658.

Morgan, P., D. D. Blackwell, R. E. Spafford, and R. B. Smith (1977), Heat flow measurements in Yellowstone Lake and the thermal structure of the Yellowstone caldera, *J. Geophys. Res.*, *82*, 3719-3732.

Murru, M., C. Montuori, M. Wyss, and E. Privitera (1999), The locations of magma chambers at Mt. Etna, Italy, mapped by *b*-values, *Geophys. Res. Lett.*, *26*, 2553-2556.

Pechmann, J. C., J. C. Bernier, S. J. Nava, F. M. Terra, and W. J. Arabasz (2001), Correction of systematic time-dependent coda magnitude errors in the Utah and Yellowstone National Park region earthquake catalogs, 1981-2001, *EOS Trans. AGU 82*(47), Fall Meet. Suppl., Abstract S11B-0572.

Pelton, J.R., and R. B. Smith (1982), Contemporary vertical surface displacements in Yellowstone National Park, *J. Geophys. Res.*, *87*, 2745-2761.

Pitt, A. M., C. S. Weaver, and W. Spence (1979), The Yellowstone Park earthquake of June 30, 1975, *Bull. Seismol. Soc. Am.*, *69*, 187-205.

Power, J. A., M. Wyss, and J. L. Latchman (1998), Spatial variations in the frequency-magnitude distribution of earthquakes at Soufriere Hills volcano, Montserrat, West Indies, *Geophys. Res. Lett.*, *25*, 3653-3656.

Puskas, C. M., R. B. Smith, C. M. Meertens, and W. L. Chang (2007), Crustal deformation of the Yellowstone-Snake River Plain volcanic system: Campaign and continuous GPS observations, 1987-2004, *J. Geophys. Res.*, *112*, B03401, doi:10.1029/2006JB004325.

Reasenberg, P. (1985), Second-order moment of central California seismicity, 1969-1982, *J. Geophys., Res.*, *90*, 5479-5495.

Sanchez, J. J., S. R. McNutt, J. A. Power, and M. Wyss (2004), Spatial variations in the frequency-magnitude distribution of earthquakes at Mount Pinatubo volcano, *Bull. Seismol. Soc. Am.*, *94*, 430-438.

Scholz, C. H. (1968), The frequency-magnitude relation of microfracturing in rock and its relation to earthquakes, *Bull. Seismol. Soc. Am.*, *58*, 399-415.

Schorlemmer, D., and S. Wiemer (2004), Earthquake statistics at Parkfield: 1. Stationarity of b values, *J. Geophys. Res.*, *109*, B12307, doi:10.1029/2004JB003234.

Schorlemmer, D., and S. Wiemer (2005), Microseismicity data forecast rupture area, *Nature*, *434*, 1086.

Schorlemmer, D., S. Wiemer, and M. Wyss (2005), Variations in earthquake-size distribution across different stress regimes, *Nature*, *437*, 539-542.

Shi, Y., and B. A. Bolt (1982), The standard error of the magnitude-frequency *b*-value, *Bull. Seismol. Soc. Am.*, *72*, 1677-1687.

Sibson, R. H. (1982), Fault zone models, heat flow, and the depth distribution of earthquakes in the continental crust of the United States, *Bull. Seismol. Soc. Am.*, *72*, no. 1, 151-163.

Smith, R. B., and M. Sbar (1974), Contemporary tectonics and seismicity of the Western United States with emphasis on the Intermountain Seismic Belt, *Bull. Geol. Soc. Am.*, *85*, 1205-1218.

Smith, R. B., and R. L. Bruhn (1984), Intraplate extensional tectonics of the eastern basin-range: Inferences on structural style from seismic reflection data, regional tectonics, and thermal-mechanical models of brittle-ductile deformation, *J. Geophys. Res.*, *89*, 5733-5762.

Smith, R. B., and W. J. Arabasz (1991), Seismicity of the Intermountain Seismic Belt, in *Neo-tectonics of North America*, edited by D. B. Slemmons, E. R. Engdahl, M. D. Zoback, and D. D. Blackwell, Geological Society of America, Boulder, Colorado., Pg. 185-228.

Smith, R. B., and L. W. Braile (1994), The Yellowstone hotspot, *J. Volcanol. Geotherm. Res.*, *61,* 121-187.

Smith, R. B., and L. Siegel (2000), *Windows into the Earth: The Geology of Yellowstone and Grand Teton Parks*, Oxford University Press, London, 247.

Smith, R. B., R. T. Shuey, J. R. Pelton, and J. P. Bailey (1977), Yellowstone hotspot, crustal properties from new earthquake and magnetic data, *J. Geophys. Res.*, *82*, 3665-3676

Smith, R.B., M. Jordan, B. Steinberger, C.M. Puskas, J. Farrell, G.P. Waite, S. Husen, W.L. Chang, and R. O'Connell (2009), Geodynamics of the Yellowstone hotspot and mantle plume: Seismic and GPS imaging, kinematics, and mantle flow, *J. Volcanol. Geotherm. Res.*, *188*, 26-56.

Sykes, L. R. (1970), Earthquake swarms and sea-floor spreading, *J. Geophys. Res.*, *75*, 6598-6611.

Taira, T., R. B. Smith, and W. -L. Chang (2010), Seismic evidence for dilatational source deformations accompanying the 2004-2008 Yellowstone accelerated uplift episode, *J. Geophys. Res.*, *115*, B02301, doi:10.1029/2008JB006281.

Toda, Shinji, R. S. Stein, and T. Sagiya (2002), Evidence from the AD 2000 Izu islands earthquake swarm that stressing rate governs seismicity, *Nature*, *419*, 58-61.

Urbancic, T. I., C. I. Trifu, J. M. Long, and R. P. Toung (1992), Space-time correlations of *b* values with stress release, *Pure Appl. Geophys.*, *139*, 449-462.

Utsu, T. (1965), A method for determining the value of *b* in a formula log $N = a - bM$ showing the magnitude frequency for earthquakes, *Geophys. Bull. Hokkaido Univ.*, *13*, 99-103.

Utsu, T. (1992), On seismicity, in *Report of the Joint Research Institute for Statistical Mathematics*, vol. 34, 139-157, Inst. For Stat. Math., Tokyo.

Utsu, T. (1999), Representation and analysis of the earthquake size distribution: A historical review and some approaches, *Pure Appl. Geophys.*, *155*, 509-535.

Vidale, J. E., K. L. Boyle, and P. M. Shearer (2006), Crustal earthquake bursts in California and Japan: Their patterns and relation to volcanoes, *Geophys. Res. Lett.*, *33*, L20313, doi:10.1029/2006GL027723.

Waite, G. P. (1999), Seismicity of the Yellowstone Plateau: Space-time patterns and stresses from focal mechanism inversion: M. S. thesis, University of Utah, Salt Lake City.

Waite, G. P., and R. B. Smith (2002), Seismic evidence for fluid migration accompanying subsidence of the Yellowstone caldera, *J. Geophys. Res.*, *107*(B9), 2177, doi:10.1029/2001JB000586.

Wall, B.R. (2005), Surface and subsurface hydrothermal flow pathways at Norris Geyser Basin, Yellowstone National Park, *Eos Trans. AGU*, *86*(52), Fall Meet. Suppl., Abstract T23B-0544.

Warren, N. W., and G. V. Latham (1970), An experimental study of thermally induced microfracturing and its relation to volcanic seismicity, *J. Geophys. Res.*, *75*, 4455-4464.

White, B. J. P., R. B. Smith, S. Husen, J. Farrell, and I. Wong (2009), Seismicity and earthquake hazard analysis of the Teton-Yellowstone region, Wyoming, *J. Volcanol. Geotherm. Res.*, *188*, 277-296, doi: 10.1016/j.jvolgeores.2009.08.015.

Wicks, C., W. Thatcher, D. Dzurisin, and J. Svarc (2006), Uplift, thermal unrest and magma intrusion at Yellowstone caldera, *Nature*, *440*, 72-75.

Wiemer, S. (2001), A software package to analyze seismicity: ZMAP, *Seism. Res. Lett.*, *72*, 373-382.

Wiemer, S., and J. P. Benoit (1996), Mapping the *b*-value anomaly at 100 km depth in Alaska and New Zealand subduction zones, *Geophys. Res. Lett.*, *24*, 189-192.

Wiemer, S., and S. R. McNutt (1997), Variations in the frequency-magnitude distribution with depth in two volcanic areas: Mount St. Helens, Washington, and Mt. Spurr, Alaska, *Geophys. Res. Lett.*, *24*, 189-192.

Wiemer, S., and M. Wyss (1997), Mapping the frequency-magnitude distribution in asperities: An improved technique to calculate recurrence times?, *J. Geophys. Res.*, *102*, 15115-15128.

Wiemer, S., and M. Wyss (2000), Minimum magnitude of completeness in earthquake catalogs: Examples from Alaska, the western United States, and Japan, *Bull. Seismol. Soc. Am.*, *90*, no. 4, 859-869.

Wiemer, S., and M. Wyss (2002), Mapping spatial variability of the frequency-magnitude distribution of earthquakes, *Adv. Geophys.*, *45*, 259-302.

Wiemer, S., S. R. McNutt, and M. Wyss (1998), Temporal and three-dimensional spatial analyses of the frequency-magnitude distribution near Long Valley Caldera, California, *Geophys. J. Int.*, *134*, 409-421.

Woessner, J., and S. Wiemer (2005), Assessing the quality of earthquake catalogues: Estimating the magnitude of completeness and its uncertainty, *Bull. Seismol. Soc. Am.*, *95*, no. 2, 684-698, doi: 10.1785/0120040007.

Wong, I., S. Olig, and M. Dober (2000), Preliminary Probabilistic Seismic Hazard Analysis; Island Park, Grassy Lake, Jackson Lake, Palisades, and Ririe Dams, U.R.S. Griener Woodward Clyde, Final report prepared for the Bureau of Reclamation, 40 pages.

Wyss, M. (1973), Towards a physical understanding of the earthquake frequency distribution, *Geophys. J. R. Astron. Soc.*, *31*, 341-359.

Wyss, M., S. Shimazaki, and S. Wiemer (1997), Mapping active magma chambers beneath the off-Ito volcano, Japan, *J. Geophys. Res.*, *102*, 413-420.

Wyss, M., F. Klein, K. Nagamine, and S. Wiemer (2001), Anomalously high *b*-values in the South Flank of Kilauea volcano, Hawaii: Evidence for the distribution of magma below Kilauea's East rift zone, *J. Volcanol. Geotherm. Res.*, *106*, 23-37.

Youngs, R. R., F. H. Swan, M. S. Power, D. P. Schwartz, and R. K. Green (1987), Probabilistic analysis of earthquake ground shaking hazard along the Wasatch Front, Utah, in *Assessment of regional earthquake hazards and risk along the Wasatch Front, Utah*, edited by P. L. Gori, and W. W. Hays, pp. M1-M110, USGS, Reston, VA.

CHAPTER 3

LARGE EARTHQUAKE SWARMS ACCOMPANYING THE TRANSITION FROM CALDERA UPLIFT TO SUBSIDENCE

A portion of this chapter is published in Geophysical Research Letters as:

Farrell, J., R. B. Smith, T. Taira, W. L. Chang, and C. M. Puskas (2010), Dynamics and rapid migration of the energetic 2008-2009 Yellowstone Lake earthquake swarm, *Geophys. Res. Lett.*, *37*, L19305, doi:10.1029/2010GL044605

Abstract

Beginning in 2004, the Yellowstone caldera commenced a time of accelerated uplift with rates up to 7 cm/yr. During this time, seismicity rates and earthquake swarm rates dramatically decreased. However, in December of 2008, Yellowstone National Park experienced an unusual earthquake swarm that included rapid northward migration of activity at 1 km per day and shallowing of the maximum focal depths from 12 to 2 km beneath northern Yellowstone Lake. The swarm consisted of 811 earthquakes, $0.5<M_W<4.1$, aligned on a N-S 12-km-long vertical plane of hypocenters. The largest earthquake of the swarm had a 50% tensile crack-opening source determined by a full waveform inversion that we interpret as a magmatic expansion component. In addition, GPS data revealed E-W crustal extension coincident with the swarm. Modeling of GPS

and seismic data is consistent with E-W opening of ~10 cm on a N-S striking vertical dike. Our interpretation is that the swarm was induced by magmatic fluid migration or propagation of a poroelastic stress pulse along a pre-existing fracture zone and may have been a "failed" magmatic event or large earthquake sequence. Then in January of 2010, a large swarm of earthquakes began near the northwest caldera boundary beneath the Madison Plateau. This swarm consisted of 2,325 events with magnitudes ranging from $-0.6<M_c<3.9$ and lasted for more than 2 months. Contrary to the 2008-2009 Yellowstone Lake swarm, the Madison Plateau swarm is dominated by strike-slip faulting events and shows little evidence for nondoublecouple source mechanisms. Both swarms occurred during a transition period from caldera uplift, to subsidence similar to the 1985 swarm. It is suggested that these swarms may act as "pressure valves" relieving fluid pressure in the crustal magma reservoir by allowing magma or magmatically-derived fluids to flow outward from the magmatic system beneath the Yellowstone caldera thus coinciding with the change from caldera uplift to subsidence.

Introduction

The Late Quaternary Yellowstone silicic volcanic system is characterized by three caldera-forming eruptions in the last 2.1 million years, the youngest occurring 640,000 years ago producing the Yellowstone caldera [*Christiansen*, 2001]. Moreover, the extraordinarily high conductive plus convective heat flow values averaging 2,000 mWm^{-2} over the caldera and exceeding 30,000 mWm^{-2} in northern Yellowstone Lake, more than 10,000 hydrothermal features, intense seismicity, and decadal-scale crustal uplift and subsidence reflects the active tectonic-magmatic nature of Yellowstone [*Smith et al.*,

2009]. Important to our study is a tomographically imaged crustal magma reservoir [this study; *Husen et al.*, 2004] that extends from ~8 km to ~16 km beneath the Yellowstone caldera.

GPS studies of the Yellowstone caldera have recorded multiple uplift and subsidence episodes at decadal scales [*Puskas et al.*, 2007]. Most recently, GPS and InSAR measurements have revealed accelerated caldera uplift at rates up to ~7 cm/yr beginning in mid-2004 and continuing into 2010 at a lower peak rate of ~2.0 cm/yr. eventually reversing to subsidence in early 2010. The source of this remarkable uplift episode was modeled as an inflating sill at ~10 km depth beneath the caldera and coincident with the top of the imaged magma reservoir [*Chang et al.*, 2007; *Chang et al.*, 2010].

We present an analysis of earthquake and GPS data associated with two large earthquake swarms that occurred in Yellowstone: the 2008-2009 Yellowstone Lake earthquake swarm and the 2010 Madison Plateau swarm and evaluate the possibility of a magmatic source. The results are key to understanding the interaction of earthquakes and volcanic sources of Yellowstone as well as plausible volcano models for assessing its geologic hazards.

Earthquake Setting

The seismic data used in this study are from the Yellowstone seismograph network, operated by the University of Utah, which includes 26 seismographs, and from 5 Plate Boundary Observatory (PBO) borehole short-period seismometers. More than 38,000 earthquakes were located in the Yellowstone area from 1973 to 2013. Since

1995, the Yellowstone area has averaged ~1,600 earthquakes per year with magnitudes from -1.4 $\leq M_C \leq$4.5 (Figure 3.1). The majority of earthquakes in the Yellowstone caldera are less than 5 km deep. The shallow nature of the maximum focal depths is attributed to the shallow depth of the brittle-ductile transition at ~400°C associated with the caldera magma reservoir [*Smith et al.*, 2009]. Maximum depths of hypocenters deepen to >15 km south and north of the caldera.

Earthquake swarms are the common mode of earthquake occurrence in Yellowstone with more than 80 distinctly identified swarms from 1995 to 2013 containing 12,504 earthquakes and representing 42% of all earthquakes [*Farrell et al.*, 2009]. The majority of the swarms were located in the zone of high seismicity northwest of the caldera, but 24 independent swarms were located within or on the rim of the Yellowstone caldera.

The 2008-2009 Yellowstone Lake Swarm

Seismic and GPS Observations

The focus of this section is the 2008-2009 Yellowstone Lake earthquake swarm that began on December 27, 2008 and lasted until January 07, 2009. Swarm hypocenters were located in the central Yellowstone Lake area where the earthquake sequence began and rapidly migrated north at a rate of ~1 km /day (Figure 3.2). Maximum focal depths shallowed markedly from ~10 km to ~2 km from south to north. Notably, the swarm initiated at ~10 km, near the top of the magma reservoir (Figure 3.2), which suggests that magmatic fluids may have been involved.

The Yellowstone Lake swarm consisted of 811 well-located earthquakes,

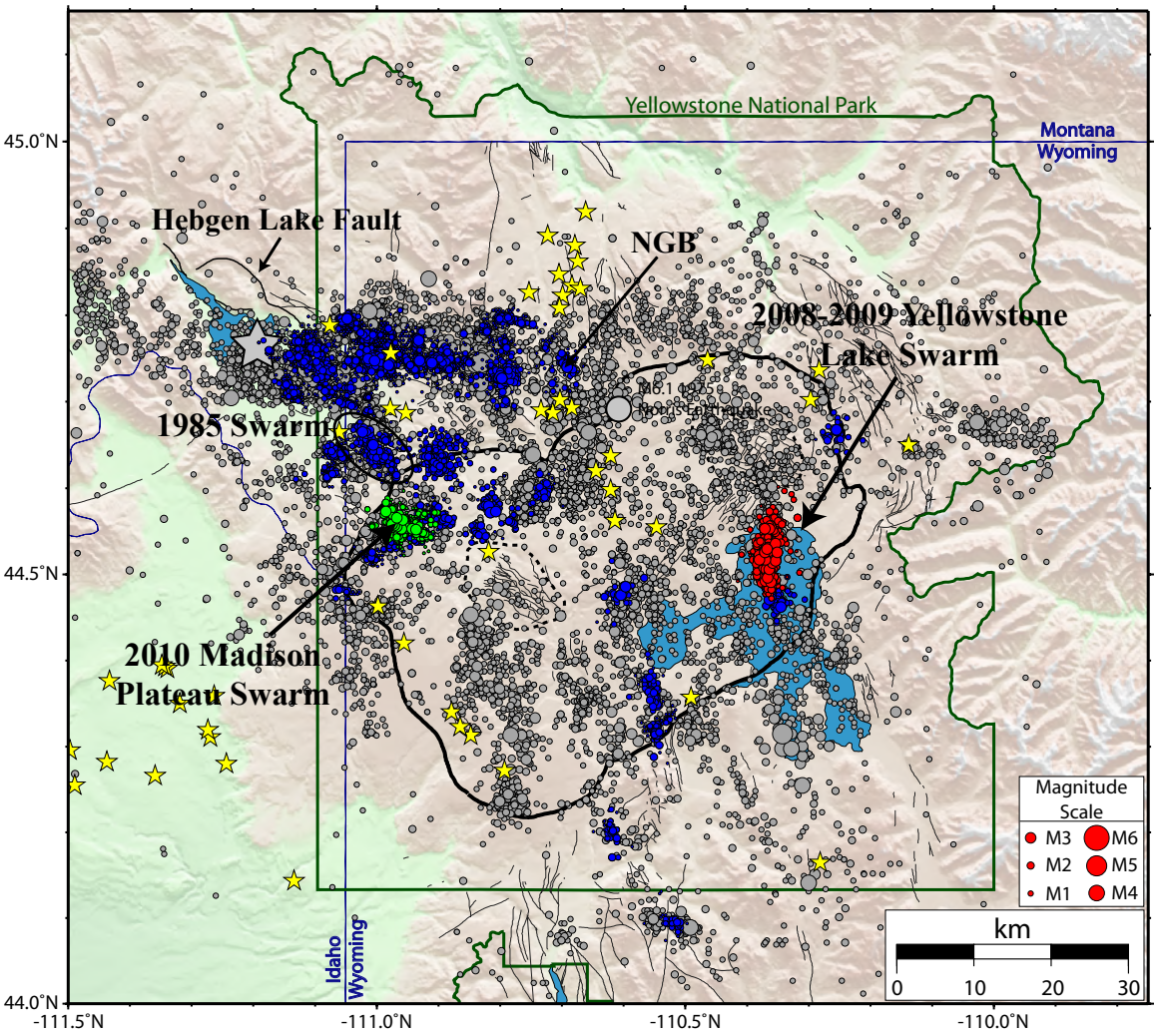

Figure 3.1. Earthquakes in Yellowstone from 1973 - 2013. Epicenters are shown as gray dots, swarm epicenters are shown as blue dots, postcaldera vents are shown as yellow stars, and Quaternary faults are shown as black lines. The outline of the caldera from the last major Yellowstone eruption is shown in black. The resurgent domes are shown as dashed lines. The 2008-2009 Yellowstone Lake swarm is shown as red circles and the 2010 Madison Plateau swarm is shown as green circles. The 1959 Mw7.3 Hebgen Lake earthquake is shown as a gray star.

Figure 3.2. Earthquake hypocenters of the 2008-2009 Yellowstone Lake earthquake swarm. (a) Circles represent swarm earthquakes with Mc< 3.0 and stars represent events with Mc≥3.0. The large star is the largest event, Mw4.1, of the swarm. Earthquakes are temporally color-coded showing the northern migration of seismicity. Small black lines are faults and the orange line is the outline of the 0.64-Ma Yellowstone caldera from *Christiansen* [2001]. Black triangles are seismic stations, blue squares are GPS stations, and inverted green triangles are borehole strainmeters and seismometers. The opaque red body is the outline of the tomographically imaged Yellowstone magma reservoir [*Husen et al.*, 2004]. (b) Cross-section showing the shallowing and northward migration of swarm hypocenters and their position relative to the top of the Yellowstone magma reservoir. (c) East-west component of GPS derived ground motion of the Yellowstone Lake area stations: WLWY (green), LKWY (red), and HVWY (blue) show the related deformation. The yellow band shows the time extent of the swarm seismicity.

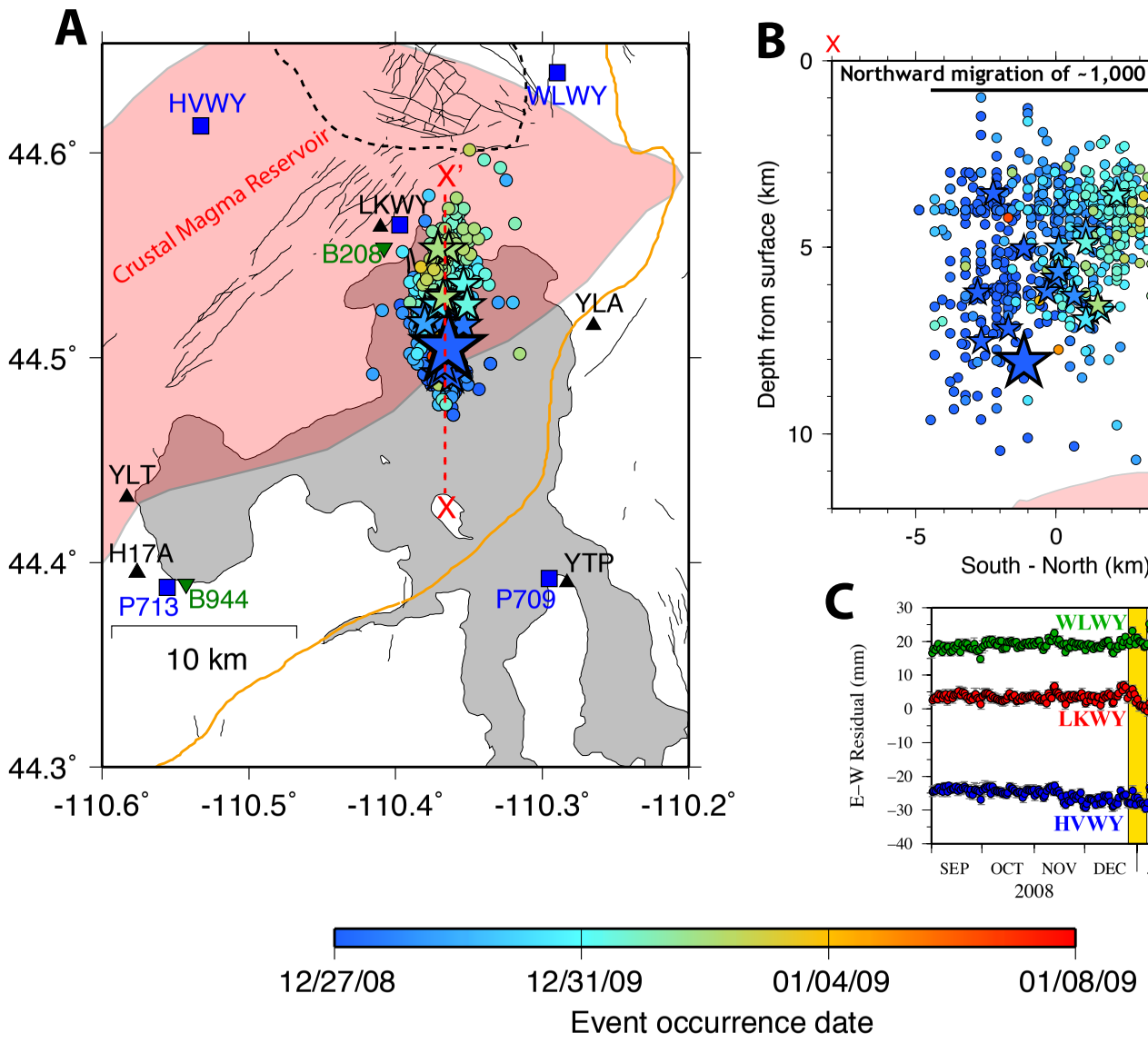
A
HVWY
WLWY
Crustal Magma Reservoir
X'
LKWY
B208
YLA
YLT
X
H17A
YTP
P713
B944
P709
10 km
44.6°
44.5°
44.4°
44.3°
-110.6°
-110.5°
-110.4°
-110.3°
-110.2°
B
X
X'
Northward migration of ~1,000 m/day
Depth from surface (km)
0
5
10
-5
0
5
South - North (km)
C
E–W Residual (mm)
WLWY
LKWY
HVWY
30
20
10
0
−10
−20
−30
−40
SEP
OCT
NOV
DEC
JAN
FEB
2008
2009
12/27/08
12/31/09
01/04/09
01/08/09
Event occurrence date

determined in a three-dimensional V_P velocity model [*Husen et al.*, 2004] with RMS residual values of 0.01 to 0.3 s and with the largest magnitude, a M_W4.1, occurring at the initiation of the swarm. The swarm contained 21 events of $M_C \geq 3.0$ with over 20 events felt in Yellowstone National Park. In contrast, for the previous year there were only two earthquakes of $M_C \geq 3.0$ in Yellowstone. The cumulative seismic moment release for all of the 2008-2009 Yellowstone Lake swarm earthquakes was 6×10^{22} dyne-cm, which is equivalent to a single M_W4.4 event, and accounted for 35% of the total moment release in the Yellowstone area for the previous year.

Nearby GPS stations (Figure 3.2a) recorded a notable episode of E-W crustal extension coincident with the swarm. The closest GPS station (LKWY), only ~1 km west of the swarm, experienced ~7 mm of westward motion associated with the swarm (Figure 3.2). Station HVWY, located ~7 km northwest of the swarm epicenters, had ~3 mm of westward motion.

Seismic Source Determinations

A seismic moment tensor solution for the largest event, a M_W4.1, revealed an unexpected result of a 50% tensile crack source and 50% shear double-couple source corresponding to an opening dislocation of 9.6 cm and a shear dislocation of 9.6 cm (Figure 3.3). The tensile crack was oriented with a strike of 185°, a dip of 90°, and a rake of 100°, which agrees with the dominantly N-S fault planes and E-W extension from the focal mechanism solutions (Figure 3.3). Details of the moment tensor solution are given in the supplemental section as well as in Tables 3.1 and 3.2.

The stress field was determined from focal mechanisms of 43 of the swarm

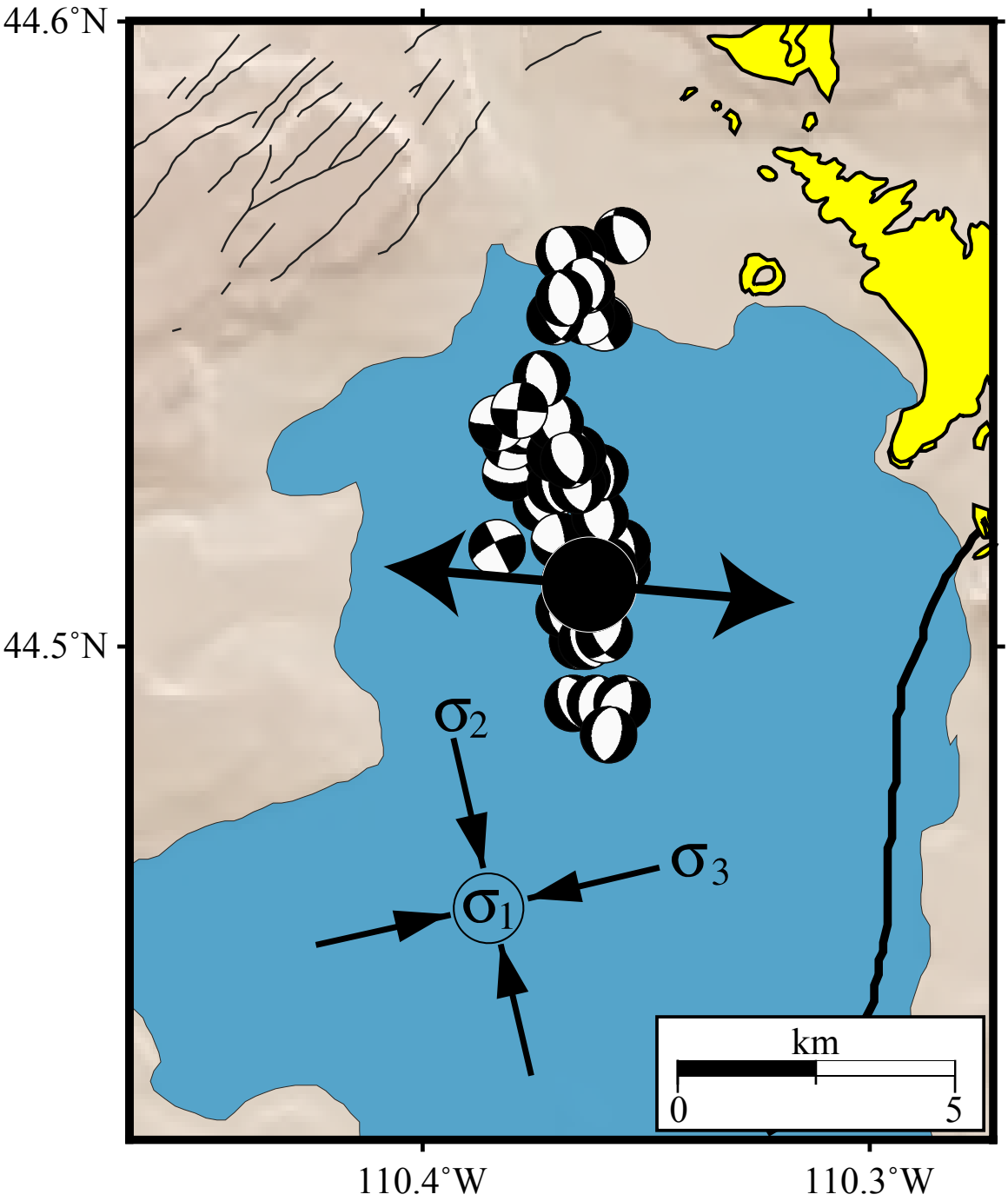

Figure 3.3. P-wave 1st-motion focal mechanisms determined for well-recorded Yellowstone Lake swarm earthquakes. The black circle is the moment tensor solution for the Mw4.1 event. The large arrows show the direction of tension based on the moment tensor solution. Stress inversions show that the maximum principal stress (σ1) is vertical, σ2 is oriented in a NNW-SSE direction, and the minimum principal stress (σ3) is oriented in an ENE-WSW direction.

Table 3.1. Results of *F* Test statistics for five different source models and moment tensor solutions for best fitting source models[a]

Location	F_{CLVD}	F_I	F_{TC}	F_F	F_{90}	M_O (10^{14} N m)	M_W	VR (%)	Best Fitting Source Model
44.5059°N, 110.3639° W	1.00	1.18	1.29	1.24	1.31	17.6	4.1	44	Shear faulting + tensile crack

[a]F_{CLVD}, F_I, F_{TC}, and F_F are *F* test statistics comparing the shear-faulting source model to shear-faulting + CLVD, shear-faulting + isotropic, shear-faulting + tensile crack, and shear-faulting + CLVD + isotropic source models, respectively. F_{90} is the threshold value of *F* test statistic for the 90% confidence level. Modified from *Taira et al.* [2010].

Table 3.2. Percentage of volumetric component, change in source volume, fault area, and opening dislocation[a]

Location	Volumetric Component (%)	Volume Change (m^3)	Fault Area (km^2)	Opening Dislocation (cm)
44.5059°N, 110.3639°W	50	62 x 10^3	0.73	8.5

[a]Modified from *Taira et al*. [2010].

earthquakes that had at least six clear first-motion arrivals. The majority of the focal mechanisms revealed dominantly normal, dip-slip fault motions with N-S fault planes interpreted to be associated with an E-W tensional stress regime (Figure 3.3) revealing a vertical principal-stress axis, σ_1, and an ENE-WSW minimum compressional stress σ_3 (Figure 3.3). This stress regime is similar to the caldera-wide tensional stress-field deduced by *Waite and Smith* [2004] and *Smith et al.* [2009] from focal mechanisms of background seismicity, GPS, and L. Quaternary fault-orientations of the entire Yellowstone region.

A moment tensor solution was computed for the largest earthquake, a M_W4.1 (M_L3.9) event of the Yellowstone Lake swarm that occurred on December 28, 2008, using the technique of *Taira et al.* [2010] and is summarized in Tables 3.1 and 3.2. The

moment tensor source is characterized by a 50% shear double-couple source plus a 50% tensile crack source (large source mechanism in Figure 3.3) with a variance reduction (VR) of 44%. The tensile crack is oriented with an azimuth of 185°, a dip of 90°, and a rake of 100°. The volumetric source change is 50% with a total volume change of 62.0 x 10^3 m^3, a fault area of 0.73 km^2, an opening dislocation of 8.5 cm, and a shear dislocation of 8.5 cm. This agrees with dominantly north-south fault planes and east-west extension from focal mechanism solutions of swarm earthquakes (Figure 3.3). The *F*-test value for this model is 1.29 which is just below the 90% confidence level of F_{90}=1.31. Note that this is the only earthquake of the swarm that was large enough to determine a moment tensor solution.

Dike-Fracture Source Modeling

We employed an elastic half-space vertical dislocation model with a shear modulus (μ) of 3x10^{10} Pa and a Poisson's ratio (υ) of 0.35 [*Simpson and Reasenberg*, 1994] to model the stress field, hypocenter geometry, and GPS-derived deformation. We defined the lateral and depth extent of the fracture model from the geometry of the swarm hypocenters, with two vertical dislocations, both 12 km long and 3 km wide (Figure 3.4). The two dislocations were adjacent to each other, with the top of the upper dislocation at 2 km depth and the top of the lower dislocation at 5 km depth (Figure 3.4).

To match the observed 7 mm westward deformation at the GPS station LKWY, the model required an E-W extensional opening of 9.7±0.7 cm for the top dislocation together with an opening of 1.5±0.4 cm with a dip-slip shear motion of 4.4±0.7 cm on the bottom dislocation (Figure 3.4). This model also provided a westward surface

Figure 3.4. Schematic model for a hypothetical fluid dike intrusion for the 2008–2009 Yellowstone Lake earthquake swarm. (a) The north-south oriented dike (orange) with modeled east-west crustal extension. Hydrothermal areas are shown in yellow. (b) Forward model of the surface deformation from a N–S oriented dike. The color background is the modeled vertical displacement in mm and the black vectors show the modeled horizontal displacement. The red vectors show the observed horizontal displacements at stations LKWY and HVWY in mm/yr. GPS stations are shown as red squares.

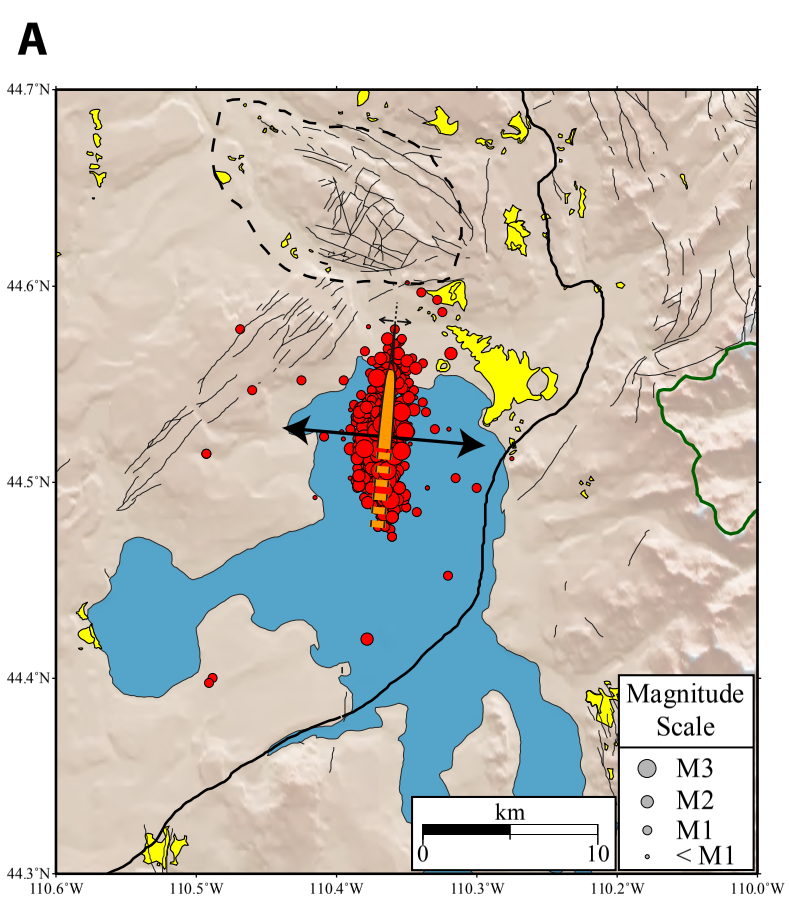
A
44.7°N
44.6°N
44.5°N
44.4°N
44.3°N
110.6°W
110.5°W
110.4°W
110.3°W
110.2°W
110.0°W
Magnitude Scale
M3
M2
M1
< M1
km
0
10

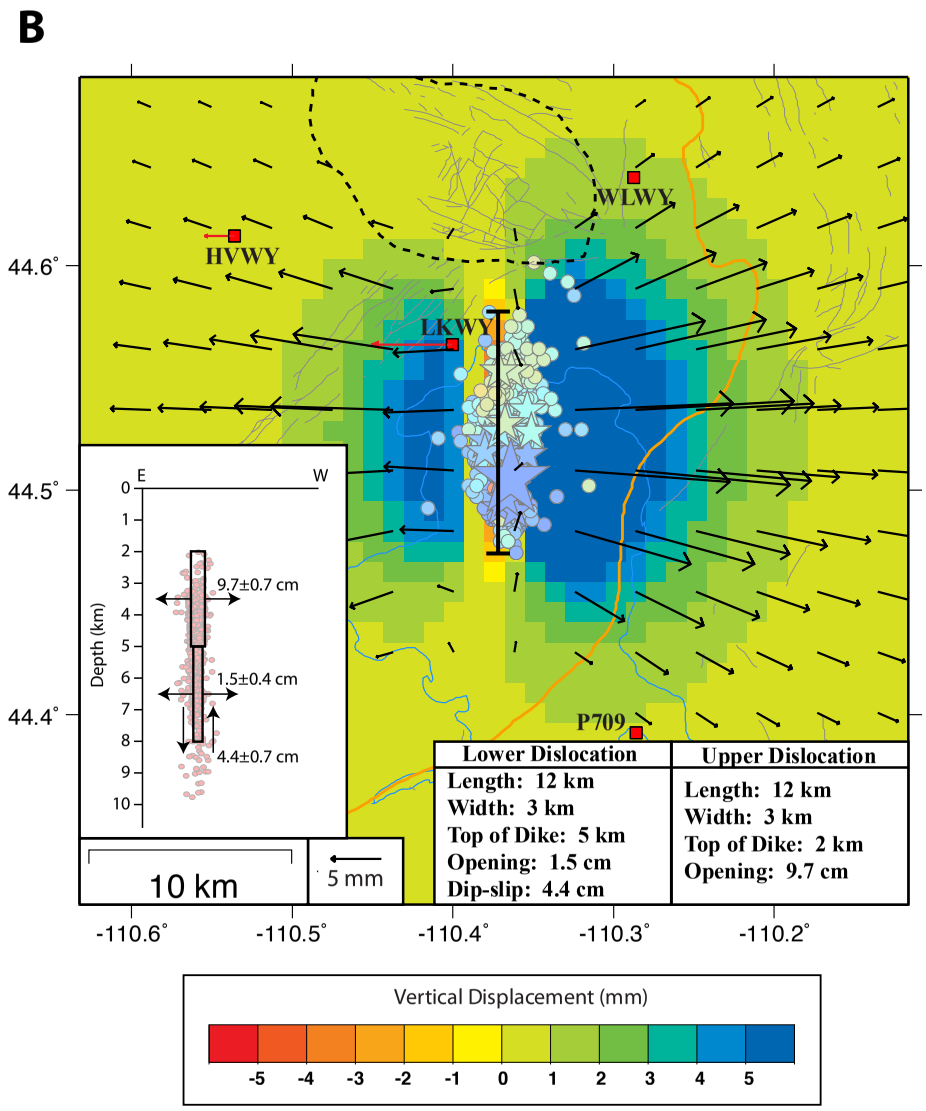
B
44.6°
44.5°
44.4°
-110.6°
-110.5°
-110.4°
-110.3°
-110.2°
WLWY
HVWY
LKWY
P709
E
W
Depth (km)
9.7±0.7 cm
1.5±0.4 cm
4.4±0.7 cm
10 km
5 mm
Lower Dislocation
Length: 12 km
Width: 3 km
Top of Dike: 5 km
Opening: 1.5 cm
Dip-slip: 4.4 cm
Upper Dislocation
Length: 12 km
Width: 3 km
Top of Dike: 2 km
Opening: 9.7 cm
Vertical Displacement (mm)
-5 -4 -3 -2 -1 0 1 2 3 4 5

deformation of ~3 mm at station HVWY, consistent with that measured by GPS, as well as eastward surface deformation at station WLWY of ~2 mm. Although there was no noticeable deformation at WLWY, at 11 km to the northeast, given the uncertainties in the GPS-determined daily position, it would be difficult to resolve the 2 mm displacement inferred by the modeling.

We then evaluated fluid properties of a modeled dike by determining the viscosity of a migrating fluid using the time-duration of the swarm. Using a numerical dike intrusion model [*Carslaw and Jaeger*, 1959; *Rubin*, 1995] we determined the width of a magmatic dike intruded into a host rock during the 10 days of swarm migration:

$$w = 2\lambda\sqrt{\kappa t} \tag{3.1}$$

where w is the half-width of the frozen margin, t is time (10 days), and κ is the thermal diffusivity of the host rock (1.5×10^{-6} m^2/s). The dimensionless parameter λ depends on the magma and host rock temperatures, the latent heat of crystallization (L=500 kJ kg^{-1}), and the heat capacity (1 kJ kg^{-1} $°C^{-1}$) [*Carslaw and Jaeger*, 1959]. For rhyolites, we used a temperature range of 750°C to 950°C, and for basalts we used a temperature range of 1,000°C to 1,300°C. This gave λ values of 0.2 to 0.4 for rhyolites and 0.4 to 0.6 for basalts. The dike needs to be at least 1 to 2 m wide to avoid freezing for rhyolite and at least 2 to 3 m wide for basalt. It should be noted that equation 3.1 assumes that advection of heat by magma is unimportant which could be a valid assumption given a 1 km/day migration rate. Using the equations [*Carslaw and Jaeger*, 1959; *Rubin*, 1995]:

$$\Delta P = \frac{w\mu}{l(1-\upsilon)}, \tag{3.2}$$

where ΔP is equal to the magma pressure minus the compressive stress, l is the half length of the dike and:

$$\eta = \frac{w^2}{3\dot{u}_x}\frac{d\Delta P}{dx}, \tag{3.3}$$

where $\dot{u}_x$ is the horizontal velocity of 1,000 m/d determined from the earthquake pattern migration rate, we calculated fluid pressures of 4-7 MPa necessary to produce the dike width for a rhyolite and 1-7 MPa for a basalt. We determined a fluid viscosity on the order of 10^3 to 10^4 Pa s for rhyolite that agrees with lower published values of rhyolite melt viscosity of 10^4 to 10^8 Pa s [*Rubin*, 1995]. In contrast, if we assume basaltic material, we calculate a viscosity on the order of 10^4 Pa s, which is two to four orders of magnitude larger than published basaltic melt viscosities ranging from 10 to 10^2 Pa s [*Rubin*, 1995].

Similar observations of migrating earthquake swarm activity and associated surface deformation have been noted at other active volcanic areas and have been attributed to dike intrusions. These include Lake Tahoe, California [*Smith et al.*, 2004], Iliamna volcano, Alaska [*Roman et al.*, 2004], the Izu Islands, Japan [*Ukawa and Tsukahara*, 1996; *Toda et al.*, 2002], Kilauea Volcano, Hawaii [*Rubin et al.*, 1998], and the Long Valley Caldera, California [*Hill et al.*, 1990].

The 2010 Madison Plateau Swarm

Seismic Observations

The focus of this section is the 2010 Madison Plateau, western Yellowstone, earthquake swarm that began on January 15, 2010 and continued until February 13, 2010 with sporadic activity occurring in the area of the swarm till the present time (Figure 3.5). Swarm hypocenters were located near the northwest boundary of the 0.64 Ma Yellowstone caldera beneath the Madison Plateau (Figure 3.1). No notable migration was observed for the swarm although later analysis by *Massin et al.* [in prep] and *Shelly et al.* [in prep] show that using cross-correlation techniques and double-difference hypocenter locations, the swarm events seem to radiate outward from a central location by several hundred meters.

The Madison Plateau swarm consisted of 2,325 well-located earthquakes, determined in a three-dimensional V_P velocity model [*Husen et al.*, 2004] with RMS residual values of 0.06 to 0.3 s and with the largest magnitude, a M_L3.9. The swarm contained 17 events of $M_C \geq 3.0$ with many of the larger events felt in Yellowstone National Park and in nearby West Yellowstone, Montana. The cumulative seismic moment release for all of the 2010 Madison Plateau swarm earthquakes was 6×10^{22} dyne-cm, which is equivalent to a single M_W4.4 event, and accounted for 86% of the total moment release in the Yellowstone area for the year 2010. Swarm earthquakes were clustered along a distinct plane striking NW-SE and dipping to the northeast (Figures 3.1 and 3.6) with depths ranging from 5-15 km (Figure 3.6).

There was no measured ground deformation coincident with the swarm although the closest GPS station is ~11 km northeast of the swarm.

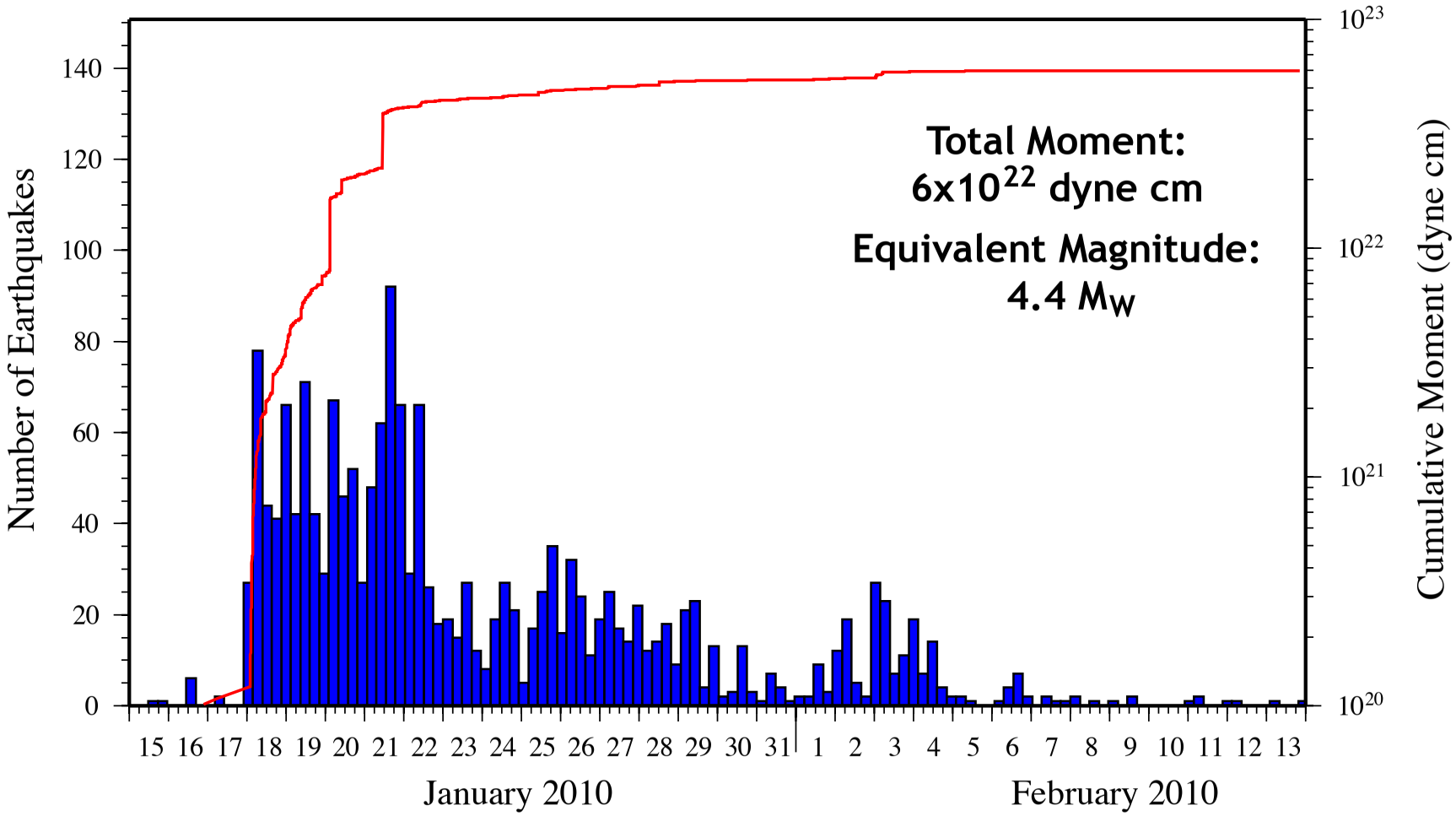

Figure 3.5. Histogram showing the seismicity with time of the 2010 Madison Plateau swarm shown as daily blue bars. The cumulative moment release is shown as a red line.

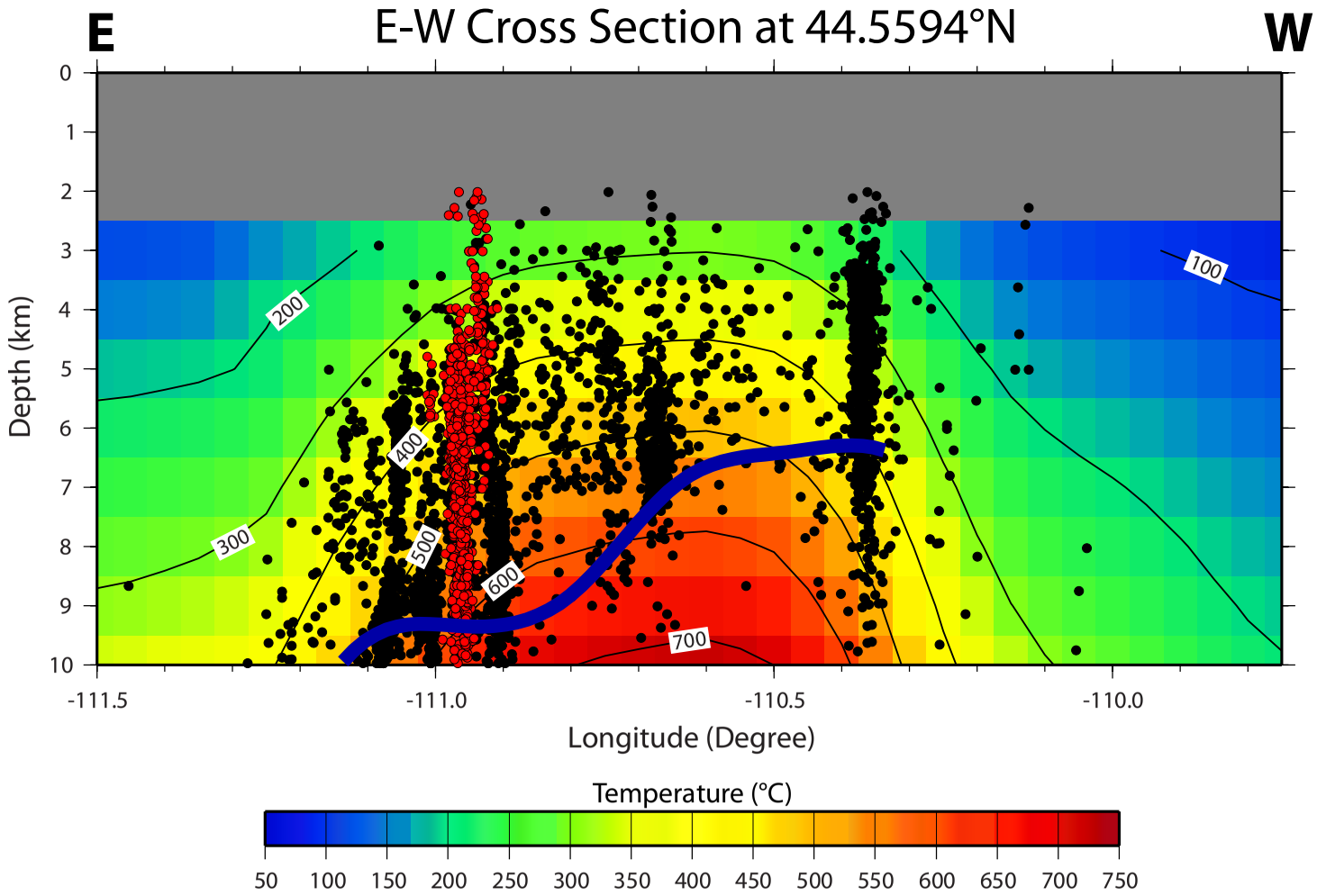

Figure 3.6. Modeled crustal temperature and the brittle-ductile transition relative to the swarm hypocenters of the 2010 Madison Plateau swarm. Background colors and contour lines are temperatures in degrees (ºC). The thick blue line is the approximate location of the brittle-ductile transition determined from the 85 percentile maximum focal depths [*Smith et al.*, 2009]. Black dots represent the earthquakes used to calculate the focal depth maxima and the red dots are the swarm hypocenters

Seismic Source Determinations

The majority of the focal mechanisms for the swarm revealed dominantly strike-slip fault motions with N-S or E-W fault planes (Figure 3.7). The stress field was determined from focal mechanisms of 94 of the swarm earthquakes that had at least six clear first-motion arrivals revealing a NW-SE principal-stress axis, σ_1, and an NE-SW minimum compressional stress σ_3 (Figure 3.7). This stress regime is very similar to the stress-field deduced by *Waite and Smith* [2002] for the 1985 swarm that occurred about 8-10 km to the north, which was also dominated by strike-slip source mechanisms.

Moment tensor solutions were computed for two of the largest events of the swarm; a M_W3.9 (M_L3.6) event that occurred on Jan. 19 and a M_W4.2 (M_L3.9) event that occurred on Jan. 21 [*Herrmann et al.*, 2011]. Both moment tensors show strike-slip solutions consistent with the first motion focal mechanisms computed for this study (Figure 3.7).

Discussion

The intense 2008-2009 Yellowstone Lake earthquake swarm was characterized by a swarm-front that migrated north at a very high rate of ~1 km/day with maximum hypocenter depths shallowing toward the north at the margin of the mapped Yellowstone caldera (Figure 3.2). In addition, GPS data revealed a westward surface extension pulse coincident with the swarm (Figure 3.2). These observations are consistent with an interpretation of magmatic fluid transport (hydrothermal, gaseous, magma, etc.) through an expanding vertical fracture that was modeled as a vertical dislocation 12 km long at a depth range of 2-8 km and is a plausible source for the observed seismic and geodetic

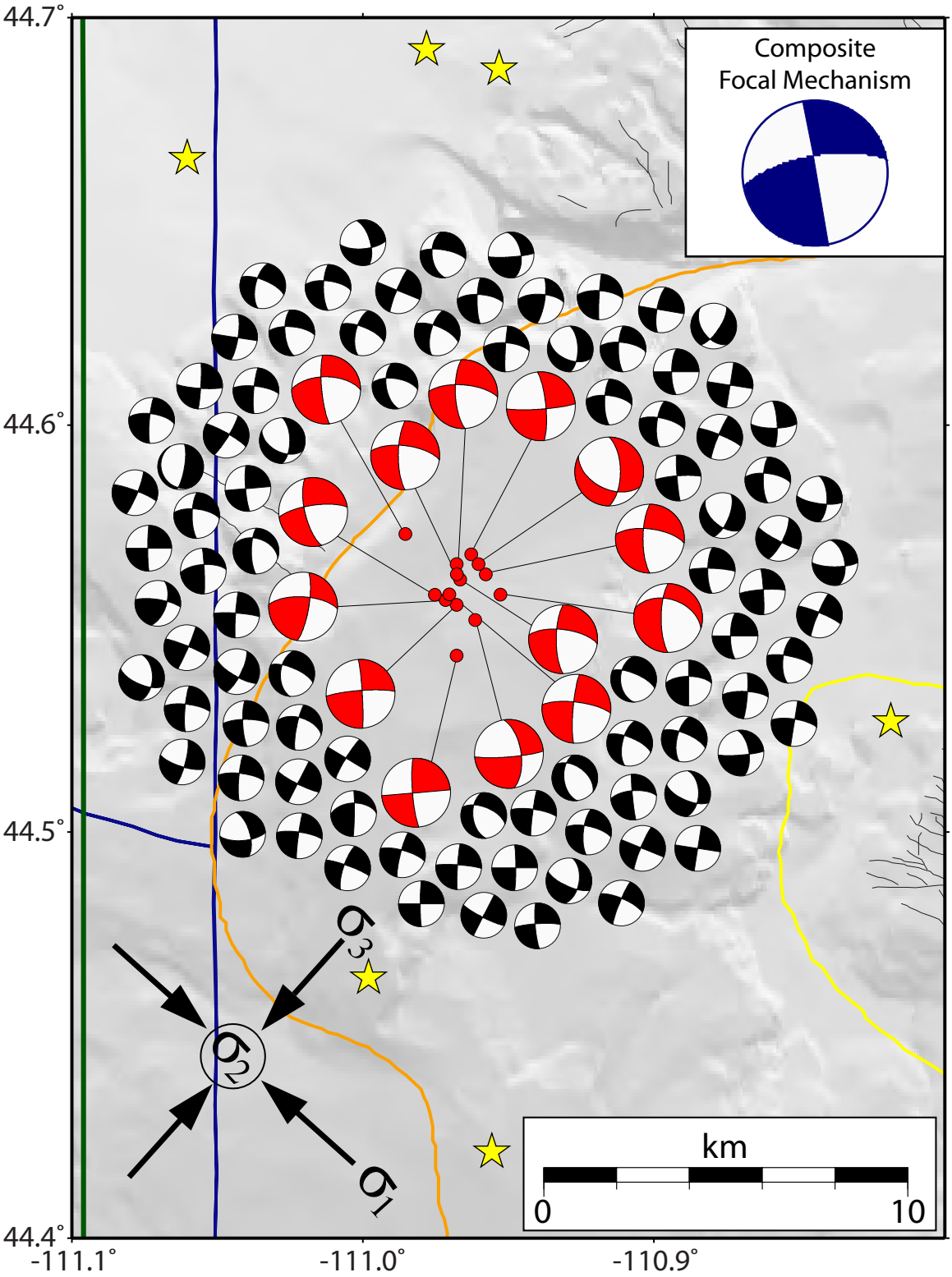

Figure 3.7. P-wave first motion focal mechanisms calculated for the 2010 Madison Plateau swarm. Black focal mechanisms are for events with M<3 and red focal mechanisms are for events with M≥3. The large blue focal mechanism is a composite solution using all events. The stress field of the swarm is shown in the lower left.

observations (Figure 3.4).

The Yellowstone Lake swarm occurred in an area of extraorinarily high heat flow in northern Yellowstone Lake (Figure 3.8) with values exceeding 2,000 mWm^{-2} [*Blackwell et al.*, 2006; *Smith et al.*, 2009]. It has been hypothesized that the extraordinarily high heat flux is due to fluid migration on a pre-existing fracture zone of high porosity allowing the rapid percolation of fluids [*Smith and Blackwell*, 2000]. The dike could be a pre-existing, long-term feature that was reactivated with an influx of new material during the swarm with 10 cm of additional opening. The N-S lobe of high heat flow (Figure 3.8) and the N-S pattern of background seismicity (Figure 3.1) could be evidence of the pre-existing fracture which allowed magmatic fluids to flow upward from the top of Yellowstone crustal magma reservoir inducing the seismicity and ground deformation that was observed during the swarm (Figure 3.8).

Waite and Smith [2002] attributed a similar source to the largest Yellowstone earthquake swarm in 1985, during which activity migrated away from the caldera rim to the northwest, although their observed rate of migration was an order of magnitude lower, ~150 m/day, than that of the 2008-2009 swarm. Their preferred scenario for the 1985 swarm involves the rupture of a self-sealed hydrothermal layer and subsequent migration of hydrothermal fluids through a pre-existing fracture zone out of the caldera [*Waite and Smith*, 2002]. Importantly, the 1985 swarm was followed by a caldera-wide reversal in the deformation from uplift to subsidence suggestive of lateral magmatic fluid transport out of the shallow hydrothermal system. While there was no observed deformation reversal following the 2008-2009 Yellowstone Lake swarm, the accelerated uplift rate determined from GPS for the period 2004-present [*Chang et al.*, 2010] has

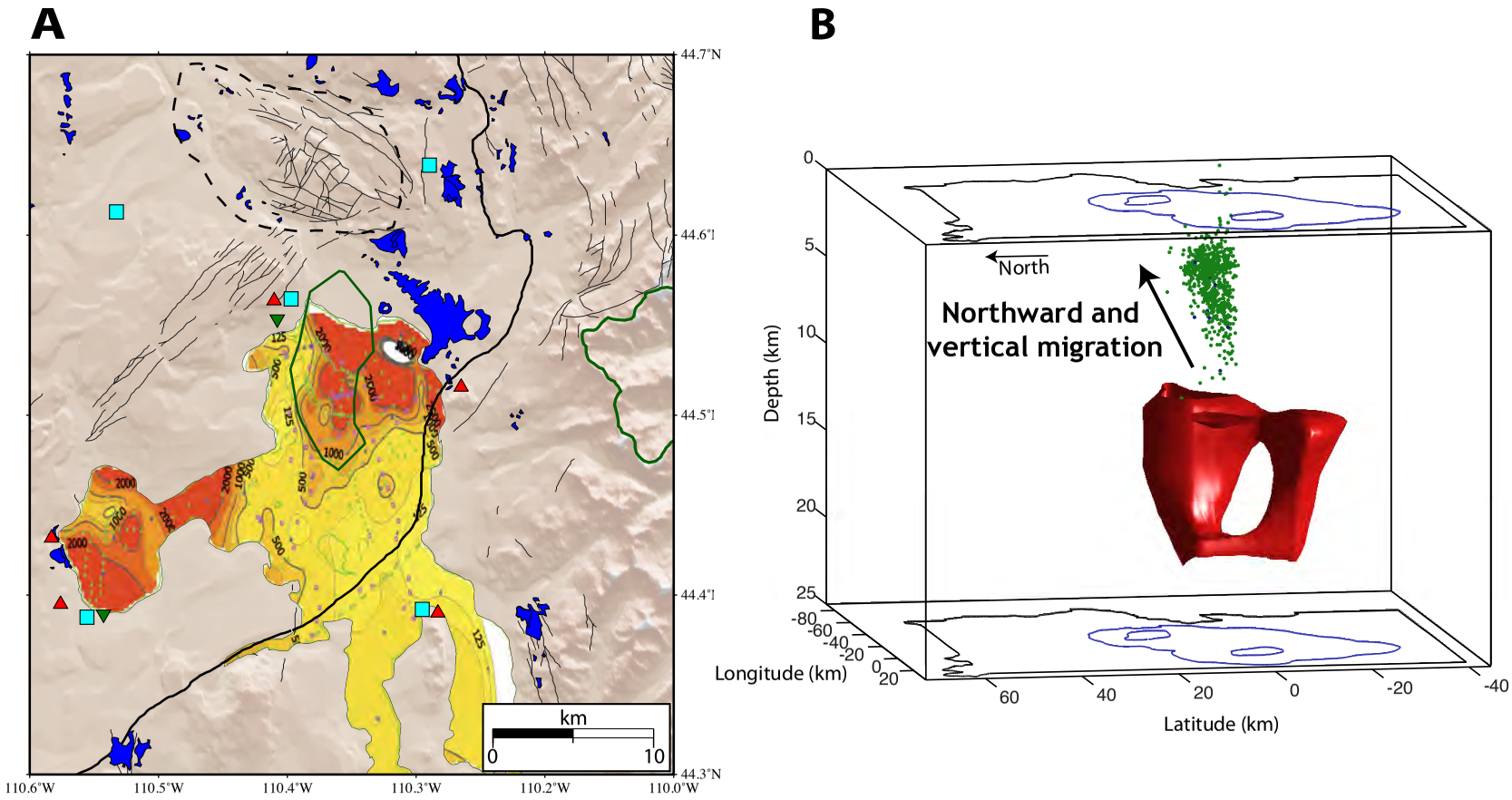

Figure 3.8. Outline of the 2008–2009 Yellowstone Lake earthquake swarm with heat flow. (a) Heat flow of Yellowstone Lake showing the north-south band of high heat flow (>2,000 mWm−2)[*Blackwell and Smith*, 2000; data from *David Blackwell*, 2005] and the outline of the swarm seismicity (blue polygon). Hydrothermal areas are shown in green. The N–S black line inside the seismicity is the modeled dike location. Seismic stations are shown as red triangles, GPS stations as blue squares. (b) Three-dimensional tomographic image showing the relation of the swarm hypocenters (green circles) and the Yellowstone crustal magma reservoir (red body).

decreased from as high as 7 cm/yr of uplift to a rate of ~2.0 cm/yr of uplift in 2009.

Moreover, the notable shallowing of maximum focal depth swarm hypocenters is consistent with the rapid shallowing of the depth of the brittle-ductile transition, as modeled as the ~400°C -500°C isotherm [*Smith et al.*, 2009], from ~10 km to ~6 km in the Yellowstone caldera (Figure 3.9). As the swarm front migrated north, the earthquakes would have encountered higher crustal temperatures that restricted earthquake nucleation.

We note another plausible cause of the migratory nature of the Yellowstone Lake earthquake swarm is a poroelastic stress pulse migrating through a series of pressurized fluid-filled fractures. Such a mechanism could have originated from expansion of the magma reservoir and nucleated earthquakes as it propagated through the pre-existing fault system. This could explain the discrepancy between the geodetically modeled opening (10 cm) and the numerically calculated dike width (1-2 m).

We prefer an interpretation of the 2008-2009 Yellowstone Lake swarm as caused by an upper-crustal dike-intrusion of magma or magmatically-derived aqueous fluids from the shallow Yellowstone magma reservoir, although we cannot specify the type of fluid (magma vs. hydrothermal). The fluid would have followed the pre-existing fracture zone that extends northward toward the largest part of the magma reservoir (Figure 3.8b). We also note that this unusual earthquake swarm may represent the first observations of a failed volcanic eruption in Yellowstone. Moreover, the observed temporal-spatial seismic and deformation pattern reflects the style of volcano-tectonic activity that can be expected in the Yellowstone volcanic field and that could lead to triggering of larger earthquakes or volcanic eruptions.

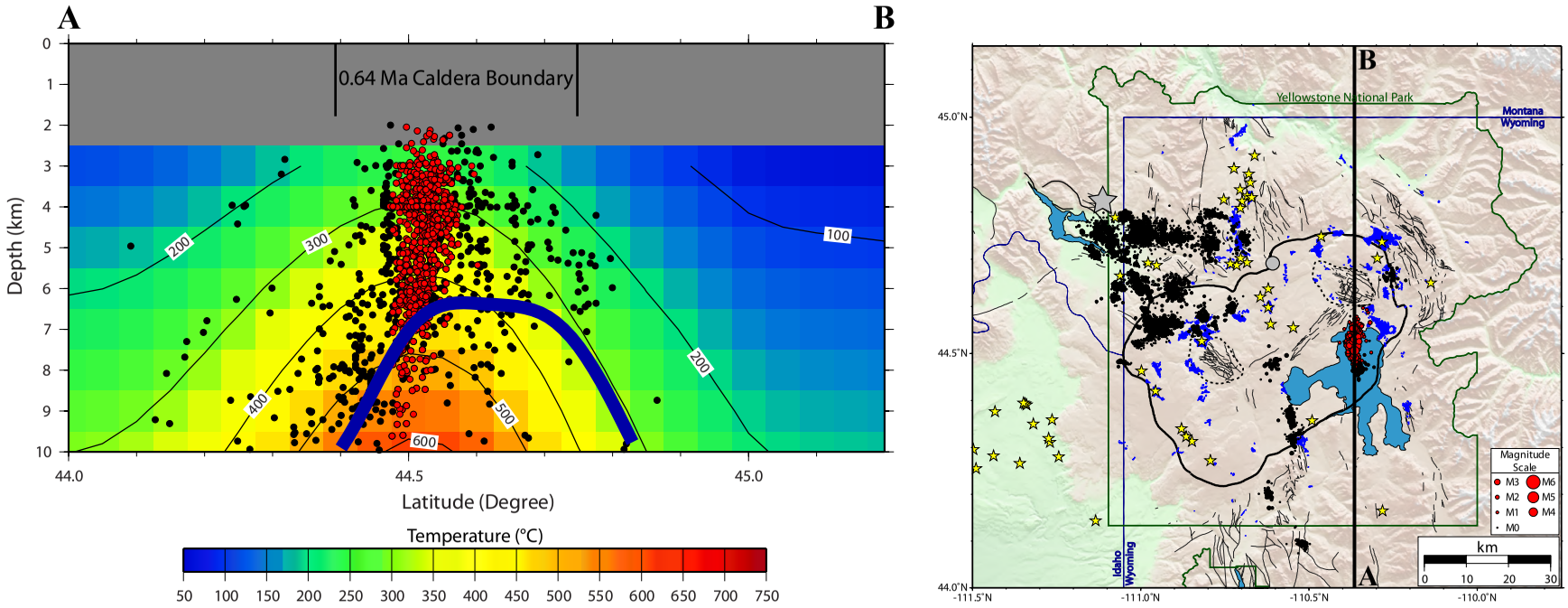

Figure 3.9. Modeled crustal temperature and the brittle-ductile transition relative to the 2008-2009 Yellowstone Lake swarm hypocenters. (a) Background colors and contour lines are temperatures in degrees (ºC). The thick blue line is the approximate location of the brittle-ductile transition determined from the 85 percentile maximum focal depths [*Smith et al.*, 2009]. Black dots represent the earthquakes used to calculate the focal depth maxima and the red dots are the swarm hypocenters, and (b) seismicity map showing the location of the cross-section in (a) with black circles showing all swarm earthquakes from 1984-2010 and red circles representing the earthquakes of the 2008-2009 Yellowstone Lake swarm. Blue areas represent mapped hydrothermal areas and yellow stars represent post 640,000 year old volcanic vents.

The 2010 Madison Plateau swarm was dominated by strike-slip to oblique strike-slip earthquakes that are tectonic in nature. The proximity and orientation of this swarm suggests that it may be occurring on a fault system related to the M_W7.3 1959 Hebgen Lake earthquake 10-20 km northwest. The swarm events are located in an area of increased Coulomb stress induced by the Hebgen Lake earthquake (Figure 3.10). Alternatively, this swarm, along with the 2008-2009 Yellowstone Lake swarm, may be related to the Yellowstone volcanic system and may play a vital roll in the release of magmatic and magmatically derived fluids from the magma reservoir to the surrounding area. We note that following the 2008-2009 Yellowstone Lake swarm, caldera uplift rates decreased from ~3.5 cm/yr to ~1.7 cm/yr. Following the 2010 Madison Plateau swarm, caldera deformation reversed from ~1.7 cm/yr of uplift to ~2.6 cm/yr of subsidence (Figures 1.6 and 3.11). A similar pattern of deformation reversal occurred coincident with the 1985 swarm as well [*Waite and Smith*, 2002].

Earthquake swarms are a common phenomenon in volcanic settings and are widely thought to be largely induced by the movement of fluids in the subsurface. Large swarms in Yellowstone may be playing an important role as "pressure valves" allowing the release of magmatic and magmatically-derived fluids flowing laterally to the surrounding area, allowing the caldera deformation pattern to return from uplift to subsidence.

Acknowledgements

Discussions with Henry Heasler, Frédérick Massin, and David Hill were helpful in preparation of this manuscript. We thank the reviews by Allan Rubin and Greg Waite that materially contributed to this paper. This research was funded in part by the USGS

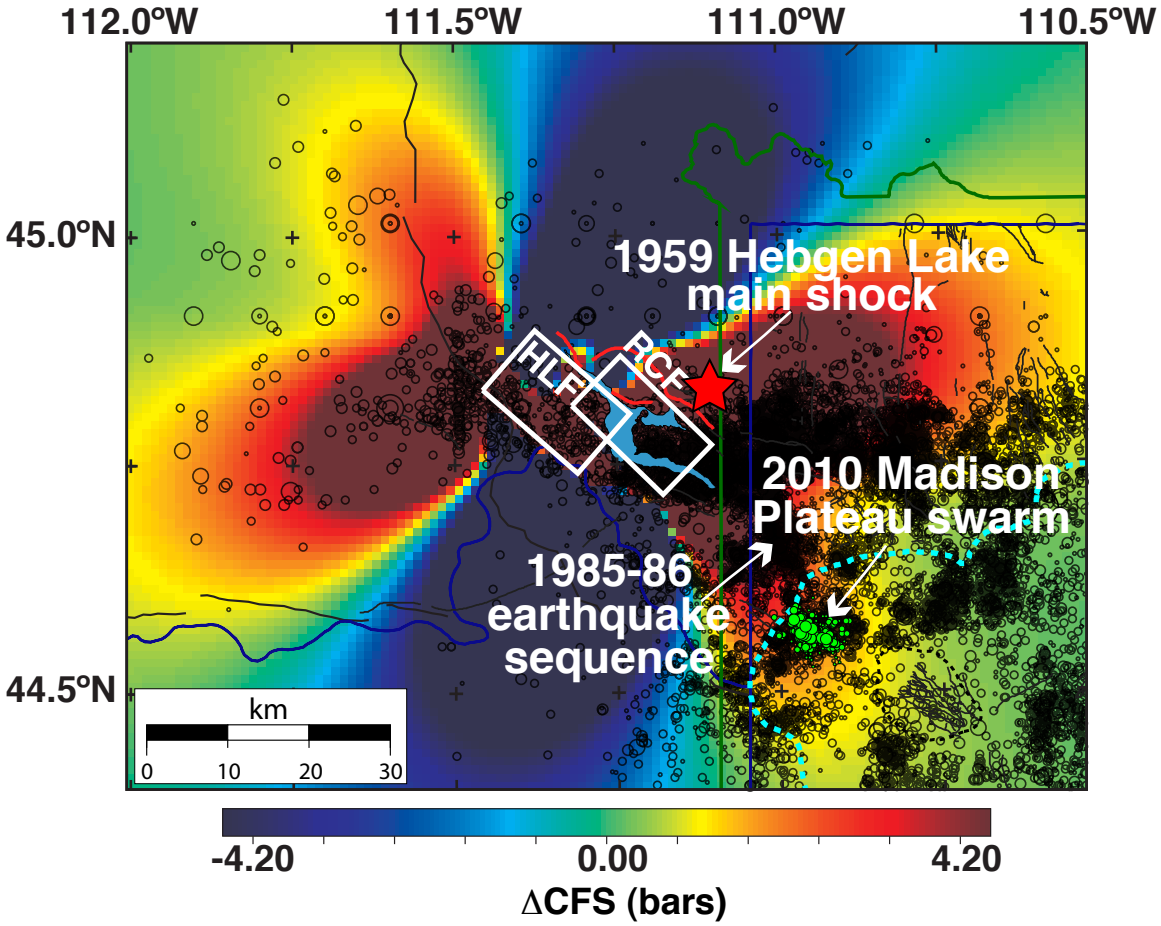

Figure 3.10. Changes of failure stress at 10-km depth induced by the 1959 Hebgen Lake earthquake (HL), with assumed N–S extensional regional stress of 150 bars. Two fault scarps were formed during the main shock: HLF, the Hebgen Lake Fault, and RCF, the Red Canyon Fault. White boxes show the surface projections of fault planes used for the stress modeling. Black open circles show Yellowstone seismicity from 1972-2013. The large red star is the location of the Hebgen Lake earthquake. Green circles show the 2010 Madison Plateau swarm. Modified from *Chang and Smith* [2002].

Figure 3.11. Vertical deformation for selected continuous GPS stations (shown in green) along with the monthly seismicity from 1993-2011. Monthly seismicity for all earthquakes is shown as a black line and seismicity with swarms events removed is shown as a red line.

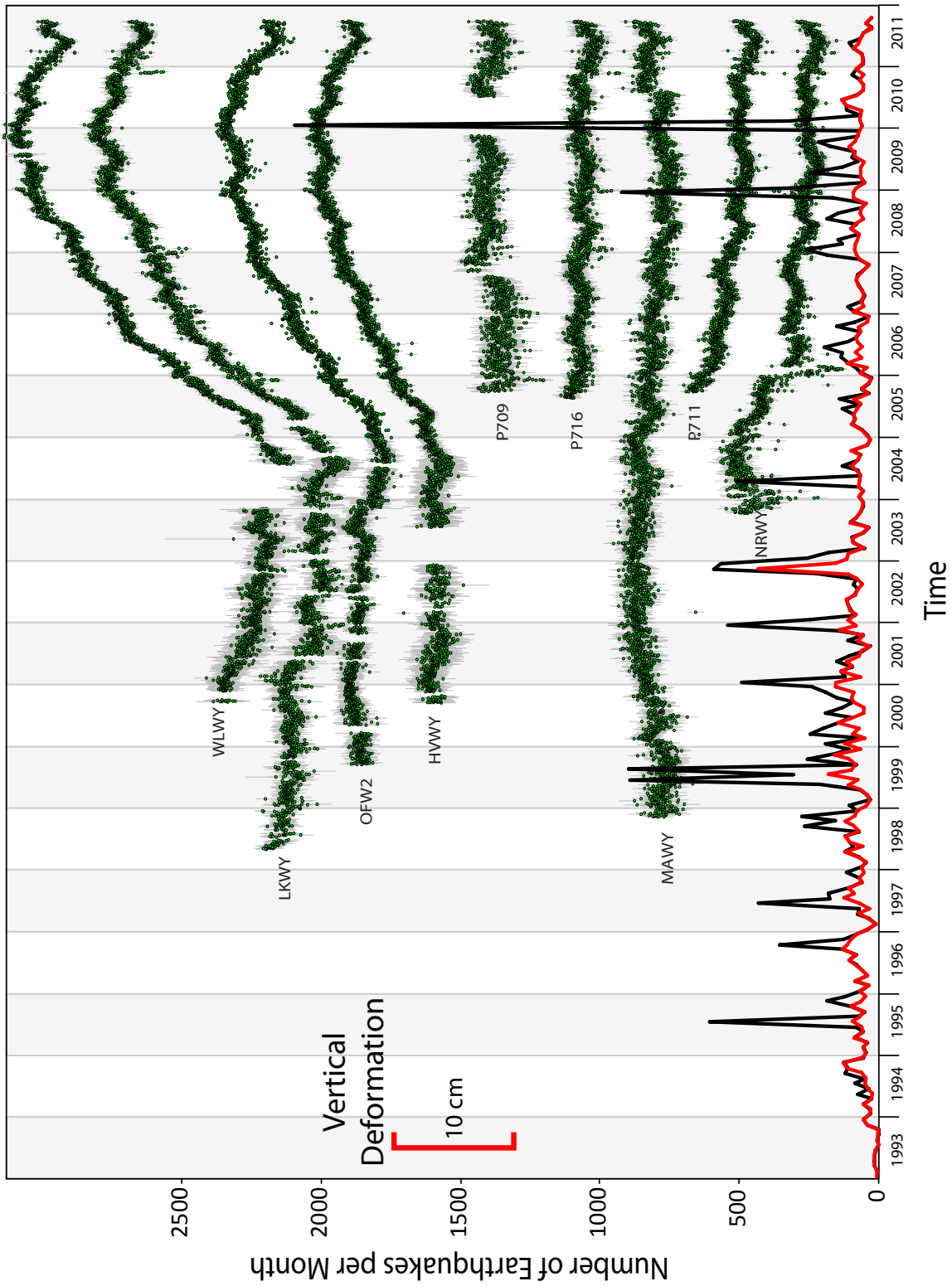
Number of Earthquakes per Month
0
500
1000
1500
2000
2500
1993
1994
1995
1996
1997
1998
1999
2000
2001
2002
2003
2004
2005
2006
2007
2008
2009
2010
2011
Time
Vertical Deformation
10 cm
WLWY
LKWY
OFW2
HVWY
P709
P716
MAWY
P711
NRWY

Yellowstone seismic network project, the Brinson Foundation and the Carrico Foundation. Seismic data was provided by the University of Utah Seismograph Stations as a partner in the Yellowstone Volcano Observatory, the EarthScope USArray project, and the Plate Boundary Observatory. GPS data were provided by the University of Utah and the NSF supported EarthScope Plate Boundary Observatory (EAR-0350028 and EAR-0732947).

References

Blackwell, D.D., P.T. Negraru, and M.C. Richards (2006), Assessment of the enhanced geothermal system resource base of the United States, *Nat. Resources Res.*, *15*(4), 283-308, doi:10.1007/s11053-007-9028-7.

Carslaw, H.S., and J.C. Jaeger (1959), *Conduction of Heat in Solids*, 2nd edition, Oxford University Press, Oxford, 510 p.

Chang, W. –L., and R. B. Smith (2002), Integrated seismic-hazard analysis of the Wasatch Front, Utah, *Bull. Seism. Soc. Am., 92*, no. 5, 1904-1922.

Chang, W. -L., R.B. Smith, C. Wicks, J. Farrell, and C.M. Puskas (2007), Accelerated uplift and magmatic intrusion of the Yellowstone caldera, 2004 to 2006, *Science*, *318*, 952, doi:10.1126/science.1146842.

Chang, W. -L., R. B. Smith, J. Farrell, and C. M. Puskas (2010), An extraordinary episode of Yellowstone caldera uplift, 2004-2010, from GPS and InSAR observations, *Geophys. Res. Lett.*, *37*, L23302, doi:10.1029/2010GL045451.

Christiansen, R.L. (2001), The Quaternary and Pliocene Yellowstone plateau volcanic field of Wyoming, Idaho, and Montana, U.S. Geol. Surv. Profess. Pap. 729-G, 145.

Farrell, J., S. Husen, and R.B. Smith (2009), Earthquake swarm and *b*-value characterization of the Yellowstone volcano-tectonic system. *J. Volcanol. Geotherm. Res.*, *188*, 260-276.

Herrmann, R. B., H. Benz, and C. J. Ammon (2011), Monitoring the earthquake source process in North America, *Bull. Seism. Soc. Am.*, *101*, no. 6, 2609-2625, doi: 10.1785/0120110095.

Hill, D.P., W.L. Ellsworth, M.J.S. Johnston, J.O. Langbein, D.H. Oppenheimer, A.M. Pitt, P.A. Reasenberg, M.L. Sorey, and S.R. McNutt (1990), The 1989 earthquake swarm beneath Mammoth Mountain, California: An initial look at the 4 May through 30 September activity, *Bull. Seismol. Soc. Am.*, *80*(2), 325-339.

Husen, S., R.B. Smith, and G.P. Waite (2004), Evidence for gas and magmatic sources beneath the Yellowstone volcanic field from seismic tomographic imaging, *J. Volcanol. Geotherm. Res.*, *131*, 397-410.

Puskas, C.M., R.B. Smith, C.M. Meertens, and W.L. Chang (2007), Crustal deformation of the Yellowstone-Snake River Plain volcano-tectonic system: Campaign and continuous GPS observations, 1987-2004, *J. Geophys. Res.*, *112*, B03401, doi:10.1029/2006JB004325.

Roman, D.C., J.A. Power, S.C. Moran, K.V. Cashman, M.P. Doukas, C.A. Neal, and T.M. Gerlach (2004), Evidence for dike emplacement beneath Iliamna Volcano, Alaska in 1996, *J. Volcanol. Geotherm. Res.*, *130*, 265-284.

Rubin, A.M. (1995), Propagation of magma-filled cracks, *Annu. Rev. Earth Planet. Sci.*, *23*, 287-336.

Rubin, A.M., D. Gillard, and J.-L. Got (1998), A reinterpretation of seismicity associated with the January 1983 dike intrusion at Kilauea Volcano, Hawaii, *J. Geophys. Res.*, *103*(B5), 10,003-10,015.

Shelly, D. R., D. P. Hill, F. Massin, J. Farrell, and R. B. Smith (2013), A fluid-driven earthquake swarm on the margin of the Yellowstone caldera, *in preparation*.

Simpson, R.W., and P.A. Reasenberg (1994), Earthquake-induced static stress changes on central California faults, in *The Loma Prieta, California earthquake of October 17, 1989--Tectonic processes and models*, edited by R.W. Simpson, *U.S. Geol. Surv. Prof. Pap. 1550-F*, F55-F89.

Smith, K.D., D.V. Seggern, G. Blewitt, L. Preston, J.G. Anderson, B.P. Wernicke, and J.L. Davis (2004), Evidence for deep magma injection beneath Lake Tahoe, Nevada-California, *Science*, *305*, 1277-1280, doi:10.1126/science.1101304.

Smith, R.B., and D.D. Blackwell (2000), Heat flow and energetics of Yellowstone Lake hydrothermal systems, *Eos Trans. AGU*, *81*(48), Fall Meet. Suppl., Abstract V22F-17.

Smith, R.B., M. Jordan, B. Steinberger, C.M. Puskas, J. Farrell, G.P. Waite, S. Husen, W.L. Chang, and R. O'Connell (2009), Geodynamics of the Yellowstone hotspot and mantle plume: Seismic and GPS imaging, kinematics, and mantle flow, *J. Volcanol. Geotherm. Res.*, *188*, 26-56.

Taira, T., R.B. Smith, and W.L. Chang (2010), Seismic evidence for dilatational source deformations accompanying the 2004-2008 Yellowstone accelerated uplift episode. *J. Geophys. Res*., *115*, B02301, doi:10.1029/2008JB006281.

Toda, S., R.S. Stein, and T. Saglya (2002), Evidence from the AD 2000 Izu islands earthquake swarm that stressing rate governs seismicity, *Nature*, *419*, 58-61.

Ukawa, M., and H. Tsukahara (1996), Earthquake swarms and dike intrusions off the east coast of Izu Peninsula, central Japan, *Tectonophysics*, *253*, 285-303.

Waite, G.P., and R.B. Smith (2002), Seismic evidence for fluid migration accompanying subsidence of the Yellowstone caldera, *J. Geophys. Res.*, *107*(B9), 2177, doi:10.1029/2001JB000586.

Waite, G.P., and R.B. Smith (2004), Seismotectonics and stress field of the Yellowstone volcanic plateau from earthquake first-motions and other indicators, *J. Geophys. Res.*, *109*, B02301, doi:10.1029/2003JB002675.

CHAPTER 4

PERSISTENT SEISMICITY AND ENERGETICS OF THE 2010 EARTHQUAKE SEQUENCE OF THE GROS VENTRE-TETON AREA, WYOMING

Abstract

Seismicity has persisted along a zone south of the Yellowstone volcanic field in the Gros Ventre Range, Wyoming, and on the eastern edge of the asesimic Quaternary high slip-rate Teton fault. Concentrated seismicity in this area occurs in sporadic sequences documented since 1923 with notable earthquakes in the decade preceding the deadly 1925 Gros Ventre slide that eventually lead to the failure of a dam created by the slide in 1927. Notable seismicity of the Gros Ventre region, using data from the Teton, Yellowstone and USArray seismic networks, has continued in the last decade with sequences in 2002 and 2004, culminating in an energetic sequence beginning in May, 2009 through a sequence of more than 200 earthquakes mainly from August 5 to August 17, 2010 of 0.5<M<~5. Ten of these events were felt. Notably the epicenters are aligned E-W, perpendicular to Quaternary normal faults of the Intermountain Seismic Belt, but occur in a domain of Laramide E-W trending thrusts. Focal mechanisms and moment tensor analysis reveal dominant oblique-slip normal fault mechanisms with components of thrust. These results are consistent with general E-W crustal extension as well as with

westward hanging-wall motion of the Teton fault from GPS data but also reveal notable compressional stress components consistent with motion on pre-existing thrust faults. Analysis of this energetic sequence along with previous sequences was done using new multiplet cross-correlation techniques, precise hypocenter relocations, and moment tensor analyses of small earthquakes. Results show that the August 2010 earthquake sequence occurred in an area of consistent seismicity and may be occurring on reactivated Laramide-aged thrust faults or buried anticline structures and that in order to accurately identify structures, more instrumentation needs to be installed to get better hypocenter locations. Moreover, this area is only 60-70 km south of the deforming Yellowstone caldera that has been shown to affect the stress on the Teton fault suggesting the possibility of stress interaction of the Yellowstone hotspot deformation and seismicity of the Gros Ventre area.

Earthquake Setting

The Teton-Gros Ventre region is part of the Intermountain Seismic Belt (ISB), a 1,300 km long diffuse zone of seismicity that extends from northern Arizona, through Utah, eastern Idaho, western Wyoming, and western Montana and marks the boundary between the Basin and Range to the west and the Rocky Mountains/Colorado Plateau to the east [*Smith and Arabasz*, 1991] (Figure 4.1). Although there have not been any historic large earthquakes on the Teton fault, large displacements of late Quaternary deposits indicate multiple M7+ events have occurred in the past in order to create the observed large fault scarps [*Gilbert et al.*, 1983]. In addition, studies by *Doser and Smith* [1983] estimate that M7.5 earthquakes occur on the Teton fault every 800 to 1,800 years

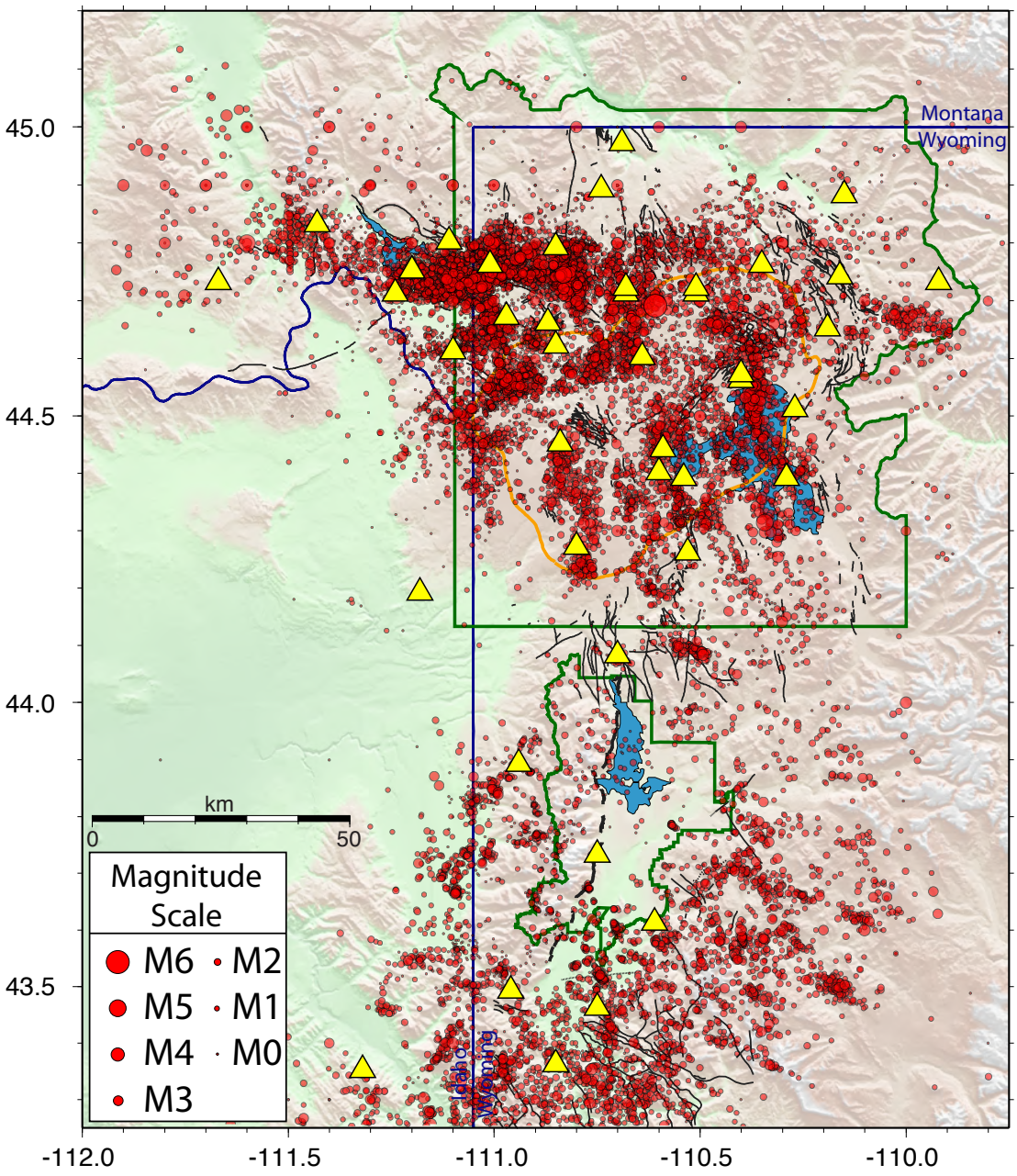

Figure 4.1. Earthquakes in the Yellowstone-Teton region, 1972-2013. Seismograph stations of the Yellowstone and Teton networks are shown as yellow triangles.

and large earthquakes ($6.5 < M < 7.5$) occur in the Teton region every 130 to 155 years. Based on Late Quaternary fault-offset trenching data, *Byrd* [1995] estimated a 0.16 mm/yr. loading rate that would make it plausible, based on linear extrapolation from the last two ruptures, that the Teton fault is capable of producing an M7+ earthquake.

Although the Teton fault is capable of producing large earthquakes, it occurs in a noticeable seismic gap, and most of the seismicity in the Teton area occurs in the region east of the Teton fault beneath the Gros Ventre range (Figure 4.1). Epicenter patterns in the Gros Ventre Range to the east of the Jackson Hole basin correlate well with southeast trending valleys throughout the Gros Ventre Range and subsurface expressions of Laramide thrust faults [*White et al*, 2009] (Figure 4.1). Focal mechanisms of these earthquakes show mainly normal faulting with a small strike slip component. These events in the Gros Ventre Range are the most consistent seismicity with earthquakes occurring regularly over the historic time [*White et al.*, 2009].

Prior to 1962, estimates of earthquake magnitudes and locations of Gros Ventre historic earthquakes are based on felt reports as instrumentation in the area was lacking (Figure 4.2). For example, reports of felt earthquakes by the inhabitants of the Teton-Jackson Hole-Kendall Valley region go back to the late 1800s, however, no earthquake has exceeded an intensity of VI on the modified Mercalli scale [*Coffman and von Hake*, 1973]. From 1923 to 1975, felt earthquakes occurred primarily in the central Gros Ventre Range, southern Jackson Hole, and Driggs, Idaho regions [*Smith et al.*, 1976]. The earliest published discussion of historical earthquakes was given by *Blackwelder* [1926], who described a slight earthquake in Jackson, on September 3, 1925 [*Smith et al.*, 1976]. The next account of earthquakes was given by *Fryxell* [1933], who documented several

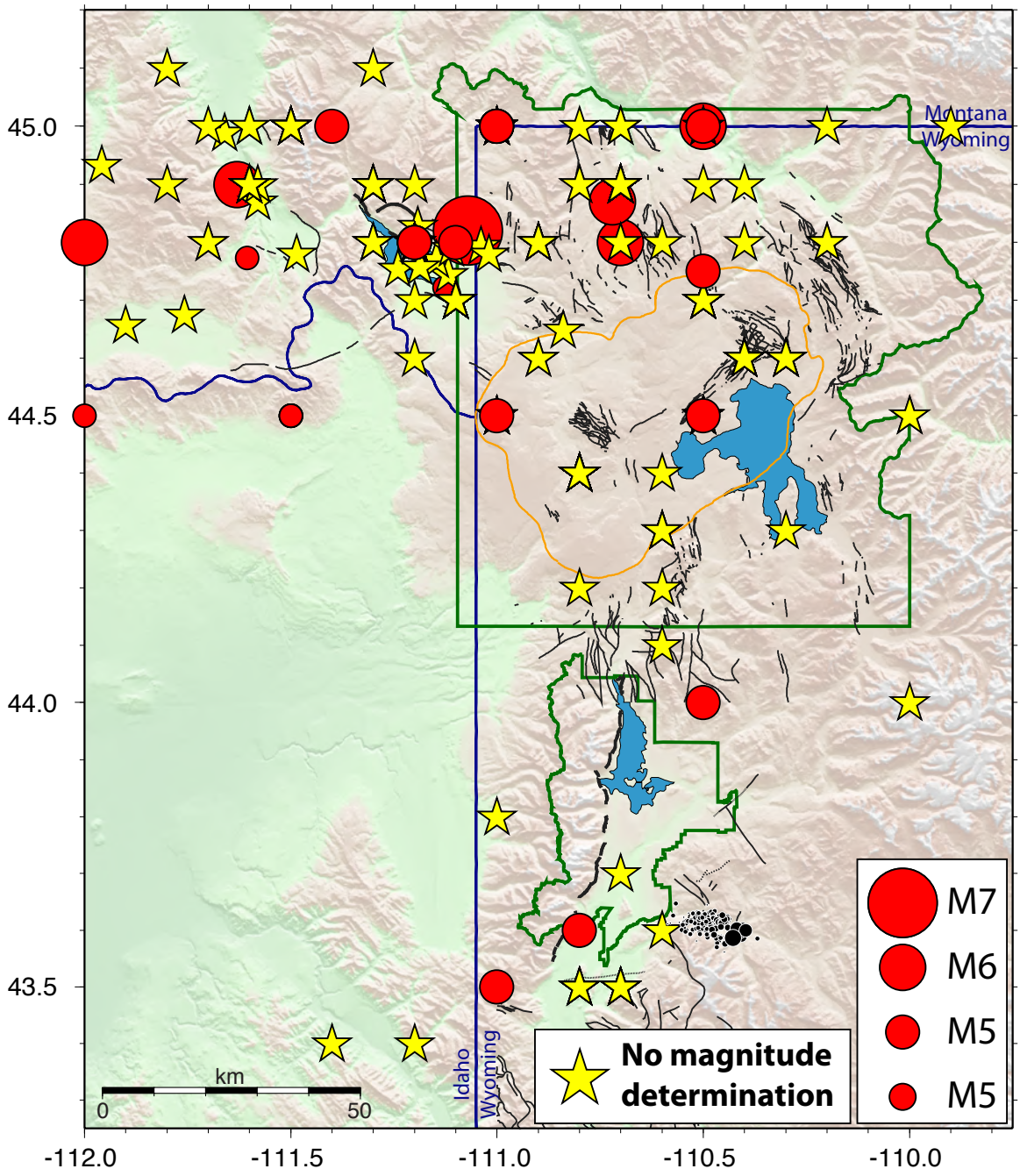

Figure 4.2. Historical seismicity of the Yellowstone-Teton region, prior to instrumentation, based on felt reports. Red circles are events where a magnitude has been estimated. Yellow stars are events that have no magnitude determination.

felt shocks in the Gros Ventre Canyon, January 25-28, 1932 [*Smith et al., 1976*]. In addition, a documented earthquake sequence [*Gale*, 1940] consisting of three shocks during the autumn of 1939 was reported. These shocks did not produce any damage, and from felt reports were judged to be near or just southwest of Jackson [*Smith et al.*, 1976]. Historical accounts of these earthquakes do not suggest that the earthquakes occurred along the Teton fault zone [*Smith et al.*, 1976].

Teton Area Seismic Hazards

Seismic hazards in the Teton region are dominated by the high slip-rate Teton normal fault, which is capable of producing ground accelerations of up to ~1g [*White et al.,* 2009]. However, in addition to the Teton fault, persistent seismicity is present to the east in the Gros Ventre range that has experienced earthquakes with magnitudes exceeding M5 (Figure 4.1). This seismicity is separate from the Teton fault and constitutes a separate hazard designation.

In addition, throughout the Gros Ventre range, glacial deposits, incompetent surface material, 50-100 cm of annual precipitation, and glacially over-steepened slopes combine to make an area that is highly susceptible to landslides [*Smith et al.*, 1976]. The most famous landslide in the area is the Lower Gros Ventre landslide, one of the largest historic landslides in the United States that occurred on June 23rd, 1925. Nearly 2 years later, on May 18th, 1927, the landslide-created dam failed, resulting in a massive flood downstream that destroyed the town of Kelly and killed 6 people. *Smith et al.* [1976] explored the possibility that the Lower Gros Ventre slide may have been triggered by seismic activity. Since there were no seismic instruments installed at the time (the

1920s), our study has to rely on historical records and accounts by people who were living in the area at the time.

One account [*Smith et al.*, 1976], for example, by Mr. Billie Bierer, a local cowboy, states, "Yes, I have noticed that and cannot see where the water can be going unless it is following the formation between two different stratifications and coming to the surface at some other water level point. If not, this mountain side would be a mushy, woozy boil. However, it may be there is a wet line running between these strata and the time will come when the entire mountain will slip down into the canyon below. For instance, some of these times these earthquake tremors that are coming so often are going to hit about the right time when the mountain is the wooziest, and down she will come" [*Smith et al.,* 1976]. There are numerous other accounts of people feeling earthquakes in the few days prior and after the Lower Gros Ventre slide [*Smith et al.*, 1976].

The August, 2010 Gros Ventre Earthquake Sequence

The August, 2010 Gros Ventre earthquake sequence began early on August 5, 2010 with a M_C=5 (M_W4.9) event that was widely felt in the area (647 felt reports on the USGS Did You Feel It page). This earthquake was followed by a series of aftershocks including three M4+ events, eight M3+ events, and 189 events with M<3 for a total of 201 earthquakes. The main-shock occurred at a depth of 5-10 km and ~10 km to the east of the Lower Gros Ventre landslide (Figures 4.3 and 4.4).

In a qualitative sense, it appears that the 2010 Gros Ventre sequence is occurring on a E-W striking structure that is ~10 km long based on the distribution of aftershocks (Figure 4.3). However, if you look at the distribution of events based on magnitude

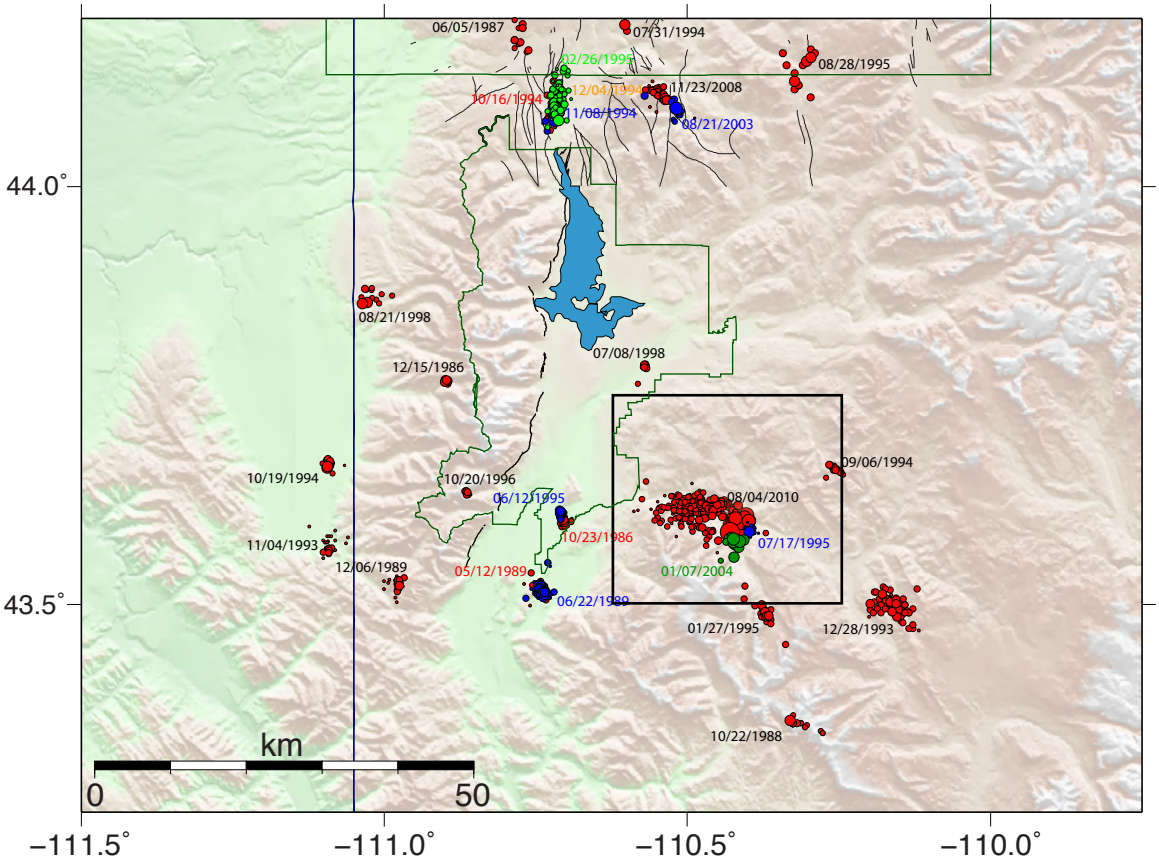

Figure 4.3. Earthquake clusters identified in the Teton region, using the method of *Farrell et al.* [2009], labeled by the date of the onset of seismicity. The black box denotes the area shown in Figures 4.4 and 4.5

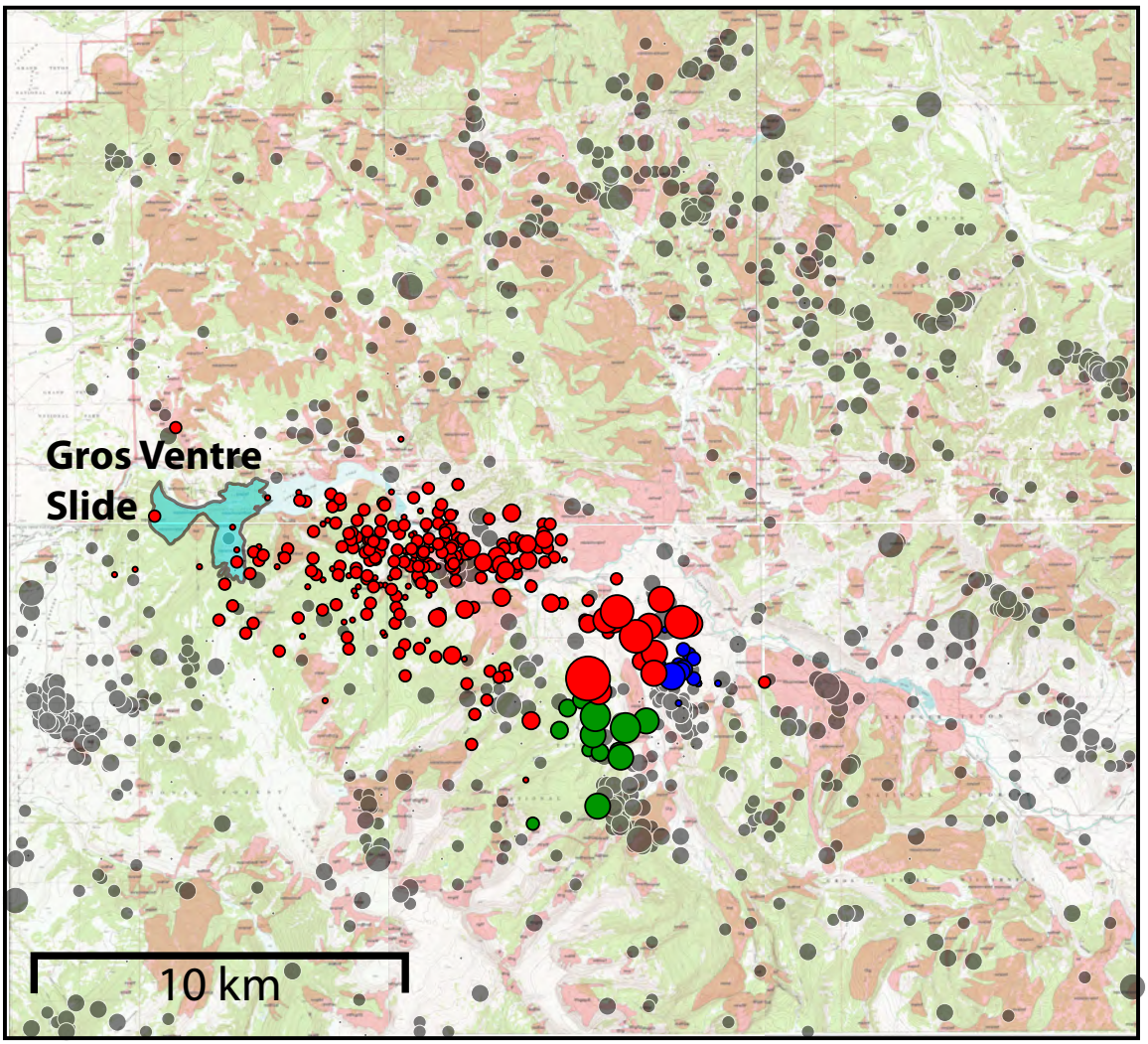

Figure 4.4. Closeup of the 2010 Gros Ventre earthquake sequence (red circles). Previous clusters of earthquakes in the same region are shown as blue circles (1995) and green circles (2004). The 1925 Lower Gros Ventre slide is outlined by the blue polygon. The background image shows topography with mapped landslides (red polygons) in the Gros Ventre range.

(Figure 4.5) you find that as magnitude decreases, events are located more westward (Figure 4.5). This is due to the uneven distribution of seismic stations that are dominantly to the west of the sequence (Figure 4.1). The larger events are recorded by distant stations to the east and have better constrained locations than the smaller events, whose locations are relying on stations primarily to the west.

Using the cross-correlation seismic data technique of *Massin et al.* [2013], multiplet (repeating) earthquakes of the 2010 Gros Ventre sequence were identified (Figure 4.6). A total of 28 individual clusters were identified with the largest cluster containing seven multiplets (Figure 4.6). Most clusters were short lived with the time between the first multiplet and the last multiplet less than 1 week, however, there are two clusters with a lifespan of multiple weeks (Figure 4.6). The main-shock of the sequence is not correlated to any other event within the sequence and has a unique waveform (Figure 4.7).

Composite focal mechanisms were computed for each cluster (grey source mechanisms in Figures 4.6 and 4.8). Focal mechanisms of the 2010 Gros Ventre sequence earthquakes were determined from P-wave first motions using an automated algorithm [*Reasenberg and Oppenheimer*, 1985] (green source mechanisms in Figure 4.8). In addition, moment tensors of selected events were calculated [*Herrmann et al.*, 2011] and are shown as red source mechanisms in Figure 4.8. The possible fault planes from the source mechanisms and using the distribution of hypocenters, possible fault plane orientations were plotted on rose diagrams in Figure 4.9. Results show that based on the source mechanisms, the fault planes are either NW-SE (~130º) or NE-SW (230º - 240º) (Figure 4.9) although slightly more solutions show a NW-SE striking fault plane.

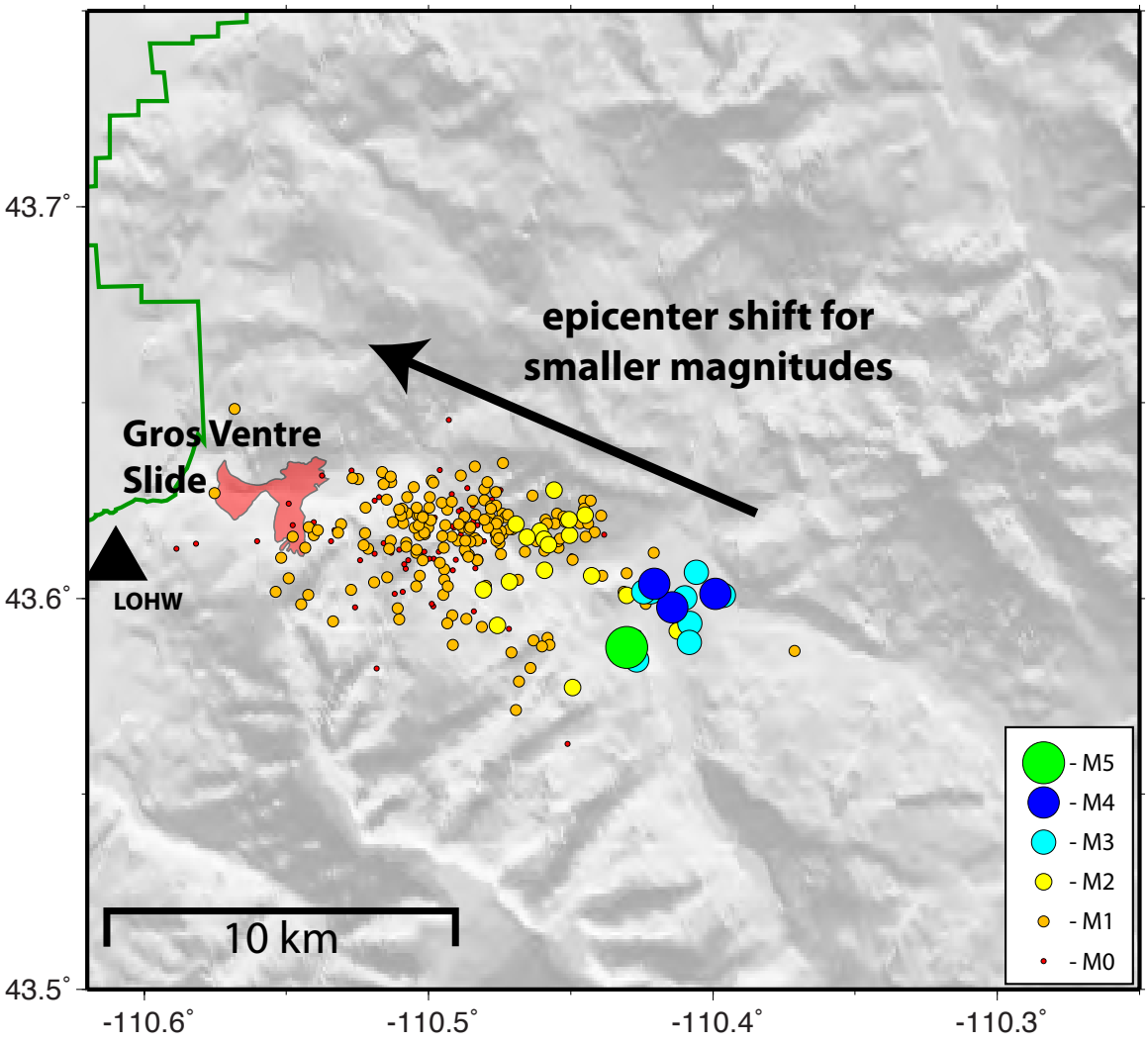

Figure 4.5. Earthquakes of the 2010 Gros Ventre sequence sized and color-coded by magnitude showing the apparent westward shift in epicentral location with decreasing magnitude. The closest seismograph station (LOHW) is shown as a black triangle. The 1925 Lower Gros Ventre slide is outlined as a red polygon.

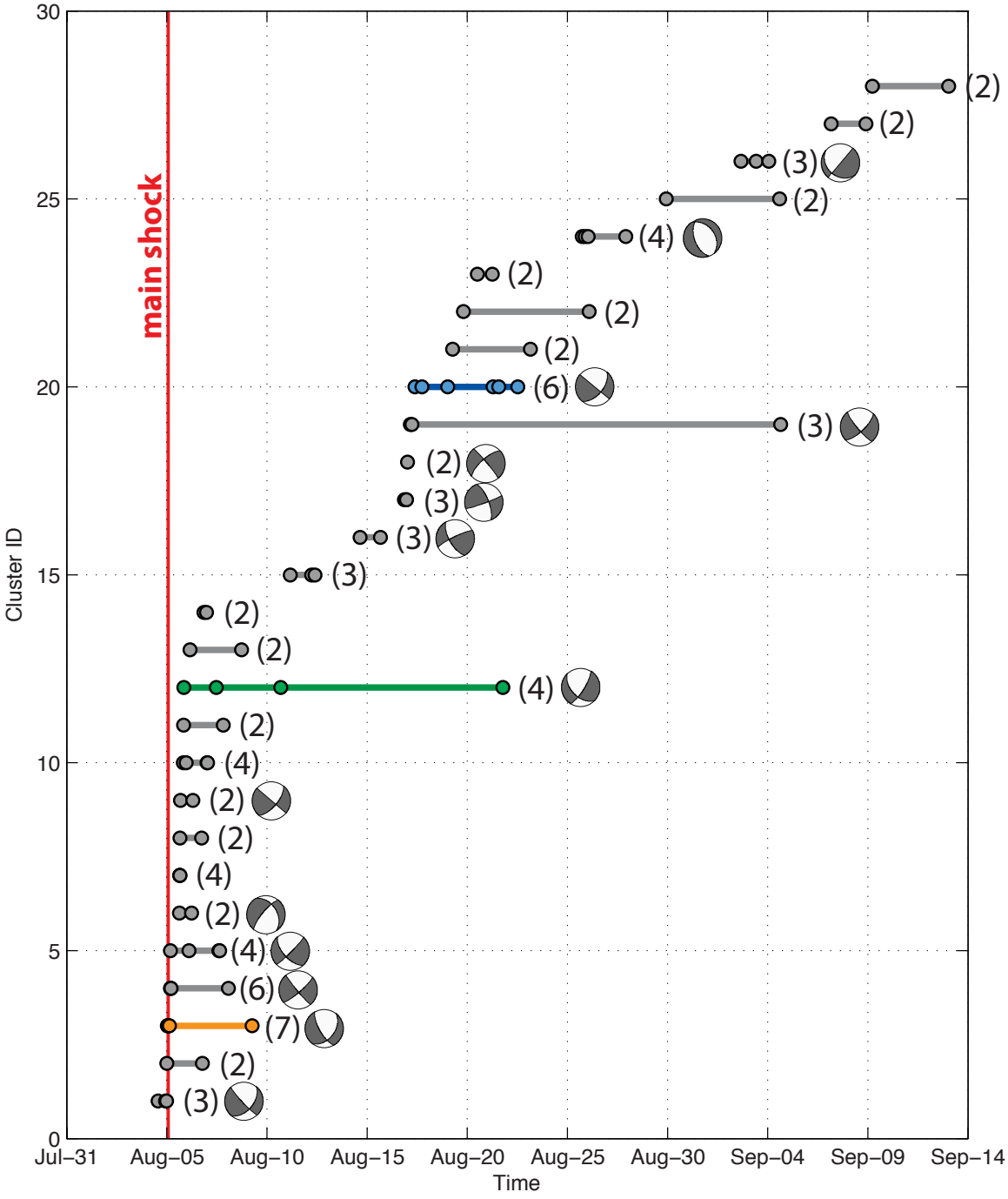

Figure 4.6. Multiplet sequences of the 2010 Gros Ventre sequence. The number of events in each cluster is shown in parentheses. Composite focal mechanisms are shown as gray beach balls. The orange, green, and blue sequences are shown in Figure 4.7.

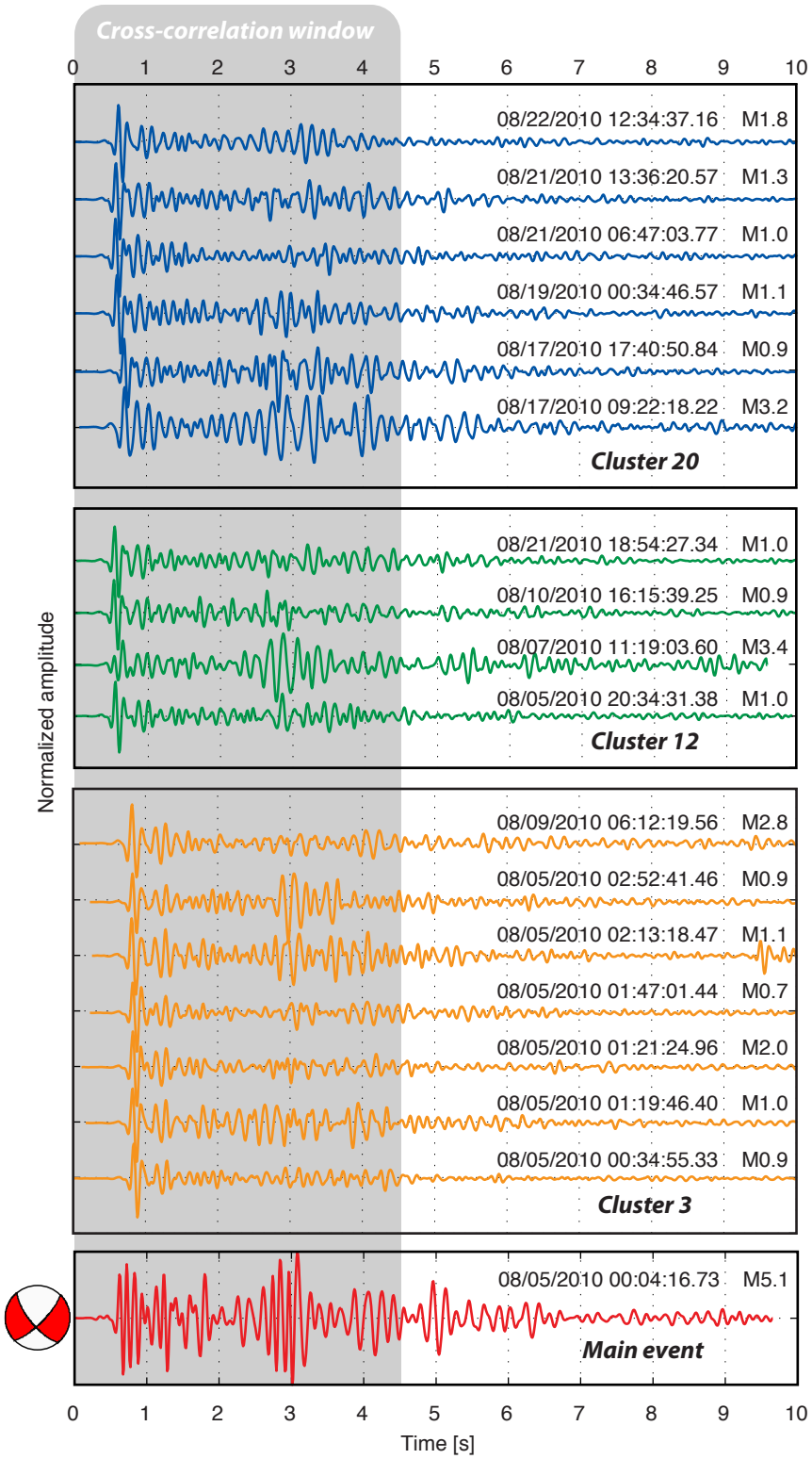

Figure 4.7. Repeating waveforms for Clusters 3, 12, and 20 (Figure 4.6). The waveform of the M5 main events is shown in red along with its moment tensor solution. The time window used to calculate cross-correlation values is shown in gray.

Date	Moment Tensor	Focal Mech.	Cluster #
08/05 00:04:17			
08/05 14:59:28			
08/05 16:30:36			 09
08/05 17:45:21			
08/06 07:13:57			 09
08/06 09:24:41			
08/06 15:34:18			
08/07 11:19:04			 12
08/14 14:39:11			
08/17 02:49:55			
08/17 04:02:34			
08/17 06:46:21			
08/17 09:22:20			 20
08/19 00:50:22			
08/25 21:21:15			 24
08/26 00:51:57			 24
09/03 10:18:15			 26
09/20 00:47:22			
10/24 17:43:59			
10/26 01:24:16			

Figure 4.8. Source mechanisms for the 2010 Gros Ventre sequence. Red mechanisms are moment tensors from the Saint Louis University moment tensor catalog. Green mechanisms are for single events. Gray mechanisms are composite mechanisms calculated using multiplet events (labeled by cluster #).

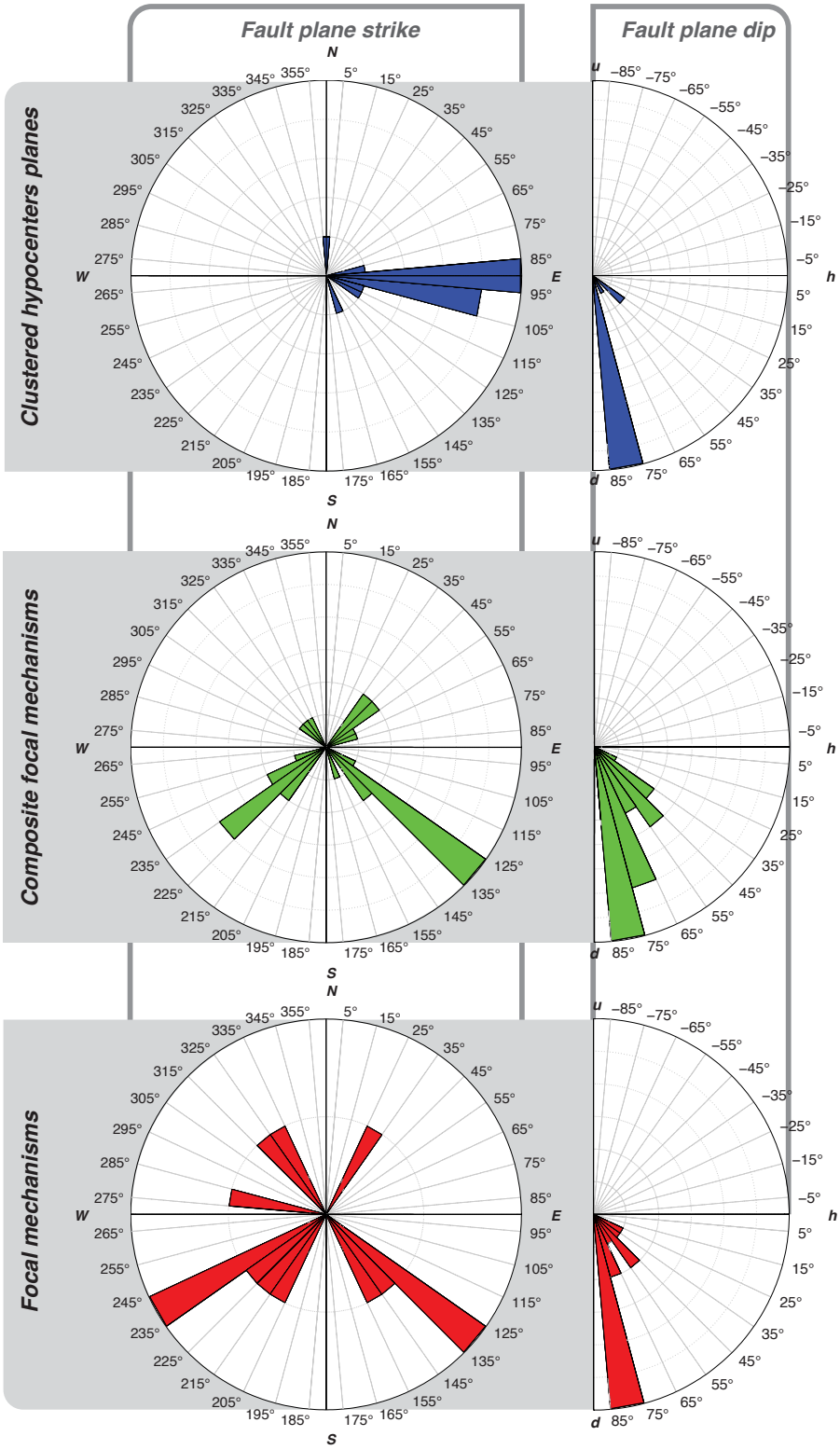

Figure 4.9. Rose diagrams for the fault plane orientations based on the best fitting plane to the hypocenter distribution (blue), composite multiplet focal mechanisms (green), and single event first motion focal mechanism solutions (red). The best fitting dip for the fault plane is shown on the right using the same color scheme.

Based on the distribution of hypocenters, the fault plane should be orientated E-W. The dip of the fault is much more clear and all three sources show that these events are happening on a plane dipping around 80º (Figure 4.9).

Using the swarm analysis technique of *Farrell et al.*, [2009], we identified numerous other clusters of events throughout the Teton region using the cataloged events (Figure 4.3). The same area as the August 2010 sequence experienced clusters of earthquakes both in 1995 and in 2004 (Figures 4.3 and 4.4). The 1995 sequence contained 20 events with the largest event a M_C=3.0. The 2004 sequence contained 14 events with two M_C4+ events, four M_C3+ events, and eight events with M_C<3. Moment tensor solutions for the 2004 events are very similar to those of the 2010 sequence. Zooming in on these three events shows their proximity to the Lower Gros Ventre landslide as well as the numerous smaller landslides that have been mapped in the region (Figure 4.4).

Discussion and Conclusions

The majority of earthquakes in the Teton region occur in an area east of the Teton fault in the Gros Ventre range. This is an area of persistent earthquake activity with historical reports of felt events dating back to the late 1800s. The high slip rate of the Teton fault is the source of most of the seismic hazard in the area, however, the Gros Ventre region is a separate hazard consideration due the persistent seismicity and the long record of felt events with magnitudes up to M5. In addition, the Gros Ventre range has over-steepened slopes that are vulnerable to mass wasting including triggered landslides from seismic sources.

The 2010 Gros Ventre sequence contained more than 200 events with a M_C=5 main-shock that was widely felt throughout the region. Analysis of the source mechanisms of the main-shock and the aftershocks shows that the events are dominantly oblique strike-slip events that are occurring on a NW-SE striking fault plane dipping 80º to the NE. There are no mapped Quaternary faults in the immediate vicinity of the Gros Ventre seismicity, however, there are numerous NW-SE striking subsurface Laramide aged thrust faults in the area identified by *Smith et al.* [1976]. In addition, there are large anticlinal structures in the area including the Spread Creek anticline to the north, and the the Ramshorn and Red Hills anticlines in the same area of the 2010 Gros Ventre sequence [*Love et al.*, 1951]. It is plausible that these events occurred on reactivated thrust faults energized by the dominant extensional stress regime or related to stress loading by the Yellowstone hotspot deformation.

To better understand the processes at seismogenic depths responsible for this persistent Gros Ventre range seismic activity, more seismographs need to be installed, in particular to the east of the Jackson Hole Basin. This would allow us to obtain better-constrained hypocenter locations. With better-constrained hypocenter locations, we could use the earthquakes to map out structures at depth.

References

Blackwelder, E. (1926), Earthquakes in Jackson Hole, Wyoming, *Seismol. Soc. America Bull.*, *16,* 196.

Byrd, J. O. (1995), Neotectonics of the Teton fault, Wyoming, Ph.D. Thesis, University of Utah, Salt Lake City, UT.

Byrd, J. O. D., and R. B. Smith (1995), Near surface fault geometry and paleoseismicity of the Teton fault, Wyoming, submitted to *Geol. Soc. Amer. Bul*.

Coffman, J.L., and C.A. von Hake (Editors) (1973), Earthquake history of the United States, U.S. Dept. of Commerce Publ. 41-1, 208.

Doser, D.L., and R.B. Smith (1983), Seismicity of the Teton-southern Yellowstone region, Wyoming, *Bull. Seis. Soc. Am.*, *73*, 1369-1494.

Farrell, J.M., S. Husen, and R.B. Smith (2009), Earthquake swarm and *b*-value characterization of the Yellowstone volcano-tectonic system. *J. Volcanol. Geotherm. Res.*, *188* (1–3), 260–276.

Fryxell, F. M. (1933), Earthquake shocks in Jackson Hole, Wyoming, *Seismol. Soc. America Bull.*, *23*, 167-168.

Gale, B.T. (1940), Communication, further earthquake shocks in Jackson Hole, Wyoming, *Seismol. Soc. Of America Bull.*, *30*, 85.

Gilbert, J. D., D. Ostenaa, and C. Wood (1983), Seismotectonic study Jackson Lake Dam and Reservoir, Minidoka Project, Idaho-Wyoming, Bureau of Reclamation Seismotectonic Report, 83-8, 123.

Herrmann, R. B., H. Benz, and C. J. Ammon (2011), Monitoring the earthquake source process in North America, *Bull. Seism. Soc. Am.*, *101*, no. 6, 2609-2625, doi: 10.1785/0120110095.

Love, J. D., W. R. Keefer, D. C. Duncan, H. R. Gergquist, and R. K. Hose (1951), Geologic map of the Spread Creek-Gros Ventre River area, Teton County, Wyoming, U. S. Geol. Survey Oil and Gas Investigations Map OM 18.

Massin, F., J. Farrell, and R. B. Smith (2013), Repeating earthquakes in the Yellowstone volcanic field: Implications for rupture dynamics, ground deformation, and migration in earthquake swarms, *J. Volcanol. Geotherm. Res.*, *257*, 159-173, doi: 10.1016/j.jvolgeores.2013.03.022.

Reasenberg, P., and D. Oppenheimer (1985), FPFIT, FPPLOT and FPPAGE: FORTRAN computer programs for calculating and displaying earthquake fault-plane solutions, U.S. Geol. Surv. Open File Rep., 85-0739, 109 pp.

Smith, R.B., J.R. Pelton, and J.D. Love (1976), Seismicity and the possibility of earthquake related landslides in the Teton-Gros Ventre-Jackson Hole area, Wyoming, *Contributions to Wyoming Geology*, 14, 57-64.

Smith, R. B., and W. J. Arabasz (1991), Seismicity of the Intermountain Seismic Belt, in *Neo-tectonics of North America*, edited by D. B. Slemmons, E. R. Engdahl, M. D. Zoback, and D. D. Blackwell, Geological Society of America, Boulder, Colorado., Pg. 185-228.

White, B. J. P., R. B. Smith, S. Husen, J. Farrell, and I. Wong (2009), Seismicity and earthquake hazard analysis of the Teton-Yellowstone region, Wyoming, *J. Volcanol. Geotherm. Res.*, *188*, 277-296, doi: 10.1016/j.jvolgeores.2009.08.015.

CHAPTER 5

TEMPORAL GRAVITY AND MASS CHANGES ACCOMPANYING THE 2004-2010 UNPRECEDENTED UPLIFT OF THE YELLOWSTONE CALDERA

Abstract

Beginning in late 2004, GPS and InSAR data revealed the onset of an unprecedented episode of uplift in the 0.64 Ma Yellowstone caldera at rates up to 7 cm/yr. The caldera tumescence has been modeled as an expanding volcanic sill of ~1200 square kilometers at 10 km depth beneath the caldera, coincident with the top of the seismically imaged crustal magma reservoir. The modeled rate of source volume increase of 0.1 cubic kilometers per year is evidence of an influx of molten material to the system as the main mechanism for the uplift and is consistent with the 2,000 mW/m2 total heat flux. To evaluate the mass rate change of the volcanic source of the accelerated uplift, temporal variations in gravity were measured from 2007-2012 at the precision Yellowstone gravity network established in 1977. We compare the changes in gravity and equivalent mass changes to infer whether the uplift is due to the influx of magma, pressurization of the hydrothermal system, or a change in the orthometric height alone.

Introduction

The Yellowstone precision gravity network, established in 1977, consists of 160 stations located along 1st-order leveling lines [*Evoy*, 1978; *Arnet et al.*, 1997]. This initial network primarily consisted of benchmarks installed along the various roads in the Yellowstone region. Beginning in 1984, an additional 40 backcountry benchmarks were added to the network bringing the total number of precision gravity stations to ~200 [*Smith et al.*, 1978; *Hollis et al.*, 1987] (Figure 5.1). Additional measurements of the Yellowstone gravity network have been carried out in 1979, 1983, 1986, 1987, 1988, 1989, 1990, 1991, 1992, 1993, and 1994 [*Arnet*, 1996]. After 1994, gravity surveys in the Yellowstone region were terminated for lack of funds.

Beginning in 2004, the Yellowstone caldera began a period of accelerated uplift that lasted until early 2010 with rates as high as 7 cm/yr [*Chang et al.*, 2007; *Chang et al.*, 2010]. It was after the onset of this accelerated uplift that the University of Utah resumed the annual gravity surveys. Beginning in 2007, a line of 24 gravity benchmarks between Canyon Junction and Sylvan Lake was surveyed. This line has continued to be surveyed annually through 2012. Beginning in 2008, 16 additional benchmarks, between Madison Junction and Lewis Falls, were added to the annual gravity survey (Figure 5.2). Together, these stations define two, roughly N-S profiles across the 0.64 Ma Yellowstone caldera passing by the two resurgent domes. The goal of these renewed annual gravity surveys is to measure precise annual gravity changes to identify mass changes related to the accelerated uplift from 2004 – 2010.

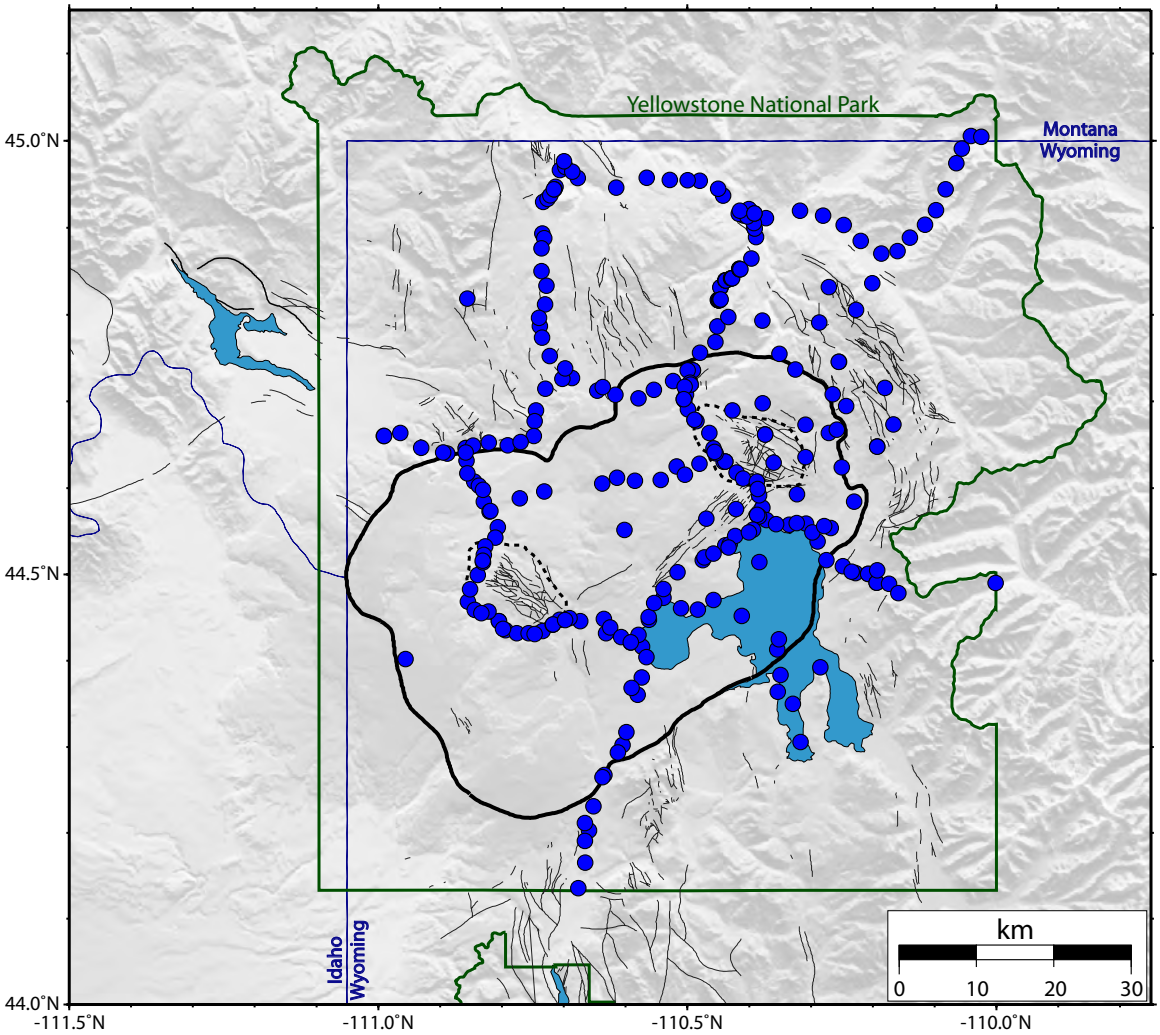

Figure 5.1. Gravity benchmarks of the Yellowstone gravity network. There are approximately 160 frontcountry benchmarks, and 40 backcountry benchmarks.

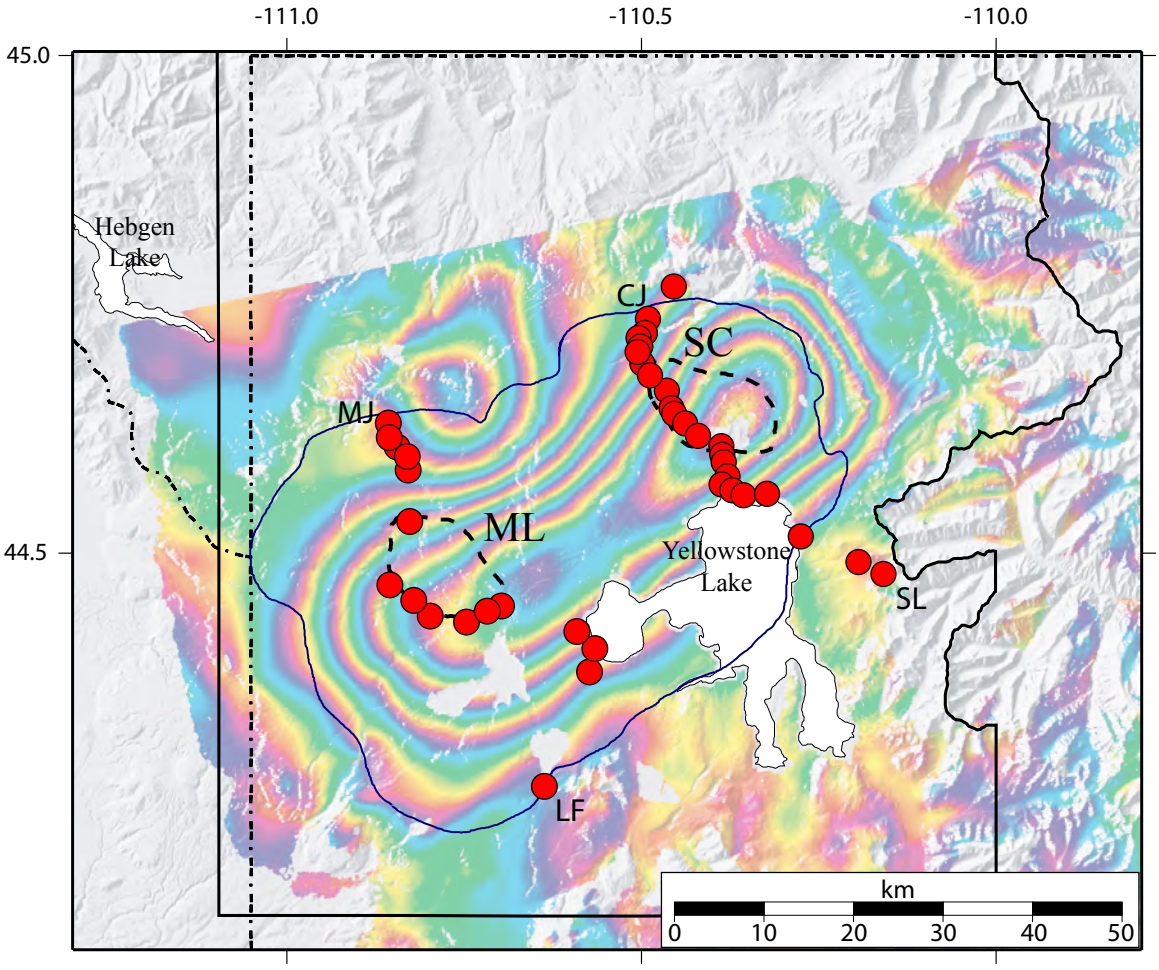

Figure 5.2. Gravity benchmarks occupied annually from 2007-2012 (red circles). Background image is InSAR data from 2005-2007 [*Chang et al.*, 2007].

Previous Gravity Surveys and Results

Results from previous precision gravity surveys from 1977-1983 and 1987-1993 show significant temporal gravity changes of up to 60 μgal [*Arnet*, 1997]. Two areas experienced the highest change in gravity: 1) across the northern caldera north of Fishing Bridge, and 2) across the southern caldera from west of Old Faithful to West Thumb (Figure 5.3a). The northern profile had a maximum gravity decrease of up to 60 μgal between 1977 and 1983 (Figure 5.3a). In the following years (1987 to 1993) an increase of 60 μgal was observed (Figure 5.3b) [*Arnet*, 1997].

For the northern caldera crossing line for the period of uplift between the years 1977-1983, a ratio of gravity change (Δg in mgal) to height change (Δz in m) was calculated at 0.17 ± 0.07 mgal/m. For the period of subsidence between the years 1986-1993, the ratio is -0.33 ± 0.10 mgal/m [*Arnet*, 1997]. A mass increase occurred during the uplift episode between 1977-1983 indicated by a change in gravity per change in height ratio of 0.17 ± 0.07 mgal/m. This increase is significantly greater than the free-air gradient (-0.3086 mgal/m) suggesting that the most likely source of the gravity decrease is related to widespread hydrothermal fluid movement, which furthermore is related to input by magma. Basaltic intrusions into the mid or upper crust, pressurization of a deep hydrothermal system by magmatic gas, or brine released by crystallization of a rhyolite melt, are also plausible sources for the uplift. This anomaly cannot have been caused solely by pressurization of the deep hydrothermal system, without any significant mass increase [*Arnet*, 1997]. In contrast, no significant mass change occurred during the period of subsidence (1986-1993) as the ratio of -0.33 ± 0.10 mgal/m is close to the free-air gradient [*Arnet*, 1997]. This is explained by depressurization of the deep

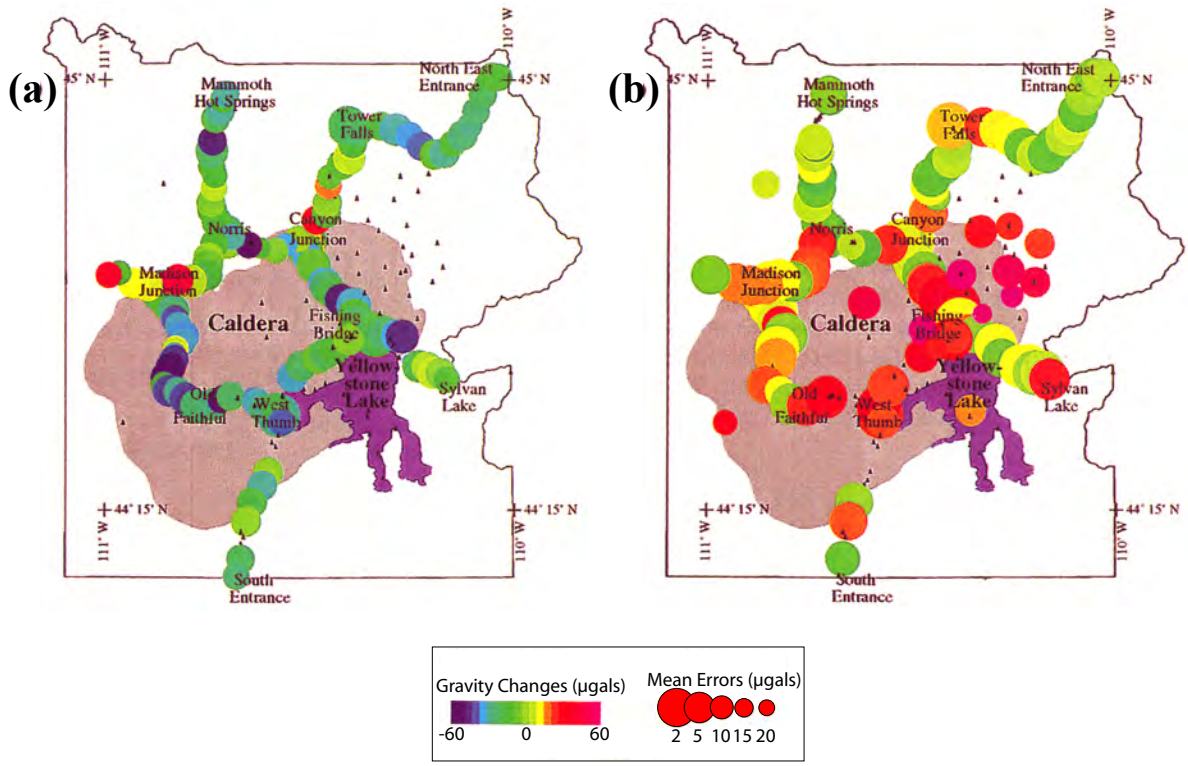

Figure 5.3. Yellowstone gravity changes (a) from 1977 to 1983, showing the gravity decrease throughout the Yellowstone caldera, (b) changes from 1987 to 1993, revealing a distinct gravity increase in the caldera. Modified from *Arnet et al.* [1997].

hydrothermal system as a result of fracturing and volatile loss to the shallow hydrothermal system [*Arnet*, 1997].

The 2007-2012 Yellowstone Caldera Surveys

Precise gravity changes were measured annually from 2007-2012 using a variety of precision gravimeters. In 2007, measurements were made using both a Scintrex CG3 gravimeter and a LaCoste and Romberg G-meter. In 2008, a LaCoste and Rombert G-meter with an Aliod system was used. From 2009 – 2012, a Scintrex CG5 meter was used.

Measurements were made using a ladder repeat schedule due to the linear nature of the network. A daily repeat schedule example is as follows (Figure 5.4):

11mdc-13mdc-hollis-lc58-22mdc-y367-24mdc-z367-24mdc-y367-22mdc-lc58-hollis-13mdc-11mdc-kaygee-z367-f11a-e11a2-arbe-27mdc-da3c-lehardy-da3c-lehardy-27mdc-arbee-e11a2-f11a-kaygee

To reduce the effect of water table variation we always carried out the measurements at the same time of the year, late summer and early fall, when the rivers and lakes are at their lowest levels. It is generally assumed that the water table will have a minimal effect on the gravity change signals if it stays at relatively constant levels during the measurements. All gravity data were processed following the technique of *Gettings et al*. [2008].

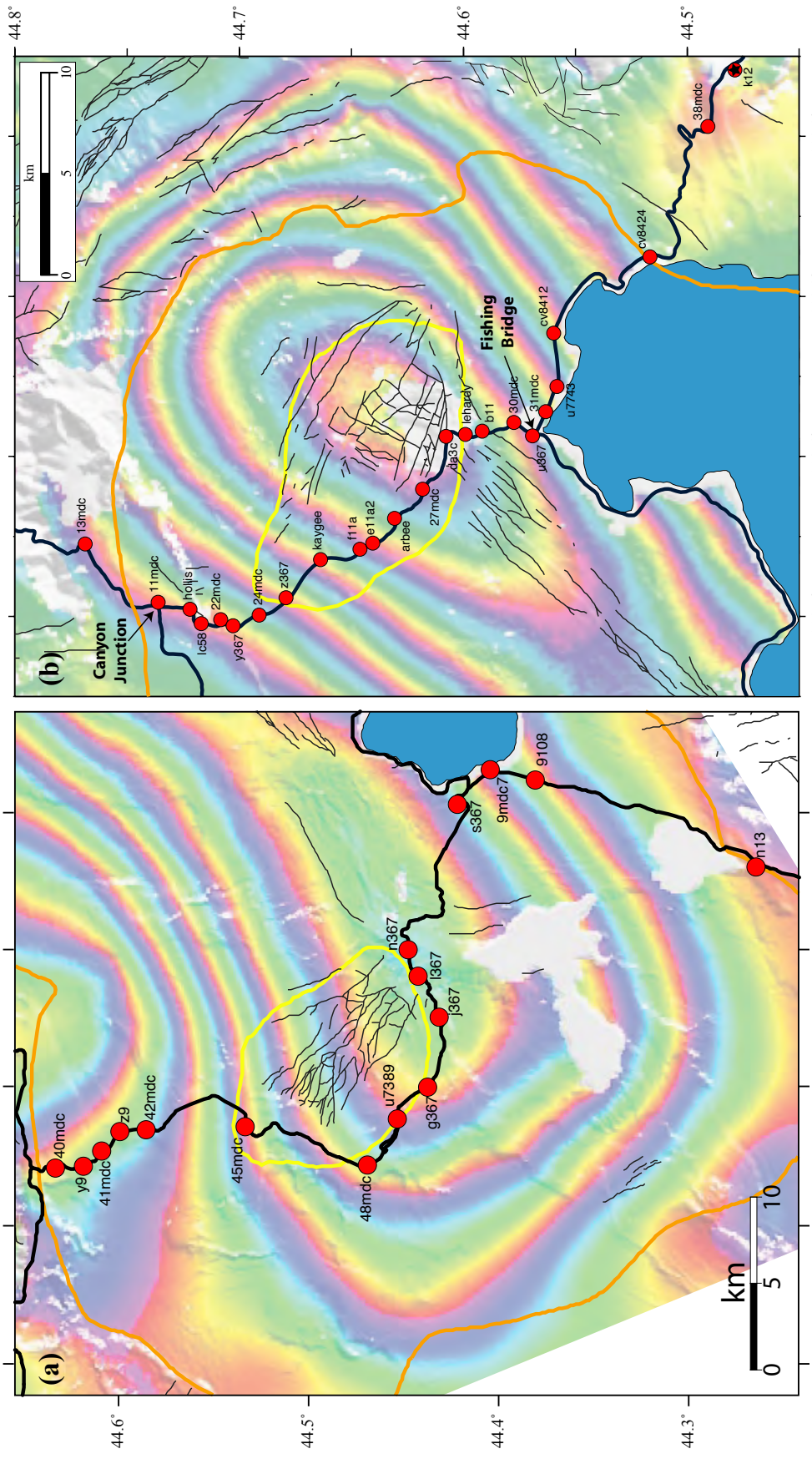

Figure 5.4. Closeup maps of (a) the west gravity line occupied annually from 2008-2012, and (b) the east gravity line occupied annually from 2007-2012. The background image is vertical deformation from 2005-2007 as recorded by InSAR [*Chang et al.*, 2007].

Precision Gravity Measurements 2007-2011

Results for annual changes in gravity from 2007-2011 can be seen in Figure 5.5 for the east line (Canyon Junction to Sylvan Lake) and Figure 5.6 for the west line (Madison Junction to Lewis Falls). Although data from 2012 were collected, these have not been processed at the time of this writing. In past surveys, station 11 mdc has been held constant as a base-station and all gravity change values have been relative to it. However, it is clear in Figure 5.4b that 11 mdc is clearly within the area of deformation, based on the InSAR data from 2005-2007, and is stable over time. In contrast, station k12 (Sylvan Lake) is well beyond the influence of the caldera deformation. Therefore, we have determined that k12 will be held fixed and all our data are relative to station k12. We have modified the past data to be relative to k12 as well.

After much effort on these surveys, it is evident in a qualitative sense that there is no consistent pattern of relative annual changes in gravity over the period 2007-2011 for either the east or west lines (Figures 5.5 and 5.6). The largest change in gravity for the east line is a decrease of -0.272 mgals that occurs between 2010-2011and is centered on the Sour Creek resurgent dome. The west line also shows the largest gravity change between 2010-2011, however, it is an increase of 0.312 mgals near the Mallard Lake resurgent dome.

Evaluating the changes in gravity at individual stations shows more coherence across the network (Figure 5.7). In Figure 5.7, blue indicates a positive relative gravity change and red indicates a negative relative gravity change. From 1993-2007, there was very little change in the gravity field in the eastern caldera, even though there was ~10 cm of net uplift (Figure 1.6) in the area over that time span. The majority of the west line

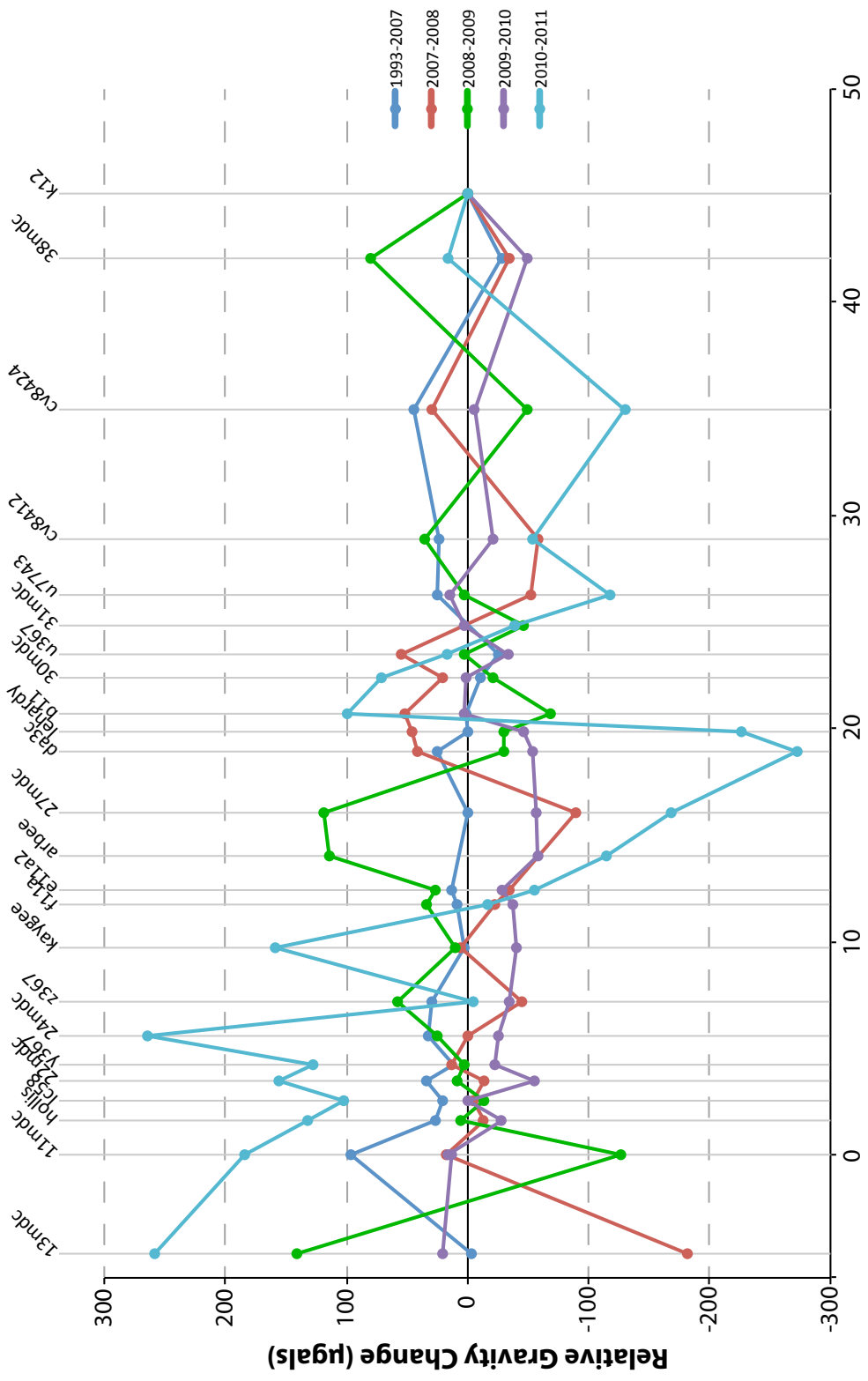

Figure 5.5. Relative gravity changes along the east line from 1993-2007 (dark blue), 2007-2008 (red), 2008-2009 (green), 2009-2010 (purple), and 2010-2011 (light blue). The corresponding station name is labeled along the top.

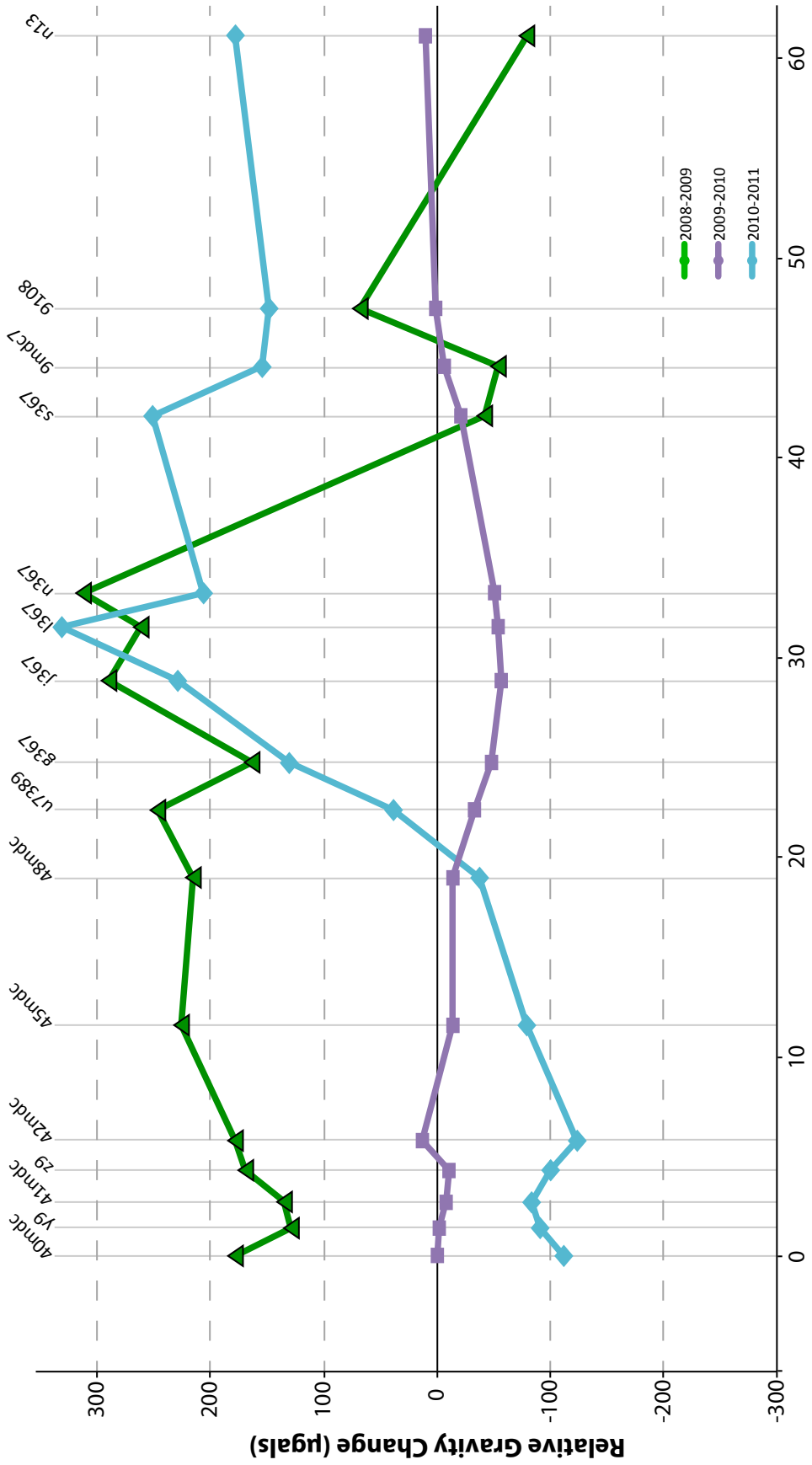

Figure 5.6. Relative gravity changes along the west line from 2008-2009 (green), 2009-2010 (purple), and 2010-2011 (light blue). The corresponding station name is labeled along the top.

Figure 5.7. Gravity change values for each station through time from 2007-2011 for (a) the east line, and (b) the west line. Red is a negative change and blue is a positive change. Changes in river gage height are shown at the top for the (a) Yellowstone River and (b) the Firehole River.

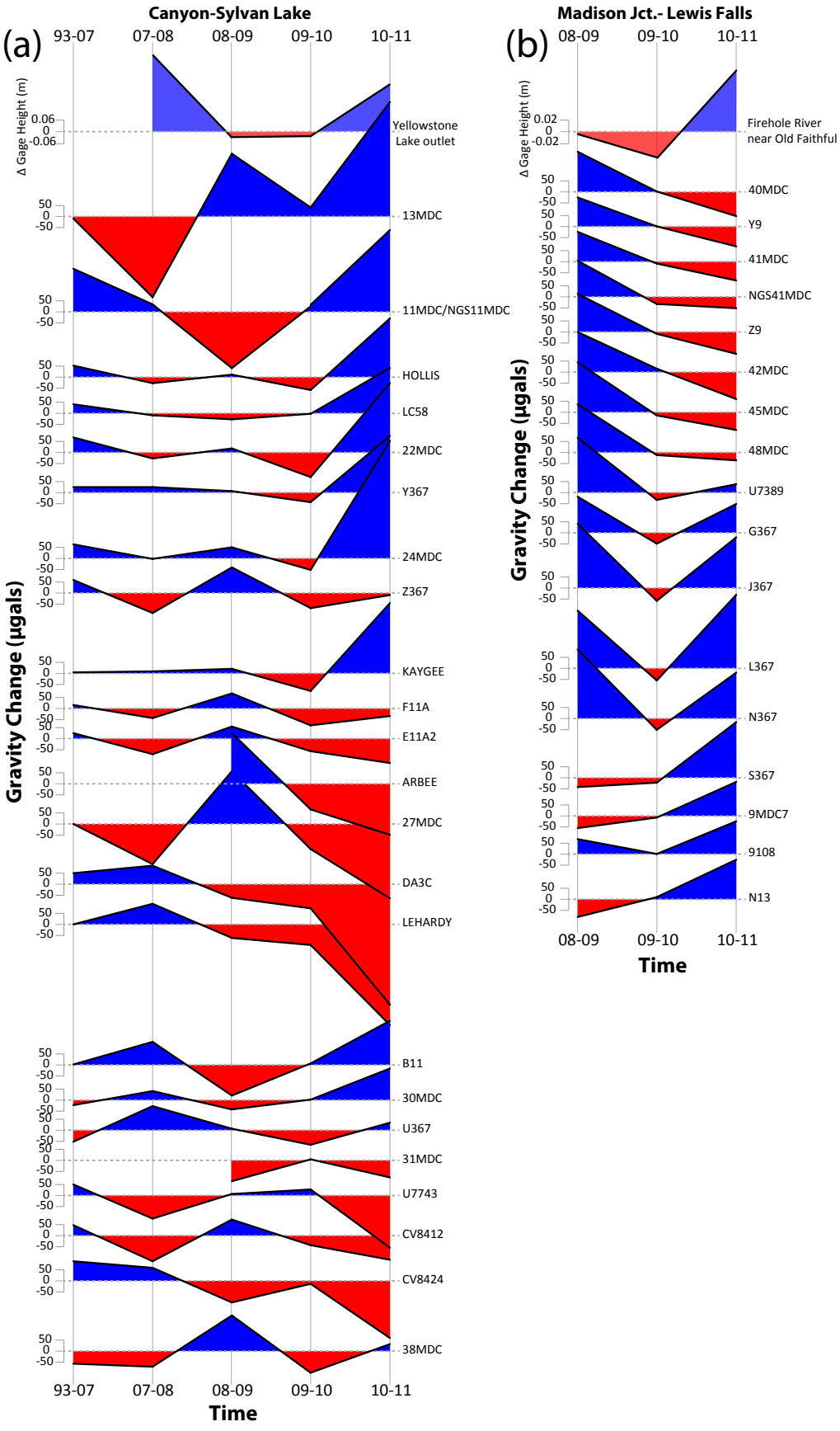
(a)
Canyon-Sylvan Lake
93-07
07-08
08-09
09-10
10-11
Δ Gage Height (m)
0.06
0
-0.06
Yellowstone Lake outlet
13MDC
11MDC/NGS11MDC
HOLLIS
LC58
22MDC
Y367
24MDC
Z367
KAYGEE
F11A
E11A2
ARBEE
27MDC
DA3C
LEHARDY
B11
30MDC
U367
31MDC
U7743
CV8412
CV8424
38MDC
50
0
-50
Gravity Change (µgals)
Time
(b)
Madison Jct.- Lewis Falls
08-09
09-10
10-11
Δ Gage Height (m)
0.02
0
-0.02
Firehole River near Old Faithful
40MDC
Y9
41MDC
NGS41MDC
Z9
42MDC
45MDC
48MDC
U7389
G367
J367
L367
N367
S367
9MDC7
9108
N13
Gravity Change (µgals)
Time

shows increases in gravity between 2008-2009 and little change between 2009-2010 (Figure 5.7). Between 2010 and 2011, the west line shows a gravity decrease in the northern half of the line but a gravity increase in the southern half (Figures 5.6 and 5.7).

As stated above, we always took our measurements at the same time of year in order to minimize the effect of changes in the water table. There are no monitored water wells in Yellowstone so our only measurement of the change in the amount of water is a few river gage height monitors. We use one on the Yellowstone River at the outlet of Yellowstone Lake for the east line, and one on the Firehole River, near Old Faithful, for the west line. The changes in gage height for these two rivers are shown at the top of Figure 5.7. Between 2007 and 2008, the Yellowstone River had an increase in gage height of ~0.2 m. It stayed at that same level in 2009 and 2010, but again showed an increase in gage height of ~0.12 m. The Firehole River stayed at the same height between 2008 and 2009, dropped 0.02 m in 2010, and rose 0.05 m in 2011. Given the fact that the majority of our gravity stations are along the roadways, immediately adjacent to these rivers, it can be assumed that these changes in the amount of water are affecting the measurements.

Gravity change values were corrected for height changes using InSAR data. However, there have not been any InSAR images for Yellowstone since 2010. There is sparse campaign GPS data (including some colocated with our gravity benchmarks) for these years but, in general, there is not good control on the height changes after 2010.

Conclusions

Qualitative results show that there is little correlation between the accelerated uplift of the Yellowstone caldera from 2004-2010 and relative changes in gravity for the same time period. This could point to the assumption that the uplift is caused solely by pressurization of the deep hydrothermal system without a mass change. However, analysis of GPS and InSAR data by *Chang et al.* [2007, 2010] show that the most likely source of the uplift is an expanding volcanic sill at the top of the magma reservoir indicating a magmatic source for the accelerated uplift.

These data will be valuable for long-term studies of the changes in the gravity field in and around the Yellowstone volcanic system [e.g., *DeNosaquo et al*., 2009] and are complimentary to other types of data being collected such as deformation using GPS and the seismic velocity structure of the system via tomographic inversions.

References

Arnet, F. (1996), Crustal deformation of the Yellowstone volcanic field from precise measurements of temporal gravity changes and supplementary leveling and GPS data. PhD thesis. ETH Zurich, No.11388, 125 pp.

Arnet, F., H. G. Kahle, E. Klingele, R. B. Smith, C. M. Meertens, and D. Dzurisin (1997), Temporal gravity and height changes of the Yellowstone caldera, 1977-1994, *Geophys. Res. Lett.*, *24*, no. 22, 2741-2744.

Chang, W. L., R. B. Smith, C. Wicks, J. Farrell, and C. M. Puskas (2007), Accelerated uplift and magma intrusion of the Yellowstone caldera, 2004-2006, *Science, 318*, no. 5852, 952-956, doi:.1126/science.1146842.

Chang, W. -L., R. B. Smith, J. Farrell, and C. M. Puskas (2010), An extraordinary episode of Yellowstone caldera uplift, 2004-2010, from GPS and InSAR observations, *Geophys. Res. Lett.*, *37*, L23302, doi:10.1029/2010GL045451.

DeNosaquo, K., R. B. Smith, and A. R. Lowry, 2009. Density and lithospheric strength models of the Yellowstone-Snake River Plain volcanic system from gravity and heat flow data, *J. Volcanol. Geotherm. Res*., *188*, 108-127.

Evoy, J. A. (1978), Precision gravity and simultaneous inversion of gravity and seismic data for subsurface structure of Yellowsone: M. S. thesis, University of Utah, Salt Lake City.

Gettings, P., D. S. Chapman, and R. Allis (2008), Techniques, analysis, and noise in a Salt Lake Valley 4D gravity experiment, *Geophysics*, *73*, no. 6, WA71-WA82.

Hollis, J. R., E. E. Klingfele, C. S. Schlinger, and R. B. Smith (1987), Precision gravity reobservations of crustal deformation in the Yellowstone caldera, *Eos*, *Trans. Am. Geophy. Union*, *68*, 1452.

Smith, R. B., J. R. Pelton, and J. A. Evoy (1978), Uplift and its relationship to mass deficiency at Yellowstone, *Am. Geophys. Union*, *Eos*, *59*, no. 12, 1189.

CHAPTER 6

CRUSTAL VELOCITY STRUCTURE OF THE YELLOWSTONE VOLCANIC SYSTEM FROM AUTOMATED WAVEFORM ANALYSIS AND LOCAL EARTHQUAKE TOMOGRAPHY

Abstract

With progress in seismic tomographic imaging algorithms, increasing earthquake data availability by expanded and upgraded seismic networks and increasing computing power, it is possible to use large earthquake travel-time datasets recorded for local and regional earthquakes to invert for much more detailed and accurate crustal velocity structure than ever before [*Lees*, 2007]. However, using large datasets, in particular using data over long time periods introduces the problem of inconsistent seismic waveform picking errors over time. To remedy this, automated repicking of P-phases must be performed on large sets of earthquake data to obtain arrival-time data appropriate for high-resolution seismic tomography.

Past tomographic studies of the Yellowstone magma system have revealed a notable, low P-wave crustal anomaly beneath the 0.64 Ma caldera that has been interpreted to be the shallow crustal magma reservoir that provides the energy for Yellowstone's youthful volcanic and hydrothermal systems. Until recently however,

limited seismometer coverage did not allow us to adequately resolve changes in seismic velocity northeast of the caldera, where recent gravity measurements reveal a mid- to upper-crustal, low density body that extends ~20 km north of the caldera. In addition, systematic upgrades and expansion of the Yellowstone Seismic Network (YSN), including the addition of nine 3-component and broadband seismic stations provide much broader and better ray coverage of the entire Yellowstone volcanic field with greater bandwidth data. This allows us to produce much-expanded and improved resolution images of the Yellowstone crustal velocity structure.

We have compiled all the digital seismic waveforms for the Yellowstone region earthquake catalog with over 45,643 earthquakes and 1,159,724 waveforms from 1984-2011 to analyze P-wave arrival times with an automatic picker based on an adaptive high-fidelity human mimicking algorithm. The automatic picker is calibrated using a reference dataset of 171 events that are manually picked based on strict criteria. The MPX software was used for automated repicking of P-waves and provided the final dataset consisting of more than 14,000 consistently picked first arriving P-phases with an average picking error of ~0.18 s after only using well-located earthquakes with at least 8 observations of weight zero or one and a gap of less than 180º. The resulting three-dimensional P-wave model reveals a low Vp body (up to -7% Vp) that is interpreted to be the Yellowstone magma reservoir and is ~50% larger than previously imaged and extends ~ 20 km NE of the 0.64 Ma caldera consistent with previous models based on the large gravity anomaly of the Yellowstone caldera.

Introduction

Important progress has been made in local earthquake tomographic inversion schemes and algorithms as well as improved computing power. These improvements make it possible to employ local earthquake tomography inversion algorithms on much larger datasets than before. Our goal is to use local earthquake tomography (LET) to image the P-wave crustal velocity structure for the Yellowstone volcanic system using data from the Yellowstone Seismic Network (YSN) from 1984 – 2011. Since the data spans seismic coverage of over 25 years, many different seismic analysts have routinely picked the data to locate events introducing a problem of inconsistent picking errors over time. To remedy this, repicking of P-phases must be performed to obtain uniform arrival-time data appropriate for high-resolution seismic tomography.

The Yellowstone volcanic system is one of the largest silicic caldera volcanic systems in the world [*Smith and Seigel*, 2000; *Christiansen*, 2001] and has experienced three major super-volcanic eruptions in the last 2.1 million years. The most recent caldera forming eruption occurred 0.64 Ma forming what is known as the Yellowstone caldera [*Christiansen*, 2001] (Figure 1.5). Since the 0.64 Ma eruption, more than 30 smaller rhyolite flows have erupted and partially filled in the caldera, the youngest being 70,000 years old [*Christiansen*, 2001]. Moreover, the extraordinarily high heat flow values averaging 2,000 mWm^{-2} over the caldera and exceeding 30,000 mWm^{-2} in northern Yellowstone Lake, [*Smith and Blackwell*, 2000; *David Blackwell* personal communication, 2005] more than 10,000 hydrothermal features, intense seismicity, and decadal-scale crustal uplift and subsidence reflects the active tectonic-magmatic nature of Yellowstone [*Smith et al.*, 2009].

There have been over 40,000 earthquakes recorded in Yellowstone since 1972 (Figure 1.4) with magnitudes ranging from $-1.4 \leq M_C \leq 6.1$. Approximately 40% of these earthquakes occur as part of earthquake swarms [*Farrell et al*., 2009]. The majority of Yellowstone earthquakes occur in an E-W band of seismicity that extends from the Hebgen Lake, Montana region, west of Yellowstone National Park, to the Norris Geyser Basin area on the northern boundary of the Yellowstone caldera (Figure 1.4). Since 1995, the Yellowstone area has averaged ~1,600 earthquakes per year with magnitudes from $-1.4 \leq M_C \leq 4.5$. The majority of earthquakes in the Yellowstone caldera are less than 5 km deep [*Farrell et al*., 2009; *Smith et al.*, 2009]. The shallow nature of the maximum focal depths is attributed to high temperatures encountered at shallow depths defining the brittle-ductile transition at ~400°C associated with the caldera magma reservoir [*Smith et al.*, 2009]. Maximum depths of hypocenters deepen from 5 km in the caldera to >15 km south and north of the caldera.

There has been a seismic monitoring system in place at Yellowstone since 1972. In 1984, the University of Utah Seismograph Stations (UUSS) took over the YSN and has constantly upgraded the network to make it one of the most modern, robust digital seismic networks in the U.S. (Figure 6.1).

Leveling and GPS crustal deformation data show decadal-scale patterns of the Yellowstone caldera (Figure 1.6) with rates up to 7 cm/yr of uplift [*Chang et al.*, 2010; *Chang et al., 2007*; *Puskas et al.*, 2007]. Large earthquake swarms recorded in Yellowstone tend to occur during times of deformation reversal from uplift to subsidence and have been attributed to the movement of magmatically-derived fluids in the crust as described earlier in Chapter 3 [*Farrell et al.*, 2010; *Massin et al.*, 2013; *Waite et al.*,

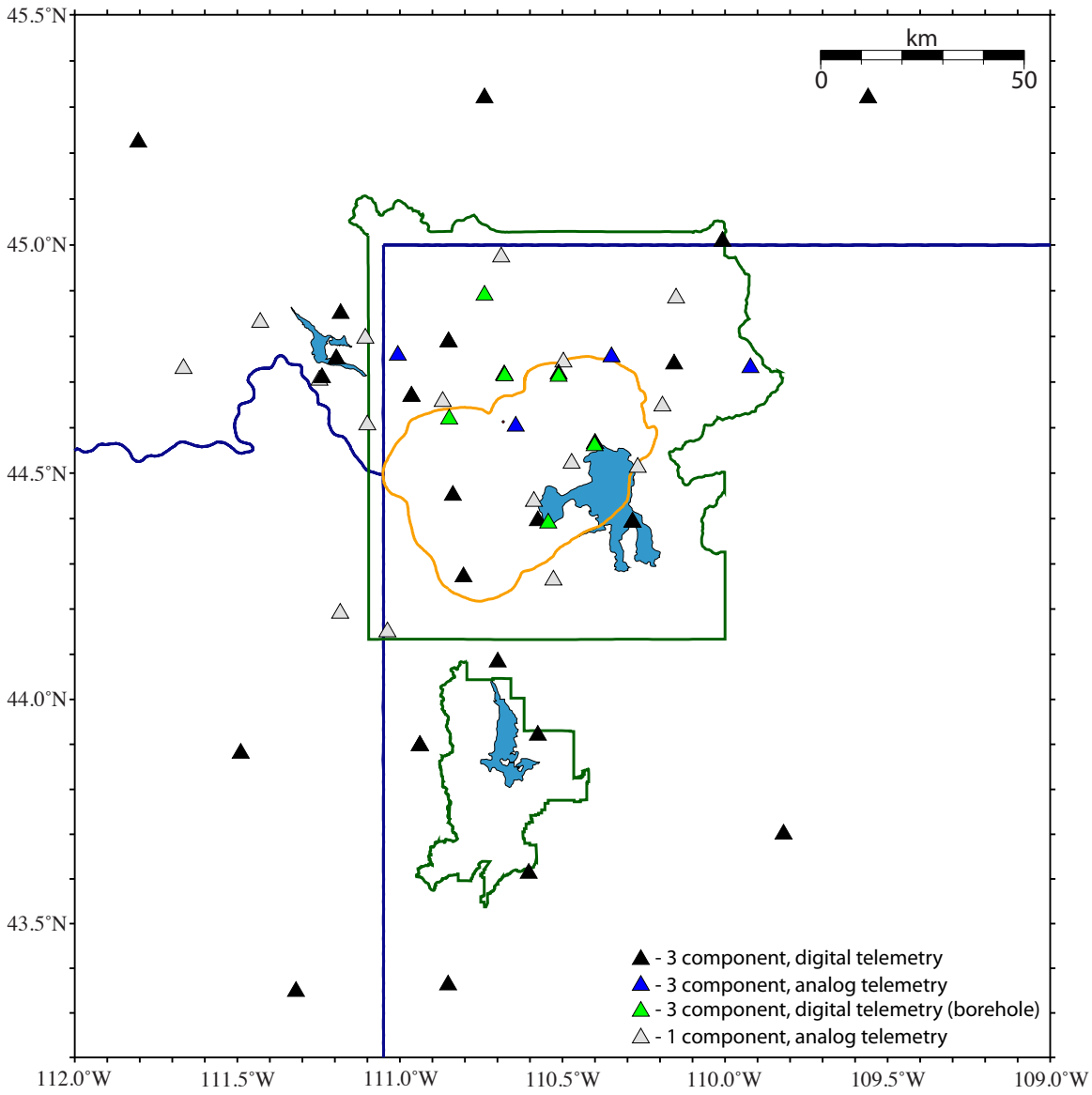

Figure 6.1. Seismograph station map of the Yellowstone region. Black triangles 3-component broadband stations. Blue triangles represent 3-component short-period stations. Green triangles represent 3-component borehole seismometers. Gray triangles represent single-component vertical short-period seismometers.

2002].

The Yellowstone crustal magma reservoir provides the energy for the more than 10,000 hydrothermal features, the high rate of earthquake activity, the decadal-scale deformation, and the high heatflow. It is essential that we understand not only the size of the magma reservoir, but also understand the composition and the percent melt that is available for the next eruption.

Method and Data

Several studies have progressively imaged the Yellowstone crustal structure using controlled source [*Schilly et al.*, 1982; *Smith et al.*, 1982; *Lehman et al.*, 1982] and local earthquake tomographic (LET) techniques [*Benz and Smith*, 1984; *Miller and Smith*, 1999; *Husen et al.*, 2004].

The first studies to find evidence of a low P-wave body beneath the Yellowstone caldera used controlled source data from eleven in-line refraction profiles, recorded with a 150-station array during the 1978 Yellowstone-Snake River Plain seismic experiment [*Schilly et al.*, 1982; *Smith et al.*, 1982; *Lehman et al.*, 1982]. *Schilly et al.* [1982] found evidence for a major low-velocity body with a decrease in velocity of at least 10%, coincident with a -30-mgal gravity low in the northeast part of the Yellowstone Plateau, with a maximum depth to the top of the body of 3 km and a minimum depth of 9 km to the bottom. Importantly, using a fan profile of stations and a source shot in the northeast corner of Yellowstone, *Schilly et al*. [1982] observed large first arrival delays (up to 1.5 s) for stations that were recording raypaths that passed through the NE caldera region (Figure 1.7).

A study by *Lehman et al.* [1982], using 173 raypaths, also found low P-wave velocities beneath the caldera with modeled Vp as low as 4.0 km/s beneath the NE caldera region that is interpreted to represent a zone of high temperature associated with a partial melt and/or large steam-water volumes near the Hot Spring Basin (Figure 1.8).

These early controlled source experiments and the first evidence of a body of low P-wave velocities beneath the caldera paved the way for later LET studies that were able to image an extended body of low P-wave velocity of around -5% to -10% Vp at depths of 6-16 km, which is interpreted to be crystallizing magma beneath the Yellowstone caldera. *Benz and Smith* [1984], using 422 raypaths, showed two zones of unusually low velocities (Figure 1.9). In the northeast, velocities are as low as 4.9 km/s and are interpreted as evidence for a possible vapor-dominated body or shallow melt. In the southwest caldera, *Benz and Smith* [1984] find velocities as low as 5.2 km/s and are interpreted as a thermally influenced fracture system.

A later LET study of the Yellowstone volcanic system by *Miller and Smith* [1999] used a combination of 7,942 local earthquakes and 16 controlled-source explosions and found a caldera-wide 15% decrease from regional P-velocities at depths of 6 to 12 km that are coincident with a -60 mGal gravity anomaly. In addition, they found a smaller but more pronounced low velocity zone underlies the northeast caldera rim from depths less than 2 km to greater than 4 km. P-velocities in this zone are as low as 3.4 km/s at 4 km depth, a 37% reduction from the starting P-velocity of 5.4 km/s and are explained by the presence of a fractured fluid (gas or gas/liquid) saturated, and possibly hydrothermally altered volume of rock [*Miller and Smith*, 1999].

The most recent LET study, prior to this study, of the Yellowstone volcanic

system used 3,374 earthquakes, including 34,538 P-arrival times and 5,875 S-P arrival times. They state that ray coverage of P-wave arrivals is dense to the northwest of the Yellowstone caldera and within the northern part of the Yellowstone caldera; lack of seismicity and sparser station distribution yield poor ray coverage in the southern and eastern part of the Yellowstone caldera [*Husen et al.*, 2004]. Nonetheless, results confirmed the existence of a low V_P-body (-6% relative to the initial one-dimensional model) beneath the Yellowstone caldera at depths greater than 8 km, possibly representing hot, crystallizing magma [*Husen et al.*, 2004] (Figure 6.2). In addition, they found a volume of anomalously low V_P (-10% relative to the initial one-dimensional model) and V_P/V_S in the northwestern part of the Yellowstone volcanic field on the NW caldera boundary at shallow depths < 2.0 km. Theoretical calculations of changes in P- to S-wave velocity ratios indicate that this anomaly can be interpreted as porous, gas-filled rock [*Husen et al.*, 2004] (Figure 6.2).

These studies use limited data from the University of Utah Seismograph Stations (UUSS) due to limited time periods or limited station coverage. Using the entire database of Yellowstone earthquakes (1984-2011) would provide better coverage due to more earthquakes and also due to the ability to use newer stations that have been installed in the NE caldera region. Using the entire dataset, from 1984 – 2011, as well as using newer stations, allows us to get better ray coverage increasing our resolution and expanding the area in which we are able to resolve crustal structures.

There has been significant effort by the University of Utah to expand geographic coverage of new seismograph stations in the Yellowstone region NE of the caldera in order to obtain much better ray coverage in that area. Three new 3-component

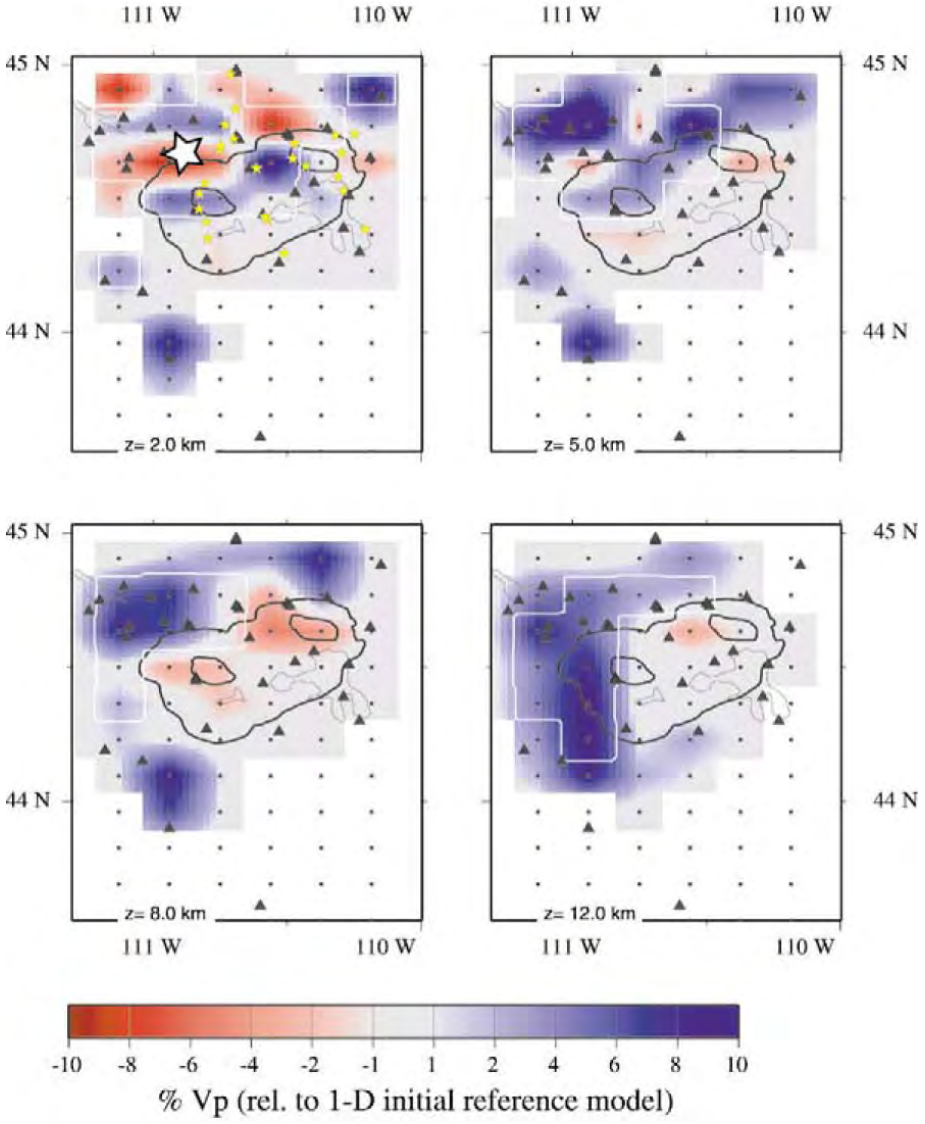

Figure 6.2. Tomographic results of three-dimensional Vp model of *Husen et al.* [2004]. Results are in horizontal cross sections at different depths as indicated. Vp velocity structure is shown as percentage change relative to one-dimensional initial reference model. Areas with no ray coverage are masked. Black triangles mark stations used in the inversion. White lines contour areas of RDE>0.05; black lines outline 0.64-Ma caldera boundary and location of resurgent domes.

seismograph stations have been added NE of the caldera since 2002 and are included in our analysis, including stations located at Parker Peak (YPK), Mirror Plateau (YMP), and a station at the Northeast Entrance (YNE).

Our goal is to use data from the entire Yellowstone digital waveform database (1984-2011) (Figure 6.3) to image the Yellowstone velocity structure and to improve resolution, particularly in the NE caldera. In order to use these data from such a large time period, repicking of P-phases must be performed to obtain arrival-time data with consistent error uncertainties throughout time. Considering the amount of data necessary for regional high-resolution tomography, algorithms combining accurate picking with an automated error assessment are required. Recently, *Aldersons* [2004] developed an automated picking software package, MPX, which integrates the robust Baer-Kradolfer picker [*Baer and Kradolfer*, 1987] with a pattern recognition technique to estimate the uncertainty of the arrival time. This method has successfully been applied to seismic data from the varied seismograph networks in the Alpine Region of Europe [*Diehl et al.*, 2009a; *Diehl et al.*, 2009b].

We follow the method of *Diehl et al.* [2009a] where we derive a reference dataset consisting of a limited number of manually, consistently picked P-phase arrival times. The reference dataset is used to calibrate and test the performance of MPX. Subsequently, the calibrated MPX is applied to the complete Yellowstone local earthquake dataset in "production-mode." The final P-phase dataset consists of more than 14,000 high-quality first arrivals from 4,520 well-located earthquakes in the Yellowstone region, which is used to invert simultaneously for hypocenter locations and three-dimensional P-wave velocity structure using the computer code simulps14

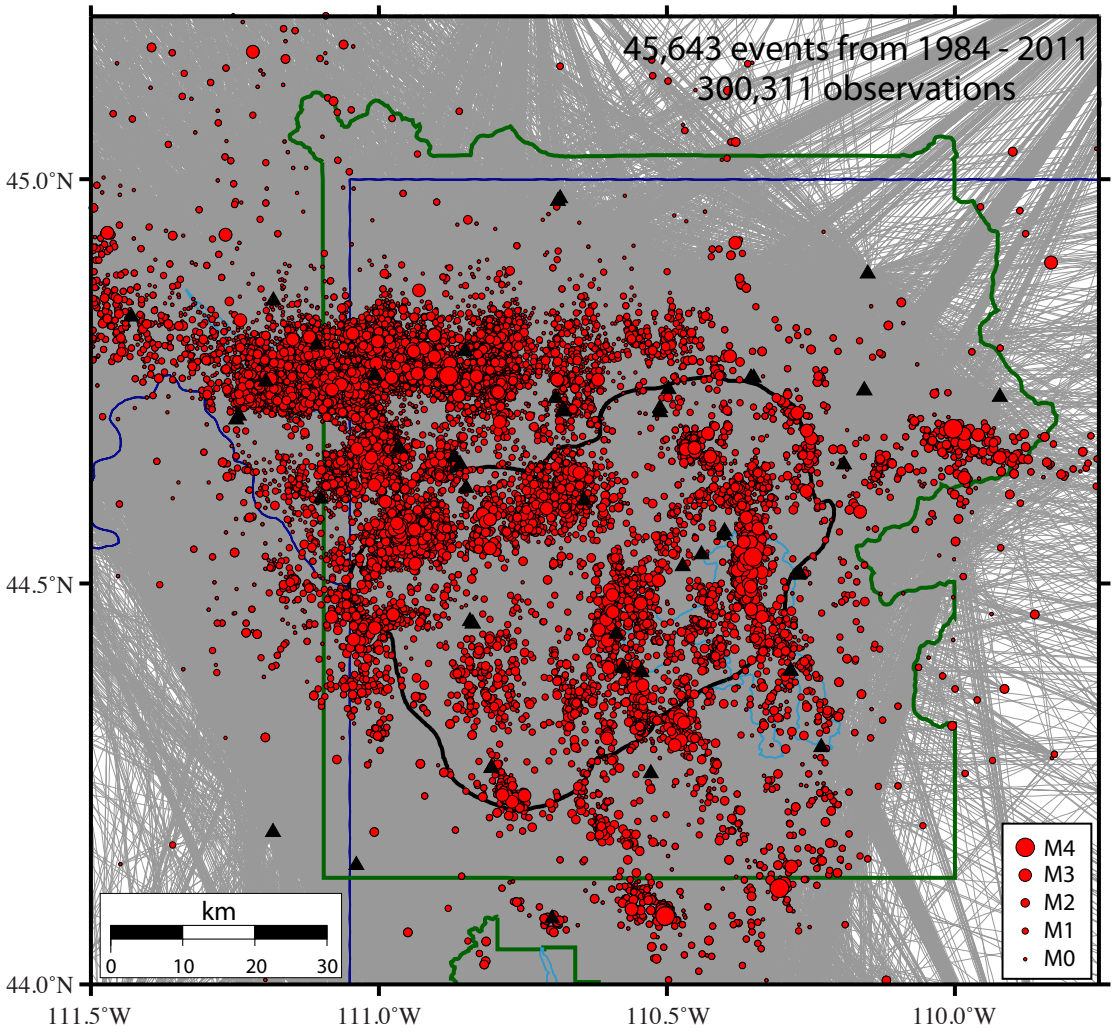

Figure 6.3. All earthquakes in the UUSS Yellowstone earthquake database located using a one-dimensional velocity model from 1984-2011 (red circles). Gray lines are ray paths connecting picked stations to epicenters. Green lines are the boundaries of Yellowstone and Grand Teton National Parks. Solid Black line outlines the 0.64 Ma Yellowstone caldera. Black triangles are seismograph stations.

[*Thurber*, 1983; *Eberhart-Phillips*, 1990; *Haslinger and Kissling*, 2001].

The mathematics of the inversion in simulps14 as described by *Thurber* [1983] are as follows: The linearized equation for simultaneous inversion relating the arrival time residual *r* to model parameter changes can be written as

$$r = \Delta t_e + \frac{\partial t}{\partial x_e}\Delta x_e + \frac{\partial t}{\partial y_e}\Delta y_e + \frac{\partial t}{\partial z_e}\Delta z_e + \sum_{n=1}^{N}\frac{\partial t}{\partial v_n}\Delta v_n \qquad (6.1)$$

where Δt_e, Δx_e, Δy_e, Δz_e, and Δv_n are perturbations to the hypocentral parameters (earthquake origin time and location) and the velocity parameters and $\partial t/\partial x_e$, $\partial t/\partial y_e$, $\partial t/\partial z_e$, and $\partial t/\partial v_n$ are partial derivatives of the arrival time with respect to the earthquake coordinates and velocity parameters, respectively (*N* is the total number of velocity parameters). There is one such equation for each observed arrival.

Each earthquake yields a set of equations (let us say *L* of them) like (1), which we write in matrix notation as

$$\underset{L\,x\,1}{\mathbf{r_i}} = \underset{L\,x\,4}{\mathbf{H_i}}\ \underset{4\,x\,1}{\mathbf{\Delta h_i}} + \underset{L\,x\,N}{\mathbf{M_i}}\ \underset{N\,x\,1}{\mathbf{\Delta m}} \qquad (6.2)$$

where $\mathbf{r_i}$ and $\mathbf{\Delta h_i}$ are vectors containing the *L* residuals and the four (unknown) hypocentral parameter adjustments for the *ith* event, $\mathbf{H_i}$, and $\mathbf{M_i}$ are the matrices of hypocentral and velocity partial derivatives for the *ith* event, and $\mathbf{\Delta m}$ is the vector of *N* velocity parameter adjustments. In a manner analogous to the parameter separation method described by *Pavlis and Booker* [1980], a matrix $\mathbf{Q_O}$ is constructed which has the property

$$\underset{(L-4)\text{ x }L}{\boldsymbol{Q_o^T}} \quad \underset{L\text{ x }4}{\boldsymbol{H_i}} \quad = \quad 0 \tag{6.3}$$

so that operating on (6.2) by $\boldsymbol{Q_o^T}$ results in

$$\underset{(L-4)\text{ x }1}{\boldsymbol{r'_i}} \quad = \quad \underset{(L-4)\text{ x }N}{\boldsymbol{M'_i}} \quad \underset{N\text{ x }1}{\boldsymbol{\Delta m}} \tag{6.4}$$

Consider the matrix $\boldsymbol{M'}$ composed of the set of submatrices $\boldsymbol{M'_i}$ and the vector $\boldsymbol{r'}$ composed of the set of subvectors $\boldsymbol{r'_i}$. As more earthquake data are added, $\boldsymbol{M'}$ and $\boldsymbol{r'}$ continually grow in size, leading to difficulties with computer storage. To circumvent this problem, the matrix $\mathbf{M'^T}\,\mathbf{M'}$ and vector $\mathbf{M'^T}\,\mathbf{r'}$ are accumulated sequentially as each event is processed, producing a symmetric matrix and a vector of fixed size:

$$\begin{aligned} \mathbf{M'^T M'} &= \sum_i \mathbf{M'_i M'_i} \\ \mathbf{M'^T r'} &= \sum_i \mathbf{M'_i}\,\mathbf{r'_i} \end{aligned} \tag{6.5}$$

The normal equations

$$\underset{N\text{ x }N}{(\mathbf{M'^T M'})} \quad \underset{N\text{ x }1}{\mathbf{\Delta m}} \quad = \quad \underset{N\text{ x }1}{(\mathbf{M'^T r'})} \tag{6.6}$$

are then solved using damped least squares, and the resolution and covariance matrices are computed [see *Crosson*, 1976; *Aki and Lee*, 1976]. Finally, the velocity parameter changes are applied to the model, the earthquakes are individually relocated (iteratively) in the new model, and the simultaneous inversion is repeated. The F test [*DeGroot*, 1975] is used to select a stopping point for the iterative procedure.

Reference Dataset

In order to calibrate the automatic picking program, a manually picked reference set must be selected. For this purpose, I selected a set of 171 earthquakes as our reference set (Figure 6.4). These earthquakes were chosen to represent a range of locations, depths, and magnitudes in order to try and represent all types of waveforms that the automatic picker will encounter. The reference dataset was hand picked based on the method of *Diehl et al*. [2009a] (Figure 6.5) where it is assumed the onset of a seismic phase is a probabilistic function $P_a(t)$. The arrival time is expressed as the "most likely" time t_A, with $P_a(t_A) = Max(P_a)$. The "earliest" possible time for the phase onset is defined at tE, where the likelihood for onset is approaching zero ($P_a(t_E) \geq 0$). The "latest" possible time for the phase onset t_L, is defined as $P_a(t_L) \geq 0$.

Figure 6.5 illustrates the concept in detail. The thick grey band between position "1" and "2" defines the time window that definitely includes the onset of the wave, while position "1" is certainly too early to be picked as t_E and "2" is too late as t_L. The band outlined by two broken lines denotes the possible threshold of the noise amplitude defined as 1.5 times the noise level [*Diehl et al.*, 2009a]. We pick the arrival of the phase at the most likely position, t_A, midway between t_E and t_L. Also, a quantitative weighting scheme has to be defined where the assigned discrete weighting classes depend only on measured time error intervals (t_L-t_E).

Another important aspect of picking the reference dataset is the correct identification of the phase as a misinterpretation can result in significantly large errors. To make sure that phases are correctly identified, velocity reduced phase picks of selected earthquakes are inspected. We are only interested in picking the first arriving

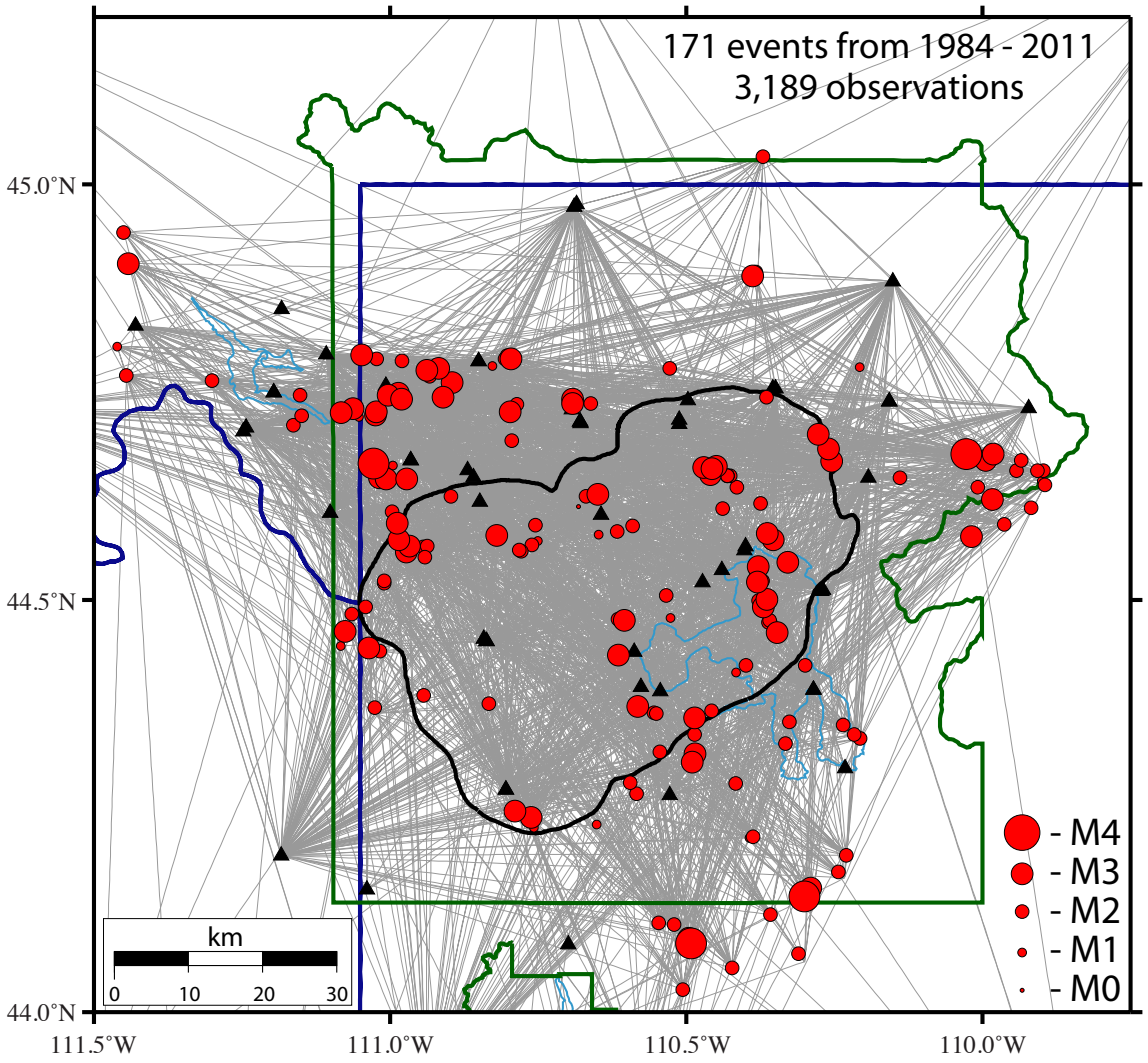

Figure 6.4. Earthquakes of the reference data set (red circles). Gray lines represent raypaths connecting picked stations (black triangles) and epicenter locations. Green lines represent boundaries of Yellowstone and Grand Teton National Parks. Black line outlines the 0.64 Ma Yellowstone caldera.

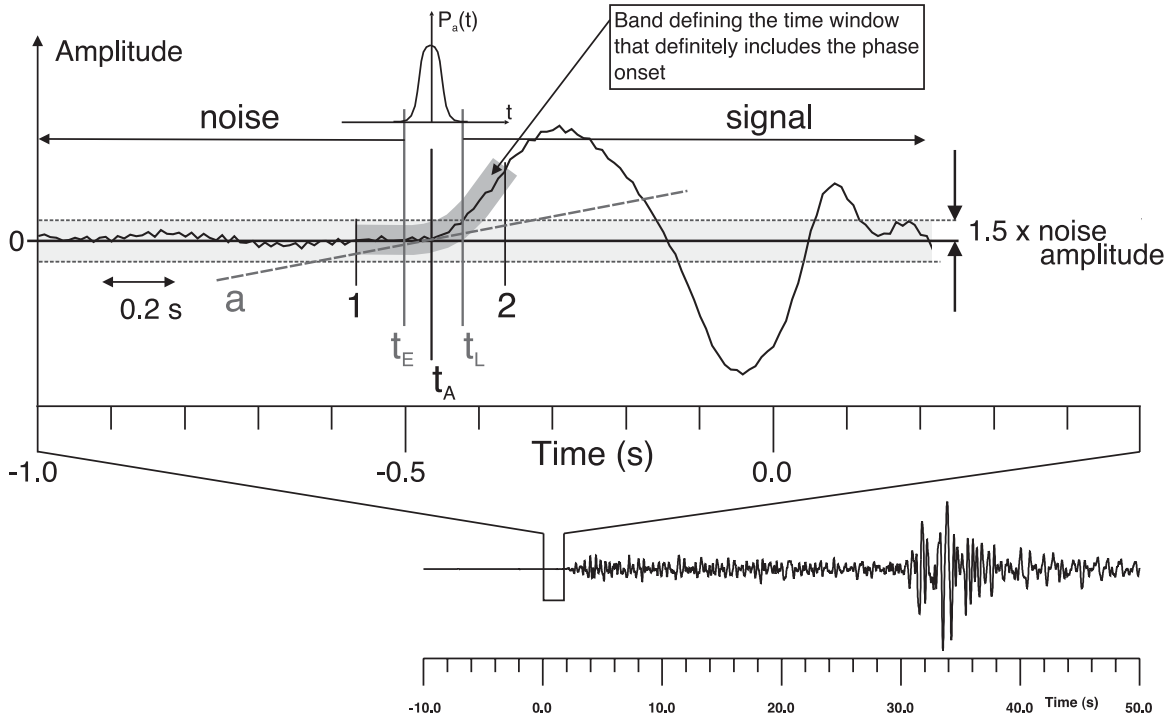

Figure 6.5. Probabilistic phase picking approach: the "earliest" possible pick corresponds to *tE*, the "latest" possible pick corresponds to *tL*. The most likely arrival time, *tA*, is located within this interval. Primarily amplitude is used for the determination of *tE* and *tL*. See text for further details. Modified from *Diehl et al.* [2009a].

phase so we look for Pg (direct ray), Pn (Moho-refracted ray), and P1 (unknown type, but certainly first arrival). Furthermore, we break up Pg arrivals into two subcategories: Pt (tectonic direct wave) and Pv (volcanic direct wave). Figure 6.6 shows an example of velocity reduced phase picks for an event in our reference dataset. The cross over point (where the first arriving phase switches from Pg to Pn) for this example occurs at around 90 km (Figure 6.6). Arrivals that deviate from the general fit can be double checked for either a phase misinterpretation, or timing issues with the station.

Additional sources of uncertainty in the picking process can be attributed to inconsistency in the picking process itself. Examples of this are random choices of window size and amplitude scaling [*Douglas et al*., 1997] during picking and inconsistent usage of filters and misinterpretation of artifacts caused by the filtering process. To minimize these errors, we prefiltered all our waveform data. For short-period analog data, we used a low-pass 10 Hz filter to filter out the relative high noise signals. For broadband digital data, we used a high-pass 0.5 Hz filter to remove the microseism. In addition, for the determination of manual P-onsets, the Matlab-GUI picking tool "PILOT" was used [*Brustle et al*., 2013] because of its use of predefined window lengths for picking and uniform amplification of amplitudes.

In total, 171 reference events were accurately hand picked for a total of 3,189 P-wave first arrival picks. The weighting scheme for the manual picking analysis is shown in Table 6.1 and Figure 6.7.

These first arrival P-wave data were then used to calculate a new minimum one-dimensional velocity model using the algorithm VELEST [*Kissling et al.,* 1995] (Figure 6.8). The minimum one-dimensional velocity model is derived in an iterative inversion

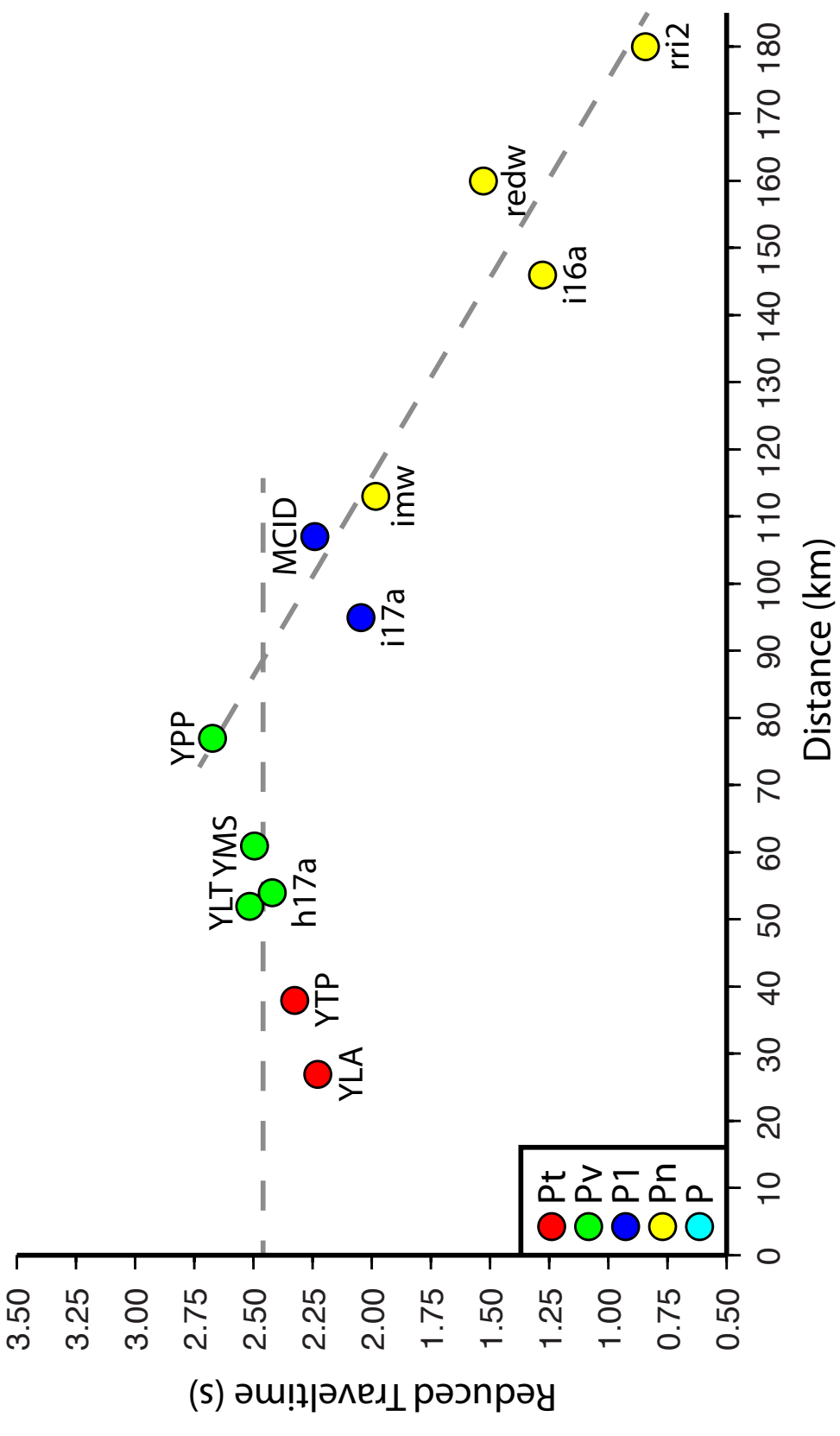

Figure 6.6. Reduced travel time vs. distance for a selected reference event. Red circles represent tectonic direct P-wave. Green circles represent volcanic direct P-waves. Blue circles represent first arriving P-waves where the type is unknown. Yellow circles represent Moho refracted P-waves.

Table 6.1. Error assessment used for reference P-phase picking and number of P-picks for each quality class derived from 171 reference events.

P-Quality Class	Error (s)	# Observations
0	± 0.06	1330
1	± 0.12	1039
2	± 0.24	470
3	± 0.48	311
4	> 0.48	110

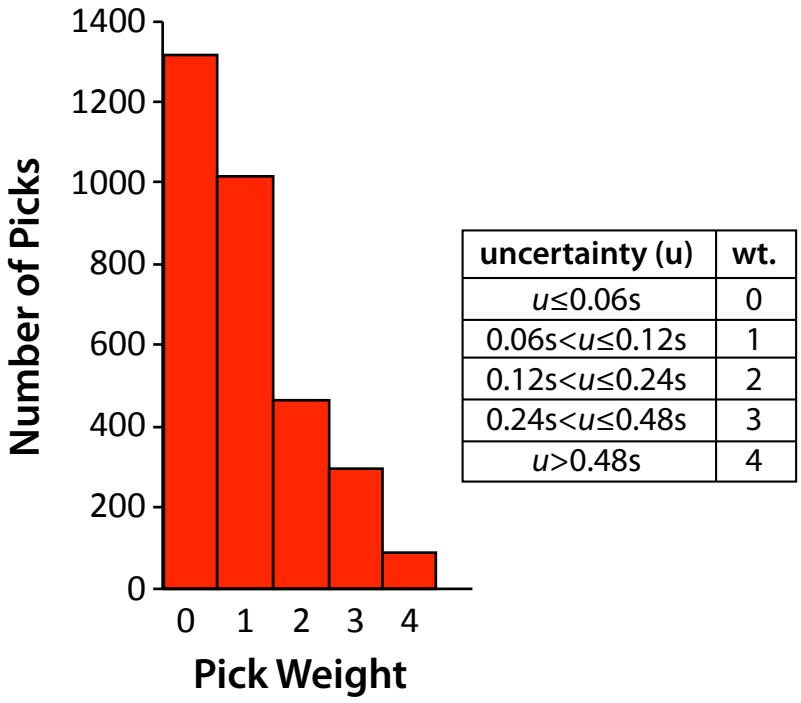

Figure 6.7. Histogram showing the distribution of P-phase pick weights for the 171 reference events and the corresponding uncertainties associated with each weight.

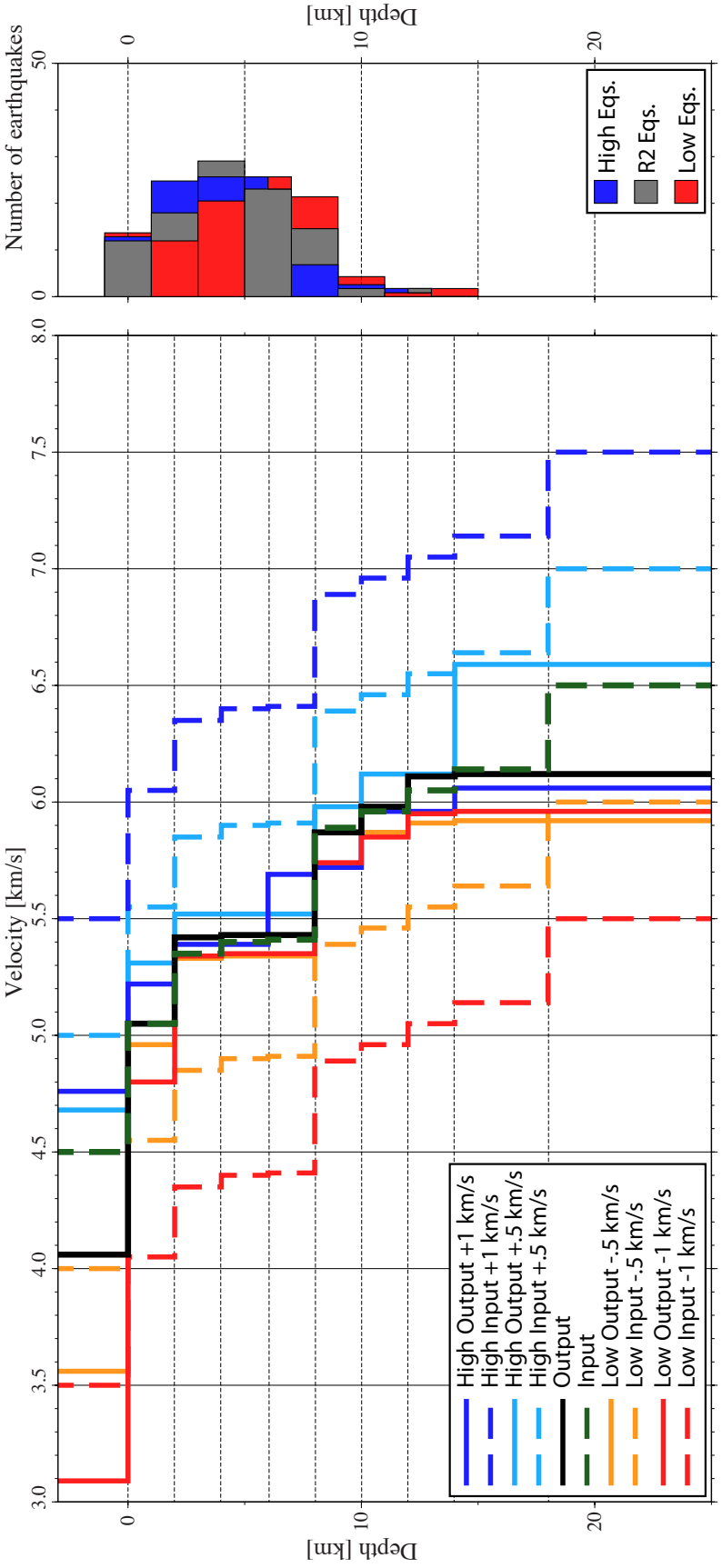

Figure 6.8. Minimum one-dimensional velocity model (black line) calculated for this study using the reference dataset. Green dashed line is the minimum one-dimensional velocity model of *Husen et al.* [2004] that was used as input for the inversion. High/low tests were used to test the robustness of the solution. Input models were modified by adding 1 km/s (dashed dark blue line), adding 0.5 km/s (dashed light blue line), substracting 1 km/s (dashed red line), and subtracting 0.5 km /s (dashed orange line). Results of the high/low tests are shown as solid lines of the same color. The depth distribution of located earthquakes is shown on the right.

procedure described by *Kissling* [1988]. The minimum one-dimensional velocity model of *Husen et al.* [2004] was used as the starting model for the inversion. This model is indicated by the green dashed line in Figure 6.8. High-low velocity tests were performed to test whether the model would converge and give robust results. This was done by adding ±1 and ±0.5 km/s to the input model and inverting for velocity. The final minimum one-dimensional velocity model is shown as the thick black line in Figure 6.8.

Station corrections of the minimum one-dimensional model are shown in Figure 6.9 and show deviations from the one-dimensional model attributed to the effects of retardation and advancement due to the three-dimensional heterogeneity of the Yellowstone crustal structure with respect to the reference station (which has a correction of zero) [*Kissling*, 1988] (yellow star in Figure 6.9). Station YMC, near the center of the region, but outside of the caldera, was chosen as the reference station. Negative corrections (circles) indicate higher velocities compared to the reference station and positive corrections (crosses) indicate lower velocities. These station corrections most likely represent site effects close to the surface that are not accounted for in the minimum one-dimensional velocity model. In general, the derived station corrections reveal a pattern of positive corrections (lower velocities) in and around the 0.64 Ma caldera and larger negative corrections (higher velocities) the farther from the caldera you get (Figure 6.9), which is consistent with what we would expect.

Automatic Picking Using MPX

The MPX automatic picking algorithm is described in detail by *Aldersons* [2004], *Di Stefano et al.* [2006], and *Diehl et al.* [2009a]. MPX requires an initial pick to guide

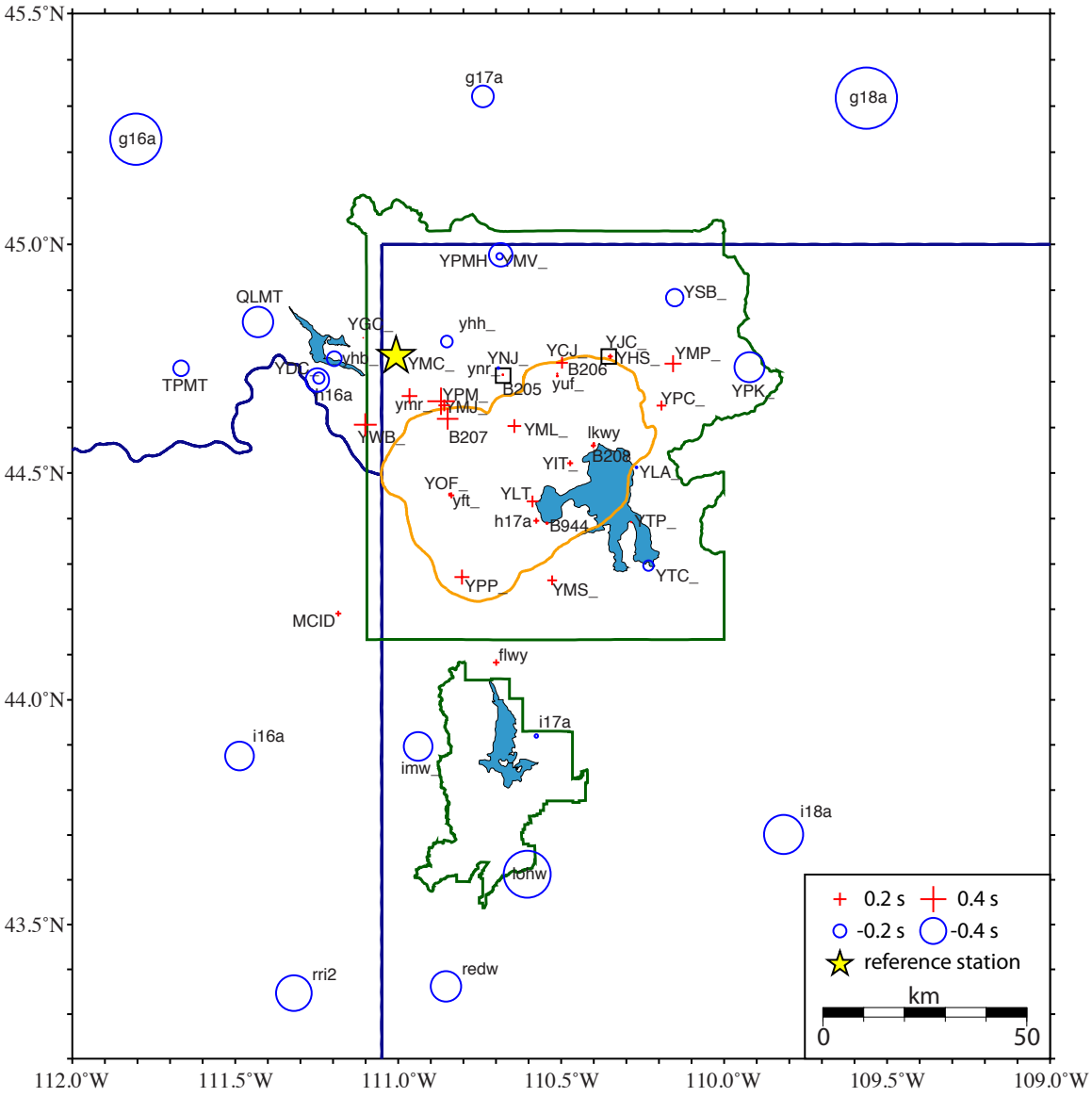

Figure 6.9. Station corrections of minimum one-dimensional model for stations with at least eight observations. Reference station YMC is represented by a yellow star. Negative corrections (blue circles) indicate higher velocities compared to reference station. Positive corrections (red crosses) indicate lower velocities. Symbol size corresponds to correction amplitude.

the picking engine to an approximate phase onset time. The initial picks in this study are provided by predicted pick times using the derived minimum one-dimensional velocity model and station corrections (Figure 6.10).

The MPX picking algorithm is an extension of the Baer-Kradolfer picker [*Baer and Kradolfer*, 1987], an adaptation of the STA/LTA picking algorithm. The threshold for the picker is derived in an adaptive way by comparing apparent noise and signal characteristics. A noise window and a signal window are centered on the initial pick and are separated by safety gaps g_N and g_S as shown in Figure 6.11. The safety gap lengths depend on the expected difference between the initial pick and the actual phase onset. The larger the safety gap, the higher probability there is for mispicks.

A pattern recognition scheme weights different waveform attributes (predictors) obtained in the time window around the automatic pick and classifies the pick in discrete quality classes. The corresponding weighting factors are the "Fisher coefficients" [*Fisher*, 1936, 1938], which have to be calibrated with a set of reference hand picks (reference data). A multiple discriminant analysis (MDA) is used to derive appropriate Fisher coefficients from the reference picks.

The set of 171 reference events was divided into two groups (group A and B). Group A was used to derive appropriate Fisher coefficients for automatic quality classification. The MDA algorithm compares the predictor values around the automatic pick with the associated reference quality class. The Fisher coefficients then are considered to represent the optimum weighting of each predictor to estimate the corresponding quality class membership [*Diehl et al.*, 2009a]. The Fisher coefficients derived using group A were then used in MPX for automatic picking on the entire

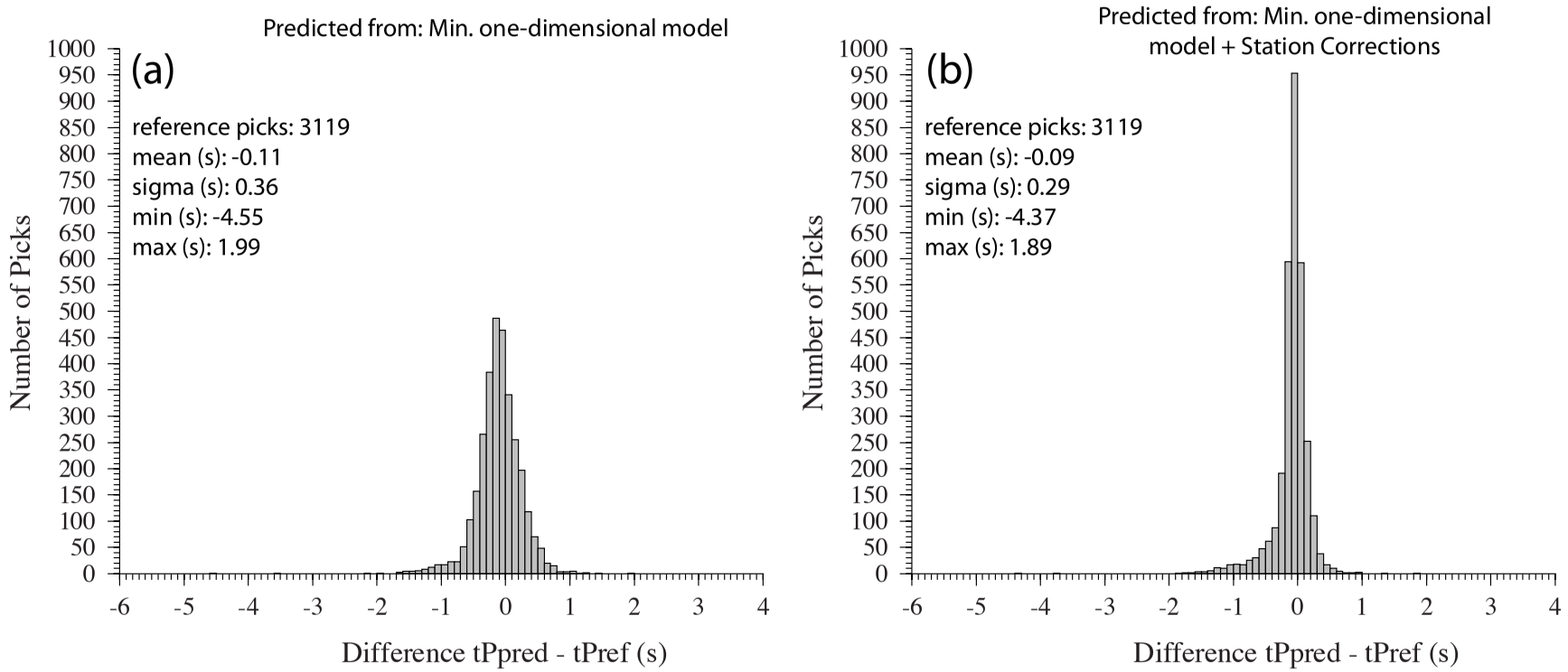

Figure 6.10. Difference between predicted and corresponding reference hand picks (*tPpred - tPref*). (a) Predicted arrival times calculated from a true minimum one-dimensional model (specifically calculated for our data set) with initial locations from Velest (using the same velocity model). (b) Predicted arrival times calculated from the same velocity model as (a) and usage of corresponding station corrections with initial locations from Velest (using the same velocity model).

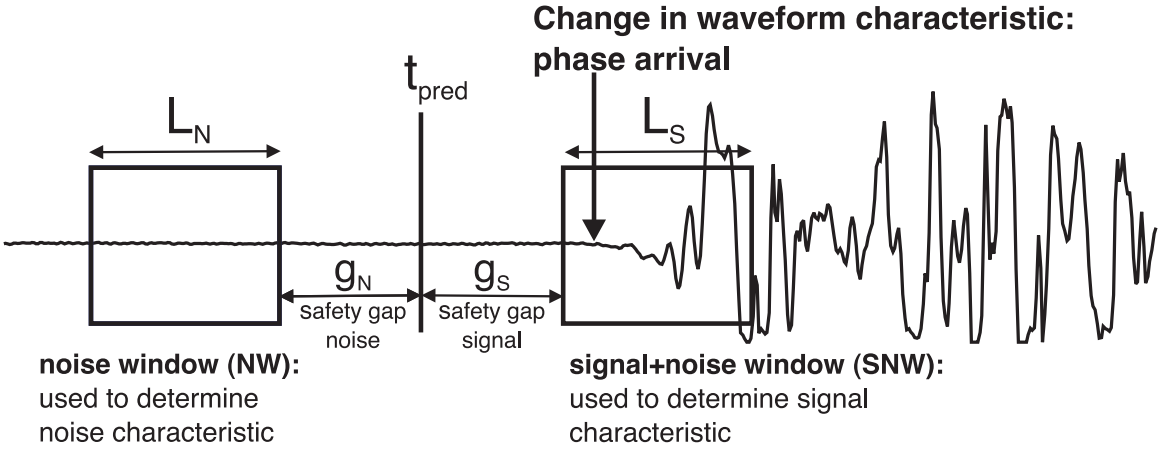

Figure 6.11. MPX search window configuration: The noise window, *NW*, and the signal+noise window, *SNW*, are centered around the initial pick (here predicted *tpred*) and are separated by safety gaps *gN* and *gS*. Modified from *Diehl et al.* [2009a].

reference dataset (groups A and B). This allows us to test how the Fisher coefficients derived for group A are applied (in MPX) to both groups A and B.

Figure 6.12 illustrates the performance of the corresponding weighting scheme in terms of accuracy and classification when applied to all reference events. N_{ij} denotes the number of picks of reference class i classified by the pattern recognition scheme as automatic class j. The σ_{ij} represent the standard deviation for differences between reference picks of class i and corresponding automatic picks of class j. A satisfactory automatic picking and quality assessment is achieved if the deviation between automatic and reference picks is within the error interval of automatic quality classification ($\sigma_{ij} \leq \varepsilon_j$) and if only few low quality reference picks are moderately upgraded to higher quality classes by MPX.

However, upgrades from worst to top quality classes lead to a distortion of the data error estimates for seismic tomography and could generate artifacts in tomographic images [*Diehl et al.*, 2009a]. Inspection of Figure 6.12 shows that a number of reference class 4 (rejected) and reference class 3 events were upgraded to automatic class zero and one weights. This can also be seen in the matrix plot in Figure 6.13. This is unacceptable for use in tomographic inversions as it could introduce large artifacts in the derived velocity model. Inspection of these data show that the majority of these picks were from either bad waveforms (spikes, etc.) that MPX picked on, or waveforms where MPX mispicked a later more impulsive arrival instead of the first-arriving emergent phase.

To remove these mispicks and bad data files, we employed the following algorithm:

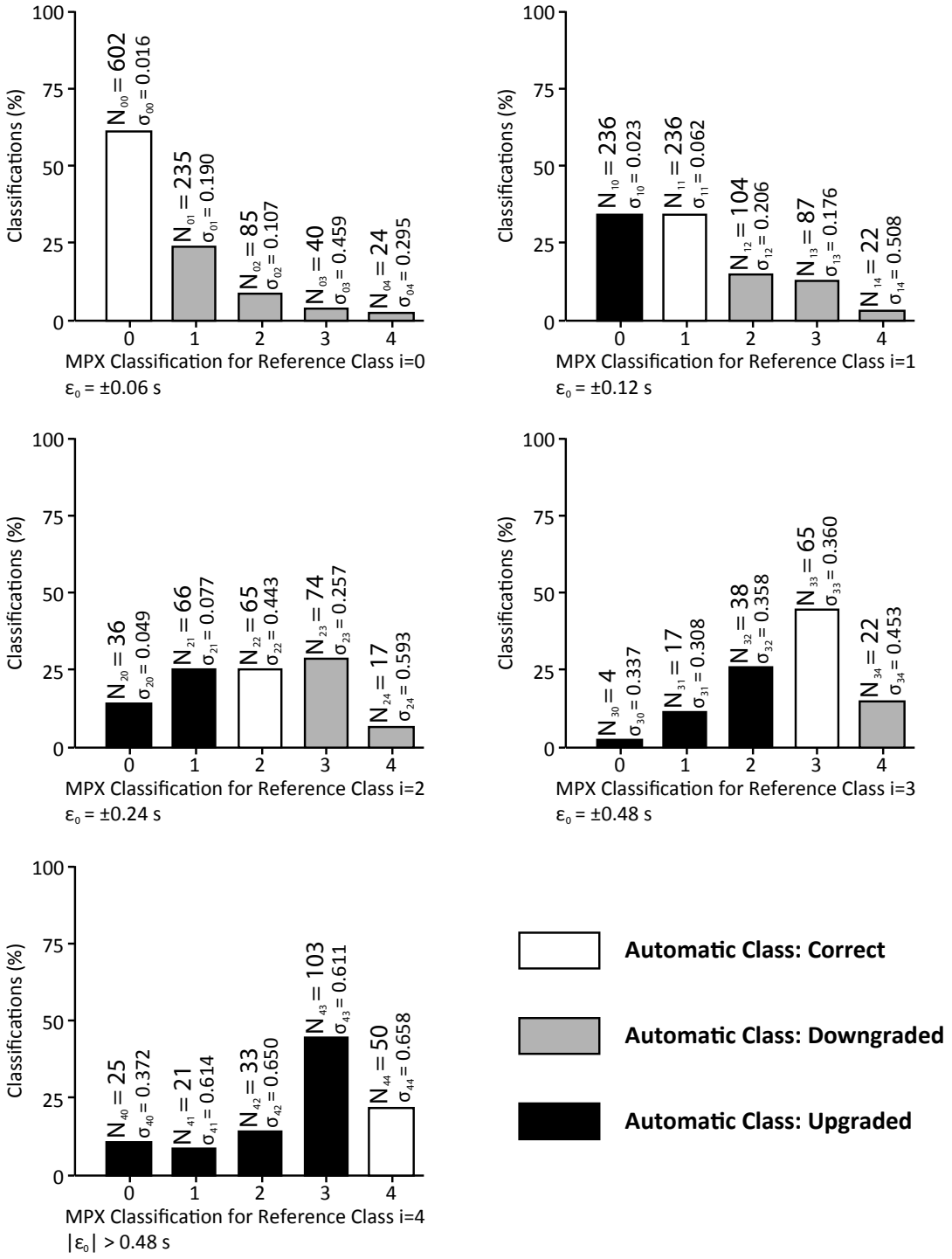

Figure 6.12. Performance of MPX for a weighting scheme derived from reference events in group A and applied to both group A and B. The *Nij* denote the number of picks of reference class *i* classified by MPX as automatic class *j*. The *σij* represent the standard deviation for differences between reference picks of class *i* and corresponding automatic picks of class *j*. White bars indicate correct classification, gray bars indicates downgrading, and black bars identify upgrading of picks by MPX. The automatic weighting classifies more than 60% of the class "0" picks correctly.

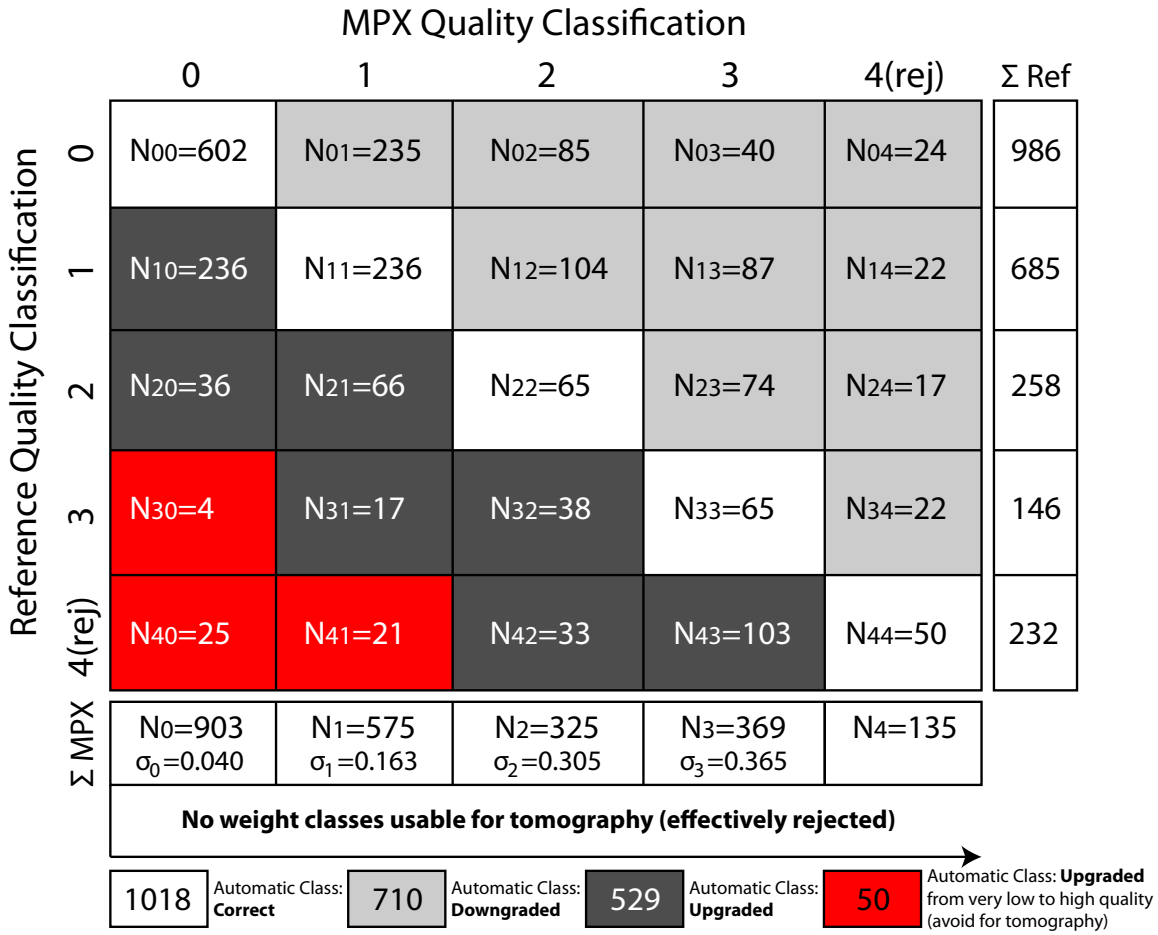

Figure 6.13. Performance of MPX for our reference data set. No automatic picks can be used for tomography due to the fact that a high number of weight 3 and 4 reference picks were upgraded to weight 0 and 1 automatic picks.

1. Only use events that have at least 8 observations (nobs ≥ 8) and a gap less than 180º from initial locations using the minimum one-dimensional velocity model.
2. Run through MPX using Fisher coefficients derived from reference group A to get automatic picks.
3. Relocate the events using automatic picks and the minimum one-dimensional velocity model.
4. Remove any station with a residual greater than 1.0 second or less than -1 second (|res| > 1 s).
5. Rerun MPX using the filtered dataset to get automatic picks of the remaining high-quality data.

Results can be seen in Figures 6.14 and 6.15. Only using well-located events and removing stations with |residuals| > 1.0 s successfully removed the majority of the bad waveforms and mispicks. Results show that there are no longer any picks that were upgraded from reference weight 4 to automatic weights 0 and 1. Also, reference weight 3 picks that were upgraded to automatic weight 0 picks have also been removed. However, there are still a relatively large number of reference weight 4 picks (32 in total) updated to automatic weight 2. In addition, if we analyze the station residuals after relocating the events using the automatic picks, we can inspect the quality of our picks. Weights 0 and 1 show well-behaved (Gaussian) distributions (Figure 6.16). However, weights 2 and 3 show less desirable distributions with uneven tails and bimodal distributions. Because of this, we only accept automatic weights 0 and 1 picks for use in the tomographic inversion.

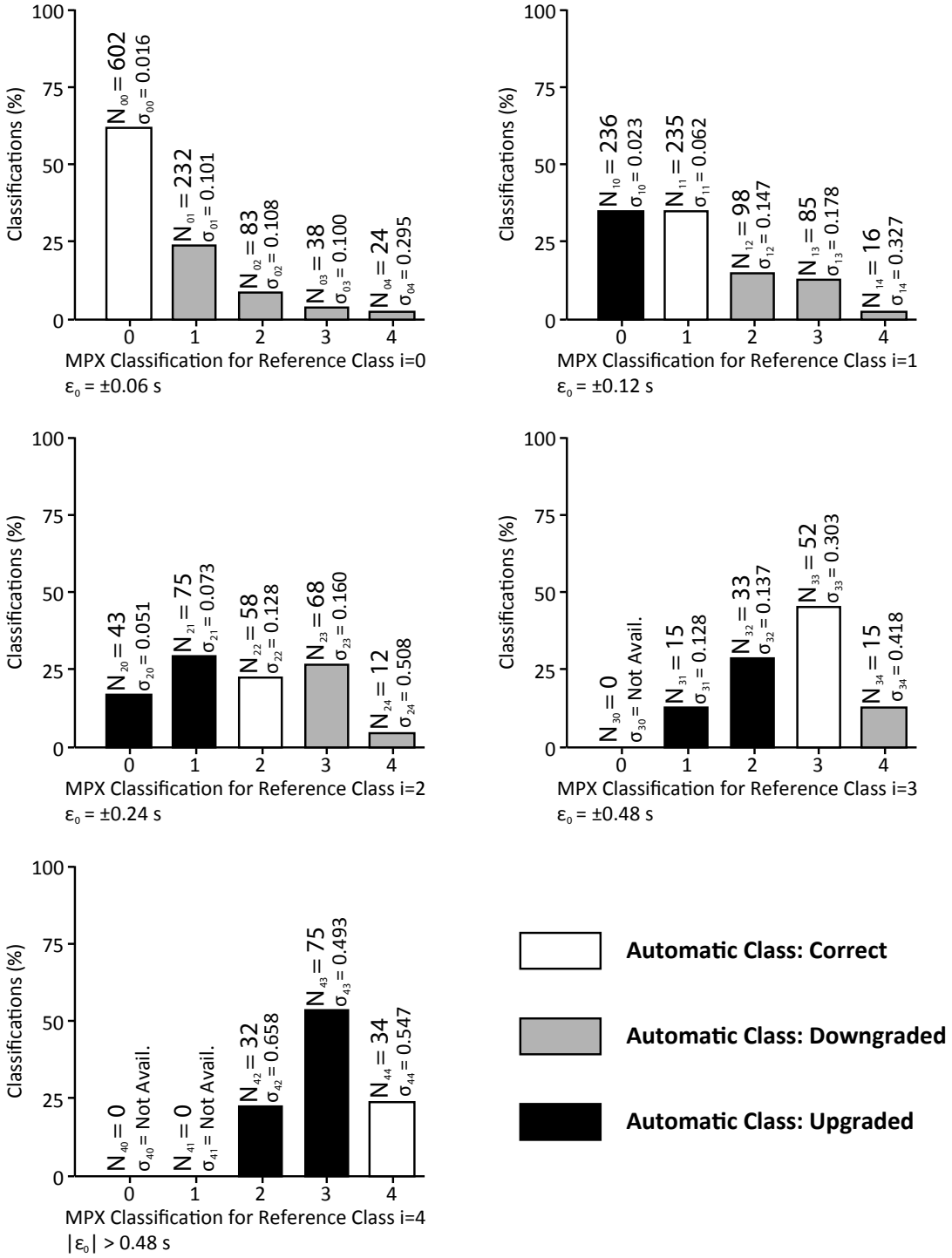

Figure 6.14. Performance of MPX for a weighting scheme derived from reference events in group A and applied to both group A and B with stations with |res|>1 removed. The *Nij* denote the number of picks of reference class *i* classified by MPX as automatic class *j*. The *σij* represent the standard deviation for differences between reference picks of class *i* and corresponding automatic picks of class *j*. White bars indicate correct classification, gray bars indicates downgrading, and black bars identify upgrading of picks by MPX. The automatic weighting classifies more than 60% of the class "0" picks correctly.

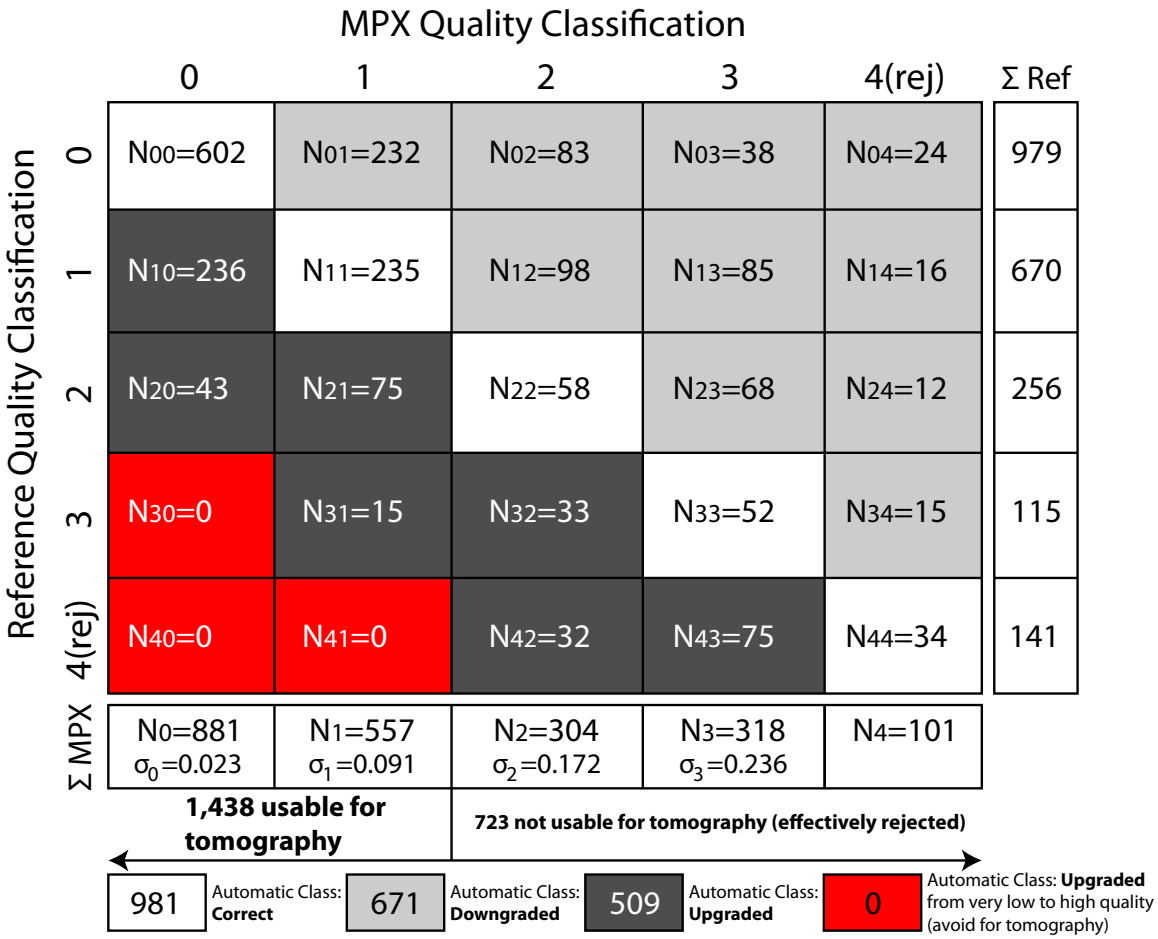

Figure 6.15. Performance of MPX for our reference data set with stations with |res|>1 s removed. Picks of weight 0 and 1 can be used for tomography.

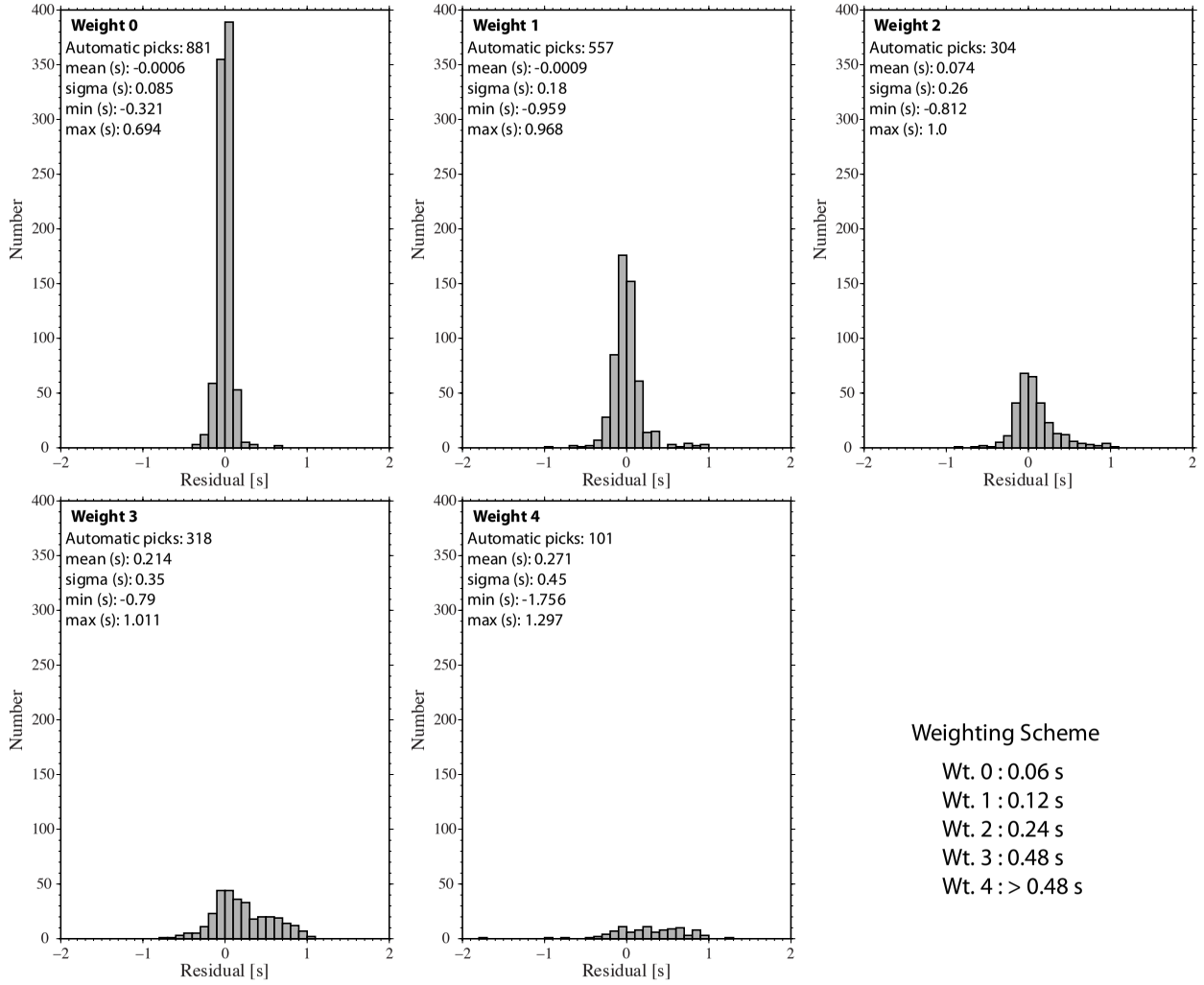

Figure 6.16. Residual distribution of weight classes located using Velest and using automatic MPX picks after stations with initial |residuals|>1.0 s removed

MPX Production Mode Results

We thus ran our entire dataset through the MPX algorithm described above. After only accepting automatic weight classes 0 and 1 and requiring that each event have at least 8 observations (of weight 0 or 1) and a gap of less than 180º, we end up with 4,520 earthquakes. Table 6.2 summarizes the final high-quality P-phase dataset for the Yellowstone system. The average picking error can be estimated from the number of picks for each class and the error interval of each class. For our final dataset we have an average picking error of $\varepsilon_t \approx \pm 0.09$ s with maximum errors not exceeding ±0.12 s. The corresponding ray-coverage for the final dataset is shown in Figure 6.17. This dataset will be used for the tomographic inversion for the velocity structure of the Yellowstone volcanic system.

Local Earthquake Tomography with High-Quality Yellowstone Data

We inverted the high-quality dataset of 4,520 local earthquakes for three-dimensional P-wave structure employing the SIMULPS14 tomography algorithm [*Thurber*, 1983; *Eberhart-Phillips*, 1990], extended by a full three-dimensional ray shooting technique [*Haslinger and Kissling*, 2001] to invert simultaneously for hypocenter locations and three-dimensional P-wave velocity structure. Since SIMULPS14 solves the nonlinear, coupled hypocenter-velocity problem by a linearized, iterative, damped, least-square approach, the solution depends on the choice of initial

Table 6.2. Final high-quality P-phase dataset.

P-Quality Class	Error (s)	# MPX Picks
0	± 0.06	24231
1	± 0.12	24391
Σ		48622

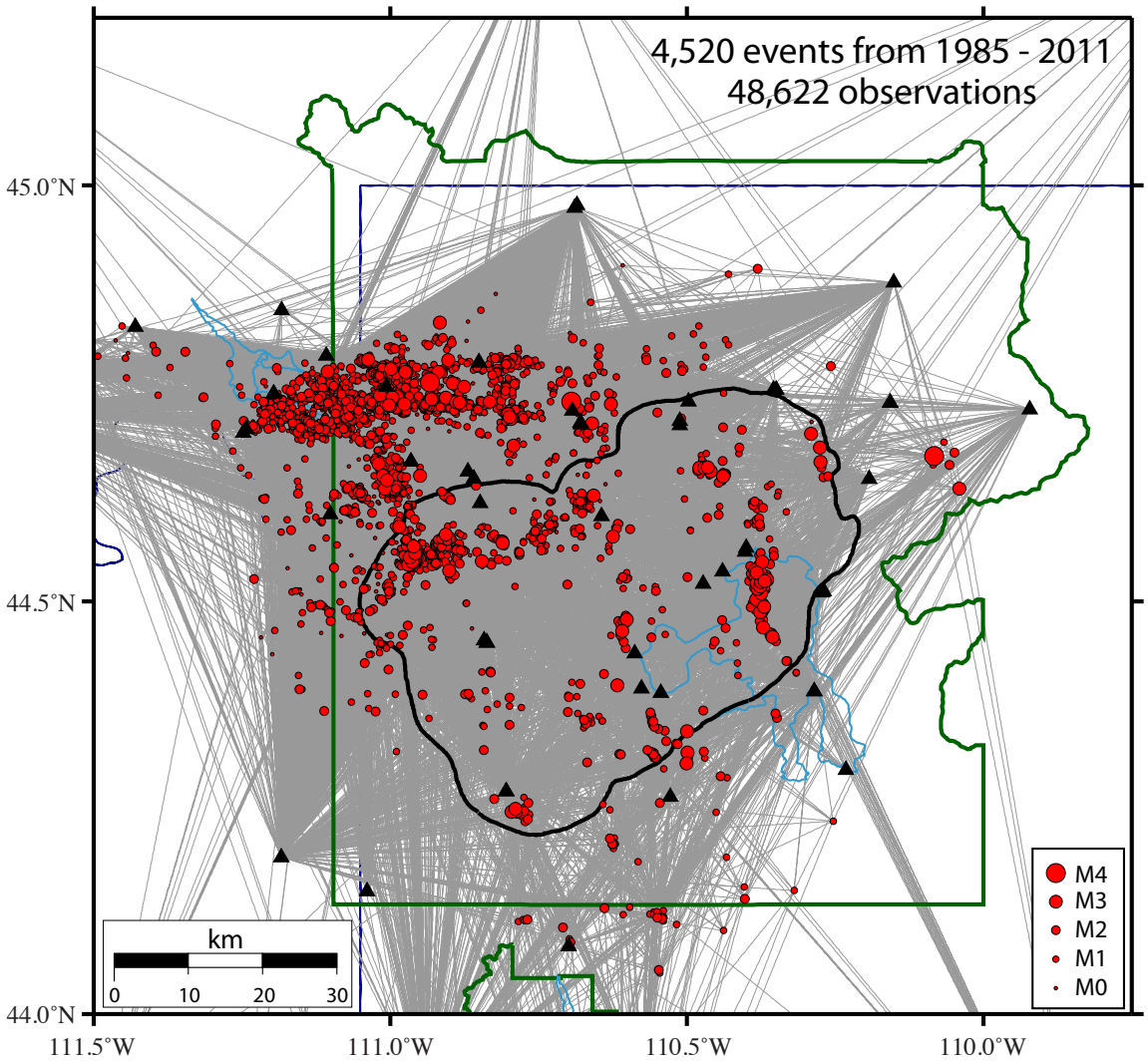

Figure 6.17. Earthquakes of the final high-quality data set (red circles). Gray lines represent raypaths connecting picked stations (black triangles) and epicenter locations. Green lines represent boundaries of Yellowstone and Grand Teton National Parks. Black line outlines the 0.64 Ma Yellowstone caldera.

model (velocities, hypocenters), damping values, and model parameterization [see *Kissling et al.*, 2001]. SIMULPS14 includes a seismic grid (representing the three-dimensional velocity structure) and a forward grid used by the three-dimensional shooting ray-tracer as described by *Kissling et al.* [2001]. In the seismic grid, seismic velocities are linearly interpolated between grid nodes.

Initial hypocenters and P-wave velocities were taken from our calculated minimum one-dimensional velocity model described earlier. We modified the model parameterization of *Husen et al.* [2004] with horizontal spacing of inversion nodes of 10 x 10 km and vertical node planes at -10 km, -4 km, 2 km, 4 km, 8 km, 14 km, 20 km, and 50 km depth.

Before we perform the inversion, we first must convert our one-dimensional minimum velocity model to a gradient model that can be used by simulps14. The gradient velocity model can be seen in Table 6.3 and Figure 6.18. The blue line represents the velocity model used in our model parameterization for the three-dimensional tomographic inversion. The black line is our one-dimensional minimum velocity model and the green dashed line represents the one-dimensional minimum velocity model of *Husen et al.* [2004].

The appropriate damping value was selected empirically from a series of inversions similar to the procedure proposed by Eberhart-Phillips [1986]. The trade-off curves were calculated for a large range of damping values (1, 10, 100, 500, 1,000, and 10,000) and, similar to *Diehl et al.*, [2009b], five iterations were performed for each damping value. The multiloop method provides additional information on the behavior of trade-off curves for increasing model variance and also allows a decision on the

Table 6.3 - Final gradiant velocity model

Depth of Grid Plane (km)	Vp (km/s)
-10	3.70
-4	3.80
2	5.24
4	5.42
8	5.65
14	6.12
20	6.30
50	6.50

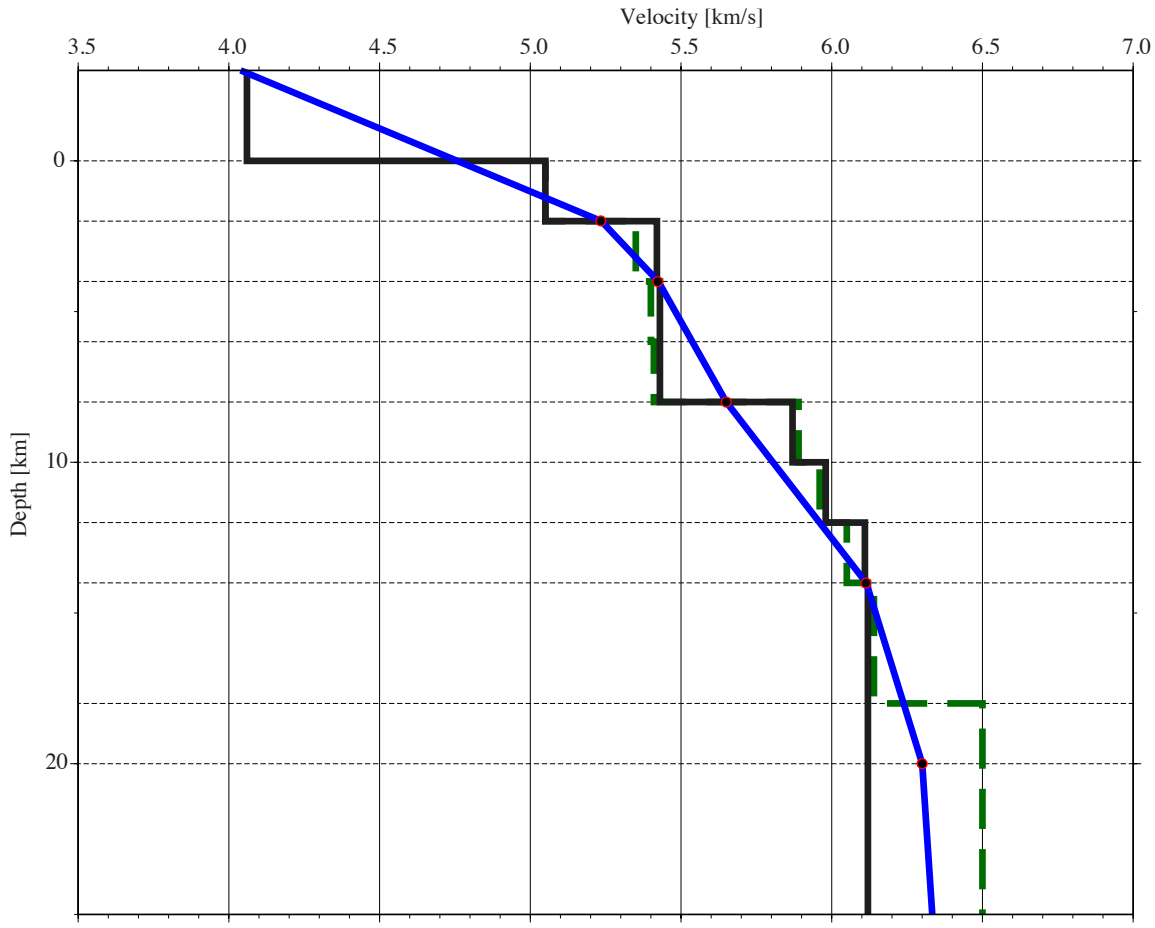

Figure 6.18. Velocity gradient and vertical grid nodes distribution for the three-dimensional inversion. The black line represents the original minimum one-dimensional velocity model of this study. The dashed green line represents the minimum one-dimensional velocity model of *Husen et al.* [2004]. The blue line represents the parameterization for the three-dimensional inversion.

maximum number of iterations reasonable for a chosen damping value [*Diehl et al.*, 2009b].

Figure 6.19a shows data variance compared against model variance for each iteration and damping value. The preferred damping value is associated with the best compromise between data misfit reduction and model variance. Figure 6.19a shows that a damping value of 100 leads to a high data reduction with a moderate model variance for our dataset and model parameterization. Figure 6.19b shows the reduction of the unweighted RMS after each iteration using the optimal damping value of 100. After iteration 2, the unweighted RMS was reduced 38%, which is less than the *a priori* picking error of 0.18 s and therefore the inversion is stopped after iteration 2.

Solution Quality

Assessing the solution quality is a crucial component in seismic tomography [*Kissling et al*., 2001]. The resolution depends on the ray-coverage (density and geometric distribution of rays). The distribution of hit count or derivative weighted sum (DWS) can be used as a first order assessment of ray coverage. However, the hit count and DWS are not necessarily sensitive to the geometric distribution of rays (*Diehl et al.*, 2009b). The diagonal element of the resolution matrix (RDE) gives information on the independence of one model parameter [*Husen et al*., 2000]. The RDE of our final three-dimensional *Vp* model is shown in Figure 6.20 for depths of 2 km, 5 km, 8 km, and 12 km.

RDE values are distributed across most of the area of interest including to the area NE of the Yellowstone caldera. Figure 6.21 shows the RDE values for a vertical cross

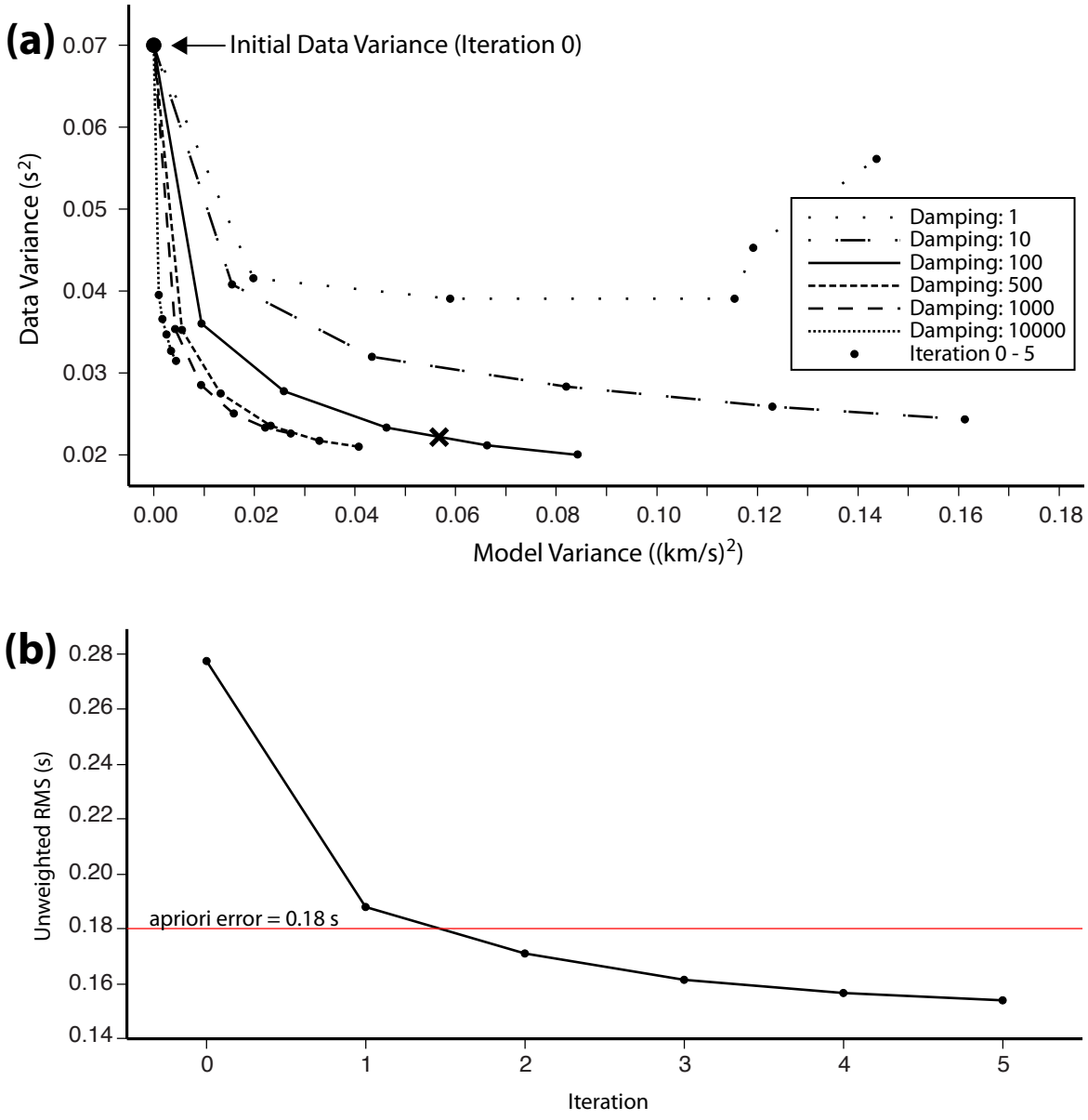

Figure 6.19. Trade-off curves to determine appropriate damping for inversion and the number of necessary iteration steps. (a) Data misfit vs. model variance. Each curve represents tradeoff for different damping values over five iterations. The optimum misfit reduction is achieved for damping value 100 after three iterations (cross). (b) Reduction of unweighted RMS after each iteration using a damping value of 100. After iteration 2 the improvement becomes insignificant.

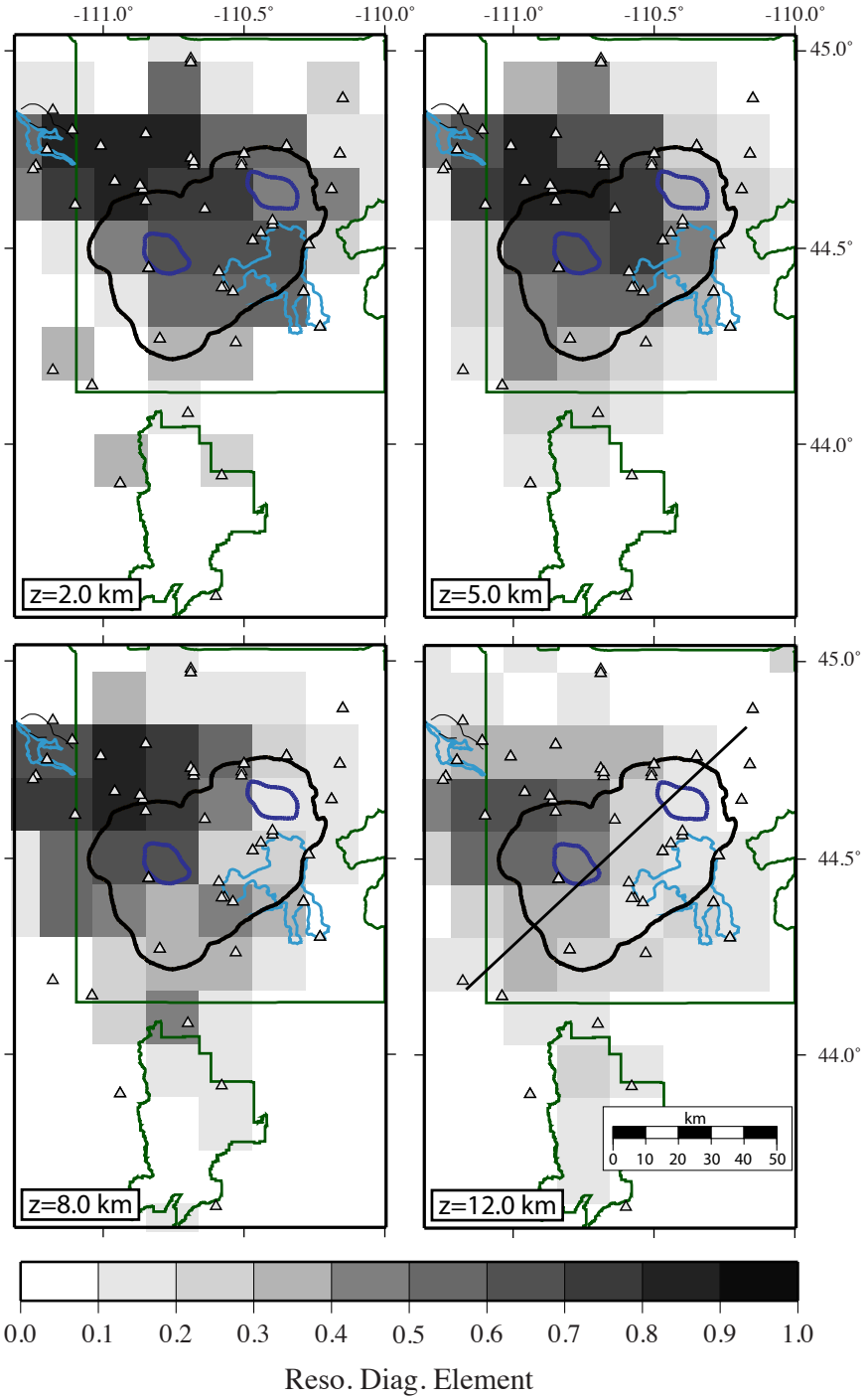

Figure 6.20. Diagonal elements of the resolution matrix (RDE) of the Vp solution at different depths. Black bold line in the bottom right image indicates location of the vertical cross section of Figure 6.21.

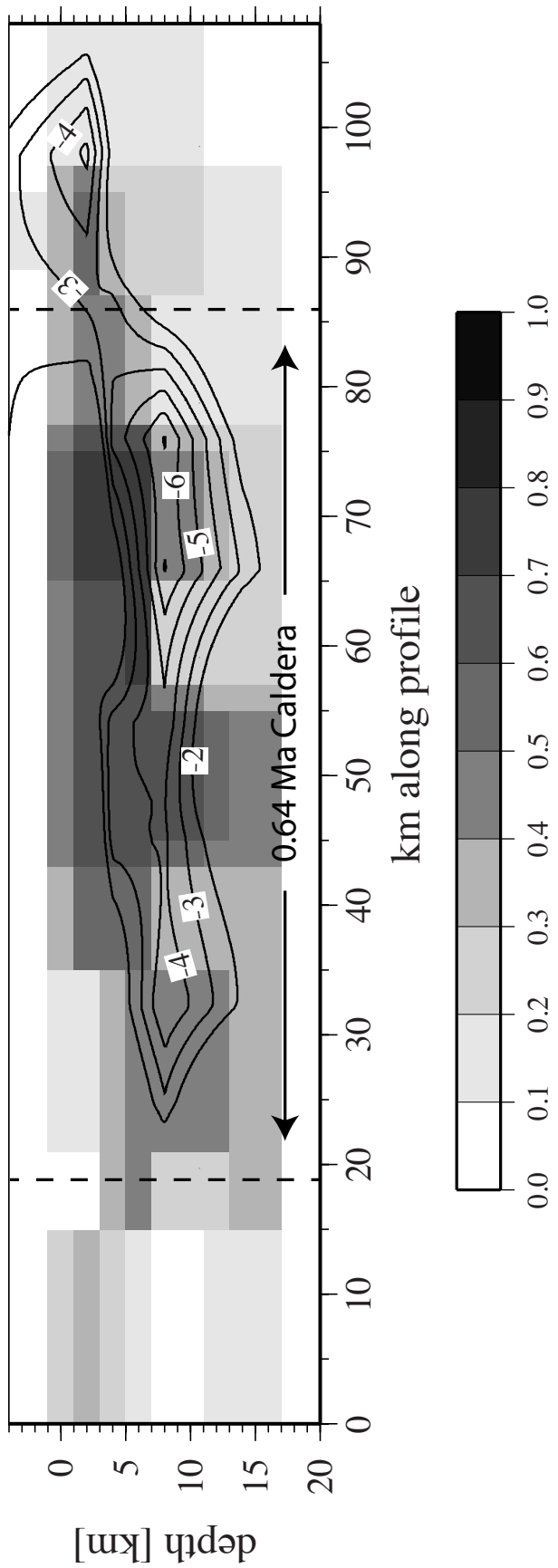

Figure 6.21. Diagonal elements of the resolution matrix (RDE) of the Vp solution for a cross section along the long axis of the caldera. Black contour lines represent the area of low Vp beneath the Yellowstone caldera.

section along the long axis of the caldera in a SW-NE direction. Figure 6.21 shows good coverage to depths of ~16km beneath the caldera and good coverage in the area NE of the caldera.

Figure 6.22 shows the result of a sensitivity test with a synthetic checkerboard model similar to those proposed by *Diehl et al.* [2009] and *Husen et al.* [2004]. To identify and estimate vertical leakage, only every other layer is perturbed by alternating high (+10%) and low (-10%) input anomalies (indicated by blue and red rectangles in Figure 6.22). To identify horizontal smearing, a gap of one grid node between the input anomalies is inserted. To distinguish between upward and downward leakage, the polarities of the input anomalies are swapped for each perturbed layer. Random noise is added to the synthetic travel times using an equally distributed error for each quality class. We use the same inversion parameters (initial model, parameterization, damping, and number of iterations) for the inversion of the synthetic travel times as we use for the real data.

The recovery of the high/low input anomalies is good for grid nodes in and around the Yellowstone caldera (Figure 6.22). There is some minor upward leakage into the -4 km layer and downward leakage into the 4 km and in the 14 km layer with much reduced amplitudes with minor horizontal smearing (Figure 6.22). In the 20 km layer, the checkerboard pattern input anomalies are no longer recovered signifying the loss of resolution at this depth (Figure 6.22).

The resolution test shown in Figure 6.23 was designed to test the recovery of the Yellowstone magma reservoir beneath and to the NE of the caldera. The SW-NE striking cross-sections shown in Figure 6.23 are along the long axis of the caldera and test for the

Figure 6.22. Sensitivity test with a checkerboard model similar to *Husen et al.* [2004]. Recovered model after two iterations is shown in plane view at different depths. Alternating high (+ 10%) and low (- 10%) input anomalies are indicated by blue and red squares, respectively.

-4 km
2 km
4 km
8 km
14 km
20 km
45°
44.5°
44°
-111°
-110.5°
-110°
10
8
6
4
2
1
-1
-2
-4
-6
-8
-10
% Vp change, rel. to input model

Figure 6.23. Assessment of resolution in the region of the expected Yellowstone magma reservoir. (A) Input model of -6% (red boxes), (B) input model of +6% (blue boxes), and (C) deep input model of -6% (red box). Cross section location is shown in Fig. 6.24.

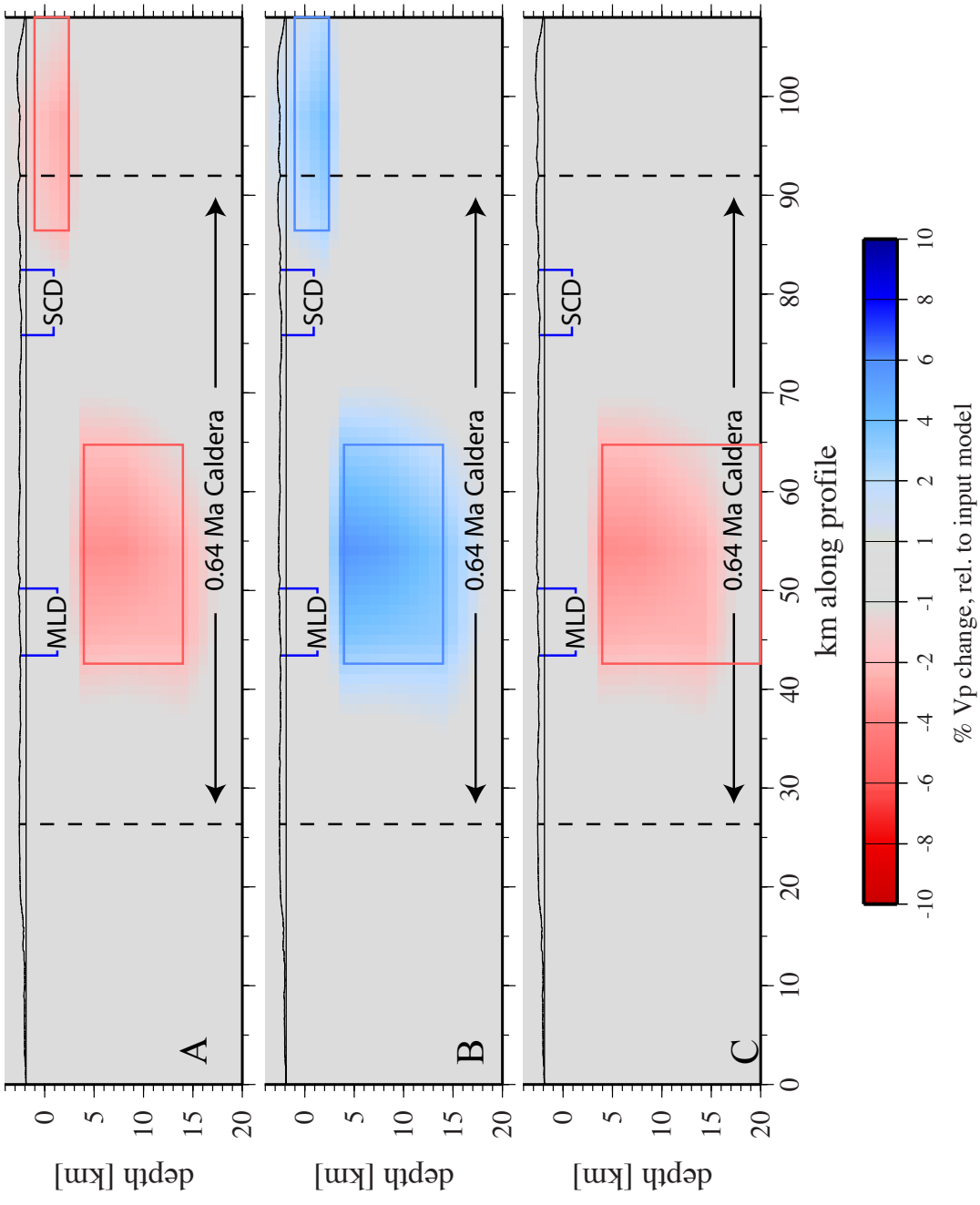
A
B
C
SCD
MLD
0.64 Ma Caldera
depth [km]
km along profile
% Vp change, rel. to input model

ability of our data to distinguish individual anomalies and to test the depth of resolution. Two separate anomalies with amplitudes of -6% are shown in Figure 6.23a. These anomalies are recovered well with little smearing. In addition, our data are able to recover these anomalies as separate low velocity bodies. Figure 6.23b shows the same two anomalies but with +6% anomalies. Again, the anomalies are recovered well with little smearing. In Figure 6.23c, a -6% anomaly from 5 to 20 km is used as input to test how deep we are able to resolve the velocity changes. Results show that we have adequate resolution down to ~17 km and we are no longer able to resolve changes in the P-wave velocity structure below this depth. This agrees with the checkerboard results discussed above and shown in Figure 6.22.

It is important to note that because we are using the high frequency approximation to the wave equation, we are underestimating the ray volume that mostly effects the travel time kernal. The volume surrounding the geometrical ray path that contributes to the travel time residual is commonly called the first Fresnel volume [*Spetzler and Snieder*, 2004] whose width depends on the distance between the source and receiver, L, and the wavelength, λ. In a homogeneous medium, the half-width of the Fresnel volume, f, is given by *Spetzler and Snieder* [2004] as:

$$\mathrm{f} = \sqrt{\frac{\lambda x(L-x)}{L}}. \tag{6.7}$$

If we take a range of frequencies of 1 Hz to 10 Hz observed for Yellowstone P-wave body wave data and using an average P-wave velocity of 6 km/s, we obtain wavelengths (λ) of 6 to 0.6 km, respectively. For a distance from source to receiver (L) of 60 km, the maximum Fresnel width occurs when x=30 km. This gives a Fresnel zone

half-width of 3-9 km and a Fresnel volume width of 6-18 km. This means that at the midpoint of the ray path, the wave is sensitive to a volume with a diameter of 6-18 km. If we take a shorter raypath (L=10 km and x=5 km), the wave is sensitive to a volume with a diameter of 1-4 km. This affects our ability to resolve structures smaller than this width. However, the structures that we are targeting are much larger than this.

Three-Dimensional P-Wave Tomographic Model of the Yellowstone Volcano-Tectonic System

After two iterations, our final tomographic model for Yellowstone achieved a data variance reduction of 60% for the three-dimensional *Vp* solution; weighted data root mean-square (RMS) misfit of the model was 0.13 s, which is in the order of the *a priori* picking uncertainty. Figure 6.24 shows the tomographic result of the three-dimensional *Vp* model as horizontal slices at depths of 2 km, 5 km, 8 km, 12 km, and 14 km. The velocity structure is shown as percentage change relative to the one-dimensional initial reference model.

Notably, a low *Vp* body, with %*Vp* changes as large as -7%, exists below the Yellowstone caldera from depths of ~5 km to ~16 km. The low velocity body beneath the Yellowstone caldera extends, although at shallower depths (≤4 km), NE of the caldera (Figure 6.25) with %*Vp* change values up to -7%. In addition, an area just north of Canyon Junction is another area of low P-wave velocities (-6% *Vp*) (Figure 6.24).

Figure 6.24. Our final three-dimensional Vp velocity model for the Yellowstone region shown at different depths. Values are in %Vp change relative to our minimum one-dimensional velocity model. The solid black line in the upper left figure represents the location of a cross-section in Figure 6.25.

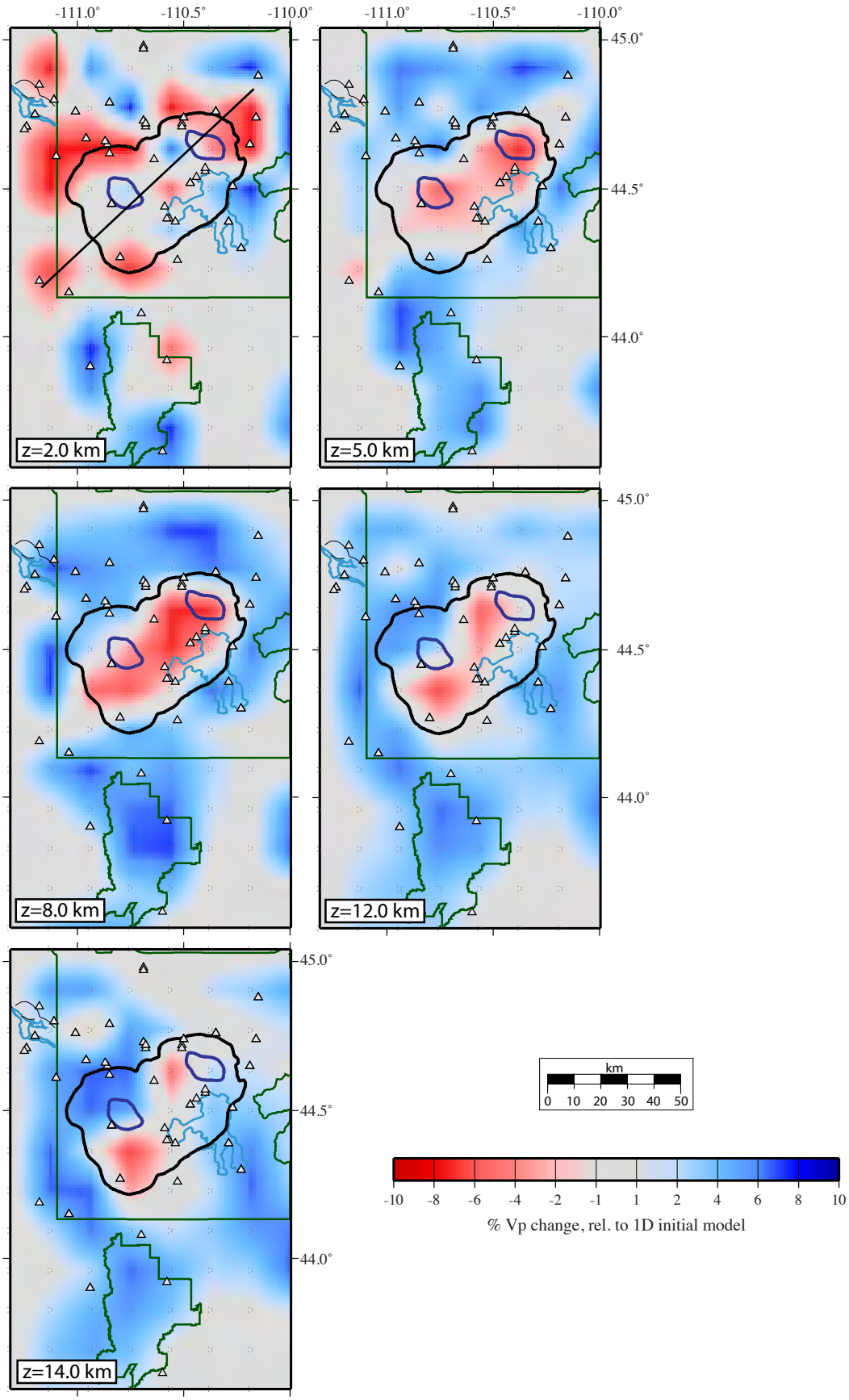
-111.0°
-110.5°
-110.0°
45.0°
44.5°
44.0°
z=2.0 km
z=5.0 km
z=8.0 km
z=12.0 km
z=14.0 km
km
0 10 20 30 40 50
-10 -8 -6 -4 -2 -1 1 2 4 6 8 10
% Vp change, rel. to 1D initial model

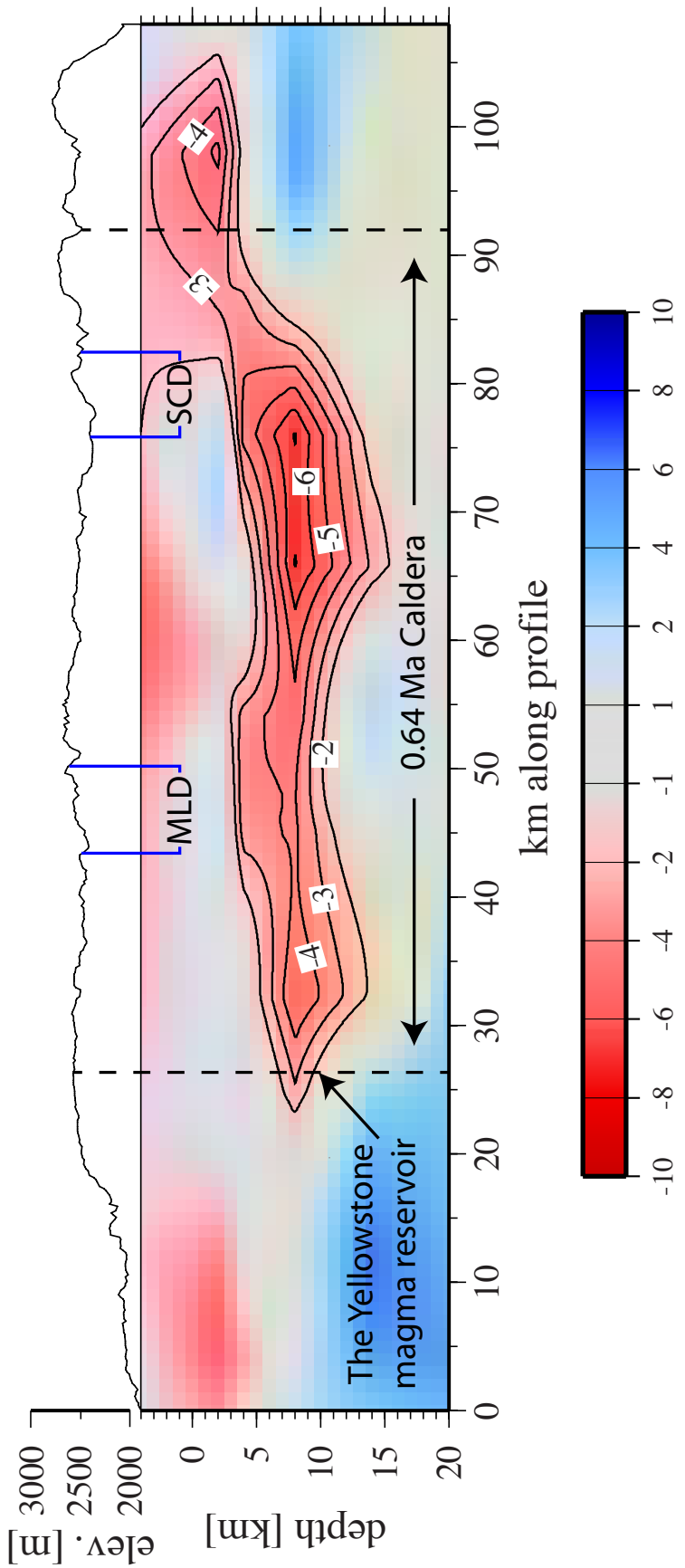

Figure 6.25. Cross section through our final three-dimensional Vp velocity model in units of %Vp change relative to our minimum one-dimensional velocity model. Black contour lines outline the Yellowstone magma reservoir. Blue lines show the surface location of the Mallard Lake resurgent dome (MLD) and the Sour Creek resurgent dome (SCD).

Relocated Yellowstone Seismicity

Using our new three-dimensional velocity model of the Yellowstone volcanic system, we relocated earthquakes from 1995-2012 using the software package NonLinLoc [*Lomax et al.*, 2000]. NonLinLoc follows the probabilistic formulation of nonlinear inverse problems by *Tarantola and Valette* [1982]. The complete description of this formulation can be found in *Tarantola and Velette* [1982] and *Moser et al.* [1992]. I will only briefly describe the relocation procedure in this section and describe the results of the relocation using the new three-dimensional velocity model.

Method

The probabilistic formulation of nonlinear inverse problems relies on the use of normalized and unnormalized probability density functions to express our knowledge about the values of parameters. If the probability density functions giving *a priori* information on the model parameters and on observations are independent, and the theoretical relationship relating a vector of observed data and unknown parameters can be expressed as a conditional density function, then a complete, probabilistic solution can be expressed as *a posteriori* Probability Density Function (PDF) [*Tarantola and Valette*, 1982].

In earthquake location, the unknown parameters are the hypocentral coordinates (x, y, and z) and the origin time T, the observed data are arrival times measured at seismograph stations, and the theoretical relation gives predicted or theoretical travel times. If the theoretical relationship and the observed travel times are assumed to have Gaussian uncertainties expressed by covariance matrices, and if the *a priori* information

on the origin time is taken as uniform, the PDF can be evaluated analytically in a marginal PDF for the spatial location and the origin time [*Husen et al.*, 2004; *Tarantola and Valette*, 1982; *Moser et al*., 1992].

In NonLinLoc, the PDF can be computed in three different ways (*Lomax et al.,* 2000): (1) via a grid-search algorithm using successively finer, nested grids; (2) via a Metropolis-Gibbs sampling algorithm performing a directed random walk within a spatial volume to obtain a set of samples that follow the PDF; and (3) via an Oct-Tree Importance sampling algorithm (Oct-Tree algorithm). The Oct-Tree algorithm gives accurate, efficient and complete mapping of the PDF of the earthquake location problem [*Lomax and Curtis*, 2001]. It uses recursive subdivision and sampling of cells in three dimensions to generate a cascade of sampled cells, where the number of sampled cells follows the values of the PDF at the cell center, thus leading to higher density of cells in areas of higher PDF (lower misfit) [*Husen et al.*, 2004]. Multiple minima in the PDF are reliably detected by the grid-search algorithm and the Oct-Tree algorithm but are missed by the Metropolis-Gibbs sampling algorithm [*Husen et al*., 2004]. The Oct-Tree algorithm outperforms the grid-search algorithm by a factor of 100 in computing time [*Lomax and Curtis*, 2001]; however, the Oct-Tree algorithm may not detect narrow, local minima in the PDF. Following *Husen et al.* [2004] and *White et al.* [2009], we used the Oct-Tree algorithm for relocating the catalog from 1995-2012 for the Yellowstone region.

Results

We relocated Yellowstone earthquakes from 1995-2012 (Figure 6.26). We classify the relocated events using the same scheme as *Husen et al.* [2004] in which quality class A (best locations) events have rms < 0.5 s, DIFF (difference between the maximum likelihood hypocenter and the expected hypocenter location) less than 0.5 km, and an average error less than 2 km. Quality class B events have the same rms and DIFF criteria as quality class A but the average error is greater or equal to 2 km. Quality class C has rms values of < 0.5 s and DIFF ≥ km. Quality class D events have rms values of ≥ 0.5 s. In total, for 1995-2012, 10,124 (35.1%) events are classified as quality class A; 5,769 (20.0%) events are classified as quality class B; 12,917 (44.7%) events are classified as quality class C; and 63 (0.2%) events are classified as quality class D (Figure 6.27).

Compared to *Husen et al.* [2004], we have increased the number of quality A locations by 697, and quality B events by 650. In addition, we have decreased the number of quality C events by 1,351 events.

Lateral variations of Yellowstone caldera focal depths reflect variations in the depth to the brittle-ductile transition [after *Smith and Bruhn*, 1984]. In Figure 6.28, we show the 80th percentile maximum depth of earthquakes as the brittle-ductile isosurface of constant temperature using only quality A and B hypocenters from 1995 – 2012 relocated using our new three-dimensional P-wave velocity model. North-south cross-sections can be seen in Figure 6.29. Assuming the brittle-ductile transition temperature of 400-500 ºC for extensional tectonic regimes allows estimates of the conductive temperature gradient. This distinctive shallowing of the seismogenic layer beneath the

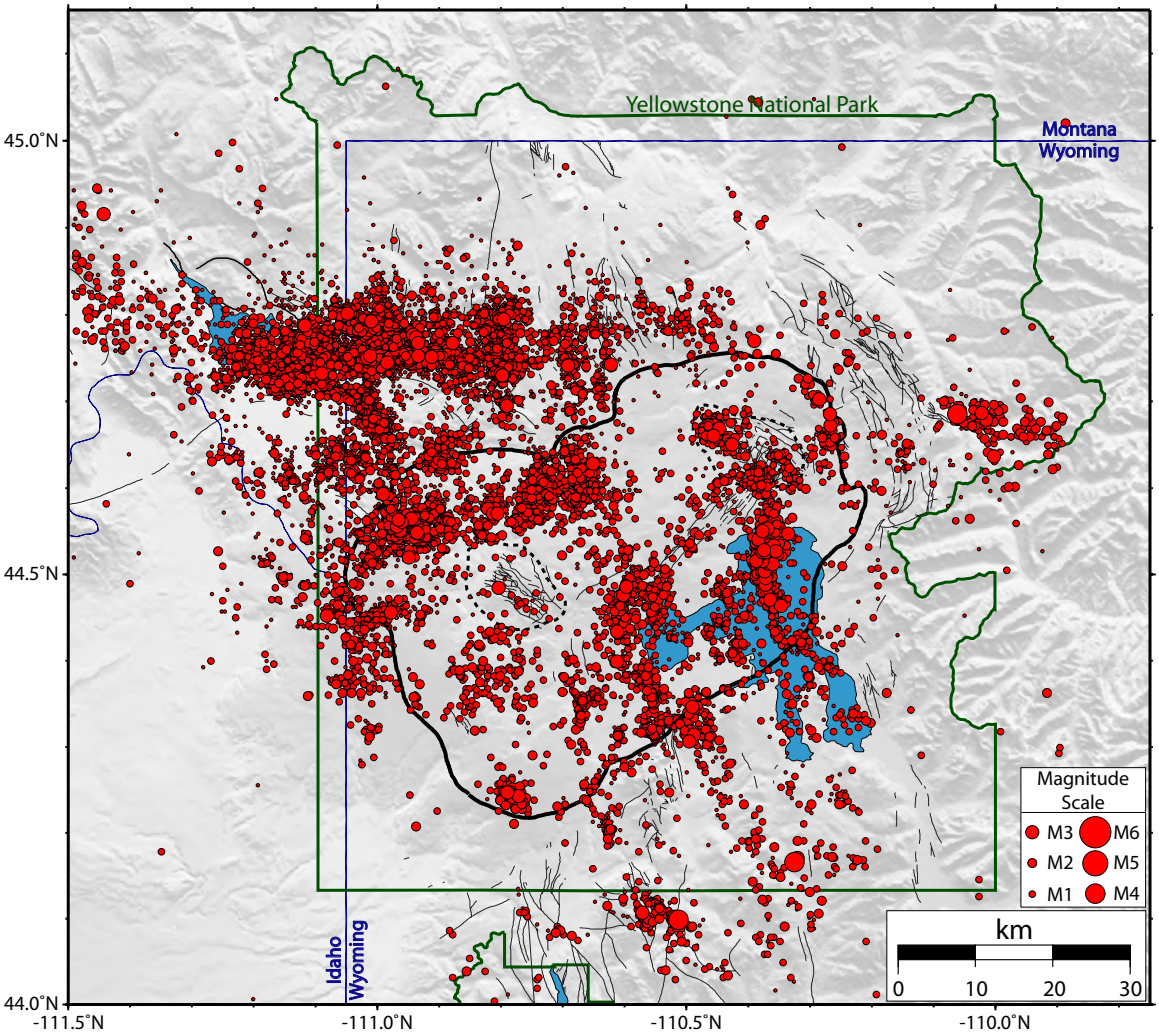

Figure 6.26. Relocated epicenters of the Yellowstone volcanic system from 1995 to 2012. Events were relocated using the new three-dimensional P-wave velocity model derived in this study.

Figure 6.27. Location quality class distribution for earthquakes relocated using the new three-dimensional P-wave velocity model derived in this study showing (a) quality class A events, (b) quality class B events, (c) quality class C events, and (d) quality class D events.

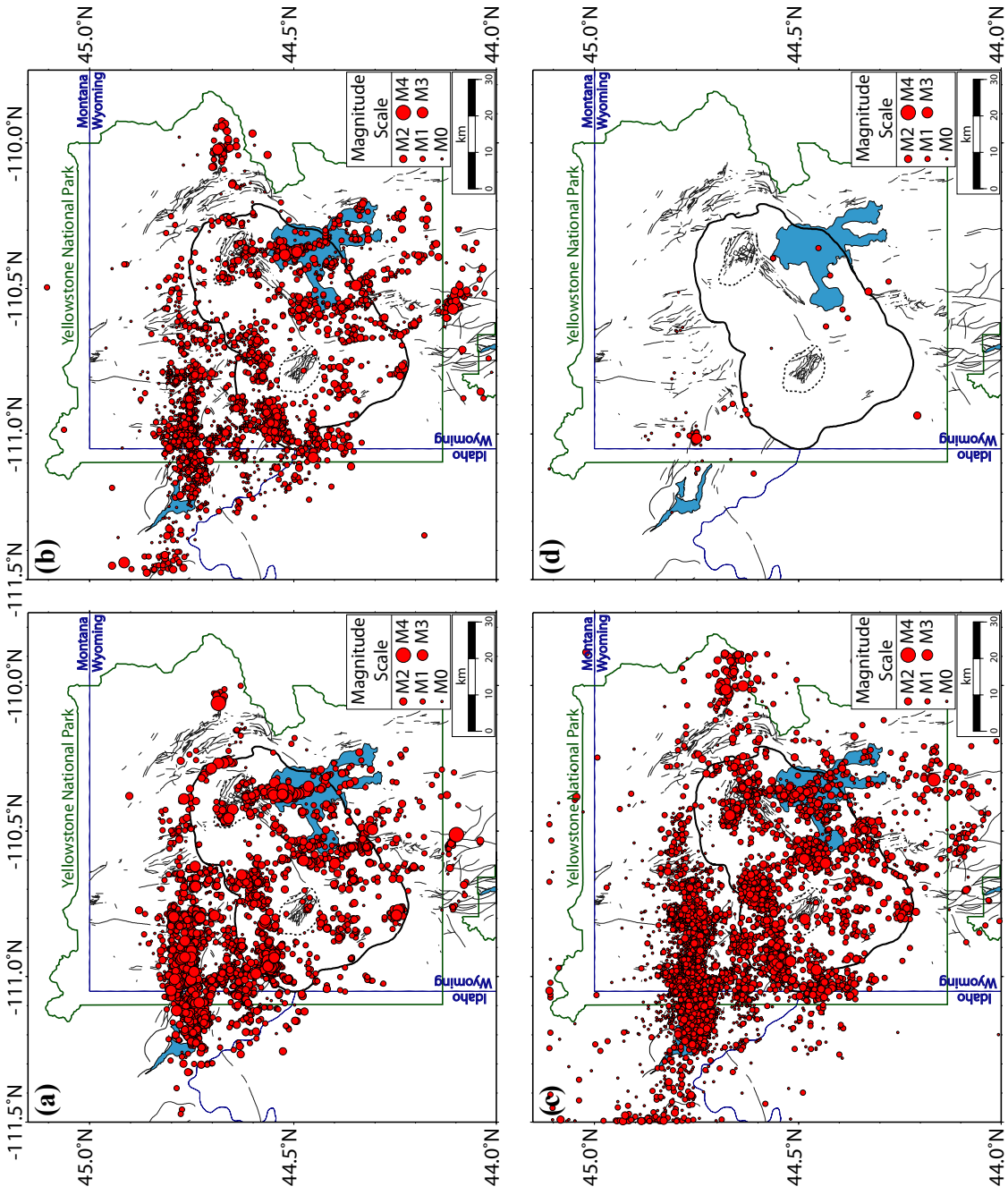
(a)
(b)
(c)
(d)
Yellowstone National Park
Montana
Wyoming
Idaho
Wyoming
Magnitude Scale
M2
M4
M1
M3
M0
km
0
10
20
30
-111.5°N
-111.0°N
-110.5°N
-110.0°N
45.0°N
44.5°N
44.0°N

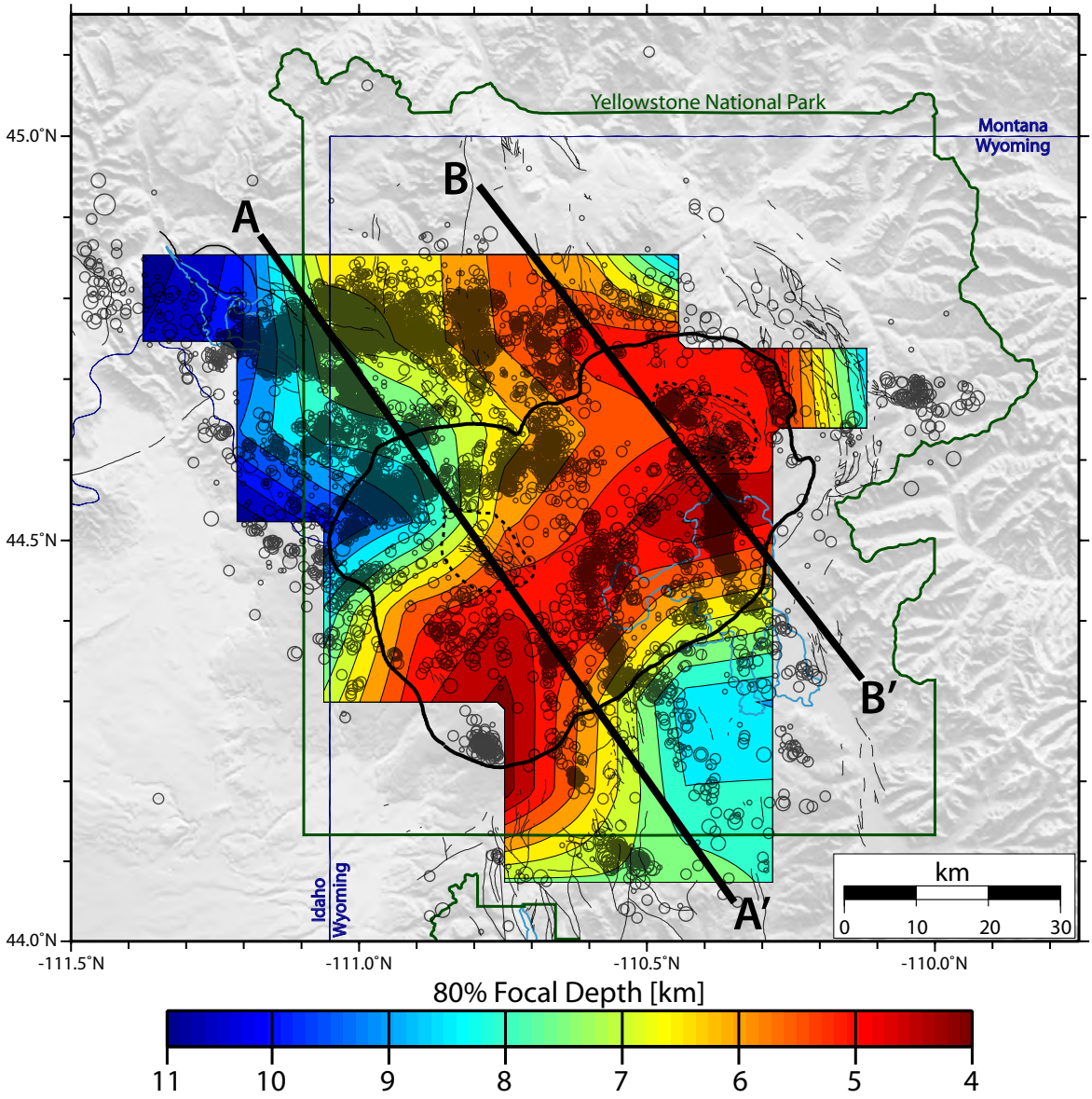

Figure 6.28. 80th percentile focal depth distribution for three-dimensional relocated quality A and B earthquakes from 1995-2012. The open black circles represent earthquakes used in the calculation of the 80th percentile depth surface. Heavy black lines represent cross-sections shown in Figure 6.29.

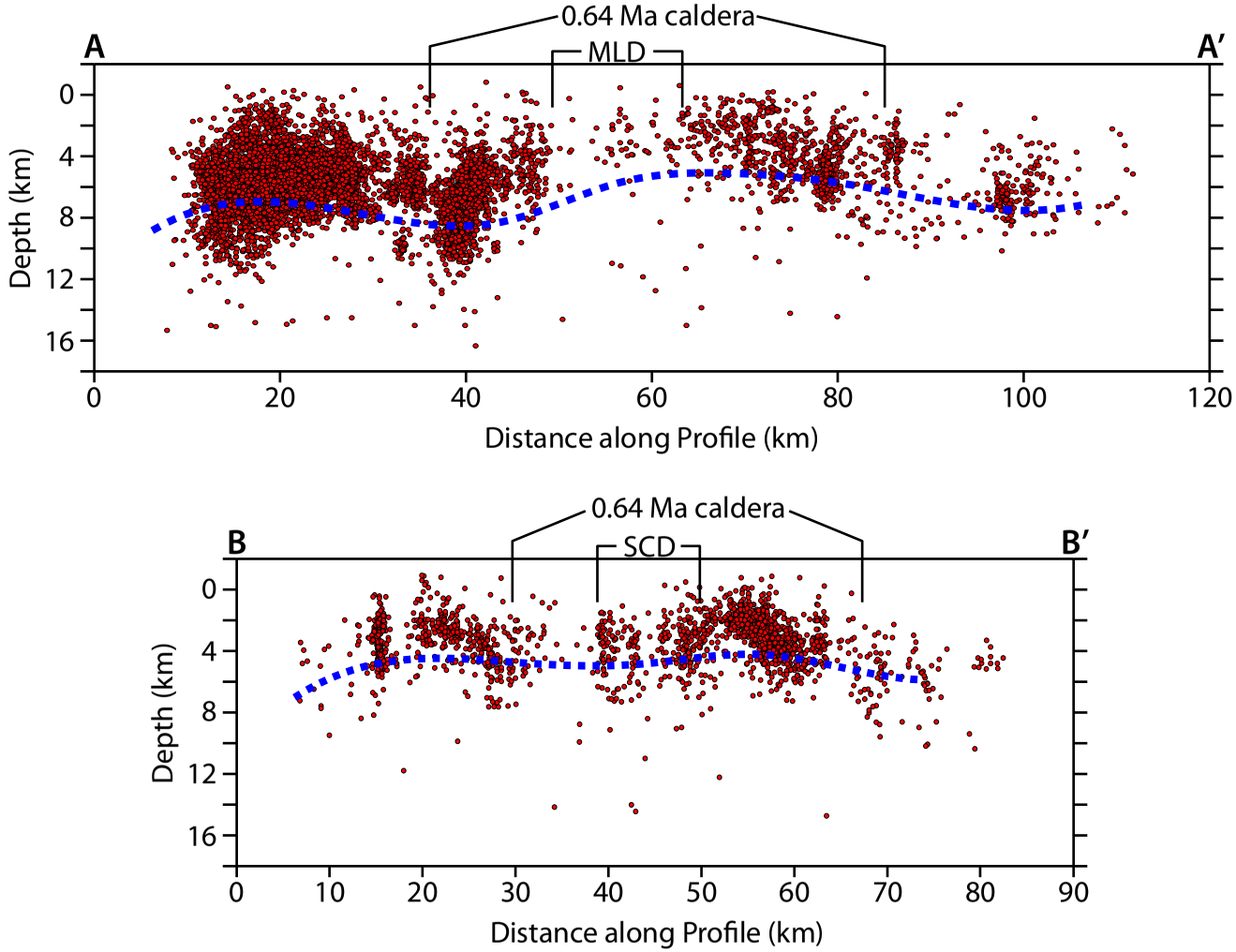

Figure 6.29. N-S cross-sections across the Yellowstone caldera showing hypocenter distributions for relocated earthquakes. The blue dashed lines represent the 80th percentile focal depth, analogous to the brittle-ductile transition. MLD and SCD refer to the Mallard Lake and Sour Creek resurgent domes, respectively.

caldera is attributed to high temperatures that reduce the strength of the rock, transforming it from brittle to ductile behavior above a shallow high-temperature source, namely a crustal magma reservoir [*Smith*, 1978]. Within the caldera, the crust appears to behave in a quasiplastic manner at depths exceeding 4-5 km at temperatures greater than 350 ºC to 450 ºC as determined from petrological constraints [*DeNosaquo et al.*, 2009]. Such high-temperature rocks are incapable of sustaining shear stresses on faults [*Smith and Bruhn*, 1984]. The maximum focal depths of > 11 km occur about 10 km from the west side of the caldera and correspond to a conductive thermal gradient of ~26 ºC/km. Inside the caldera, the average 80th percentile depth is 4 to 6 km and corresponds to a gradient of 110 ºC/km to 65 ºC/km. These values are considered a proxy for the conductive component of heat flow and would correspond to heat flow values of ~250 mWm^{-2}, while a corresponding convective heat flow of ~1750 mWm^{-2} would be required to produce the total observed heat flow of ~2000 mWm^{-2} [*Smith et al.,* 2009]. The shallowing of focal depths inside the Yellowstone caldera as well is in the NE caldera region is coincident with the low V_P body, described earlier, interpreted to be the Yellowstone crustal magma reservoir.

Discussion and Conclusions

The large, low Vp body that spans the length of the caldera from 5 – 16 km is interpreted as the Yellowstone crustal magma reservoir (Figures 6.24 and 6.25). P-wave velocity reductions for this body are as high as -7%. This is similar to the low *Vp* body *Husen et al.* [2004] found in which they saw %Vp change values of up to -6%. However, *Husen et al.* [2004] noted low Vp values in the caldera starting from ~8 km and we see

them starting from ~5 km. Similar results have also been reported in previous tomographic studies of the Yellowstone system [*Benz and Smith*, 1984; *Miller and Smith*, 1999].

Similar to *Husen et al*. [2004], our model resolves a strong, shallow, low Vp body located in the northwestern part of the model on the NW boundary of the Yellowstone caldera (Figure 6.24). Based on the fact that they saw low Vp and low Vp/Vs ratios, *Husen et al.* [2004] interpreted this as a CO_2 filled gas body.

These two low Vp bodies can be seen in Figure 6.30 where the -2% isosurface (red) is plotted to show the outline of the newly imaged Yellowstone magma reservoir and the -6% isosurface (blue) is plotted to show the shallow low Vp body on the NW boundary of the Yellowstone caldera. The newly mapped crustal magma reservoir is ~50% larger than previously mapped by *Husen et al*. [2004].

The new feature in our model is the strong, low Vp body that extends off of the Yellowstone magma reservoir at shallower depths of less than 5 km with a P-wave velocity reduction up to -5% (Figures 6.24 and 6.30). A similar feature was imaged, with lower resolution, by *Miller and Smith* [1999] (Figure 6.31b), however, due to limited ray coverage due to a lack of earthquakes and station coverage in the northeast caldera area, *Husen et al.* [2004] was unable to resolve this anomaly.

The low P-wave velocities to the NE of the Yellowstone caldera coincide with the largest Bouguer gravity low in Yellowstone (Figure 6.32a). The large gradient in the gravity field NE of the caldera, suggests that the source is shallower here than in other parts of the region. *DeNosaquo et al.* [2009] modeled the gravity data and found that the lowest density material extends ~20 km to the NE of the caldera (Figure 6.32b) similar to

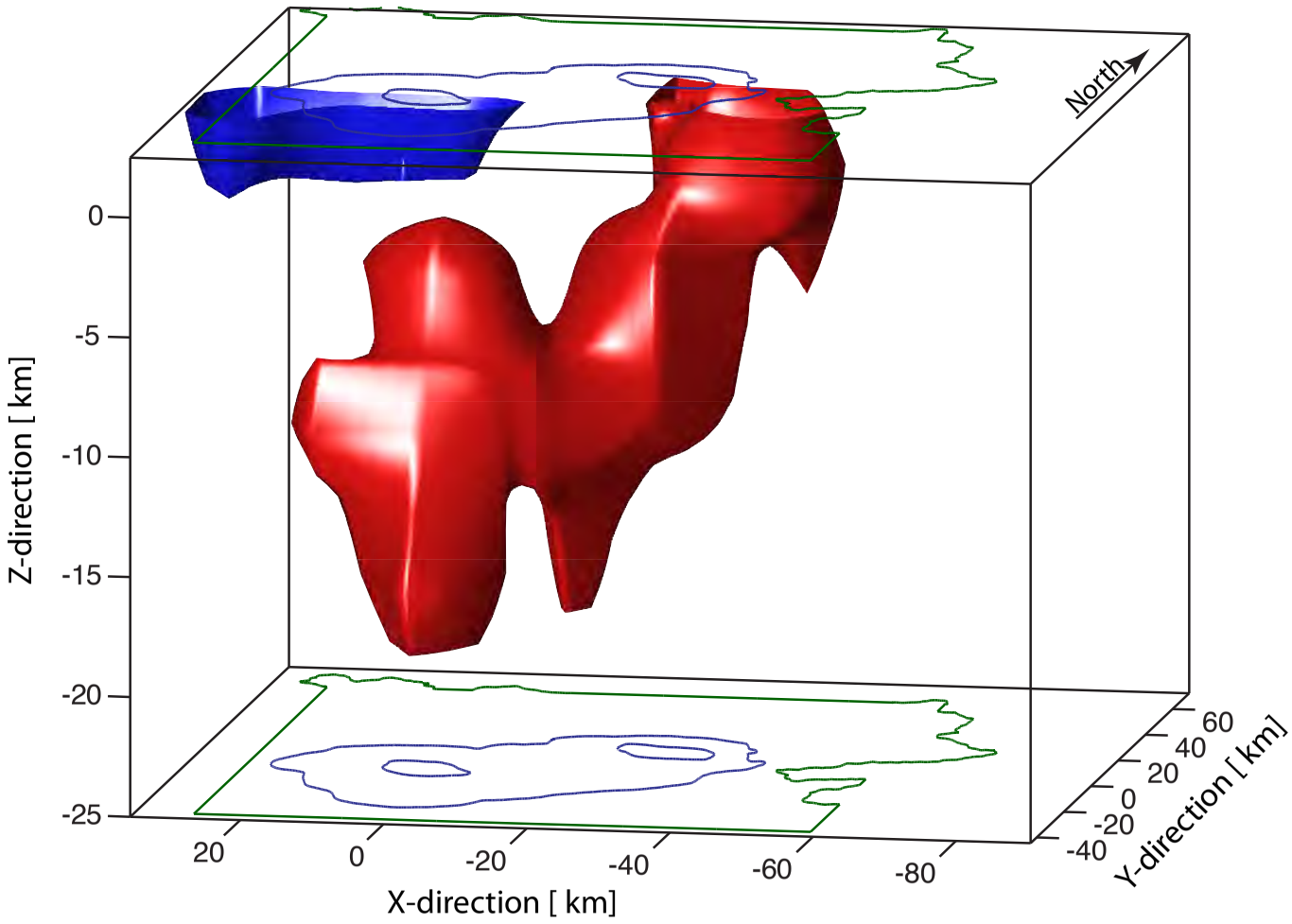

Figure 6.30. A -2% isosurface of the Yellowstone magma reservoir (red) and -6% isosurface of the low Vp body that *Husen et al.* [2004] interpreted as a CO2 gas body (blue). Green line denotes the Yellowstone National Park boundary. Blue lines outline the 0.64 Ma Yellowstone caldera and the two resurgent domes.

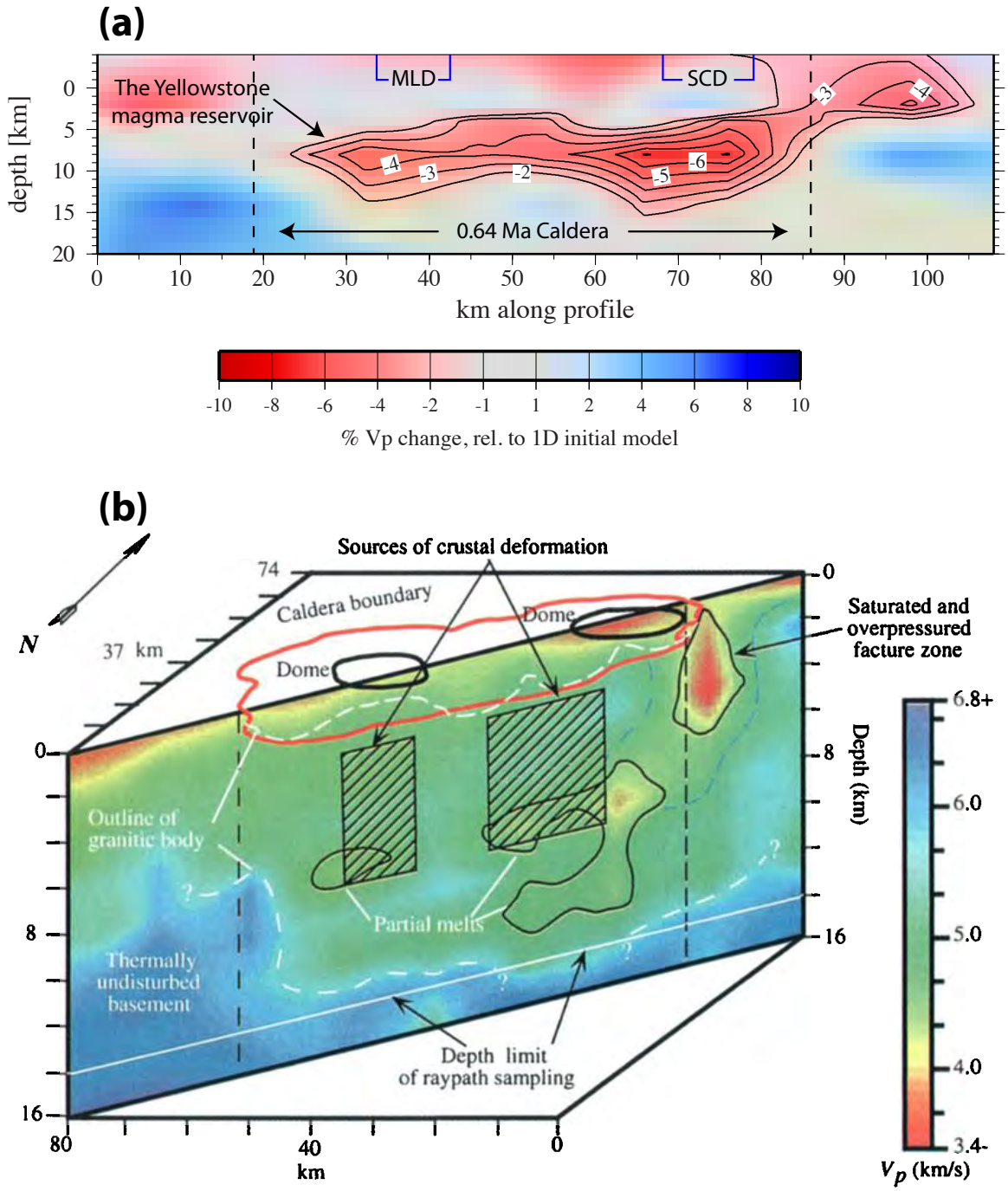

Figure 6.31. Comparison of (a) our final Yellowstone Vp model with that of (b) *Miller and Smith* [1999]. Both models show a shallow, low Vp anomaly just NE of the caldera that is coincident with a low gravity anomaly (shown in Figure 6.32).

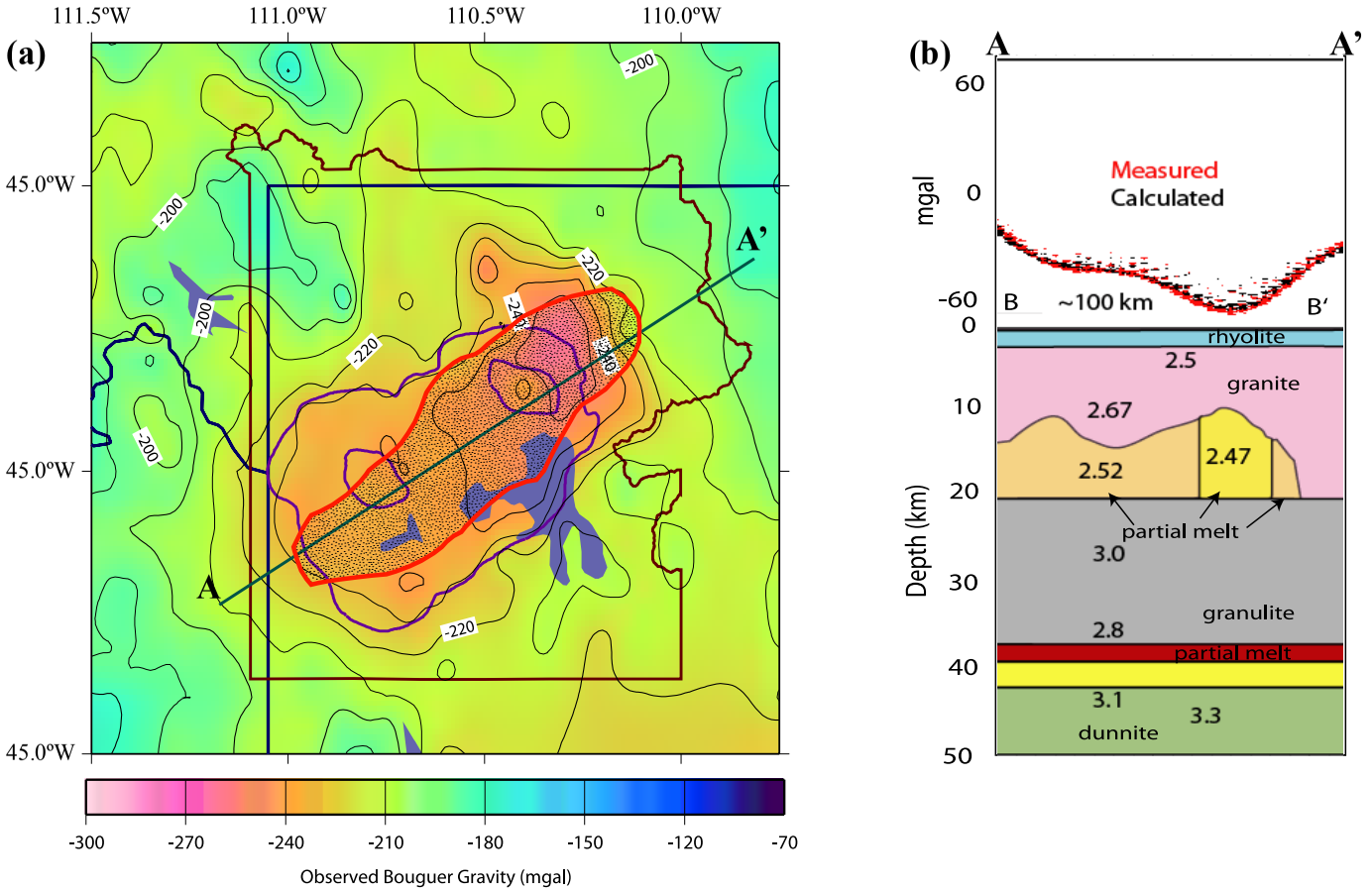

Figure 6.32. (A) Gravity profile, and (B) cross section through the density model for the Yellowstone area. Densities in kg/m^3. The lowest density material extends ~20 km beyond the northeastern edge of the caldera. Red stippled body represents the approximate location of the seismic low velocity body tomographically imaged in this study. The steep gravity gradient in this area indicates that the body responsible for the gravity low is closer to the surface here than inside the caldera. Modified from *DeNosaquo et al.* [2009].

our new results.

Tomographic imaging in the Yellowstone region has revealed a larger Yellowstone magma reservoir that is in much better agreement with previous geophysical datasets such as Bouguer gravity. The new magma reservoir is approximately 90 km long by 30 km wide by 10 km deep giving a total volume of 27,000 km^3. If the magma reservoir has about 10-15% partial melt, that gives a total volume of melt of 2,700 km^3 – 4,050 km^3. In comparison, it is estimated that the largest of the three Yellowstone super eruptions 2.1 million years ago erupted ~2,500 km^3 of material [*Christiansen*, 2001].

Focal depth distribution of hypocenters, from three-dimensional relocations using the new P-wave velocity model derived in this study, reveals a shallowing of hypocenters by ~6 km relative to the surrounding region (Figures 6.28 and 6.29). This is due to the influence of the immense heatflow from the Yellowstone crustal magma reservoir. The shallowest hypocenters occur near the two resurgent domes as well as the NE caldera region (Figure 6.28) corresponding the to strongest low V_P anomalies in the tomographically imaged P-wave velocity model.

As we are better able to image the Yellowstone crustal magma reservoir, our understanding of how it affects the surrounding area will increase. For example, we will be able to better model the observed surface deformation, heat flow, gravity changes, and seismicity patterns with an improved understanding of the areal extent and composition of the magma reservoir. Having a better understanding of the size and composition of the Yellowstone magma reservoir will help us better understand the volcanic and seismic hazards that are present in the world's first national park.

References

Aki, K., and W. H. K. Lee (1976), Determination of three-dimensional velocity anomalies under a seismic array using first P arrival times from local earthquakes, 1, A homogeneous initial model, *J. Geophys. Res.*, *81*, 4381-4399.

Aldersons, F. (2004), Toward three-dimensional crustal structure of the Dead Sea region from local earthquake tomography, Ph.D. thesis, Tel Aviv University, Israel.

Baer, M., and U. Kradolfer (1987), An automatic phase picker for local and teleseismic events, *Bull. Seism. Soc. Am.*, *77*, 1437–1445.

Benz, H. M., and R. B. Smith (1984), Simultaneous inversion for lateral velocity variations and hypocenters in the Yellowstone region using earthquake and refraction data, *J. Geophys. Res.*, *89*, 1208-1220.

Brustle, A., L. Kupperkoch, T. Meier, and W. Friederich (2013), Consistent phase onset determination and their real uncertainties using the example of a test dataset of the temporary EGELADOS network, DGG General Assembly, Leipzig, Germany.

Chang, W. -L., R.B. Smith, C. Wicks, J. Farrell, and C.M. Puskas (2007), Accelerated uplift and magmatic intrusion of the Yellowstone caldera, 2004 to 2006, *Science*, *318*, 952, doi:10.1126/science.1146842.

Chang, W. -L., R. B. Smith, J. Farrell, and C. M. Puskas (2010), An extraordinary episode of Yellowstone caldera uplift, 2004-2010, from GPS and InSAR observations, *Geophys. Res. Lett.*, *37*, L23302, doi:10.1029/2010GL045451.

Christiansen, R.L. (2001), The Quaternary and Pliocene Yellowstone plateau volcanic field of Wyoming, Idaho, and Montana, *U.S. Geol. Surv. Profess. Pap.* 729-G, 145.

Crosson, R. S. (1976a), Crustal structure modeling of earthquake data 1, simultaneous least squares estimation of hypocenter and velocity parameters, *J. Geophys. Res., 81*, 3036-3046.

Crosson, R. S. (1976b), Crustal structure modeling of earthquake data 2, velocity structure of Puget Sound region, Washington, *J. Geophys. Res., 81*, 3047-3054.

DeGroot, M. H. (1975), *Probability and Statistics*, 607 pp., Addison-Wesley, Reading, Mass.

DeNosaquo, K., R. B. Smith, and A. R. Lowry (2009), Density and lithospheric strength models of the Yellowstone-Snake River Plain volcanic system from gravity and heat flow data, *J. Volcanol. Geotherm. Res*., *188*, 108-127.

Di Stefano, R., F. Aldersons, E. Kissling, P. Baccheschi, C. Chiarabba, and D. Giardini (2006), Automatic seismic phase picking and consistent observation error assessment: Application to the Italian seismicity, *Geophys. J. Int*., *165*, 121–134, doi:10.1111/j.1365-246X.2005.02799.x.

Diehl, T., E. Kissling, S. Husen, and F. Aldersons (2009a), Consistent phase picking for regional tomography models: Application to the greater Alpine region, *Geophys. J. Int.*, *176*, 542-554, doi:10.1111/j.1365-246X.2008.03985.x.

Diehl, T., S. Husen, E. Kissling, and N. Deichmann (2009b), High-resolution three-dimensional P-Wave model of the Alpine crust, *Geophys. J. Int.*, *179*, 1133-1147, doi:10.1111/j.1365-246X.2009.04331.x.

Douglas, A., D. Bowers, and J. B. Young (1997), On the onset of P seismograms, *Geophys. J. Int*., *129*, 681–690.

Eberhart-Phillips, D. (1986), Three-dimensional velocity structure in northern California Coast Range from inversion of local earthquake arrival times, *Bull. Seism. Soc. Am.*, *76*, 1025–1052.

Eberhart-Phillips, D. (1990), Three-dimensional P and S velocity structure in the Coalinga region, California, *J. Geophys. Res.*, *95*, 15,343–15,363.

Farrell, J.M., S. Husen, and R.B. Smith (2009), Earthquake swarm and *b*-value characterization of the Yellowstone volcano-tectonic system. *J. Volcanol. Geotherm. Res.*, *188* (1–3), 260–276.

Farrell, J., R. B. Smith, T. Taira, W. L. Chang, and C. M. Puskas (2010), Dynamics and rapid migration of the energetic 2008-2009 Yellowstone Lake earthquake swarm, *Geophys. Res. Lett.*, *37*, L19305, doi:10.1029/2010GL044605.

Fisher, R. A. (1936), The use of multiple measurements in taxonomic problems, *Ann. Eugenics*, *7*, 179–188.

Fisher, R. A. (1938), The statistical utilization of multiple measurements, *Ann. Eugenics*, *8*, 376–386.

Hampel, A., and R. Hetzel (2008), Slip reversals on active normal faults related to the inflation and deflation of magma chambers: Numerical modeling with application to the Yellowstone-Teton region, *Geophys. Res. Lett.*, *35*, L07301, doi:10.1029/2008GL033226.

Haslinger, F., and E. Kissling (2001), Investigating effects of three-dimensional ray tracing methods in local earthquake tomography, *Phys. Earth Planet. Inter*., *123*, 103–114.

Husen, S., E. Kissling, and E. R. Flueh (2000), Local earthquake tomography of shallow subduction in north Chile: A combined onshore and offshore study, *J. Geophys. Res.*, *105*, 28,183–28,198.

Husen, S., R. B. Smith, and G. P. Waite (2004), Evidence for gas and magmatic sources beneath the Yellowstone volcanic field from seismic tomographic imaging, *J. Volcanol. Geotherm. Res., 131*, 397–410.

Kissling, E. (1988), Geotomography with local earthquake data, *Rev. Geophys.*, *26*, 659–698.

Kissling, E., U. Kradolfer, and H. Maurer (1995), VELEST user's guide – short introduction, Tech. rep., Institute of Geophysics and Swiss Seismological Service, ETH, Zurich.

Kissling, E., S. Husen, and F. Haslinger (2001), Model parametrization in seismic tomography: A choice of consequence for the solution quality, *Phys. EarthPlanet. Inter., 123*, 89–101.

Lehman, J. A., R. B. Smith, and M. M. Schilly (1982), Upper crustal structure of the Yellowstone caldera from seismic delay time analyses and gravity correlations, *J. Geophys. Res.*, *87*(B4), 2713-2730.

Lomax, A., and A. Curtis (2001), Fast, probabilistic earthquake location in 3D models using Oct-Tree Importance sampling, *Geophys. Res. Abstr.*, 3.

Lomax, A., J. Virieux, P. Volant, and C. Thierry-Berge (2000), Probabilistic earthquake location in 3D and layered models, *Advances in Seismic Event Location*, 101-134 pp., Kluwer Acad., Norwell, Mass.

Massin, F., J. Farrell, and R. B. Smith (2013), Repeating earthquakes in the Yellowstone volcanic field: Implications for rupture dynamics, ground deformation, and migration in earthquake swarms, *J. Volcanol. Geotherm. Res.*, *257*, 159-173, doi: 10.1016/j.jvolgeores.2013.03.022.

Miller, D. S., and R. B. Smith (1999), *P* and *S* velocity structure of the Yellowstone volcanic field from local earthquake and controlled source tomography, *J. Geophys. Res.*, *104*, 15105-15121.

Moser, T. J., T. van Eck, and G. Nolet (1992), Hypocenter determination in strongly heterogeneous earth models using the shortest path method, *J. Geophys. Res*., *97*, 6563-6572.

Pavlis, G. L., and J. R. Booker (1980), The mixed discrete-continuous inverse problem: Application to the simultaneous determination of earthquake hypocenters and velocity structure, *J. Geophys. Res., 85*, 4801-4810.

Puskas, C.M., R.B. Smith, C.M. Meertens, and W.L. Chang (2007), Crustal deformation of the Yellowstone-Snake River Plain volcano-tectonic system: Campaign and continuous GPS observations, 1987-2004, *J. Geophys. Res.*, *112*, B03401, doi:10.1029/2006JB004325.

Schilly, M. M., R. B. Smith, L. W. Braile, and J. Ansorge (1982), The 1978 Yellowstone-Eastern Snake River Plain seismic profiling experiment: Data and upper crustal structure of the Yellowstone region, *J. Geophys. Res.*, *87*(B4), 2692-2704.

Smith, R. B., and R. L. Bruhn (1984), Intraplate extensional tectonics of the eastern basin-range: Inferences on structural style from seismic reflection data, regional tectonics, and thermal-mechanical models of brittle-ductile deformation, *J. Geophys. Res.*, *89*, 5733-5762.

Smith, R.B., and D.D. Blackwell (2000), Heat flow and energetics of Yellowstone Lake hydrothermal systems, *Eos Trans. AGU*, *81*(48), Fall Meet. Suppl., Abstract V22F-17.

Smith, R. B., and L. Siegel (2000), *Windows into the Earth: The Geology of Yellowstone and Grand Teton Parks*, Oxford University Press, London, 247.

Smith, R. B., M. M. Schilly, L. W. Braile, J. Ansorge, J. L. Lehman, M. R. Baker, C. Prodehl, J. H. Healy, S. Mueller, and R. W. Greensfelder (1982), The 1978 Yellowstone-Eastern Snake River Plain seismic profiling experiment: Crustal structure of the Yellowstone region and experiment design, *J. Geophys. Res*., *87*(B4), 2583-2596.

Smith, R.B., M. Jordan, B. Steinberger, C.M. Puskas, J. Farrell, G.P. Waite, S. Husen, W.L. Chang, and R. O'Connell (2009), Geodynamics of the Yellowstone hotspot and mantle plume: Seismic and GPS imaging, kinematics, and mantle flow, *J. Volcanol. Geotherm. Res.*, *188*, 26-56.

Spetzler, J., and R. Snieder (2004), The Fresnel volume and transmitted waves, *Geophysics*, *69*, 653– 663, doi:10.1190/1.1759451.

Tarantola, A., and B. Valette (1982), Inverse problems = Quest for information, *J. Geophys. Res.*, *50*, 159-170.

Thurber, C. H. (1983), Earthquake locations and three-dimensional crustal structure in the Coyote Lake area, central California, *J. Geophys. Res*., *88,* 8226–8236.

Waite, G.P., and R.B. Smith (2002), Seismic evidence for fluid migration accompanying subsidence of the Yellowstone caldera, *J. Geophys. Res.*, *107*(B9), 2177, doi:10.1029/2001JB000586.

CHAPTER 7

DISCUSSION AND CONCLUSIONS

The 2008-2009 Yellowstone Lake Swam and the 2010 Madison Plateau Swarm

The 2008-2009 Yellowstone Lake swarm was interpreted to be caused by an upper-crustal dike-intrusion of magmatically-derived fluids (partial melt, hydrothermal fluids, and gases) derived from the shallow Yellowstone magma reservoir. The fluid would have migrated along the pre-existing fracture zone down a pressure gradient that extends northward toward the largest part of the magma reservoir (Figure 3.8b). We also note that this unusual earthquake swarm with a high northward migration rate, ~1 km/day, and distinct shallowing toward the surface, may represent the first observations of a dike intrusion involving magmatic fluid derived from the crustal magma reservoir that failed to break the surface. Moreover, the observed temporal-spatial seismic and deformation pattern reflects the style of volcano-tectonic activity that can be expected in the Yellowstone volcanic field and that could lead to triggering of larger earthquakes or volcanic eruptions.

The 2010 Madison Plateau swarm, of over 2,300 earthquakes with magnitudes ranging from $-0.6 \leq M_C \leq 3.9$, in contrast was dominated by strike-slip to oblique strike-slip earthquakes that appear to be more tectonic in nature. This swarm may have

occurred on a fault associated with the M_W7.3 1959 Hebgen Lake earthquake but was covered by young lava flows of the youthful Yellowstone caldera volcanism. Events for this swarm were located in an area of increased Coulomb stress induced by the M_W7.3 Hebgen Lake earthquake (Figure 3.10) [*Chang and Smith*, 2002] and therefore also may have been triggered by the long-term stress perturbation caused by the MW7.3 1959 earthquake.

Alternatively, this swarm, along with the 2008-2009 Yellowstone Lake swarm, may be related to ongoing seismicity and volcanic activity of the Yellowstone volcanic system and may play a vital roll in the release of magmatic and magmatically derived fluids from the magma reservoir to the surrounding area. We note that following the 2008-2009 Yellowstone Lake swarm, caldera uplift rates decreased from ~3.5 cm/yr to ~1.7 cm/yr. Following the 2010 Madison Plateau swarm, caldera deformation reversed from ~1.7 cm/yr of uplift to ~2.6 cm/yr of subsidence (Figures 1.6 and 3.11). A similar pattern of deformation reversal occurred coincident with the 1985 swarm as well [*Waite and Smith*, 2002].

Earthquake swarms are a common phenomenon in volcanic settings and are widely thought to be induced in part by the migration of fluids in the subsurface. Thus, large swarms in Yellowstone may play an important role as "pressure relief valves" allowing the release of magmatic and magmatically-derived fluids from the constantly recharging magma reservoir into the crustal volume outside the caldera, allowing the caldera deformation pattern to change from uplift to subsidence. The swarms indicate the fracturing of rock, with may act to release pressure within the magmatic and hydrothermal reservoir.

These changes in pressure and the changing deformation pattern of the Yellowstone caldera may have an influence on the surrounding region and can potentially induce seismicity such as the 2010 Gros Ventre Eartqhuake Sequence near Grand Teton National Park to the south of Yellowstone.

The 2010 Gros Ventre Earthquake Sequence

The majority of the seismicity in the Teton region occurs in an area east of the high slip-rate Teton fault in the Gros Ventre range. This is an area of persistent earthquake activity with historical reports of felt events dating back to the late 1800s. While the Teton fault is the source of most of the seismic hazard in the area, the Gros Ventre region is a separate hazard consideration due the persistent seismicity and the long record of felt events with magnitudes up to M5. In addition, the Gros Ventre range has steep slopes with rocks vulnerable to mass wasting including triggered landslides from seismic sources.

Speculatively, we also point out that the Teton-Gros Ventre area lies within the area that is directly affected by stress perturbations, loading and unloading, caused by inflation and deflation of the Yellowstone caldera that markedly triggers earthquakes on pre-existing faults that are at near failure. This idea is emphasized by the recent study by *Hampel and Hetzel* [2008] who employed finite element models to explain how Yellowstone caldera deformation sufficiently perturbs the stresses on the Teton fault to advance or retard the return time of earthquakes.

The 2010 Gros Ventre sequence contained more than 200 events with a M_C=5 main-shock that was widely felt throughout the region. Analysis of the source

mechanisms of the main-shock and the aftershocks shows that the events are dominantly oblique strike-slip events that are occurring on a NW-SE striking fault plane dipping 80º to the NE. There are no mapped faults in the immediate area of the seismicity, however, there are numerous NW-SE striking Laramide aged thrust faults in the area. In addition, there are many anticline structures in the area including the Spread Creek anticline to the north, and the the Ramshorn and Red Hills anticlines in the same area of the 2010 Gros Ventre sequence [*Love et al.*, 1951]. It is plausible that these events are reactivating these structures.

In order to better understand the processes at depth that are causing this persistent seismic activity in the Gros Ventre region, more seismographs need to be installed, in particular to the east of the Jackson Hole Basin. This would allow us to obtain better-constrained hypocenter locations. With better-constrained hypocenter locations, we could use the earthquakes to map out structures at depth.

In addition to seismicity, other geophysical characteristics of the Yellowstone volcanic system can give us further insight into how the system works and how these different processes interact with each other.

Temporal Gravity Changes in Relation to the 2004-2010 Accelerated Uplift of the Yellowstone Caldera

Our results to date show that there is little correlation between the accelerated uplift of the Yellowstone caldera from 2004-2010 and relative changes in gravity for that time period. This finding points to the assumption that the uplift may be caused solely by pressurization of the deep hydrothermal system, lacking sufficient mass transfer.

However, the independent analysis of GPS and InSAR data by *Chang et al.* [2007, 2010] reveal that the most likely source of the uplift is an expanding sill at the top of the magma reservoir indicating a magmatic source for the accelerated uplift.

These gravity measurements will be valuable for long-term comparisons of the changes in the gravity field in and around the Yellowstone volcanic system [e.g., *DeNosaquo et al*., 2009] and are a complimentary dataset to other types of data being collected such as deformation using GPS and the seismic velocity structure of the system via tomographic inversions.

Given the large Bouguer gravity low associated with low-density material beneath the Yellowstone caldera, it is natural to investigate the seismic velocity structure in the shallow crust to identify and analyze a possible magma reservoir that occupies the shallow crust beneath the Yellowstone caldera.

Tomographic Imaging of the Yellowstone Volcanic System

The main research in this study focused on an extensive analysis of all the digital Yellowstone seismic network data, starting from 45,643 events (1,159,724 waveforms) and finalizing the analyses using 4,520 earthquakes considered of highest quality for tomographic inversion. We then applied local earthquake tomography that revealed a surprising result, namely the elucidation of a large, low Vp body that spans the length of the caldera from as shallow as 5 km to a maximum depth of 16 km. This low Vp body is interpreted as the Yellowstone crustal magma reservoir and is larger than previously imaged by *Husen et al*. [2004] (Figures 6.24 and 6.25).

The P-wave velocity reductions for this body are as high as -7%. This is similar to

the low *Vp* body *Husen et al.* [2004] found in which they saw %Vp change values of up to -6%. However, *Husen et al.* [2004] showed low Vp values in the caldera starting from ~8 km and we see them starting from ~5 km. Similar results have also been reported in previous tomographic studies of the Yellowstone system [*Benz and Smith*, 1984; *Miller and Smith*, 1999].

Similar to *Husen et al*. [2004], our model resolves a strong, shallow, low Vp body located in the northwestern part of the model on the NW boundary of the Yellowstone caldera (Figure 6.24). Based on that fact that they saw low Vp and low Vp/Vs ratios, *Husen et al.* [2004] interpreted this as a CO_2 filled gas body.

These two low Vp bodies can be seen in Figure 6.30 where the -2% isosurface (red) is plotted to show the outline of the newly imaged Yellowstone magma reservoir and the -6% isosurface (blue) is plotted to emphasize the shallow low Vp body on the NW boundary of the Yellowstone caldera. The newly mapped Yellowstone magma reservoir is thus ~50% larger than previously mapped by *Husen et al*. [2004] and implies a much larger partial melt volume that has been previously considered as a volcano hazard source. The new magma reservoir is approximately 90 km long by 30 km wide by 10 km deep giving a total volume of 27,000 km^3. If the magma reservoir has about 10-15% partial melt, that gives a total volume of melt of 2,700 km^3 – 4,050 km^3, respectively. In comparison, it is estimated that the largest of the three Yellowstone super eruptions 2.1 million years ago erupted ~2,500 km^3 of material [*Christiansen*, 2001].

My new tomographic image reveals a low Vp body that extends ~20 km NE of the caldera boundary at depths less than 5 km with a P-wave velocity reduction up to -5%

(Figures 6.24 and 6.30). A similar feature was imaged, but with lower resolution, by *Miller and Smith* [1999] (Figure 6.31b). However, due to limited ray coverage, *Husen et al.* [2004] was unable to resolve this anomaly. The low P-wave velocities to the NE of the Yellowstone caldera coincide with the largest Bouguer gravity low in Yellowstone (Figure 6.32a). The large gradient in the gravity anomaly NE of the caldera, suggests that the source is shallower here than in other parts of the region. *DeNosaquo et al.* [2009] modeled the gravity data and found that the lowest density material extends ~20 km to the NE of the caldera (Figure 6.32b) similar to our new results.

New tomographic imaging in the Yellowstone region has revealed a larger Yellowstone magma reservoir that is in better agreement with previous geophysical datasets such as Bouguer gravity. In addition, focal depth distribution of hypocenters, from three-dimensional relocations using the new P-wave velocity model derived in this study, reveals a shallowing of hypocenters by ~6 km relative to the surrounding region (Figures 6.28 and 6.29). This is due to the influence of the high heatflow from the Yellowstone crustal magma reservoir. The shallowest hypocenters occur near the two resurgent domes as well as the NE caldera region (Figure 6.28) corresponding the to strongest low V_P anomalies in the tomographically imaged P-wave velocity model.

The new understanding of the size of the magma reservoir allows us to better estimate the volume of partial melt that exists below the caldera. In addition, using tools such as Finite Element Models (FEM) with the new, larger magma reservoir allows us to better model the observed deformation and associated crustal properties as well as how the Yellowstone volcanic system interacts with the surrounding large Basin and Range normal faults. Having a better understanding of the size and composition of the

Yellowstone magma reservoir will help us better understand the volcanic and seismic hazards that are present in the world's first national park.

References

Benz, H. M., and R. B. Smith (1984), Simultaneous inversion for lateral velocity variations and hypocenters in the Yellowstone region using earthquake and refraction data, *J. Geophys. Res.*, *89*, 1208-1220.

Chang, W. –L., and R. B. Smith (2002), Integrated seismic-hazard analysis of the Wasatch Front, Utah, *Bull. Seism. Soc. Am., 92*, no. 5, 1904-1922.

Chang, W. -L, R. B. Smith, C. Wicks, C. M. Puskas, and J. Farrell (2007), Accelerated uplift and source models of the Yellowstone caldera, 2004-2006, from GPS and InSAR observations, *Science, 318*(5852): 952-956, doi:10.1126/science.1146842.

Chang, W. -L., R. B. Smith, J. Farrell, and C. M. Puskas (2010), An extraordinary episode of Yellowstone caldera uplift, 2004-2010, from GPS and InSAR observations, *Geophys. Res. Lett.*, *37*, L23302, doi:10.1029/2010GL045451.

Christiansen, R. L. (2001), The Quaternary and Pliocene Yellowstone plateau volcanic field of Wyoming, Idaho, and Montana, *U.S. Geol. Surv. Profess. Pap. 729-G*, 145.

DeNosaquo, K., R. B. Smith, and A. R. Lowry (2009), Density and lithospheric strength models of the Yellowstone-Snake River Plain volcanic system from gravity and heat flow data, *J. Volcanol. Geotherm. Res*., *188*, 108-127.

Hampel, A., and R. Hetzel (2008), Slip reversals on active normal faults related to the inflation and deflation of magma chambers: Numerical modeling with application to the Yellowstone-Teton region. *Geophys. Res. Lett.*, *35*, L07301, doi:10.1029/2008GL033226.

Husen, S., R. B. Smith, and G. P. Waite (2004), Evidence for gas and magmatic sources beneath the Yellowstone volcanic field from seismic tomographic imaging, *J. Volcanol. Geotherm. Res.*, *131*, 397-410.

Love, J. D., W. R. Keefer, D. C. Duncan, H. R. Gergquist, and R. K. Hose (1951), Geologic map of the Spread Creek-Gros Ventre River area, Teton County, Wyoming, U. S. Geol. Survey Oil and Gas Investigations Map OM 18.

Miller, D. S., and R. B. Smith (1999), *P* and *S* velocity structure of the Yellowstone volcanic field from local earthquake and controlled source tomography, *J. Geophys. Res.*, *104*, 15105-15121.

Waite, G. P., and R. B. Smith (2002), Seismic evidence for fluid migration accompanying subsidence of the Yellowstone caldera, *J. Geophys. Res.*, *107*(B9), 2177, doi:10.1029/2001JB000586.

CHAPTER 8

CONCLUDING REMARKS

Earthquake data from the Yellowstone Seismic Network were used to produce a new three-dimensional P-wave velocity model of the upper and midcrustal structure of the Yellowstone volcanic system. An automatic picking algorithm was calibrated specifically for our Yellowstone data and was used to produce a high-quality, consistent set of P-wave first motion arrival times for Yellowstone from 1984-2011. Using only the highest quality automatic picks and locations, we were able to produce a new velocity model using 4,520 earthquakes and 48,622 arrival times. The derived model reveals that the Yellowstone magma reservoir is ~50% larger than previously imaged and notably extends ~20 km beyond the NE caldera boundary and shallows to depths of less than 5 km. This body of low P-wave velocities is coincident with the largest negative Bouguer gravity anomaly in the region of -60 mGals indicating a shallow, low-density, low-velocity body of material that we interpret to be the Yellowstone magma reservoir. This is the largest magma reservoir tomographically imaged in the world. The Toba caldera may be slightly larger than the Yellowstone caldera but tomographic imaging of Toba shows individual pockets of low velocity material that is not continuous [*Masturyono et al.*, 2001]

The Yellowstone magma reservoir is a body of partial melt of rhyolitic

composition that is fed by a mantle plume related to the Yellowstone hotspot (Figure 8.1). The magma reservoir provides the heat and energy to produce high seismicity rate, high heatflow, ground deformation, and hydrothermal activity that we see and record on the surface. In addition, the large earthquake swarms that occur in Yellowstone may be related to the movement of magmatic or magmatically-derived fluids as they move away from the magma reservoir and eventually escape the caldera into the surrounding brittle regime. These fluids in turn produce earthquakes that are recorded by the Yellowstone seismic network. These swarms may be acting as "pressure relief valves" as fluids escape the volcanic system and allow the caldera deformation pattern to reverse from uplift to subsidence. The fracturing of the rock both creates swarm earthquakes and releases fluid pressure.

In addition, the effects of the constantly deforming Yellowstone volcanic system may extend regionally to the Teton area to the south. A recent earthquake sequence in 2010 beneath the Gros Ventre range may have occurred on buried, reactivated Laramide thrust faults or anticlinal structures and may have been induced due to the stresses imparted on the system by the Yellowstone deformation ~ 70 km to the north.

All together, this study elucidates the importance of having an integrative approach to studying the active processes of the Yellowstone volcanic system. There are many active processes at play and each one affects the other in certain ways. The Yellowstone hotspot is fed by a mantle plume, which feeds a crustal magma reservoir. The crustal magma reservoir provides the heat and energy to feed the world famous hydrothermal features of Yellowstone as well as the surface deformation, high seismicity rate, high heatflow, and large caldera-forming eruptions that have occurred in the past (Figure 8.2).

Figure 8.1. Schematic diagram showing the upper mantle and crustal structure beneath the Yellowstone region. The Yellowstone volcano is fed by a deep mantle plume source, which in turn feeds the Yellowstone crustal magma reservoir. The magma reservoir feeds the hydrothermal system and provides the heat and energy that is needed to produce the intense seismicity, ground deformation, and heatflow that are measured on the surface.

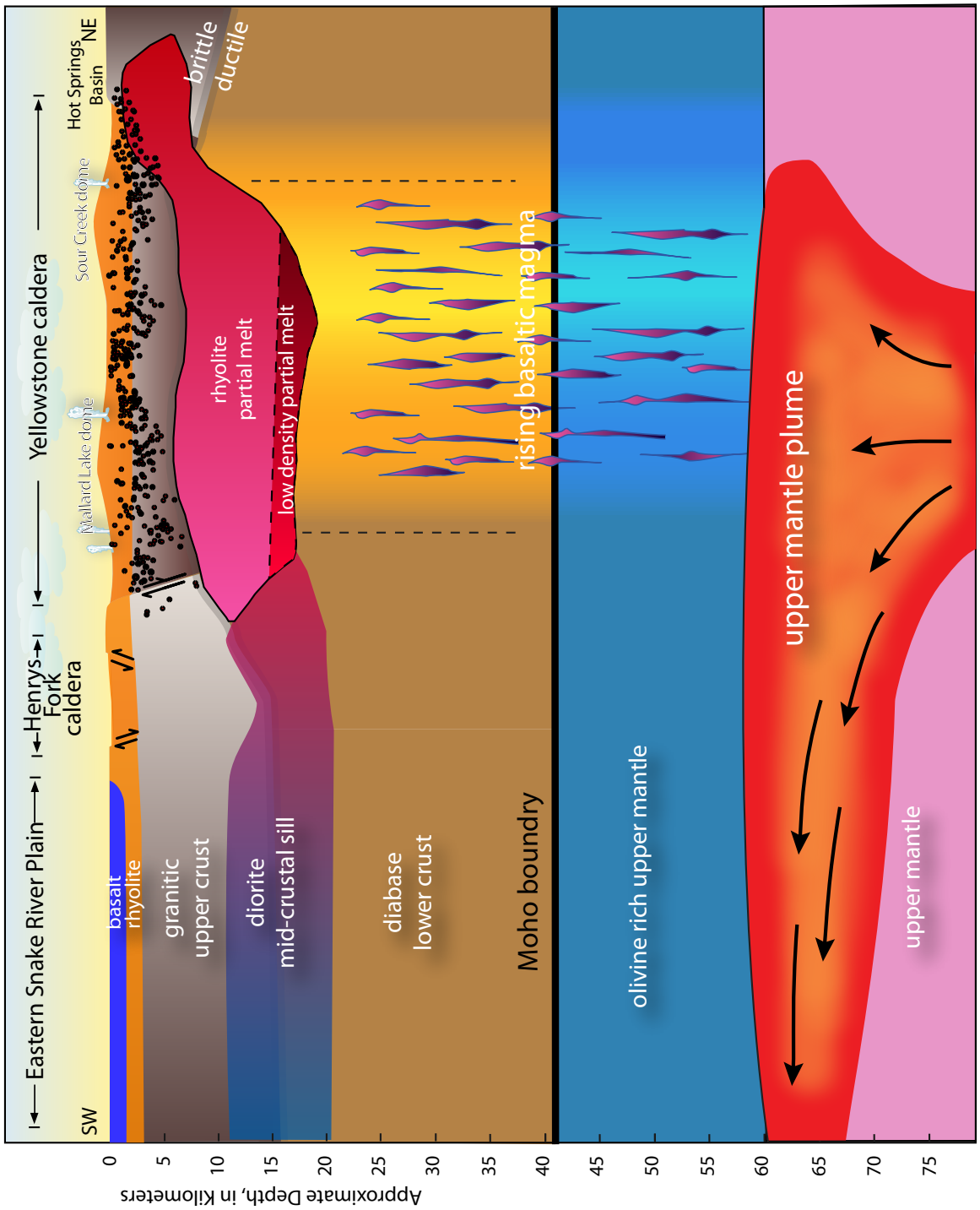
Eastern Snake River Plain
Henrys Fork caldera
Yellowstone caldera
SW
NE
Hot Springs Basin
Sour Creek dome
Mallard Lake dome
basalt
rhyolite
granitic upper crust
diorite mid-crustal sill
diabase lower crust
Moho boundry
olivine rich upper mantle
upper mantle
rhyolite partial melt
low density partial melt
rising basaltic magma
upper mantle plume
brittle
ductile
Approximate Depth, in Kilometers
0
5
10
15
20
25
30
35
40
45
50
55
60
65
70
75

Figure 8.2. The integrated Yellowstone volcanic system showing (a) the numerous inter-related active processes that make up the Yellowstone volcanic system, (b) the Yellowstone mantle plume, (c) the Yellowstone crustal magma reservoir, and (d) the associated surface deformation. All these processes are related and it is necessary to understand how they relate, and affect each other in order to understand the system as a whole.

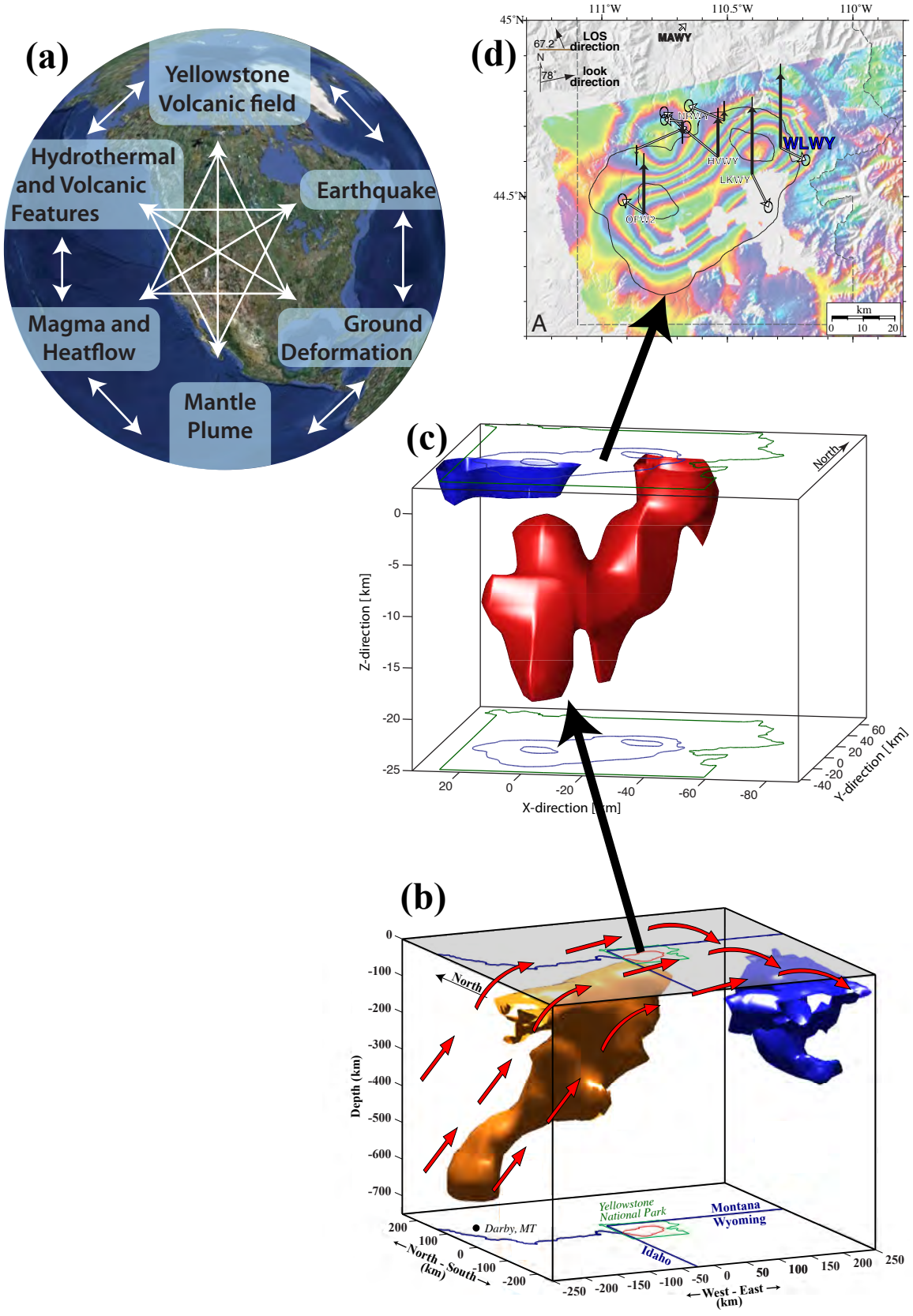
(a)
Yellowstone Volcanic field
Hydrothermal and Volcanic Features
Earthquake
Magma and Heatflow
Ground Deformation
Mantle Plume
(d)
111°W
110.5°W
110°W
45°N
44.5°N
LOS direction
look direction
MAWY
WLWY
HWWY
LKWY
OFWY
A
km
0 10 20
(c)
North
Z-direction [km]
X-direction [km]
Y-direction [km]
(b)
North
Depth (km)
Darby, MT
Yellowstone National Park
Montana
Wyoming
Idaho
North - South (km)
West - East (km)

Having a better understanding of the size and composition of the Yellowstone magma reservoir, allows us to better understand the other active processes that are directly related to it. Understanding the amount of partial melt available will help us better understand the volcanic hazards related to large volcanic eruptions. Understanding how and why earthquake swarms occur in Yellowstone will help us better respond to the next large swarm and be able to provide accurate information to the Park Service and general public.

References

Masturyono, R. McCaffrey, D. A. Wark, S. W. Roecker, F. Ibrahim, G. Ibrahim, and Sukhyar (2001), Distribution of magma beneath the Toba caldera complex, north Sumatra, Indonesia, constrained by three-dimensional P wave velocities, seismicity, and gravity data, *Geochem. Geophys. Geosyst.*, *2*, doi:10.1029/2000GC000096.